Università Politecnica delle Marche
Scuola di Dottorato di Ricerca in Scienze dell'Ingegneria
Corso di Dottorato in Ingegneria Industriale

Inverse methods for three-dimensional volumetric acoustic mapping

Ph.D. Dissertation of:
Gianmarco Battista

Supervisor:
Prof. Paolo Castellini

Assistant Supervisor:
Dr. Paolo Chiariotti

Ph.D. Course coordinator:
Prof. F. Mandorli

XVII edition - New series

Abstract

This thesis provides a study on volumetric acoustic source mapping with microphone array measurements. The topic has rarely been addressed in literature, despite its importance in some applications such as aeroacoustics. The aim is to remove the hypothesis of acoustic sources confined on surfaces, typical of common acoustic imaging applications. This assumption may not be true and produce misleading results. After the identification of additional issues to deal with, inverse methods have been chosen to cope them. Two methods have been proposed and both are based on the method of Iteratively Re-weighted Least Squares (IRLS) to obtain sparse solutions. This approach is applied to Equivalent Source Method and Covariance Matrix Fitting, thus leading to ESM-IRLS and CMF-IRLS techniques. A tailored version of IRLS for acoustic problems has been developed in this work and is strictly linked to Bayesian Approach to inverse acoustic problems. An improved regularization strategy, rooted on Bayesian Regularization, has been developed to fulfil the needs of IRLS. Indeed, Bayesian Iterative Regularization makes IRLS able to produce accurate and reliable results. A novel use of CLEAN-SC as decomposition tool of Cross-Spectral Matrix is proposed and compared with the standard Eigenmode Decomposition, when combined with inverse methods. Methods proposed have been validated on simulated test cases that represent the conditions of standard and volumetric mapping. Also validation on experimental data is provided. The first is an airfoil in open jet, which is mapped with single planar array. The second is an aircraft model in wind tunnel, where a comparison between the use of one or two planar arrays is performed. This work aims at showing the feasibility of volumetric acoustic mapping with inverse methods, despite its intrinsic difficulty. A detailed discussion on theoretical hypothesis and algorithmic tricks necessary to achieve this result is provided.

Contents

List of Figures

List of Tables

Chapter 1

Introduction

Acoustic source characterisation is a research area of interest for many industrial sectors, such as aeronautics or automotive. Indeed, vehicle manufacturer in general are requested to observe specifications and regulations in force regarding noise emission. From a commercial point of view, acoustic comfort is a crucial aspect for passengers that affects quality perceived by customers. Therefore, engineers need tools to characterise and study acoustic noise radiation of products during their design phase, test phase and after their realization. In this way, focused intervention can be done in order to reduce noise emissions and meet the acoustic performance requested. Identification of sound sources means obtaining spatial information about their location and providing quantitative information about their level. Several techniques were developed over last decades in order to achieve these results. In industrial context, time required for testing plays a key role in the choice of measurement technique. For this reason, microphone array based techniques are of great interest for this application. Basically, an array is a set of microphones, arranged in known locations, put in front of the object to characterise. Once measurement setup is ready, only few seconds of data acquisition are sufficient to produce the acoustic map which makes possible to retrieve both location and strength of sound sources. These techniques are commonly referred to as "acoustic imaging", since the output is an acoustic map, hence an "image of acoustic emission" by analogy with photography. What really makes the difference is the method used to elaborate pressure data acquired by microphones. Commonly, acoustic imaging techniques are used to produce a map on a plane or a three-dimensional surface representing the object to characterise. If this assumption is true in some applications, it may not be true in others, such as aeroacoustic ones, and return misleading results. In fact, acoustic sources are not always confined in the surface chosen to produce the map. For this reason, a method capable of returning an acoustic map of a volume will improve the effectiveness of acoustic imaging in this kind of applications

The core idea of this thesis is to provide a systematic study in the field of volumetric three-dimensional acoustic mapping, since this topic has rarely been addressed in literature, despite its importance. The the aim is to develop acoustic mapping techniques tailored to volumetric applications. Starting from same data used in common applications, the methods proposed in this work can recover location of sound sources in the three-dimensional space and estimate their strengths. The problem has been faced from two points of view. On the one hand, the use of a single planar array is made, since it is the commonest measurement setup. Even though it is not well suited for volumetric source localization, a method capable of volumetric mapping in this condition allows to not modify the measurement setup or to re-process data already acquired and simply obtain more information from maps. On the other hand, the use of multiple planar arrays looking at the object of interest from different views is investigated with the same methods and aims. Two aeroacoustic experimental applications are presented, since this is the field that mostly gains advantage from the volumetric approach, but the methods and the strategies developed in this work are general enough for any application that requires volumetric sound source identification.

The thesis is organised as follows. Chapter 2 provides an overview of acoustic source mapping techniques useful for the scope of this work. This part firstly introduces basic techniques, such as beamforming, and then more refined and complex methods, i.e. deconvolution techniques and inverse methods. In the following part, a literature review about three-dimensional volumetric mapping is provided. The last part of this chapter treats the theory useful as basis for the rest of the thesis. Chapter 3 is the core of this thesis. Its first part is dedicated to the analysis of the problem of volumetric acoustic mapping and related additional issues which entails with respect to common approach. In the second part, inverse methods developed in this work are discussed in detail. Finally, the last part is devoted to application of proposed methods on simulated experiments and to the analysis of results. Chapter 5 is entirely dedicated to experimental applications of volumetric mapping, where two aeroacoustic test cases are presented. The first one is the acoustic mapping of an airfoil in open jet with a single planar array. The aim of this application is to show the feasibility of volumetric mapping using only a planar array. The second application is on a 1/7-th scaled model of a regional aircraft in Pinifarina Wind Tunnel. This facility hosts two planar arrays: one on top of the test section and one broadside. In this case, advantages and drawbacks of combining data from multiple array are investigated. Chapter 6 draws the conclusions of the entire work. Further developments and research paths are also discussed in this same chapter.

Chapter 2

Acoustic mapping techniques: Review and Theory

2.1 Literature review

Acoustic source mapping techniques based on microphone arrays are extensively used for noise source localization and quantification. These techniques are important tools for engineers that helps to identify and rank acoustic noise produced by an object. Application range is wide, but it is worth mentioning, in particular, automotive and aeronautics industrial sectors. Several techniques were developed for specific applications and/or to overcome specific limitations. A first classification can be done distinguishing *time domain* from *frequency domain* techniques. The former can be used, for example, as super-directive microphones for signal extraction, while the latter, which are object of interest in this thesis, are the most common for source characterization. Other classifications can be found in literature that group methods depending on different characteristics, problem formulation, array shape and others. A complete review of concepts about acoustic imaging techniques, from the very basics to more advanced ones, can be found in [12]. In the same work, best practice to design an acoustic test, having the purpose of sound source localization and quantification, is treated. Literature review of this thesis focuses the attention on three kind of techniques: *beamforming*, *deconvolution techniques* and *inverse methods*. After a brief description of most diffused techniques available in literature, the review is focused on three-dimensional volumetric mapping studies conducted in literature, since they represent the starting point of this thesis.

2.1.1 Beamforming

The oldest and commonest technique for acoustic source mapping is the *acoustic beamforming* [34, 17]. A *beamformer* is intended as the combination of a microphone array and an algorithm which applies a spatial filter on pressure data. Beamforming algorithms, such as *Delay-and-Sum* (DAS) [4] and *Conventional Beamforming* (CB) [55], virtually focus the array on a point/direction and return the source level as if there were only the source in that point/direction. Once scanned all points/directions in the region of interest, the whole map is obtained. When plane waves are assumed the beamformer is steered towards a specific direction (infinite distance focusing), instead when spherical waves are assumed the beamformer is focused on a point source (finite distance focusing). Beamformer characteristics are strongly linked to microphone layout and frequency of analysis, which determine the array spatial impulse response, the so-called Point Spread Function (PSF). The ideal PSF is a *Dirac delta*, i.e. a unique and unitary peak in the source position and zero everywhere else. Real PSFs give only finite resolution due to the *mainlobe* size and limited dynamics due to artefacts named *sidelobes*. Resolution is the ability to distinguish close sources and is limited by the *mainlobe width*, defined as the distance between the main peak and the first minimum according to *Rayleigh criterion*. Sidelobes are caused by the non perfect ability to suppress source waves coming from other directions with respect to the focusing one. A measure of useful dynamics of a beamforming system is the *Maximum Sidelobe level* (MSL), intended as the level of the highest sidelobe.

The main issue is to design an array having desired characteristics, since it is difficult to foresee PSF characteristics of particular microphone layout. Some rule of thumb are known. For example regular arrays have a lot of regularly spaced sidelobes and high MSL, therefore they are not appropriate for beamforming. In fact, irregular layouts are preferred for these techniques, but a trial-and-error procedure for array design is very time consuming and not feasible in industrial context. Different strategies are proposed in literature to generate a microphone layout in order to control some characteristics. For example Malgoezar et al. [32] proposed a method to optimize microphone positions in order to reduce the presence of sidelobes in a region around the mainlobe and this is obtained minimizing a proper objective function. Instead, Sarradj [48] proposed to arrange microphone using Vogel spirals, leading to the possibility to generate really different layouts setting varying only two parameters. The approach proposed allows to design arrays with Pareto-optimal properties in terms of mainlobe width and MSL. However, it is shown that is not possible to have fine spatial resolution (narrow mainlobe) and high dynamics (low MSL) at the same time and this limits the application of simple beamformers. Beamforming techniques are widely used for their easiness of implementation and robustness, but they provide mediocre performance in terms of resolution and dynamics. Many variants are present in literature to overcome limitations, such as *Functional Beamforming* [18] or *Minimum Variance Distortionless Response Beamforming* (MVDR or Capon) [9].

2.1.2 Deconvolution approaches

Deconvolution techniques have been developed in order to overcome beamforming limitations in terms of spatial resolution and quantification of source strengths. The aim of these methods is to remove the effect of PSF from beamforming map and return as output the real source distribution that has generated the beamforming map, hence pressure data measured at microphone locations. There are different approaches in deconvolution algorithms. The *Deconvolution Approach for the Mapping of Acoustic Sources* (DAMAS) [5, 7] aim to retrieve the source distribution solving a linear system. The unknowns are the source autopowers and the constant term is the beamforming map. Each column of the system matrix is the PSF from each focus point to all other focus points. Even though the system is square, the rank of the matrix is low for practical applications and therefore ill-conditioned. In the original formulation, the system is solved using Gauss-Seidel algorithm with a non-negativity constraint at each iteration to obtain meaningful results. The critical point of the basic DAMAS version is to estimate the optimal number of iterations of Gauss-Seidel procedure. Many variants of DAMAS are present in literature with the aim to speed up the calculations and/or improve the results. The variants DAMAS2 and DAMAS3 [16] are a step forward in terms of speed and robustness but restrict PSF to be traslationally-invariant. Yardibi et al. [51] proposed to add a *sparsity constraint* to DAMAS problem, hence obtaining the *Sparsity Constrained DAMAS* (SC-DAMAS). In this version, the problem is solved minimizing the fitting error and the number of non-zeros elements in the solution. The DAMAS problem can also be reformulated to be solved with different methods such as Non-Negative Least Squares (NNLS), Least Angle Regression Lasso or Orthogonal Matching Pursuit [25]. A further version is the DAMAS-C [8], that makes it possible to deal with correlated source at cost of a non-negligible increase of computational cost.

Another possible deconvolution approach is to decompose *Cross-Spectral Matrix* (CSM) of pressure data in single coherent source components and retrieve position and level of each of them, therefore having no sidelobes in the final map. *Orthogonal Beamforming* (OB) [47] makes the assumption that uncorrelated source components are orthogonal. For this reason an *Eigenmode Decomposition* (ED) of CSM is performed, then CB map is calculated for each component and finally the maximum of each component map is used to build the deconvolved source map. The family of CLEAN algorithms [38] works in slightly different way performing the following steps:

- Calculate the CB map, i.e. the *dirty map*.
- Find the peak of the current dirty map.
- Subtract a properly scaled PSF from the dirty map.
- Put the peak in the *clean map*.

This process is iterated until all sources are extracted from the map. The simplest algorithm is CLEAN-PSF in which the theoretical PSF of point sources are subtracted from the map. Since the theoretical PSF may not be representative of real sources, a more refined method was developed by Sijtsma [38] that estimates actual PSF directly from pressure data exploiting the spatial source coherence [36]. This method is named CLEAN *based on spatial Source Coherence* (CLEAN-SC). This algorithm is one of the most used for deconvolution purposes, due to its robustness and low computational cost. Localization accuracy of OB and CLEAN algorithms are strictly linked to CB accuracy, in contrast with DAMAS algorithm family.

2.1.3 Inverse methods

Beamforming methods aim at solving the inverse problem of source reconstruction from pressure measurements identifying the strength of each potential source independently from the others. This means solving a scalar inverse problem. The aim of inverse methods is to define the direct propagation from a set of elementary sources to measurement locations and retrieve the whole source distribution which optimally approximates measured pressure at microphone locations. In this way, it is possible to take into account also the interaction between coherent and spatially-distributed sources. Clearly, resulting maps are influenced by size, location and discretization of the region of interest with elementary sources, in contrast with beamforming approach. The choice of different kind of elementary sources (e.g. monopoles, dipoles, plane waves) and solution strategies give rise to different methods such as *Generalized Inverse Beamforming* (GIBF) [50], *Equivalent Source Method* (ESM) [43], *Bayesian*

Approach (BA) [1] or *Covariance Matrix Fitting* (CMF) [56] approach (or CMF-C and MACS [57] variants for correlated sources). Inversion of direct acoustic propagation has typical characteristics of ill-posed problem in Hadamard sense [21]. Moreover, source reconstruction with inverse methods suffers the under-determination of the problem due to practical aspects, because generally the number of measurement points is much lower than the number of potential sources. They can be very sensitive to measurement noise and/or other causes of uncertainty. Even though all these added complexities, inverse methods are the most promising in terms of localization and quantification ability, for this reason are of wide interest in literature.

2.2 Three-dimensional volumetric acoustic mapping

In most applications, acoustic source maps are calculated on a plane or on a three-dimensional surface representing the object which is radiating noise. This entails the assumption that all acoustic sources are located on the chosen surface. However, real sources are not necessarily located there and this might cause misleading results. For this reason, it is interesting to extend the region of interest to a volume, thus considering the "volumetric acoustic mapping" approach. In literature, the expression "three-dimensional acoustic mapping" very often means a map on three-dimensional surface in contrast with the the volumetric approach that is the object of interest of this thesis. The most part of attempt in acoustic volumetric imaging available in literature consists of applications of standard techniques to an extended spatial domain. When dealing with volumetric acoustic source mapping, limitations of beamforming become even more evident, mainly because direct beamformers have poor spatial resolution along the focusing direction. Sarradj [46, 45] analyzed the problem for direct beamformers using a single planar array and pointed out that different steering vector formulations (i.e. different spatial filters) are able to provide either correct location or correct level. The conclusion is that deconvolution algorithms are the only possibility to effectively use CB for volumetric mapping. Inverse methods can be successfully used for this purpose with single planar array. Battista et al. [3] presented a specific study about volumetric acoustic mapping and used CMF and ESM approaches to produce maps for accurate localization and quantification of sound sources. Ning et al. [35] exploited Compressed Sensing techniques to produce volumetric maps with a planar array. When multiple planar arrays looking at the object from different point of view are combined, sidelobe level increases dramatically, thus making the use of CB unfeasible even in simple cases. For example, Döbler et al. [14] used CLEAN-SC and three planar arrays in a wind tunnel on a real-sized car. They combined maps obtained from each single array on a part of the car surface that was in line-of-sight with the array, rather than using all microphone as unique array. Another approach is the Multiplicative Beamforming in which maps obtained by different arrays are multiplied together to increase the accuracy and the compactness of localization [19, 44] when two or more arrays on orthogonal planes are utilized. Padois et al. [39] compared the behaviour of different known acoustic mapping methods using one or two planar arrays on simulated data. Instead, Battista et al. [20] compared results obtained with one and two arrays on both simulated and experimental data in a wind tunnel setup, using inverse methods for aeroacoustic source identification. The use of multiple planar arrays can be successfully used to increase the localization and quantification ability of deconvolution techniques or inverse methods. In addition, it is possible to detect sources that are not directly seen by single array because are masked by the object itself and to obtain more informations on source directivity.

2.3 Theory: problem formulation and inverse operators

Let consider the acoustic field generated by a radiating body and a surface/volume of interest Γ which contains the body. Region of interest not necessarily has to coincide with the body surface/volume. The propagation problem, at given angular frequency ω, is completely determined by the following Fredholm equation of first kind:

$$p(\mathbf{r}_m) = \int_\Gamma q(\mathbf{r}) G(\mathbf{r}_m|\mathbf{r}) d\Gamma(\mathbf{r}) \,, \tag{2.1}$$

where $\mathbf{r} \in \Gamma$ is a generic location vector. This equation relates the source field $q(\mathbf{r})$ with the acoustic pressure $p(\mathbf{r}_m)$ at receiver locations $\mathbf{r}_m$, by means of Green propagation function $G(\mathbf{r}_m|\mathbf{r})$.

Source reconstruction techniques rely on *Wave Superposition Method* [28] which states that the acoustic field, generated by a complex radiator, can be reproduced as a superposition of fields caused by a set of simple sources enclosed within the radiator. This makes possible to define a spatial distribution of elementary sources (e.g. monopoles, dipoles, plane waves etc.) reproducing the same acoustic field of complex sources. With this purpose, source-receiver propagation problem of Eq. 2.1 is discretized, i.e. $q(\mathbf{r})$ is not considered as continuous source distribution but as finite set of N elementary sources and pressure $p(\mathbf{r}_m)$ is evaluated at M receiver locations. Therefore, the actors of discrete acoustic problem are:

$$q_n = q(\mathbf{r}_n) \tag{2.2}$$

$$p_m = p(\mathbf{r}_m) \tag{2.3}$$

$$G_{mn} = G(\mathbf{r}_m|\mathbf{r}_n) \tag{2.4}$$

where $n = 1, ..., N$ and $m = 1, ..., M$. Once defined elementary sources (type and location), receiver positions and acoustic propagator (speed of sound, scattering effects, flow, etc.), the direct acoustic problem is a linear transformation applied to source coefficients $\mathbf{q} \in \mathbb{C}^{N \times 1}$ using the acoustic transfer matrix $\mathbf{G} \in \mathbb{C}^{M \times N}$. For each frequency, pressure $\mathbf{p} \in \mathbb{C}^{M \times 1}$ at receivers can be written as:

$$\mathbf{G}\mathbf{q} = \mathbf{p} \,. \tag{2.5}$$

The calculation of acoustic pressure $\mathbf{p}$ (effect) from a given $\mathbf{q}$ (cause) is the *direct acoustic problem* which is well-posed and has unique solution. The *inverse acoustic problem* aims to retrieve the source distribution $\mathbf{q}$ (cause) from measurement at microphone locations $\mathbf{p}$ (effect). This problem results to be ill-posed in the Hadamard sense [21, 24], i.e. existence, uniqueness and stability of the solution are not guaranteed. Inverse problem formulation can be also expressed as a linear transformation:

$$\hat{\mathbf{q}} = \mathbf{T}\mathbf{p} \,, \tag{2.6}$$

where $\hat{\mathbf{q}}$ is the solution for a particular inverse operator $\mathbf{T} \in \mathbb{C}^{N \times M}$. Indeed, as it will be shown ahead, the latter term can assume different forms depending on the assumptions, a priori information considered and, in most cases, on the input data

$\mathbf{p}$. When the acoustic field is stationary, the both direct and inverse problem can be rearranged in terms of auto and cross power spectra:

$$\mathbf{G}\mathbf{Q}\mathbf{G}^H = \mathbf{P}\ . \tag{2.7}$$

The matrix $\mathbf{P} = \langle \mathbf{p}\mathbf{p}^H \rangle$ is the CSM of pressure at microphone locations and $\mathbf{Q} = \langle \mathbf{q}\mathbf{q}^H \rangle$ is the CSM of source strengths ($\langle \cdot \rangle$ represents the average operator). The superscript ^{H} stands for the complex conjugate transpose operator. Using the quadratic form, the solution of the inverse problem can be obtained as

$$\hat{\mathbf{Q}} = \mathbf{T}\mathbf{P}\mathbf{T}^H\ . \tag{2.8}$$

Despite the enormous number of different acoustic mapping methods, many of them can be expressed in the same formulation. A complete review about different inverse operators is provided by Leclere et al. in [31].

2.3.1 Beamforming

Beamforming approach faces each degree of freedom of source distribution independently from the others. Beamforming algorithms solve a scalar inverse problem as if it were only one active source and the inverse operator is built using columns of $\mathbf{G}$. Each column $\mathbf{g}_n$ represents the propagation of a unitary source on microphone positions. What differentiates each beamforming algorithm is the specific spatial filter to apply on measured pressure. For each focus point the filter can be expressed as function $f(\cdot)$ of the propagator

$$\mathbf{t}_n = f(\mathbf{g}_n^H)\ , \tag{2.9}$$

these complex vectors are called *steering-vectors* in literature. It is also possible to apply different weights to each microphones and source scaling strategies to correct the source amplitude (e.g. to compensate very different source-array distances). Sarradj proposed four different formulation of steering-vectors in [46]: two of them can provide correct source location with an error on source level, the other two can provide the exact source level with an error on source position. Usually, steering-vectors are data-independent, but some beamformers calculates them taking into account measured data. For example, MVDR beamformer minimize the contribution of all sources except the one in the focusing point considering measured data. In any case, the beamformer output for each focus point is

$$\hat{q}_n = \mathbf{t}_n \mathbf{p}\ , \tag{2.10}$$

or

$$\hat{\mathbf{A}}_{\mathbf{q},n} = \mathbf{t}_n \mathbf{P} \mathbf{t}_n^H \tag{2.11}$$

in the common quadratic form, where source autopowers $\hat{\mathbf{A}}_{\mathbf{q}} = diag(\hat{\mathbf{Q}})$ are estimated from microphone CSM. It is worth noticing that the product $\mathbf{TG} \neq \mathbf{I}$ for beamformers and this causes the non-ideal source reconstruction. Each column of $\mathbf{TG}$ represents the PSF of a source in the *n-th* scanning point to all other scanning points. From this expression, it is straightforward to write the linear system for deconvolution with DAMAS approach

$$\mathbf{B}_{PSF}\mathbf{A}_{\mathbf{q}} = \hat{\mathbf{A}}_{\mathbf{q}}\ . \tag{2.12}$$

The matrix $\mathbf{B}_{PSF} = \mathbf{TG}$ that is the real coefficient matrix containing the PSFs and $\mathbf{A}_{\mathbf{q}} = diag(\mathbf{Q})$ is the vector of unknowns representing the ”real” source autopowers which have generated the CB map.

2.3.2 Inverse methods

In opposition to direct beamforming approach, inverse methods aim to consider all potential sources together and retrieve the whole source distribution at once. This should lead to better results in terms of source strength quantification, especially in presence of correlated and/or spatially distributed sources. However, in common applications the number of equivalent sources is usually much greater than the number of microphones, thus leading to an under-determined problem. On one hand, this enhances the ill-conditioning of the problem, but, on the other hand, it gives the opportunity to find the particular solution that optimally fits a property. Depending on assumptions, a priori information and/or cost functions to optimize, different inverse operators will come out.

Moore-Penrose pseudo-inverse

A straightforward approach for solving Eq. 2.5 is the Moore-Penrose pseudo-inverse that is one possible generalization of inverse matrix to rectangular matrices. When the linear system is over determined, left pseudo-inverse is used as inverse operator $\mathbf{T}$ to obtain the *Least Square Error Solution*:

$$\hat{\mathbf{q}} = \mathbf{G}^{+L}\mathbf{p} \ = \arg\min_{\mathbf{q}} \left(\|\mathbf{G}\mathbf{q} - \mathbf{p}\|_2^2 \right) . \tag{2.13}$$

$$\mathbf{T} = \mathbf{G}^{+L} = (\mathbf{G}^H\mathbf{G})^{-1}\mathbf{G}^H \, , \tag{2.14}$$

In common application cases, the linear system is under determined and a possible solution is provided by the right pseudo-inverse. This inverse operator returns the *Least Square Solution*, i.e. the solution with the smallest L_2 norm among all those satisfying the linear system of equations in Eq. 2.5 :

$$\hat{\mathbf{q}} = \mathbf{G}^{+R}\mathbf{p} \ = \arg\min_{\mathbf{q}} \left(\|\mathbf{q}\|_2^2 \ \text{subject to} \ \ \mathbf{G}\mathbf{q} = \mathbf{p} \right) . \tag{2.15}$$

$$\mathbf{T} = \mathbf{G}^{+R} = \mathbf{G}^H(\mathbf{G}\mathbf{G}^H)^{-1} \, , \tag{2.16}$$

From a physical point of view, this represents the solution with minimum energy which exactly matches the measured pressure data. This is often referred to as *naïve solution*. Both $\mathbf{G}^{+R}$ and $\mathbf{G}^{+L}$ can be computed using the *Singular Value Decomposition* (SVD) of $\mathbf{G}$:

$$\mathbf{G} = \mathbf{U}\mathbf{S}\mathbf{V}^H \tag{2.17}$$

$$\mathbf{G}^+ = \mathbf{V}\mathbf{S}^+\mathbf{U}^H \, , \tag{2.18}$$

where, for $M < N$, $\mathbf{U} \in \mathbb{C}^{M\times M}$ is a unitary matrix, $\mathbf{V} \in \mathbb{C}^{N\times M}$, is such that $\mathbf{V}^H\mathbf{V} = \mathbf{I}_M$ and $\mathbf{S} \in \mathbb{R}^{M\times M}$ is a diagonal matrix which contains singular values in decreasing order $s_1 \geq ... \geq s_k \geq ... \geq s_M \geq 0$. The matrix $\mathbf{S}^+$ is the pseudo-inverse of $\mathbf{S}$, obtained replacing diagonal terms by its reciprocal. Although the pseudo-inverse approach for under determined inversion provides a simple solution, it suffers of critical drawback: the solution may not be stable under (even small) variation of $\mathbf{G}$ and $\mathbf{p}$, i.e. errors in the propagation model and noise in measured data. To better address the stability of solution, it is useful to rewrite the naïve solution as sum of orthonormal basis associated to each singular value:

$$\hat{\mathbf{q}} = \sum_{i=k}^{M} \frac{\mathbf{u}_k^H \mathbf{p}}{s_k} \mathbf{v}_k \ . \tag{2.19}$$

This expression allows to introduce the *Discrete Picard Condition* (DPC) [22]. A given right-hand term $\mathbf{p}$ of Eq. 2.5 satisfies the DPC if, for all numerically non-zero singular values, the corresponding Fourier coefficients $\mathbf{u}_k^H \mathbf{p}$ decay to zero faster than s_k on the average. This means that, once defined the terms ε_k as

$$\varepsilon_k = \frac{|\mathbf{u}_k^H \mathbf{p}|}{s_k}, \tag{2.20}$$

named here *Picard coefficients*, the solution is stable if ε_k are constant, or decreasing, on the average. This condition can be checked by visual inspection of a *Picard plot*, which shows the trend of Picard coefficients. The noise has effect on Fourier coefficient, in particular those related to the smallest singular values, and is amplified during the inversion thus making the solution unstable.

Tikhonov Regularization

A common approach to lower this amplification effect of noise is to exploit *Tikhonov regularization* [52]. The Tikhonov approach consists in jointly minimizing the solution norm $\|\mathbf{q}\|_2^2$ and residuals norm $\|\mathbf{Gq}-\mathbf{p}\|_2^2$, thus leading to the following minimization problem:

$$\hat{\mathbf{q}}(\eta) = \arg\min_{\mathbf{q}} \left(\|\mathbf{Gq} - \mathbf{p}\|_2^2 + \eta^2 \|\mathbf{q}\|_2^2 \right) \tag{2.21}$$

where the *regularization parameter* $\eta^2 \geq 0$ controls the trade-off between the amplitude of the solution and the fitting error. The regularization parameter amplifies the singular values $s_k < \eta$, while the singular values $s_k > \eta$ remain almost unaltered. Therefore, when matrix inversion is performed, the smallest singular values are smoothly filtered preventing the over amplification of noise and stabilizing the solution. The inverse operator is

$$\mathbf{T} = \mathbf{G}^{+\eta} = \mathbf{G}^H (\mathbf{G}\mathbf{G}^H + \eta^2 \mathbf{I})^{-1} = \mathbf{V}(\mathbf{S}^2 + \eta^2 \mathbf{I})^{-1} \mathbf{S} \mathbf{U}^H \ , \tag{2.22}$$

where $\mathbf{G}^{+\eta}$ is the pseudo inverse regularized by η. In other words, Tikhonov regularization controls the energy of the solution trading this for a small fit error. As the "cut-off" on singular values is adjusted varying η, the most critical aspect is to estimate the correct regularization parameter for each specific problem. Some strategies are commonly used in acoustic problems, such as *L-curve criterion* or *Generalized Cross-Validation*, or a combination of them [23],[27],[29]. In addition, the general form of Tikhonov regularization makes it possible to have more control on the solution considering the following problem:

$$\hat{\mathbf{q}}(\eta, \mathbf{W}) = \arg\min_{\mathbf{q}} \left(\|\mathbf{Gq} - \mathbf{p}\|_2^2 + \eta^2 \|\mathbf{Wq}\|_2^2 \right) \tag{2.23}$$

where the term $\|\mathbf{Wq}\|_2^2$ is named discrete smoothing norm. The square invertible matrix $\mathbf{W}$ is used to introduce additional information about the solution. This problem boils down to a standard Tikhonov formulation substituting $\tilde{\mathbf{q}} = \mathbf{W}\mathbf{q}$ and $\tilde{\mathbf{G}} = \mathbf{G}\mathbf{W}^{-1}$:

$$\hat{\tilde{\mathbf{q}}}(\eta, \mathbf{W}) = \arg\min_{\tilde{\mathbf{q}}} \left(\|\tilde{\mathbf{G}}\tilde{\mathbf{q}} - \mathbf{p}\|_2^2 + \eta^2 \|\tilde{\mathbf{q}}\|_2^2 \right) . \tag{2.24}$$

The solution of original problem is obtained from $\hat{\mathbf{q}} = \mathbf{W}^{-1}\hat{\tilde{\mathbf{q}}}$. Considering $\mathbf{W}$ as diagonal matrix, the inverse operator is:

$$\mathbf{T} = \mathbf{W}^{-1}(\mathbf{G}\mathbf{W}^{-1})^{+\eta} = \mathbf{W}^{-2}\mathbf{G}^H(\mathbf{G}\mathbf{W}^{-2}\mathbf{G}^H + \eta^2\mathbf{I})^{-1} . \tag{2.25}$$

Bayesian Framework

A more general approach to inverse problems has been proposed by Antoni in [1]. He exploited Bayesian inference for developing a method that is able to

- identify the optimal basis functions which minimize the reconstruction error of the source field;
- include *a priori* information on source field to better condition the problem and ease the reconstruction task;
- provide a robust regularization criterion with no more than one minimum.

This method finds an estimate of the source field $\hat{q}(\mathbf{r})$ in the following form:

$$\hat{q}(\mathbf{r}) = \sum_{k=1}^{K} c_k \, \phi_k(\mathbf{r}) = \mathbf{\Phi}\mathbf{c} \, , \quad K \geq M \tag{2.26}$$

where $\phi_k(\mathbf{r})$ are the spatial basis functions which interpolate the source field independently of the measurements, c_k are the coefficients which depend on measurements; K is the dimension of the basis and M is the number of microphones. In other words, the unknowns of the problem are the spatial functions that guarantee the smallest reconstruction error possible, their coefficients and their number. The model considered for direct problem is more general than Eq. 2.5, since it takes into account also the presence of measurement noise $\mathbf{n} \in \mathbb{C}^{M\times 1}$, thus leading to the following form:

$$\mathbf{G}\mathbf{q} + \mathbf{n} = \mathbf{p} \, . \tag{2.27}$$

The core idea of the *Bayesian approach* (BA) *to sound source reconstruction* is to endow all unknown quantities of interest with a probability density function. Indeed, the randomness of the source field reflects the lack of knowledge in the reconstruction process and its probability distribution is conditioned by measurements. Therefore, the unknown source field probability density function (pdf) can be expressed as $[q(\mathbf{c}, \mathbf{\Phi})|\mathbf{p}]$ and it is called *posterior probability distribution.* Maximization of "posterior" with respect to $\mathbf{c}$ and $\mathbf{\Phi}$ will return the optimal parameters $\hat{\mathbf{c}}$ and $\hat{\mathbf{\Phi}}$ that best explain measured data $\mathbf{p}$:

$$\hat{\mathbf{q}}(\hat{\mathbf{c}}, \hat{\mathbf{\Phi}}) \;= \arg\max_{\mathbf{c}, \mathbf{\Phi}} \, [q(\mathbf{c}, \mathbf{\Phi})|\mathbf{p}] \tag{2.28}$$

that is a maximum a posteriori (MAP) estimate. The Bayesian inference is used to solve the inverse problem, since Bayes' theorem allows to express the inverse probability in terms of direct probabilities:

$$[q(\mathbf{c}, \mathbf{\Phi})|\mathbf{p}] = \frac{[\mathbf{p}|q(\mathbf{c}, \mathbf{\Phi})][q(\mathbf{c}, \mathbf{\Phi})]}{[\mathbf{p}]} \, . \tag{2.29}$$

The first term on the numerator, $[\mathbf{p}|q(\mathbf{c},\mathbf{\Phi})]$, is the *likelihood function* which represents the probability of observing measured data $\mathbf{p}$, given the source field $q(\mathbf{c},\mathbf{\Phi})$, and has the same probability density function of measurement noise $\mathbf{n}$. The other term on the numerator is the *a priori probability distribution* of source field before measurements are considered. The denominator $[\mathbf{p}]$ is the evidence, that is the probability of measuring $\mathbf{p}$ over the whole space of sources. Noise pdf is assumed as circular complex Gaussian, thus having:

$$\mathbb{E}\{\mathbf{n}\} = \mathbf{0} \tag{2.30}$$

$$\mathbb{E}\{\mathbf{n}\mathbf{n}^H\} = \beta^2\mathbf{\Omega}_n \tag{2.31}$$

where $\mathbf{\Omega}_n$ is the structure of noise covariance matrix, normalized such that $\mathrm{trace}(\mathbf{\Omega}_n) = M$, so that β^2 represents the mean energy of noise averaged over microphones. In most cases $\mathbf{\Omega}_n = \mathbf{I}$ is chosen, since it is the most neutral choice and no a priori information are introduced. The choice of prior pdf is more flexible and is linked to the user knowledge on source field before data is measured. A priori information about spatial distribution and source correlation can be introduced in the spatial covariance function of the random source field:

$$\mathbb{E}\{\mathbf{q}\mathbf{q}^H\} = \alpha^2\mathbf{\Omega}_q \tag{2.32}$$

even in this case covariance matrix is normalized such that $\mathrm{trace}(\mathbf{\Omega}_q) = N$, so that α^2 represents the mean source energy. Off-diagonal terms represent the correlation coefficient between sources, while diagonal elements of $\mathbf{\Omega}_q$ can be used to introduce spatial information about the regions where sources are most likely to be found. The latter is often referred to as *aperture function* that shrinks the source reconstruction task to a restrained region and enhance the performance in terms of spatial resolution, quantification accuracy and frequency range. This plays a fundamental role in the so-called *Bayesian focusing* mechanism. The implicit assumption of deterministic approaches is that all sources are uncorrelated and therefore $\mathbf{\Omega}_q = \mathbf{I}_N$. By assuming circular complex Gaussian also for source parameters, the reconstructed source field can be written as:

$$\hat{q}(\mathbf{r}) = \sum_{k=1}^{M} \frac{s_k}{s_k^2+\eta^2}\phi_k(\mathbf{r})\mathbf{u}_k^H\mathbf{\Omega}_n^{-1/2}\mathbf{p} \tag{2.33}$$

with $\eta^2 = \beta^2/\alpha^2$. Instead, vectors $\mathbf{u}_k$ are the columns of $\mathbf{U}$ and s_k the singular values resulting from the following SVD:

$$\mathbf{\Omega}_n^{-1/2}\mathbf{G}\mathbf{\Omega}_q^{-1/2} = \mathbf{U}\mathbf{S}\mathbf{V}^H\ . \tag{2.34}$$

The dimension of the basis is $K = M$ and optimal basis functions are calculated as

$$\mathbf{\Phi} = \mathbf{\Omega}_q^{1/2}\mathbf{G}^H\mathbf{\Omega}_n^{-1/2}\mathbf{U}\mathbf{S}^{-1}\ , \tag{2.35}$$

which depend only on the topology of the problem and a priori information considered. The Bayesian focusing mechanism is rooted in the fact that propagation operator is passed through the aperture function and the basis functions are adapted to the specific a priori information introduced. Instead, the optimal basis coefficients can be written as:

$$\mathbf{c} = (\mathbf{S}^2+\eta^2\mathbf{I})^{-1}\mathbf{S}\mathbf{U}^H\mathbf{\Omega}_n^{-1/2}\mathbf{p} \tag{2.36}$$

The solution obtained assuming circular complex Gaussian as prior pdf is similar to Tikhonov regularization mechanism. If a different prior is assumed, different solution and regularization mechanisms would appear from Bayesian formalism. Moreover, Bayesian approach identifies the regularization parameter η^2 in the Noise-to-Signal Ratio (NSR), i.e. the ratio between noise energy β^2 and source energy α^2.

Empirical Bayesian regularization (BR) provides different strategies for the estimation of these quantities directly from measured data. The interested reader might refer to [41] for a deeper insight into empirical Bayesian regularization, while hereinafter only theory useful to the scope of this thesis is reported. The simplest (and worst) case is when all outcomes of β^2 and α^2 are assumed a priori equiprobable, i.e. $[\alpha^2, \beta^2] \propto 1$. In this condition, the empirical BA is equivalent to maximum likelihood and two strategies can be adopted, namely the *Maximum A Posteriori* (MAP) and the *Joint* approach. The latter consist of a MAP estimation resulting from the evaluation of joint pdf of α^2 and β^2, given the measurements, and then their ratio is calculated. The cost function to minimize with respect to η^2 is:

$$\mathbf{J}_{Joint}(\eta^2) = \sum_{k=1}^{M} \ln(s_k^2 + \eta^2) + M \ln \left(\frac{1}{M} \sum_{k=1}^{M} \frac{|y_k|^2}{s_k^2 + \eta^2} \right) \tag{2.37}$$

$$\hat{\eta}^2_{Joint} = \arg\min_{\eta^2} \mathbf{J}_{Joint}(\eta^2) \tag{2.38}$$

where s_k are the singular values and $y_k = \mathbf{u}_k^H \mathbf{p}$ are the Fourier coefficients. The MAP approach comes from the direct estimation of η^2 without the intermediate estimation of noise and source energy:

$$\mathbf{J}_{MAP}(\eta^2) = \sum_{k=1}^{M} \ln(s_k^2 + \eta^2) + (M-2) \ln \left(\frac{1}{M} \sum_{k=1}^{M} \frac{|y_k|^2}{s_k^2 + \eta^2} \right) \tag{2.39}$$

$$\hat{\eta}^2_{MAP} = \arg\min_{\eta^2} \ \mathbf{J}_{MAP}(\eta^2) \ , \tag{2.40}$$

Source and noise mean energy can be calculated from the estimated regularization parameter as:

$$\hat{\alpha}^2 = \frac{1}{M} \sum_{k=1}^{M} \frac{|y_k|^2}{s_k^2 + \hat{\eta}^2}, \quad \hat{\beta}^2 = \hat{\eta}^2 \cdot \hat{\alpha}^2 \ . \tag{2.41}$$

These two approaches are closely related, in fact

$$\mathbf{J}_{MAP}(\eta^2) = \mathbf{J}_{Joint}(\eta^2) - 2 \ln(\hat{\alpha}^2(\eta^2)) \ , \tag{2.42}$$

but they are not identical since a MAP estimate of a ratio ($\hat{\eta}^2_{MAP}$) is generally not equal to the ratio of MAP estimates ($\hat{\eta}^2_{Joint}$). These two cost functions share the property of having a unique global minimum with an high probability, under certain conditions that are verified in most practical configurations. This property is rather unique among regularization criteria, in addition, they return similar estimate of regularization parameter for many practical applications. The value of η^2 obtained from these two criteria is often near to the optimum one that minimize the mean squared error with the exact solution (see [43, 41]). The main difference between MAP and Joint approaches is that the latter may return an unbounded estimate of η^2 for bad signal-to-noise ratios, while MAP cost function always forces a finite value for the regularization parameter.

Another possible scenario is that the user may have some information about expected noise energy β^2. Bayesian approach gives the possibility to introduce this knowledge in the estimate of η^2. One possible choice is to use an inverse Gamma pdf for β^2 that leads to:

$$[\alpha^2, \beta^2] \propto [\beta^2] = \mathcal{G}^{\text{-}1}(a, b) \propto \beta^{-2a} \mathrm{e}^{-b\beta^{-2}}, \quad a \geq 0, b \geq 0\,. \tag{2.43}$$

From this assumption, modified cost functions come out. For the Joint approach, Eq. 2.37 becomes

$$\mathbf{J}_{Joint,\mathcal{G}^{\text{-}1}}(\eta^2) = \sum_{k=1}^{M} \ln(s_k^2 + \eta^2) + (M + a) \ln\left(\hat{\alpha}^2_{\mathcal{G}^{\text{-}1}}\right) + a \ln(\eta^2) \tag{2.44}$$

where the subscript $\mathcal{G}^{\text{-}1}$ indicates the use of the inverse Gamma as prior pdf of β^2. The mean source and noise energy are modified as follows

$$\hat{\alpha}^2_{\mathcal{G}^{\text{-}1}} = \frac{1}{(M + a)} \left(\sum_{k=1}^{M} \frac{|y_k|^2}{s_k^2 + \eta^2} + \frac{b}{\eta^2} \right), \quad \hat{\beta}^2_{\mathcal{G}^{\text{-}1}} = \hat{\eta}^2_{\mathcal{G}^{\text{-}1}} \cdot \hat{\alpha}^2_{\mathcal{G}^{\text{-}1}}\,. \tag{2.45}$$

Modified cost function of MAP approach follows from Eq. 2.42. It is worth noticing that this second scenario is more general and include the first one when $a = 0$ and $b = 0$. A particular and useful choice is when only the mean value is imposed, i.e. $\mathbb{E}\{\beta^{-2}\} = b^{-1}$ and $a = 0$ having the Maximum Entropy solution. From practical point of view, this helps in reducing the risk of under-estimation of η^2.

Once the inverse problem is solved, Bayesian framework returns several byproducts providing further information on reconstructed source field, like:

- quantity of information provided by the array measurements in attempting to reconstruct the source field;
- measure of the quality of reconstructed source field;
- sensitiveness of the acoustic inverse problem to regularization.

The knowledge of these information turn out to be useful in many contexts, but are usually not available with other approaches. A complete discussion about this aspects is out of the scope of this thesis. Only a short description about the measure of quality of the result is reported here, since it will be used in the following chapter. A possible measure of the quality of reconstructed sources is the relative variance

$$\mathcal{P} = \frac{1}{M} \sum_{k=1}^{M} \frac{1}{1 + s_k^2/\eta^2} \tag{2.46}$$

that is a normalized measure limited between 0 and 1. As the regularization parameter increases this value approaches to 1 and reflects the fact that the reconstruction is more reliable but with bad spatial resolution [1].

Sparse solutions

The L_2 norm minimization process takes advantage in spreading the energy of the source field into several equivalent sources to reduce the total energy of the solution.

In addition, in [43] it is shown the tendency of sources reconstructed by L_2 norm minimization to have a directivity pattern towards the array, especially at high frequency, and this leads to systematically underestimate source powers. Actually, the choice to seek the solution with minimum energy is in a way arbitrary in this context. If localization can be satisfactory with minimum L_2 norm solution, quantification requires further a priori information about sources. This can be done assuming that source distribution can be represented by only few non-zero elements in the solution, when proper basis is used. In fact, the choice of elementary sources is crucial, since it represents the basis with respect to the sparsity is assumed. Sparsity can be measured by the L_0 norm of the solution, that is the number of non-zero components of a vector. However, the exact solution is difficult to obtain since it is a non-convex optimization problem and the solution may not be unique. Therefore, the L_0 norm is commonly relaxed with the L_1 norm, because it turns to be a convex optimization problem. A more general formulation makes use of the generic L_p norm to finely adjust the amount of sparsity:

$$\hat{\mathbf{q}}(\eta, p) = \arg\min_{\mathbf{q}} \left(\|\mathbf{G}\mathbf{q} - \mathbf{p}\|_2^2 + \eta^2 \|\mathbf{q}\|_p^p \right) , \tag{2.47}$$

where the solution L_p norm is minimized jointly to the fitting error similarly to Tikhonov solution. The L_p norm of a generic vector $\mathbf{x} \in \mathbb{C}^{N\times 1}$ is defined as:

$$\|\mathbf{x}\|_p^p = \sum_{i=1}^{N} |x_i|^p . \tag{2.48}$$

A clarification about the definition of L_p norm is needed. For $p \geq 1$, $\|\mathbf{x}\|_p$ is a proper norm because it satisfies the triangle inequality, but this property is lost for $p < 1$. However, for $0 < p < 1$, $\|\mathbf{x}\|_p^p$ is a metric and can be used to measure distances in vector spaces. When $p = 0$, $\|\mathbf{x}\|_0^0$ should be called L_0 "norm" (with quotation marks) and it counts the number of non-null elements in the vector. Anyway, for sake of simplicity, in this work the name L_p norm is used in general for $\|\mathbf{x}\|_p^p$, with $0 \leq p \leq 2$. As already said, L_0 norm minimization is difficult to solve exactly, but can be approximated using heuristic algorithms that search a solution near the optimum one without any guarantee to provide the global optimum. Examples are *Matching Pursuit* [33] or *Orthogonal Matching Pursuit* (OMP) [40] algorithms. Instead, different algorithms exist for L_1 norm minimization [54, 53], such as *Least Absolute Shrinkage and Selection Operator* (LASSO) or *Basis Pursuit Denoise* (BPDN).

Another possible approach is related to the *Iteratively Reweighted Least Squares* (IRLS) family of algorithms [11, 13]. The idea is to solve a Weighted Least Square problem at each iteration, that is the Eq. 2.23, and use the result of current iteration to calculate weights for the next one and converge to a sparse solution. The inverse operator has the same form of Eq. 2.25, but is the result of certain number of iterations. For example, to obtain a solution to the L_p norm minimization of Eq. 2.47, weights can be computed using the following consideration:

$$\|\mathbf{q}\|_p^p = \sum_{n=1}^{N} |q_n|^p = \sum_{n=1}^{N} w_n^2 |q_n|^2 = \|\mathbf{W}\mathbf{q}\|_2^2 . \tag{2.49}$$

The weighting matrix $\mathbf{W}$ is a real diagonal matrix and the set of weights depends on the result of the previous iteration with the following expression:

$$w_{nn}^{(it)} = \left| \hat{q}_n^{(it-1)} \right|^{\frac{(p-2)}{2}} \tag{2.50}$$

where it is the current iteration and w_{nn} is the generic diagonal element of $\mathbf{W}$. From a Bayesian point of view this method can be seen as an Expectation-Maximization algorithm which converges to MAP solution [10]. In addition, there is a direct link between the exponent p of the norm and the a priori pdf of source distribution, i.e. the generalized Gaussian law, as demonstrated in [30].

Chapter 3

Inverse methods for volumetric acoustic source mapping

This chapter is dedicated, in its first part, to the analysis of volumetric acoustic source mapping and the requirements needed to fulfil this task. Literature is poor about specific and systematic study on volumetric acoustic source mapping and mainly evaluation of existing techniques applied to an extended spatial domain are available. The first objective is to describe the additional issues to face when dealing with volumetric mapping and explain how to address them. Then, strategies and algorithms developed in this work are described in detail. The most common measurement setup in acoustic imaging, independently from the specific technique utilized, is a planar array placed in front of the source/sources of interest and the acoustic map is calculated on a plane or surface which represents the object of interest. Figure 3.1 shows the common mistake when sources are out of plane. One of the aims of new techniques developed in this thesis is to give the possibility to successfully map volumes at simple cost of (re)processing acquired data and no additional hardware request. Unfortunately, this kind of setup represents a really challenging layout for volumetric mapping, since the radial spatial resolution in the direction from array centre is bad and this is particularly evident in volumetric maps obtained with CB (Fig. 3.2). Given the nature of the volumetric acoustic problem, there are some limitations (frequency range, array-source distance, etc.) for the applicability of these techniques to obtain good accuracy, especially when single array is utilized. However, a powerful characteristic of techniques described here is that they can be used with arrays of any kind and therefore they give the possibility to process data acquired, for example, by two or more planar arrays, looking at the same object, as a unique array. When beamforming is performed with multiple arrays sidelobe level increase dramatically and deconvolution techniques are still needed to obtain useful results. Contrarily, inverse methods benefit of multiple planar arrays when they are utilized for volumetric mapping: the lower limit of frequency range is extended, the accuracy of localization is improved and more information of source directivity can be extracted from maps. In addition to the set of problem with inverse methods, volumetric acoustic imaging compels to face additional issues. Two methods for acoustic mapping are proposed: one is based on the Equivalent Source Method and the other on the Covariance Matrix Fitting approach. Both rely on a specific version of Iteratively Re-weighted Least Squares algorithm suited for acoustic inverse problem which exploits the Bayesian Approach.

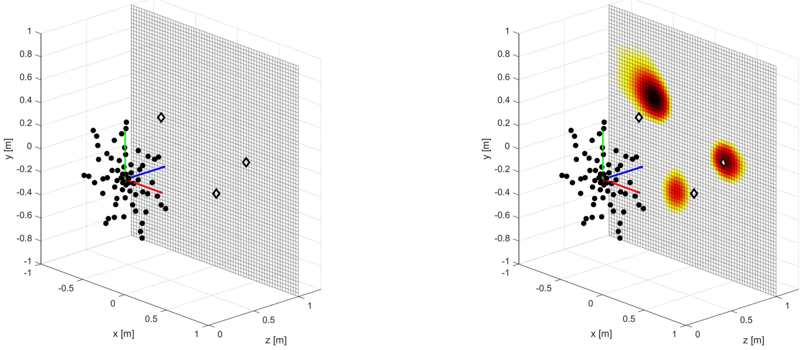

(a)

(b)

Figure 3.1: 2D planar mapping of sources with single planar array and CB

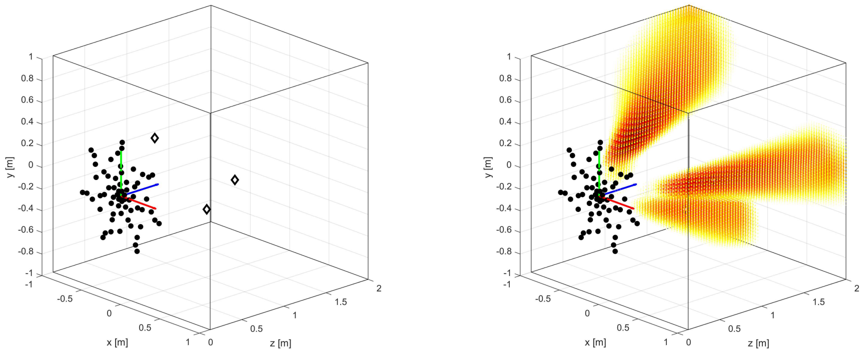

(a)

(b)

Figure 3.2: 3D volumetric mapping of sources with single planar array and CB

3.1 Issues in volumetric mapping

From the analysis of volumetric acoustic mapping , three additional issues emerged:

- potential sources located at very different distances from the array centre;
- poor spatial resolution of arrays in radial direction from the array centre;
- high number of potential sources with no contribution to the acoustic field.

The first issue can be faced balancing energy needed by each potential source to produce the same pressure on a microphone, therefore, the different source-receiver distances must be somehow compensated. This can be done exploiting the strength-to-pressure acoustic transfer function in pair with a weighting strategy, as suggested by Pereira et al. [42]. For example, when monopoles and free-field propagation are considered, the elements of **G** can be computed as

$$G_{mn} = \frac{\mathrm{e}^{-\mathrm{j}kr_{mn}}}{4\pi r_{mn}}\,, \tag{3.1}$$

where $k = \omega/c$ is the wavenumber, c is the speed of sound in the medium and the terms r_{mn} represent the geometric distance between the generic points m (microphone) and n (source). In this case, the greater is the distance of a generic source from microphones the more energy is needed to generate a certain pressure on them. Therefore, a diagonal weighting matrix can be used for compensating the effect of source-microphone distances, whose generic diagonal elements are $W_{nn} = 1/r_{0n}$. The point named as "0" ($\mathbf{r}_0$) is a reference point that has to be chosen by the user. The other possible choice to achieve the same result, is to use a pressure-to-pressure acoustic transfer function formulation:

$$G_{mn} = \frac{r_{0n}}{r_{mn}}\mathrm{e}^{-\mathrm{j}k(r_{mn}-r_{0n})}\,. \tag{3.2}$$

This propagator returns the acoustic pressure at microphone location m depending on sound pressure at reference point "0" caused by the monopole source at location n. This formulation automatically balances the energy needed by sources to produce a certain pressure at microphone locations without any weighting strategy needed. The second point of the list is a limitation due to the finite sampling of the acoustic field. Even when multiple planar arrays are combined radial spatial resolution from the array centre may be problem. The high number of potential sources makes the inverse acoustic problem heavily under-determined and increases the difficulty of retrieving correctly the source field. Last two issues are addressed together enforcing a sparsity constraint on the solution. On one hand, the "lobe" effect in radial direction is reduced or eliminated, but the accuracy still depends on many other factors (e.g. frequency, calculation grid step, source-array distance, noise level etc.), on the other hand, the assumption that only "few" potential source are active in the source field is introduced. The assumption of sparse solution gives critical importance to the choice of basis function to describe the direct problem. For example, the most common choice is to use a spatial distribution of monopoles to discretize the region of interest. When real source can be approximated with monopoles, the resulting sparse solution will be accurate, but, for example, when real source has relevant spatial extension, the sparse solution may not give the same accuracy. In the latter case, the strength of sparsity constraint is important.

3.2 IRLS algorithm for sparse source field reconstruction

A specific version of IRLS algorithm has been formulated for (volumetric) acoustic inverse problems. The sparsity constraint on solution is enforced in terms of L_p norm minimization (Eq. 2.47), where p gives the possibility to choose different levels of sparsity. The IRLS procedure can be formalized with the following expression:

$$\hat{\mathbf{q}}^{(it)} = F\left(\hat{\mathbf{q}}^{(it-1)}, \mathbf{W}^{(it)}, \eta^{2\,(it)}, \mathbf{G}^{(it)}, \mathbf{p}, p\right) , \tag{3.3}$$

where the function F is given by Eq. 2.23 or the equivalent version from Bayesian framework obtained with $\boldsymbol{\Omega}_n = \mathbf{I}$ and $\boldsymbol{\Omega}_q = \mathbf{W}^{(it)}$. The solution is calculated using the following procedure:

1. Set the weighting matrix $\mathbf{W}^{(it)}$ for the current iteration:

   $$\mathbf{W}^{(it)} = \mathbf{W}_0\, \mathbf{W}_{sp}^{(it)} , \tag{3.4}$$

   where Eq. 2.50 is used to force the sparsity, $\mathbf{W}_{sp}^{(1)} = \mathbf{I}$. A second diagonal matrix $\mathbf{W}_0$ is used to introduce further a priori information on source distribution. Both matrices are normalized such that $\|\mathbf{W}_0\|_\infty = \|\mathbf{W}_{sp}^{(it)}\|_\infty = 1$. The resulting matrix $\mathbf{W}^{(it)}$ is normalized such that $\mathrm{trace}(\mathbf{W}^{(it)}) = N$.

2. Estimate the regularization parameter $\eta^{2\,(it)}$ for the current iteration using Bayesian regularization.

3. Calculate the solution $\hat{\mathbf{q}}^{(it)}$ using Eq. 2.25.

4. Discard potential sources which do not contribute significantly to the acoustic field using the following criterion

   $$10 \log_{10}\left(\frac{\hat{\mathbf{q}}^{(it)}}{\|\hat{\mathbf{q}}^{(it)}\|_\infty}\right) < THR_{dB} . \tag{3.5}$$

   Therefore, propagation matrix $\mathbf{G}^{(it)}$ is updated removing columns associated to discarded sources.

5. Evaluate a convergence criterion, if not fulfilled go back to step 1 otherwise the algorithm ends.

This procedure returns a sparse solution for the inverse acoustic problem. In the next paragraphs, a detailed discussion on each aspect of IRLS is conducted.

3.2.1 Influence of sparsity constraint

The norm exponent can be set in the range $0 \leq p \leq 2$ to vary the amount of sparsity desired. When $1 < p < 2$ the solution norm minimization process still gain advantage in spreading energy over more source coefficients. In this case, the sources can be detected with better spatial resolution and slightly wider dynamics with respect $p = 2$. The convergence is fast, but dynamics and spatial resolution of maps obtained are still not satisfying, especially for volumetric mapping. Contrarily, when $p < 1$, there is the advantage in squeezing the total energy in few non-null source coefficients. For this reason, maps returned contain the minimum number of equivalent sources that match well pressure data. In case of real sources with spatial extension, the reconstruction is made with a certain number of equivalent sources that may not be contiguous. The more p is near to zero the quicker is the convergence. The case $p = 1$ gives the maximum sparsity achievable with convex optimization and represents the edge between the convex and non-convex optimization. It is a neutral condition that tends to preserve the real source shape. Unfortunately, this case has the slowest convergence.

One drawback of trying to get the source field with a sparse estimate occurs when a real source is between the grid of potential sources (e.g. grid of monopoles). In fact with $1 < p < 2$, the spread of energy allows some strategy to retrieve the accurate source position such as the calculation of centroid weighted with strength of equivalent sources. The latter strategy can be adopted also with $p = 1$. When $p < 1$, the sparse estimation usually converges on the potential source nearest to the real one. When the grid of potential sources is fine enough, the error committed is in the order of magnitude of half grid step in case of regular grids and can be easily predicted. As the grid step increases, real sources are mapped into two or more equivalent sources and the strategy of centroid can be adopted. The difficulty can be to recognise which phenomenon occurs in a particular application.

3.2.2 Convergence criterion

A crucial aspect of iterative methods is the convergence criterion. A good stopping criterion is rather important to guarantee uniformity of results because the optimal number of iterations is strongly dependent on characteristics of the specific problem, such as number/shape of real sources, frequency or noise level and IRLS parameters such as p. In [37], it is suggested the following convergence criterion:

$$\varepsilon^{(it)} = 10 \log 10 \left(\left\langle \left| \hat{q}_n^{(it)} / \hat{q}_n^{(it-1)} \right| \right\rangle \right) \tag{3.6}$$

where the operator $\langle \cdot \rangle$ represents the spatial average. This criterion requires that source complex amplitudes remain almost unaltered in the last 2 iterations to stop the algorithm. The value of $\varepsilon^{(it)}$ starts from big negative values and approaches 0 dB. The discarding strategy or other phenomena that occur throughout IRLS iterations may cause sudden variation of $\varepsilon^{(it)}$. In order to improve the reliability of results, in [3], a slightly different criterion is proposed:

$$\varepsilon^{(it)} = 10 \log_{10} \left(MSR - \left| \frac{\mathrm{d}(MSR)}{\mathrm{d}(it)} \right| - \left| \frac{\mathrm{d}^2(MSR)}{\mathrm{d}(it)^2} \right| \right) \tag{3.7}$$

$$MSR = \left\langle \left| \hat{q}_n^{(it)} / \hat{q}_n^{(it-1)} \right| \right\rangle \tag{3.8}$$

where MSR stands for *Mean Source Ratio*. This criterion can be evaluated only for $it > 2$ and is more restrictive because it requires that variation in the solution are small at least over last 3 iterations. When sudden variation of MSR occurs in consecutive iterations, the absolute value of first and second derivative (actually finite differences) prevent the end of IRLS procedure despite the sign of the variation. The algorithm stops when $\varepsilon^{(it)} \geq -0.1$ dB.

3.2.3 Discard of potential sources

The discard of sources, which do not contribute to the acoustic field, is done for avoiding the division by zero in weights calculation, progressively reduce the under-determination and speeding up the algorithm. Number of left potential sources at each iteration is indicated as $N^{(it)}$. The threshold used in this work is $THR_{dB} = -100$ dB. Such a value ensures that discarded potential sources are not relevant any more in $\hat{\mathbf{q}}^{(it)}$, considering the total energy of solution, thus resulting non-intrusive in the final result. Contrarily, threshold values closer to 0 dB might be intrusive and have an effect on the final result.

3.3 Regularization strategies for IRLS

Regularization is the most critical aspect of inverse problems and solutions returned by IRLS are heavily affected by the chosen strategy. Several different regularization mechanisms can be included in IRLS. In this thesis, the regularization mechanism proposed is based on Bayesian framework. The aim of this section is to explain how Bayesian regularization has been adapted to the IRLS requirements to improve the robustness and the accuracy of final results.

3.3.1 Bayesian Regularization

The simplest and straightforward way to estimate the amount of regularization is to find the minimum of Eq. 2.39 or Eq. 2.37 provided by BR. Otherwise, if an estimate of noise energy is available, it is possible to introduce this information using for example Eq. 2.44. The global minimum is sought in two steps. Firstly, a rough estimation is obtained taking the value of η^2 that minimize the cost function among a grid of values from 0 to an upper bound η^2_{max}. After that, the real minimum is calculated with a numerical optimizer in a neighbourhood of the rough estimate. When the linear system switches from being under-determined to over-determined, because of the discarding of potential sources, some troubles happen in the regularization process. Over-determined systems with few columns occur frequently when the sparsity constraint is strong ($p \leq 1$) and, in the very last IRLS iterations, few potential sources remain in the inverse problem.

The first issue is that the minimum of cost functions moves towards or beyond the maximum singular value (s_1^2), thus having systematically overestimated values of η^2. This leads to systematically underestimated source strengths, even though maps can be considered reliable for localization purposes because instabilities are suppressed even more than necessary. To avoid this effect, the value of M in cost functions must be changed from the number of microphones (rows) to the number of left potential sources (left columns, $N^{(it)}$) for over-determined systems, in other words, the number of singular values used to define the cost function. However, even with this correction, when the number of columns becomes much smaller than the number of rows ($N^{(it)} \to 1$), the acoustic problem is described by very few singular values (and related basis) and this undermines the robustness of regularization parameter estimation of BR. In this condition, a critical issue happens: both cost functions tend to have a minimum towards 0 or η^2_{max}, depending on the particular case, with no guarantee of robust regularization. Bayesian MAP cost function tends very often to have a minimum towards zero, thus giving under-regularized solutions. Contrarily, the Bayesian Joint approach keeps more often its well defined minimum, resulting a bit more reliable. Furthermore, it has been experienced that local minima or stationary points appears in the cost functions when the problem size gets smaller.

3.3.2 Dummy columns for minimum system size

A simple strategy is proposed here to enable BR to work properly even in condition of few singular values. The idea is to add dummy columns (DC) $\mathbf{z}_i$ to propagation matrix $\mathbf{G}^{(it)}$ in sufficient number to keep a minimum dimension of the system. These columns are associated to fake unknowns with no physical meaning. In this case, the matrix used to solve the inverse problem is modified as:

$$\mathbf{G}_{mod}^{(it)} = \left[\mathbf{G}^{(it)}, \mathbf{Z}\right] . \tag{3.9}$$

In order to avoid that these fake sources affect the physical unknowns of the inverse problem, they must be severely penalized with low weights in $\mathbf{W}_{mod}^{(it)}$. Weights of dummy columns w_d can be set as fraction of the mean of $\mathbf{W}^{(it)}$, in order to assure a fixed ratio on the average, between weights of real and fake unknowns. Empirically, it has been experienced that $w_d = 10^{-6} \cdot \langle \mathbf{W}^{(it)} \rangle$ is a good compromise between the non-intrusiveness of fake unknowns and reliability with respect to numerical issues. In this thesis, elements of dummy columns are generated using the complex noise model available in [43]:

$$z_m = 10^{-SNR/20} \left(\gamma \mathrm{e}^{\mathrm{i}\varepsilon} g_{max,m} + \delta \mathrm{e}^{\mathrm{i}\zeta} \sqrt{\frac{\|\mathbf{g}_{max}\|^2}{M}} \right) , \tag{3.10}$$

where γ and δ are zero mean Gaussian random variables ($Var(\gamma) = Var(\delta) = 1$), ε and ζ are random variables uniformly distributed between 0 and 2π and m is the microphone (row) index. The complex vector $\mathbf{g}_{max}$ is the column of $\mathbf{G}^{(it)}$ corresponding to the source coefficient with the maximum amplitude at the current IRLS iteration. Signal-to-Noise ratio in Eq. 3.10 is set to 0 dB, thus returning columns with the same order of magnitude of $\mathbf{g}_{max}$. The choice of the "seed" column and the realization of random columns are made irrelevant with the proper weights mentioned before. This practice makes cost functions of BR (Joint and MAP) able to keep their well defined unique minimum, since the number of singular values remains above a minimum. Once calculated the solution with dummy columns, fake unknowns are removed from solution vector.

3.3.3 Upper bound of regularization parameter

The maximum value of regularization parameter may be beyond s_1^2 in poor signal-to-noise ratio conditions. The upper bound in the search of the minimum of cost function can be set for example $\eta_{max}^2 = s_1^2$. This limit works well in a great variety of cases, but there is no control on the quality of solution. As previously mentioned in the description of BA, it is possible to have a measure of quality of reconstruction using Eq. 2.46. Values of $\mathcal{P}$ near to 1 (or 100%) mean reliable solutions. The same formula can be used in the reverse way, i.e. it is possible to retrieve the value of the regularization parameter that guarantees a certain level of good reconstruction. In other words:

$$\hat{\eta}_{95\%}^2 = \arg\min_{\eta^2} \left(\|\mathcal{P}(\eta^2) - 0.95\|_2 \right) . \tag{3.11}$$

In this work, the upper bound of regularization parameter is set selecting the maximum value between $\hat{\eta}_{95\%}^2$ and s_1^2:

$$\eta_{max}^2 = \max(\hat{\eta}_{95\%}^2, s_1^2) . \tag{3.12}$$

3.3.4 Bayesian Iterative Regularization

Before explaining the regularization strategy proposed, it is important to better understand the reason behind the need of an improvement of this aspect. One of the requirements of IRLS for obtaining a good final solution is to have reliable, rather than optimal, solution at each iteration. In fact, the result of each iteration is normalized and introduced as a priori information for the next one, with exception of the last one that returns the final output of IRLS. Sure enough, the "shape" of the solution is more important than the absolute level that is actually used for the convergence criterion only (see Eq. 3.8). For this reason, at first iterations of IRLS procedure, it is important to suppress all instabilities, so that the last iteration needs the least regularization possible, in order to recover the correct source level. These intuitive considerations can be translated in the principle that over-regularization is preferred to under-regularization, especially at the beginning of the procedure because the solution is not yet addressed. It is worth to remember that the higher is η^2 the less is the energy of the solution according to Eq. 2.41 or 2.45.

From these considerations, it has been developed an iterative method to estimate the regularization parameter that naturally matches the characteristics just described. The name coined here for this procedure is *Bayesian Iterative Regularization* (BIR). Indeed, the starting point is the BR, in particular the scenario that allows to include noise energy in the estimation of regularization parameter using the inverse Gamma as prior pdf for β^2 (Eq. 2.43). The idea is to use the value of $\hat{\eta}^2_{\mathcal{G}^{-1}}$ to get an estimate of $\hat{\beta}^2_{\mathcal{G}^{-1}}$ and insert this value in a new estimate of the regularization parameter until a convergence is met. The parameter a of inverse Gamma is always set to 0. Instead, $b = \hat{\beta}^2_{\mathcal{G}^{-1}}{}^{(0)} = 0$ is the initialization that boils down to the simple BR without a priori information on the noise energy. The procedure to obtain an estimate of regularization parameter with BIR is the following:

1. Find the minimum of Eq. 2.44 to get $\hat{\eta}^2_{\mathcal{G}^{-1}}{}^{(ir)}$ using $b = \hat{\beta}^2_{\mathcal{G}^{-1}}{}^{(ir-1)}$.
2. Calculate $\hat{\beta}^2_{\mathcal{G}^{-1}}{}^{(ir)}$ from Eq. 2.45.
3. Evaluate $\|\hat{\eta}^2_{\mathcal{G}^{-1}}{}^{(ir)}/\hat{\eta}^2_{\mathcal{G}^{-1}}{}^{(ir-1)} - 1\| < \delta$.
4. If the convergence is met stop the algorithm, otherwise go back to step 1.

The superscript ${}^{(ir)}$ indicates the iteration of BIR process, that is different from the current IRLS iteration. The final estimate of regularization parameter obtained from this strategy is indicated as $\hat{\eta}^2_{BIR}$. The tolerance used in this work is $\delta = 10^{-6}$, in other words, the BIR procedure ends when the ratio of consecutive estimate of η^2 tends to 1. This algorithm always increases the value of the regularization parameter, with respect to BR, due to the insertion of a priori information about β^2. As rule of thumb, the minimum increase of η^2 is about of a factor 2. Another aspect to consider is that the Bayesian Joint cost function may return an unbounded value of η^2, and this characteristic still holds when $a = 0$ and $b \geq 0$. This means that there may not be an upper limit to the increase of regularization parameter with respect to simple BR. Such a phenomenon, that may occur especially in the early iterations of IRLS, represents a critical condition, i.e. the inverse problem is not well addressed and the regularization strategy sees only noise. In this case, the over-regularized solution helps to keep a "safe" condition suppressing the instabilities until the problem is better addressed. However, the upper bound of regularization parameter is set as Eq. 3.12 to avoid uncontrolled values of η^2.

This strategy significantly increases the amount of regularization when the noise level is under-estimated by BR and reduces the risk of instabilities at each iteration. When this happens, the convergence of IRLS gets slower, but its reliability is improved. However, the risk of instabilities and/or under-estimated source level are not completely avoided but drastically reduced. In Section 4.1, a comparison of different regularization strategies is provided, focusing the attention on quantification accuracy. Both Joint and MAP cost functions can be used with BIR, but, where not explicitly specified, the cost function used with BIR is the Joint approach.

3.4 ESM-IRLS

The Equivalent Source Method developed in this work aims at finding a sparse solution of the inverse acoustic problem using the IRLS algorithm explained in the previous section. In this approach, IRLS is applied to linear formulation of direct propagation, Eq. 2.5. The acoustic transfer matrix **G** is built after the propagation model is chosen and the volume of interest is discretized using monopoles. Clearly, also different type of elementary sources can be used. The regularization strategy adopted is BIR with the method of dummy columns. The minimum problem size is kept $M \times M$. Measured data can be used in different forms. Indeed, the generic vector of complex pressure **p** can be: the Fourier Transform of time data acquired by microphones, the averaged Fourier Transform over several snapshots using a phase reference sensor or a component of CSM obtained by proper decomposition. Since acoustic imaging techniques commonly utilize the CSM as input data, CSM decomposition is chosen here. An inverse problem is set for each relevant component and all partial results are summed together to have the total map. Section 3.6 provide further information on different CSM decompositions.

3.5 CMF-IRLS

The Covariance Matrix Fitting approach, described in [51], aims at finding the source field that best approximates the pressure CSM on microphones. Therefore, the solution is sought in quadratic formulation. In the standard version of CMF, the assumptions of uncorrelated sources is done, hence source CSM **Q** becomes diagonal since all the cross-terms are set to zero. This allows to easily rewrite Eq. 2.7 as a standard linear system of equation:

$$\mathbf{P_c} = \mathbf{G_c}\,\mathbf{A_q} \tag{3.13}$$

where $\mathbf{A_q} = diag(\mathbf{Q})$, $\mathbf{P_c}$ is the CSM of measured pressure in vector form and the matrix $\mathbf{G_c}$ is computed using the terms of direct operator $\mathbf{G}$. The explicit form of

Eq. 3.13 is:

$$\begin{bmatrix} p_1p_1^* \\ p_1p_2^* \\ \vdots \\ p_ip_j^* \\ \vdots \\ p_Mp_M^* \end{bmatrix} = \begin{bmatrix} G_{11}G_{11}^* & \dots & G_{n1}G_{n1}^* & \dots & G_{N1}G_{N1}^* \\ G_{11}G_{12}^* & \dots & G_{n1}G_{n2}^* & \dots & G_{N1}G_{N2}^* \\ \vdots & \dots & \vdots & \dots & \vdots \\ G_{1i}G_{1j}^* & \dots & G_{ni}G_{nj}^* & \dots & G_{Ni}G_{Nj}^* \\ \vdots & \dots & \vdots & \dots & \vdots \\ G_{1M}G_{1M}^* & \dots & G_{nM}G_{nM}^* & \dots & G_{NM}G_{NM}^* \end{bmatrix} \begin{bmatrix} q_1q_1^* \\ q_2q_2^* \\ \vdots \\ q_nq_n^* \\ \vdots \\ q_Nq_N^* \end{bmatrix} \tag{3.14}$$

where $i, j = 1, \dots, M$ are the indices of microphones and $n = 1, \dots, N$ is the index of potential sources. Each term $G_{ni}G_{nj}^*$ represents the cross-spectrum between microphones i and j, when the n-th source with unitary power is active. The system has N unknowns and M^2 equations. Since the CSM is hermitian, only the upper (or lower) triangular part is needed to totally define the problem. Therefore, the number of equations can be reduced to $M_c = (M^2 - M)/2 + M$ when auto-powers are considered, or to $M_c = (M^2 - M)/2$ if only cross-power terms are used for setting the problem. The latter formulation is useful to exclude self-noise on microphones and it is the one utilised in this work. The values $Q_{nn} = q_nq_n^*$ must be real and non-negative to have the physical meaning of auto-powers. In order to force a real solution, the system can be solved in the following form:

$$\begin{bmatrix} \mathrm{Re}(\mathbf{P_c}) \\ \mathrm{Im}(\mathbf{P_c}) \end{bmatrix} = \begin{bmatrix} \mathrm{Re}(\mathbf{G_c}) \\ \mathrm{Im}(\mathbf{G_c}) \end{bmatrix} \mathbf{A_q}\,. \tag{3.15}$$

This system of equation is real and of size $2M_c \times N$, since each complex equation is split in two real ones. This trick is equivalent to assume that the solution has only a real part. The IRLS algorithm described in this chapter is used to obtain a solution to the inverse problem exploiting the quadratic formulation of Eq. 3.15. Since this formulation forces the solution to be real but not positive, at each IRLS iteration a positivity constraint is applied and sources having negative power are forced to 0 as in the Gauss-Seidel procedure of DAMAS [6]. Therefore, sources having negative power are removed from calculation, in addition to the discard of sources already mentioned in the IRLS description. The regularization strategy adopted is the same of ESM-IRLS with the only difference of the minimum system size. In fact, the $2M_c \times M$ is sufficient to have enough singular values to have reliable regularization. The IRLS-CMF can be used to fit the whole CSM, but also the single component extracted from CSM by a proper decomposition.

3.6 Cross-Spectral Matrix decompositions

In acoustic imaging, pressure data is commonly processed in frequency domain to obtain the CSM. This is required in some contexts, such as aeroacoustic measurements, where the nature of noise is random. When multiple sources are present at same time, it is useful to be able to separate different contribution to the acoustic field. The problem of source separation has been explained and faced in [15]. In this section, two methods of coherent source component extraction from CSM are described: the typical Eigenmode Decomposition and the possibility to exploit the CLEAN-SC as method to extract spatially coherent components. Other methods can be used to decompose microphone CSM and used in combination with inverse methods proposed in this thesis.

3.6.1 Eigenmode decomposition

Eigenmode Decomposition (ED) relies on the property of CSM to be Hermitian and non-negative definite by construction. Therefore, it can be decomposed as

$$\mathbf{P} = \mathbf{E}_{vec}\,\mathbf{E}_{val}\,\mathbf{E}_{vec}^{H}\,, \tag{3.16}$$

where $\mathbf{E}_{vec}$ is a unitary matrix of M orthonormal eigenvectors and $\mathbf{E}_{val}$ is a diagonal matrix containing the corresponding real positive eigenvalues. It is possible to define the eigenmode $\mathbf{e}_i$ as the eigenvector including its amplitude

$$\mathbf{e}_i = \sqrt{e_{val,i}}\,\mathbf{e}_{vec,i} \qquad i = 1, \ldots, M \tag{3.17}$$

where $\mathbf{e}_{vec,i}$ is the i-th eigenvector and $e_{val,i}$ is the corresponding eigenvalue. Under the constraint of orthogonality, each eigenvector represents a coherent signal across the microphones. For this reason Suzuki [50] proposes to solve an inverse problem for each eigenmode

$$\mathbf{G}\mathbf{q}_i = \mathbf{e}_i \qquad i = 1, \ldots, C \tag{3.18}$$

where $C \leq M$ is the number of most energetic eigenmodes that are considered as relevant. Under some conditions explained in [15], each real uncorrelated source is associated to a single eigenmode, otherwise each ED component is a mixture of several contributions. This is an issue when a sparse solution is sought for each eigenmode because the hypothesis of sparse source field is not fulfilled. Indeed, the orthogonal transformation ensures only that the sum of the powers of all components equals the sum of the powers of all real sources observed at the array location. The choice of C is complicate task for several reasons. First of all, the number of real sources is unknown. In any case, it would be difficult to know how many eigenmodes contains the sources of interest since a real source can be split into several components. In simple cases with spatially separated sources and with low background noise, the most energetic eigenvalues are associated to the sources of interest, but, when dealing with aeroacoustic measurements, the trend of CSM eigenvalues is typically smooth, thus making difficult to properly set C for each frequency.

3.6.2 CLEAN-SC decomposition

A different method to extract source components from CSM is to exploit the CLEAN-SC procedure described in the paragraph 2.4 of reference [38]. This approach was originally developed for deconvolution purposes but here it is exploited as a tool to decompose CSM and combined with inverse methods for the first time, according to the author's knowledge. The iterative procedure extracts the coherent source components exploiting the fact that side lobes of single source CB map are spatially coherent with the main lobe. The concept of spatial source coherence is explained in [36]. The procedure utilized is summarized here (the superscript in the parentheses refers to the iteration):

1. Initialize the degraded CSM: $\overline{\mathbf{D}}^{(0)} = \overline{\mathbf{P}}$ (overline stands for removing diagonal elements).
2. Begin the new iteration calculating the CB map (the so called "dirty map"); the degraded CSM of previous iteration $\overline{\mathbf{D}}^{(it-1)}$ is used.

3. Find the peak location of the current dirty map and identify the source power $P_{max}^{(it-1)}$ and the steering-vector $\mathbf{w}_{max}^{(it)}$ associated to the peak.

4. Calculate the single coherent source component $\mathbf{h}^{(it)}$ solving the following equation

$$\mathbf{h}^{(it)} = \frac{1}{\left(1 + \mathbf{w}_{max}^{H\,(it)}\,\mathbf{H}^{(it)}\,\mathbf{w}_{max}^{(it)}\right)^{1/2}} \left(\frac{\overline{\mathbf{D}}^{(it-1)}\mathbf{w}_{max}^{(it)}}{P_{max}^{(it-1)}} + \mathbf{H}^{(it)}\mathbf{w}_{max}^{(it)}\right) , \quad (3.19)$$

   where $\mathbf{H}^{(it)}$ contains the diagonal elements of $\mathbf{h}^{(it)}\mathbf{h}^{H\,(it)}$. This is an implicit expression that can be solved iteratively staring with $\mathbf{h}^{(it)} = \mathbf{w}_{max}^{(it)}$.

5. Update the degraded CSM

$$\overline{\mathbf{D}}^{(it)} = \overline{\mathbf{D}}^{(it-1)} - P_{max}^{(it-1)}\mathbf{h}^{(it)}\mathbf{h}^{H\,(it)}. \quad (3.20)$$

6. Go back to step 2 and iterate until the following stop criterion is not satisfied:

$$\|\overline{\mathbf{D}}^{(it)}\|_1 \geq \|\overline{\mathbf{D}}^{(it-1)}\|_1 \, . \quad (3.21)$$

This procedure was originally developed to create a "clean map" where only peaks $P_{max}^{(it-1)}$ identified at each iteration (position and level) are considered, thus having a map without sidelobes. The source location and the overall level can be correctly reconstructed from clean maps. However, a loss of spatial information happens when distributed and/or coherent sources are present. In these cases, phase information of coherent/distributed sources is actually contained in $\mathbf{h}^{(it)}$, but it is not exploited to produce the map. The original idea presented here is to use all information extracted from the degradation process of CSM to build coherent source components $\mathbf{c}_i$ similarly to the eigenmodes:

$$\mathbf{c}_i = \sqrt{P_{max}^{(i-1)}}\,\mathbf{h}^{(i)} \qquad i = 1, \ldots, IT \quad (3.22)$$

$$\mathbf{G}\mathbf{q}_i = \mathbf{c}_i \qquad i = 1, \ldots, C \quad (3.23)$$

where IT is the number of iterations for each frequency. Similarly to the eigenmode decomposition approach, an inverse problem is solved for each component (Eq. 3.23) and the full map is obtained summing all contributes. In this case the number of relevant components C for each frequency is given directly by the number of iterations IT, which corresponds to the number of components extracted. When sources are uncorrelated and spatially well separated in CB maps, CLEAN-SC returns distinct components and each of them contains the information of a single source. Otherwise, if two uncorrelated sources are not spatially well separated, the peak location in CB map is detected somewhere in between and the components returned are a mixture of two contributions. In case of correlated sources, they are contained in a single component (e.g. source and its reflections, distributed radiators). The CSM decomposition procedure described above is named here CLEAN-SC Decomposition (CSCD) to differentiate it from the original deconvolution algorithm.

3.7 General guidelines on how to set-up an inverse problem

The success in solving correctly an inverse problem is strictly linked to the choice made in its definition and then in the solution strategy. As rule of thumb it is possible to say that the more the hypothesis in the definition of the problem are realistic the less is the risk of inaccurate solution. The first step is to define the direct problem. This entails the choice of position and extent of ROI and the definition of the direct discrete operator $\mathbf{G}$. The chosen ROI should contain the entire object to map and should be even wider because sound sources near the edge cause artefacts that may address solution in a wrong direction. In fact, sources inside the ROI, but near its edge, cause a concentration of energy in the very last layers of equivalent sources with sharp increase of amplitude. This is particularly evident for low Helmholtz number and when no a priori information is considered in the problem. The first iteration of IRLS seeks a simple (Weighted) Least-Squares solution that spreads the energy all over the equivalent sources. From heuristic point of view, it is possible to compare this kind of solution to a CB map where the PSF depends on ROI, its discretization and the a priori information. The "edge effect" happens because the border of ROI represents a barrier for splitting the energy among equivalent sources close to the real one. Consequently, equivalent sources at the edge take much more energy than others and this result in an evident increase of amplitude. Therefore, following IRLS iteration are contaminated by these artefacts. A good practice to deal with this issue is to have a ROI with sufficient extension to contain the object and use an aperture function in $\mathbf{W}_0$ that strongly penalise potential sources near the edges. A similar effect is generated by sources outside the ROI, therefore when it is possible, it is better to include the zones of all active sound sources in the ROI. As regard the direct operator $\mathbf{G}$, the first choice is the type of elementary sources and the propagation law. In addition, it is possible to consider any effect such as propagation in a flow field, scattering effects, reflections and others. Also discretization of ROI plays a crucial role. Indeed, the more is the density of equivalent sources the finer is the accuracy achievable, but, on the other hand, as the problem size increases the major is the ill-posedness of inverse problems. When dealing with volumetric imaging, the number of equivalent sources easily becomes huge ($10^5 - 10^6$), even with discretization of moderate spatial resolution. Therefore, two conflicting needs occurs: size of ROI large enough to avoid edge effects and the huge problem size when the spatial density of equivalent sources increases. A good meeting point between this two needs is the following: at low Helmholtz numbers it is convenient to have bigger ROI and coarse grid of potential sources. The former reduces edge effects, while the latter keeps the ill-posedness under control, since an ultra-fine grid of potential sources may be counter-productive for large wavelength. With the increase of the Helmholtz number, i.e. with smaller wavelength, ROI can be made smaller, while the density of potential sources can be increased to match the reduction of wavelength in order to keep the problem size under control. In any case, a priori spatial information, or aperture function, reduces the ill-posedness of the problem and helps the source reconstruction task, even with coarse information that is usually available (e.g. CB maps). The more focused on real sources is the a priori information, the more accurate is the result obtained.

Chapter 4

Application and validation on simulated experiments

4.1 Test cases description and algorithm settings

Simulated experiments are used to evaluate localization and quantification capability of the methods proposed in this thesis. In order to ease the readability of results, the volumetric problem with a planar array is reduced to a planar problem with a linear array. Acoustic maps of two regions of interest (ROI) are provided: maps on a line of monopoles and maps on a plane which extends in orthogonal direction with respect to the array line. The former provides the same problems of typical acoustic mapping, the latter provides the same issues of volumetric mapping. A non-uniform array layout is designed giving 31 equally spaced numbers in the range $[-1, 1]$ to the function $\arcsin(\cdot)/\pi$. Microphone coordinates obtained in such a way are scaled by the array aperture D, that has been chosen to be equal to 1 m for these simulations. The IRLS procedure discussed in the previous section allows different settings that lead to different characteristics of results. The norm exponent p and a priori information are the "user-defined" inputs that mostly affect the final result. As already said, the strength of sparsity constraint is given by the particular p chosen. Three meaningful values of p are tested:

- $p = 2$: no sparsity constraint, simple (Weighted) Least-Square solution;
- $p = 1$: maximum sparsity constraint achievable in case of convex optimization;
- $p = 0$: maximum sparsity constraint, non-convex optimization.

Also the choice of W_0 heavily affects the final result because it allows to include any spatial information on source distribution that the user have a priori. Even though several choices can be done, only two are tested in this work:

- $\mathbf{W}_0 = \mathbf{I}$: no a priori information introduced;
- $\mathbf{W}_0 =$ CB map: robust and smooth information are introduced.

Conventional Beamforming maps are calculated using Eq. 2.11 on same pressure data of each inverse problem. In case of ESM, pressure data is always a single component resulting from CSM decomposition, instead, in case of CMF may be also the whole

Method	Pressure decomposition	p	W_0
ESM-IRLS	ED CSCD	$0, 1, 2$	none , CB
CMF-IRLS	none ED CSCD	$0, 1, 2$	none , CB

Table 4.1: Algorithm settings applied to all Test Cases

	x (m)	y (m)	step (m)	N
1D	$[-0.5, 0.5]$	1.0	0.01	101
2D	$[-0.5, 0.5]$	$[0.1, 2.0]$	0.01	19291

Table 4.2: Regions of interest and its discretization used for Test Cases

CSM. The a priori information injected in ESM-IRLS is square root of source autopowers estimated with CB, while in CMF-IRLS source autopowers are used. The threshold THR_{dB} and the convergence criterion tolerance are set to the default values already defined in this chapter. The estimate of regularization parameter is obtained here exploiting BIR with the trick of dummy columns. The analysis is conducted here in terms of *Hemlholtz Number* (He), that is a non-dimensional number proportional to frequency and normalized by the array aperture ($He = D/\lambda = Df/c$). In such way, it is possible to generalize results to any array size. The analysis is conducted in the range from $He = 2$ to $He = 16$.

Simulations of three Test Cases (TC) have been created with *Acoular* (*Acoustic testing and source mapping software*) that is an open source object-oriented Python package for microphone array data processing. Simulations are obtained using free-field propagation with *PointSource* class to simulate monopoles and *WNoiseGenerator* class to generate white noise as source signals. Further information about *Acoular* are available in [49]. The speed of sound is $c = 343$ m/s and the sampling frequency is set to provide an Helmholtz number equal to $He = 64$ (21952 Hz). Length of simulation is 40 s. Microphone CSM is estimated with Welch's method using 1024 samples as block size, an overlap of 50% and Hanning window. This leads to a frequency resolution of $\Delta f = 21.4375$ Hz corresponding to $\Delta He = 0.0625$. The first test case (TC1, Fig.4.1(a)) is a monopole at 1 m of distance from the array that emits white noise. Source level is 1 Pa rms at 1 m distance from the monopole. The other two cases (TC2 and TC3, Fig.4.1(b)) consist of 2 monopoles emitting respectively uncorrelated and correlated white noise. Even in these cases, source level for both sources is 1 Pa rms at 1 m distance from the monopoles. Table 4.2 summarizes the information about two different regions of interest discretized with regular grids of monopoles. It is worth noticing the increase in the order of magnitude of problem size between 1D and 2D problem, since it reflects the same issue encountered switching from surface to volume mapping in common applications. Microphone locations (black dots), source positions (blue diamonds) and regions of interest are depicted in Fig. 4.1, where the black rectangle represents 2D problem and the green line represent 1D problem.

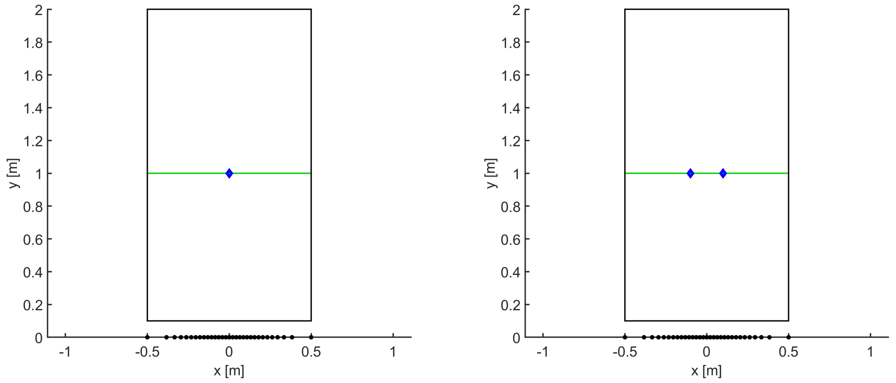

(a) Test Case 1 - One monopole (b) Test Case 2 and 3 - Two monopoles

Figure 4.1: Test Case setups. Black dots: microphone locations. Blue diamonds: source positions. Green line: 1D ROI. Black rectangle: 2D ROI.

4.2 Analysis of results

The three test cases just described, allow to analyse the behaviour of the methods presented in this thesis in controlled conditions. The analysis is mainly focused on the difference in source reconstruction between 1D and 2D ROI, remembering that the former is representative of classic planar mapping with a planar array while the latter is representative of volumetric mapping with a planar array. Results are analysed in terms of source localization and quantification, in particular, how these aspects are influenced by different parameters. All maps show the output of these methods obtained with the acoustic transfer function of Eq. 3.2, i.e. pressure induced at the reference point by a monopole in a generic point of the region of interest. In this case, the reference point is the array centre, that is the origin of coordinate system $\mathbf{r}_0 = \mathbf{0}$. Dynamics of maps shown here is fixed at 30 dB. Maps of 1D ROI show the results for all spectral lines in the range $He = [2, 16]$. While for 2D ROI, maps of only 4 spectral lines are shown, i.e. $He = 2, 4, 8, 16$. Exact source positions are depicted on maps by means of green vertical dotted lines for 1D maps and blue diamonds for 2D maps. All maps and source spectra obtained from maps are depicted in Appendix A to keep the readability of the text, because of the large number of figures.

First simulated experiment (TC1) aims at showing results of source reconstruction with inverse methods when only one monopole is active and no noise is present. In such simple and ideal case, both CSM decomposition methods used in this work (ED and CSCD) return components with negligible difference, hence the same map is obtained as solution of inverse problem. For this reason, results shown are representative of both decompositions. Instead, CMF-IRLS is applied to whole CSM since any separation of source components is needed in this scenario. The same happens in TC3: the sources emit exactly the same signal and again only one relevant component is available. Contrarily, in the second experiment (TC2), two uncorrelated sources are active at same time, therefore, some difference between ED and CSCD are experienced. This experiment makes it possible to evaluate the effect of CSM decomposition on results obtained with ESM-IRLS and CMF-IRLS. The two most energetic components are considered as relevant with both decompositions. Total map for each spectral line is the energetic sum of inverse problem solutions of all components.

4.2.1 Localization ability

All maps show the huge advantage in enforcing sparsity of solution both in 1D and 2D case. In fact, L_2 norm solution minimization returns a map similar to those obtained with beamformers, therefore, even with a single point source, maps have lots of artefacts and poor dynamics. Besides, minimum L_2 norm solutions may produce the edge effect previously described, especially at low frequencies. This effect can be reduced broadening ROI or with a proper spatial window as aperture function (this is partially done by CB map). However, when sparse solution is sought, the most part of artefacts disappears. If the constraint is strong enough, exactly a single source is retrieved from solution of inverse problem in TC1. For example, in 1D case (Figs. A.1 and A.2), it can be seen that for $p = 0$ a single monopole is reconstructed in the whole frequency range analysed, while for $p = 1$, this still depends on frequency and method. In 2D case, sparsity constraint is mandatory to reconstruct the correct source-array distance, since the L_2 minimum norm returns a lobe that may not have its maximum in the correct location, especially at low frequencies. A priori information introduced by CB map helps the source reconstruction process. This is much more effective at high frequency, where CB has finer resolution and wider dynamics. In spite of this, there are some benefits even in the lower frequency range. At $He = 2$, ESM-IRLS necessarily needs sparsity constraint and a priori information to retrieve the correct source position. Indeed, when the problem is strongly ill-conditioned, great part of energy in the solution may be concentrated near the array, as happens in Fig. A.3. Instead, in the same conditions, CMF-IRLS can recover the exact source position even without a priori information (Fig. A.4). As frequency increases, these effects tend to be less relevant since the problem is better conditioned (Figs. A.9 and A.10).

When two uncorrelated sources are present (TC2), in the low frequency range ($He < 6$), both decomposition have problems in separating components such that correct source positions are not retrieved. However, this issue is related only to CSM decomposition, indeed, when CMF is applied to whole CSM, it returns good source localization both in 1D (Fig. A.17) and 2D mapping (Fig. A.22). A particular phenomenon happens in with ESM-IRLS (Figs. A.15 and A.16). In 1D mapping with CB as a priori and $p = 0$, hence in the most simple case, some spectral lines have hugely over-estimated source level, even if the accuracy of localization is satisfying. This might occur when the problem is well addressed and low level of noise is present in data, indeed, the regularization mechanism under-estimates the amount of regularization needed, but non-ideal component separation still may cause numerical instabilities. When two correlated sources are present (TC3) and no sparsity constraint is imposed, they are seen as a unique radiator at low frequencies and start to be separated at different Helmholtz number depending on method and settings. In 1D condition, sparse solutions obtained with ESM-IRLS show two separate sources in the whole range analysed (Fig. A.50). Instead, CMF-IRLS has more difficulty especially in the low frequency range, since it happens that they are reconstructed as two sources closer each other than their real distance (Fig. A.51). Major problems experienced with CMF-IRLS in this test case may be related to the hypothesis of uncorrelated sources made in the problem definition. In 2D mapping, both inverse methods shows more difficulty in source localization of these two correlated sources.

4.2.2 Quantification ability

Reconstructed source spectra (RSS) are obtained from integration of maps over a circle of 0.1 m radius around the exact source position. The error between exact source spectra (ESS) and RSS is reported in terms of difference in dB. Source quantification again shows the need of sparsity constraint to obtain good accuracy in strength estimation. In fact, independently on 1D or 2D problem, L_2 norm solution minimization with ESM approach leads to a severe underestimation of source level due to the strong directivity pattern toward the array that have the equivalent sources when they are re-propagated. This effect is well explained in [43]. With CMF approach, L_2 norm solution minimization also leads to incorrect estimation of source strength. In the latter, no information about phase are obtained, but only about amplitude, therefore, nothing about directivity pattern can be said. In case of ESM-IRLS approach, L_0 norm generally produces the best results in the whole frequency range, while L_1 norm behaviour varies with the frequency, in fact, good strength estimation is obtained only at higher frequencies where a sparse solution is reached even with weak sparsity constraint. Switching from 1D to 2D ROI, ESM-IRLS suffer a decrease of performance in source quantification. Results obtained with CMF-IRLS (L_0 and L_1 norm minimization) are the most reliable and accurate in terms of source strength estimation. The decrease of performance is less evident when ROI switches from 1D to 2D, but the main issues are mostly related to CSM decomposition and correlated sources.

Instabilities experienced in source strength estimation can be classified in two categories: wrong source localization or regularization issues. When the detected source position is outside the zone of integration, RSS is null or under-estimated for these spectral lines. The other aspect is the regularization that is as crucial as challenging task. In fact, a degradation of performance in quantification may be experienced when the degree of difficulty of the problem increases. For example: 1D vs 2D ROI, single vs multiple sources or uncorrelated vs correlated sources. Some steps or peaks in the error of RSS are present. Peaks in RSS are due to under-regularization that does not sufficiently suppress instabilities. Steps are usually generated by significant difference in the regularization process between adjacent spectral lines. These test cases are particularly challenging for Bayesian approach because of the total absence of noise, hence there is an high risk of under-estimated regularization parameter even with BIR.

4.2.3 Effect of different regularization strategies on quantification

As already mentioned, the IRLS algorithm allows to include different regularization mechanism that influence the final result in a non-negligible way. The effect of regularization on result is not easily predictable since IRLS procedure involves several parameters and inputs that are really different among the multitude of practical configurations. However, general consideration can be made, by means of an example, about the effect of regularization on sound source quantification. Two different regularization approaches are described in this work: BR and BIR; in combination with them, two types of cost functions can be used: Joint and MAP. Four combinations can be obtained, that become eight considering the trick of dummy columns to make the regularization process more stable. The limit of η^2 is fixed by Eq. 3.12. The comparison between regularization strategies is made applying ESM-IRLS to TC1 in case of 2D mapping. In all cases, $p = 0$ and CB map as a priori information are used. From the point of view of localization ability, all these regularization strategies provide comparable and satisfying results. Therefore, only RSS vs ESS are depicted in Fig. 4.2.

The first consideration is that MAP cost function generally produces over-estimated and unstable source spectra. This is symptom of under-regularization and amplification of small instabilities in the inversion process. The only exception is BIR-MAP combination that produces an accurate source spectrum. On the contrary, Joint cost function tends to over-regularize the solution. The worst case is BIR-Joint combination that produces an under estimation of more than 10 dB because of the non-bounded estimation of η^2 that tends to η^2_{max}. The most stable case is BIR-Joint with dummy columns, even if it gives a constant offset of about -1.5 dB. Hence, this example suggest BIR-MAP and BIR-Joint with dummy columns as the best candidates for regularization strategy in IRLS. Another test conducted compares the robustness to noise of these two regularization strategies. The conditions are exactly the same of previous test but complex noise is added to pressure vector used in the inverse problem. Complex noise is generated using Eq. 3.10 for two signal-to-noise ratios: 20 and 10 dB.

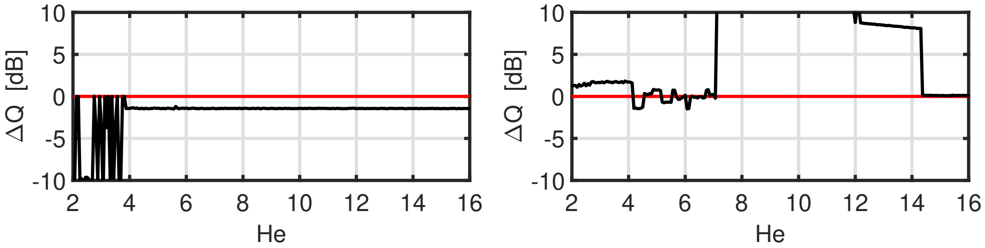

(a) BR - Joint

(b) BR - MAP

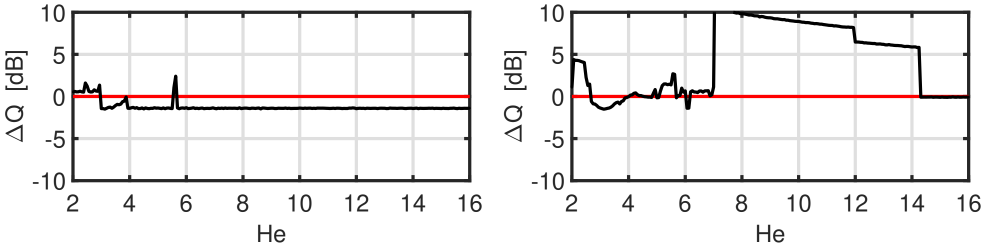

(c) BR with DC - Joint

(d) BR with DC - MAP

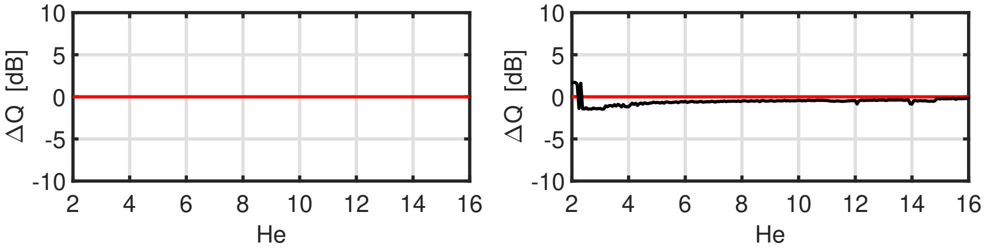

(e) BIR - Joint

(f) BIR - MAP

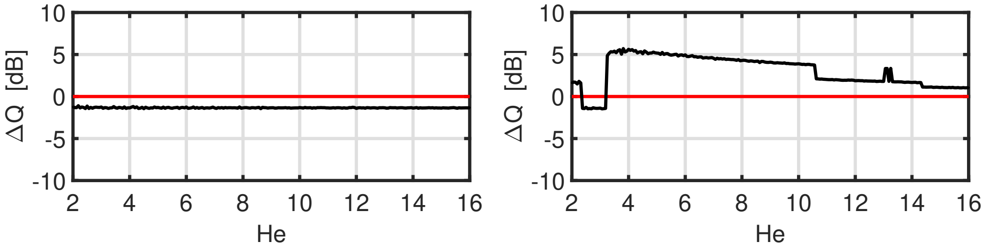

(g) BIR with DC - Joint

(h) BIR with DC - MAP

Figure 4.2: Test Case 1 (2D) - Errors in source spectrum reconstruction with ESM-IRLS ($p = 0$ and $\mathbf{W}_0 = \text{CB}$) using different regularization strategies. Red line: target error. Black line: error of reconstructed spectrum.

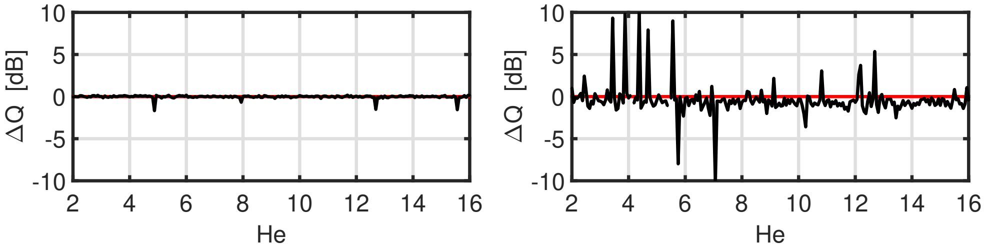

(a) BIR with DC - Joint - SNR 20 dB (b) BIR - MAP - SNR 20 dB

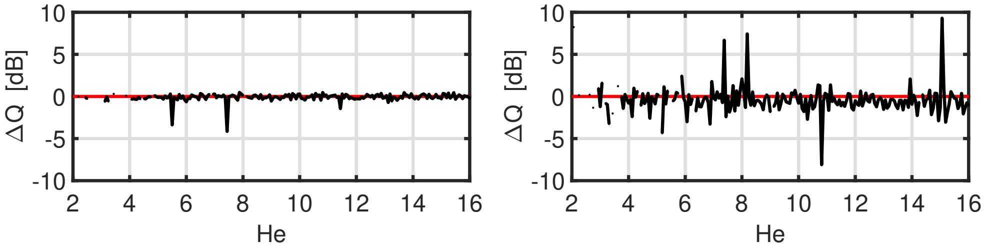

(c) BIR with DC - Joint - SNR 10 dB (d) BIR - MAP - SNR 10 dB

Figure 4.3: Test Case 1 (2D) - Errors in source spectrum reconstruction with ESM-IRLS ($p = 0$ and $\mathbf{W}_0 = \text{CB}$) with different levels of noise. Red line: target error. Black line: error of reconstructed spectrum.

The second test shows a clear trend: BIR-Joint with dummy columns produces much more stable and reliable estimation of source strength. Indeed, it outperforms BIR-MAP strategy and the offset experienced in noise-free condition disappears. Reminding also at the theoretical discussion about regularization strategies, it is possible to conclude that BIR with Joint cost function and dummy columns perfectly matches the needs of IRLS. For these reasons, it has been adopted in this work for ESM-IRLS and CMF-IRLS. The effect of different regularization strategies on CMF-IRLS is not showed here since results in Appendix A widely demonstrate the accuracy of quantification achieved with the same regularization mechanism chosen for ESM-IRLS.

4.2.4 Applicability to volumetric acoustic imaging

From the analysis of these results, it is possible to conclude that inverse methods proposed in this thesis can deal successfully with volumetric acoustic mapping. Degradation of performance is experienced, turning from 1D to 2D (i.e. from planar to volumetric) mapping, in the low frequency range. The effectiveness of methods depends on different factors. Surely, one of the most important is frequency of analysis, or better the Helmholtz number. As rule of thumb it is possible to claim that $He > 8$ is a condition to fulfil to have reliable maps in most applications. When satisfied, these methods provide good accuracy in source localization, while some instabilities may remain in source quantification. For $He < 8$, the results are not always satisfying, especially when CSM is decomposed in components. Indeed, in these conditions, better results are achieved with CMF-IRLS applied to whole CSM. Two approaches proposed, ESM and CMF, have different advantages and drawbacks. On one hand, ESM-IRLS has better behaviour with correlated sources and provide also information about phase. On the other hand, CMF-IRLS works better in the low frequency range and provide more reliable strength estimation.

Chapter 5

Results of application on experimental data

In this chapter, experimental applications of volumetric mapping with inverse methods are shown. Both the cases of study shown in the following sections are typical measurement setups for aeroacoustic applications. Sound sources generated by the interaction of an objects with air flow are not bounded to be on the object surface, hence this kind of applications benefits of volumetric mapping. The first experimental test is an airfoil placed in an open jet, where pressure data are acquired with a single planar array. This application represents, from the author's point of view, a breakthrough in acoustic source mapping techniques. Indeed, it will be shown that much more information can be extracted from volumetric maps without changing the hardware and the experimental setup. The second application of inverse methods for volumetric acoustic mapping is on 1/7th scale aircraft model placed in a large Low Speed Wind Tunnel. In this typical wind tunnel setup, two arrays looking at the model from different points of view are present. Acoustic mapping techniques presented in this thesis allow to combine data of multiple arrays as it were a unique array without any change in the algorithm. Therefore, the experimental configuration gives the opportunity to study drawbacks and advantages in using a single array or multiple planar arrays combined together.

5.1 Volumetric mapping with single planar array

The application here is an experiment conducted in the aeroacoustic wind tunnel at Brandenburg University of Technology [25]. A NACA 0012 airfoil is positioned in an open jet of diameter 0.2 m and core velocity 50 m/s. The airfoil has a span of 0.28 m and a chord length of 0.25 m. The boundary layer tripping was realized with a 2.5 mm anti-slip tape applied at 10% of the chord, both on the suction and the pressure side. The array utilized has 56 microphones and a diameter of 1.3 m; it was placed 0.715 m above the airfoil, outside the flow. Figure 5.1 shows the position of the airfoil and the nozzle with respect to the array. Data were sampled at 51200 samples/s for 40 s and the CSM is estimated averaging 4000 blocks of 1024 samples (overlap 50 %) using Hanning window. The frequency resolution obtained is 50 Hz. Sound propagation through the flow field is calculated using *Acoular OpenJet* environment class and virtual propagation distances, corresponding to actual travel time through

Algorithm	p	CSM decomposition	$\mathbf{W}_0$
ESM-IRLS	0	ED	CB map
		CSCD	
CMF-IRLS	0	ED	
		CSCD	
	1	none	

Table 5.1: Algorithm settings used for volumetric mapping with single planar array.

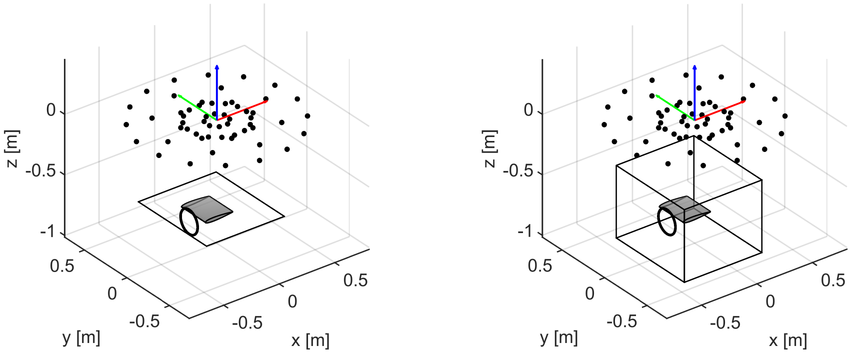

(a) 2D - Planar problem

(b) 3D - Volumetric problem

Figure 5.1: Measurement setup and regions of interest.

the flow field, are used in Eq. 3.2 instead of geometric ones. Reference point for acoustic propagator is the coordinate system origin $\mathbf{r}_0 = \mathbf{0}$ that coincides with the array centre.

A comparison between 2D planar mapping and 3D volumetric mapping is presented here. The objective is to show advantages and issues encountered in practical applications. Table 5.1 summarizes algorithm settings used in this application on experimental data. Both ED and CSCD are used in combination with ESM and CMF, enforcing the maximum sparsity with L_0 norm minimization. The number of eigenmodes is empirically set to $C = 20$ for all frequency bands of interest. Instead, the number of iterations of CSCD (i.e. the maximum number of components) is limited to be $C \leq 20$ for each frequency within the bands analysed. Also an approach without decomposition is tested: CMF-IRLS with $p = 1$ applied to whole CSM with the aim of minimizing the total source energy. In all cases, CB map is introduced as a priori. Maps are produced for three one-third octave bands: 2000 Hz, 4000 Hz and 8000 Hz. These bands correspond approximately to following Helmholtz number ranges: $He \approx [6.7, 8.2]$, $He \approx [13.5, 16.7]$ and $He \approx [26.8, 33.5]$. This means that only the first band might have issues in source identification for volumetric case, while planar mapping should not suffer any problem related to frequency range. All maps in this section are depicted with a dynamic range of 25 dB.

	x (m)	y (m)	z (m)	step (m)	N
Plane	$[-0.400, 0.300]$	$[-0.400, 0.400]$	-0.715	0.05	255
				0.01	5751
Volume	$[-0.400, 0.300]$	$[-0.400, 0.400]$	$[-1.015, -0.415]$	0.05	3315
				0.01	350811

Table 5.2: Regions of interest and their discretization with regular grid of monopoles used for airfoil noise mapping.

5.1.1 Maps on regular grids

The commonest choice is to map the region of interest using a regular grid. Table 5.2 reports ROI of planar and volumetric mapping. It is worth noticing that the problem size increases considerably from 2D to 3D. Two different steps are used and tested for regular grids: 1 cm and 5 cm. These maps show the evident difference between volumetric acoustic mapping and the classic approach, indeed, some sources are located on the chord plane but others are located outside. As example, some volumetric maps are depicted from different views to underline the difference between 2D and 3D mapping. Figures 5.3(b),5.7(b) and 5.11(b) can be compared with top and side views of their 3D analogous, i.e. Figs 5.14,5.15 and 5.16. Common planar/surface mapping approach forces the mapped noise sources to be located on the chosen surface, thus giving misleading results. Exploiting methods described in this thesis, more spatial information can be extracted from volumetric maps, at the only cost of re-processing data. In the lowest band, not always clear structure can be recognized on volumetric maps, while clear source identification can be done for higher bands. As shown on simulated experiments in previous chapter, $He = 8$ represents somehow a practical limit of these techniques at lower frequency, when single planar array is used for volumetric applications. In volumetric mapping, CMF-IRLS returns better maps, while in 2D mapping both methods have comparable results. Difference between ED and CSCD is also well evident from maps shown. Decomposition based on CLEAN-SC makes the inverse methods capable to suppress lots of artefacts due to background noise present in pressure data. Good results are also obtained with CMF-IRLS applied to whole CSM with $p = 1$, but in this case, sources having lower level than the principal one may not be detected. The drawback CMF-IRLS with CSM decomposition, is that it is computationally demanding given the problem size. For this reason can be useful a first quick rough estimation of sound source location on a coarse grid (e.g. 5 cm step in this application). This information can be used to better address the problem and get similar results of those obtained with fine grid resolution, but with less computational effort. In the next section non-uniform discretization of ROI is tested.

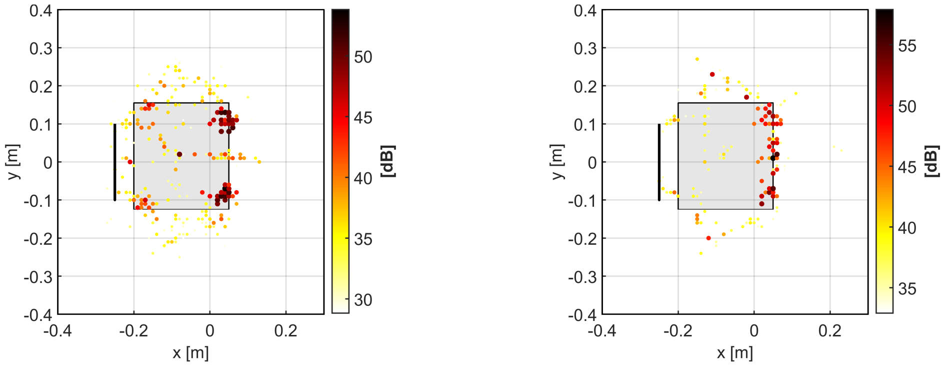

(a) ED (b) CSCD

Figure 5.2: 2000 Hz one-third octave band - 2D mapping on regular grid with 1 cm step - ESM-IRLS with $p = 0$.

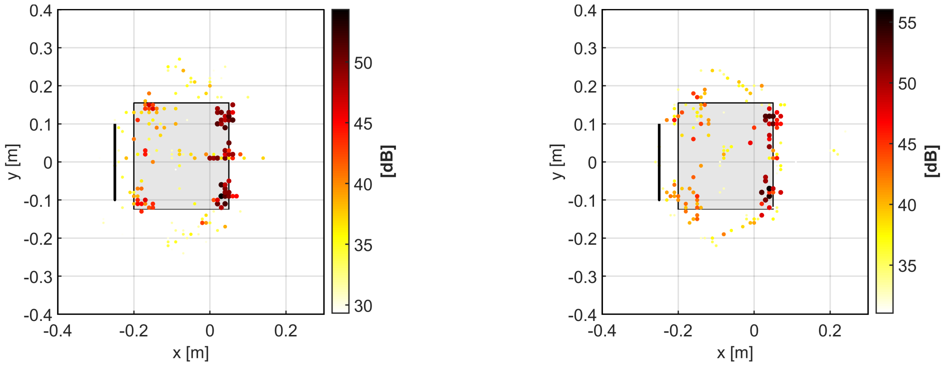

(a) ED (b) CSCD

Figure 5.3: 2000 Hz one-third octave band - 2D mapping on regular grid with 1 cm step - CMF-IRLS with $p = 0$.

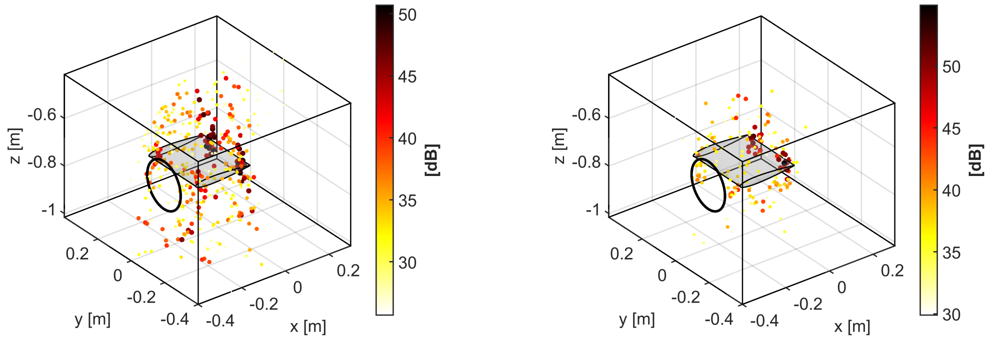

(a) ED (b) CSCD

Figure 5.4: 2000 Hz one-third octave band - 3D mapping on regular grid with 1 cm step - ESM-IRLS with $p = 0$.

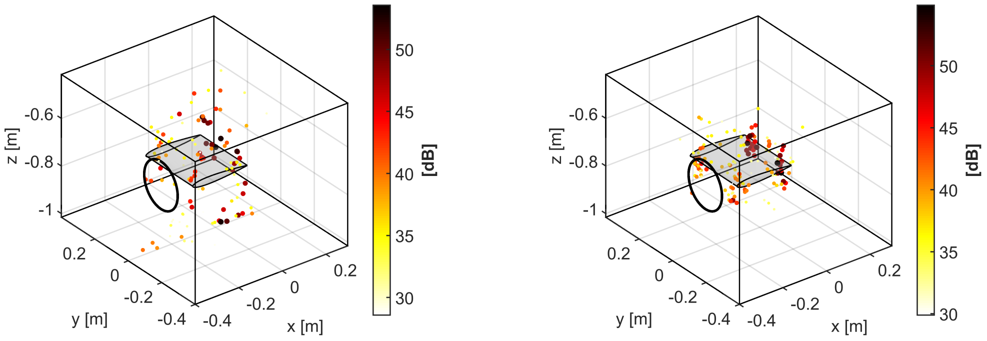

(a) ED (b) CSCD

Figure 5.5: 2000 Hz one-third octave band - 3D mapping on regular grid with 1 cm step - CMF-IRLS with $p = 0$.

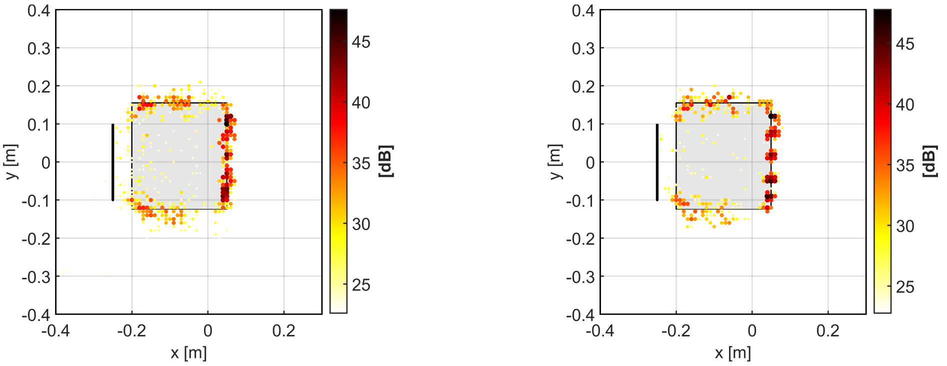

(a) ED (b) CSCD

Figure 5.6: 4000 Hz one-third octave band - 2D mapping on regular grid with 1 cm step - ESM-IRLS with $p = 0$.

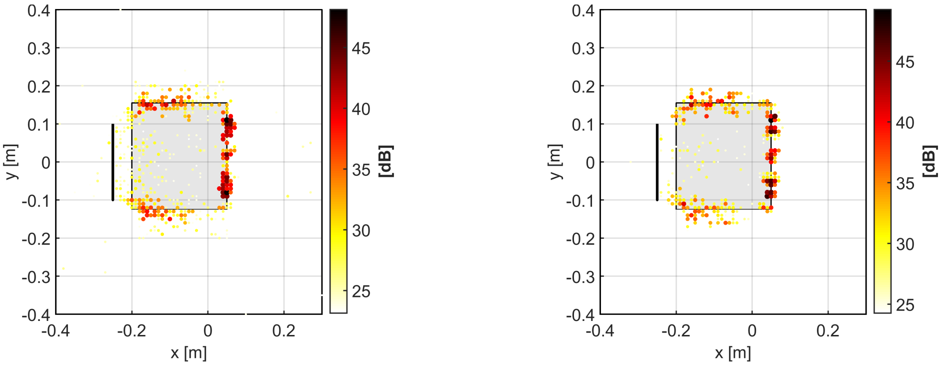

(a) ED (b) CSCD

Figure 5.7: 4000 Hz one-third octave band - 2D mapping on regular grid with 1 cm step - CMF-IRLS with $p = 0$.

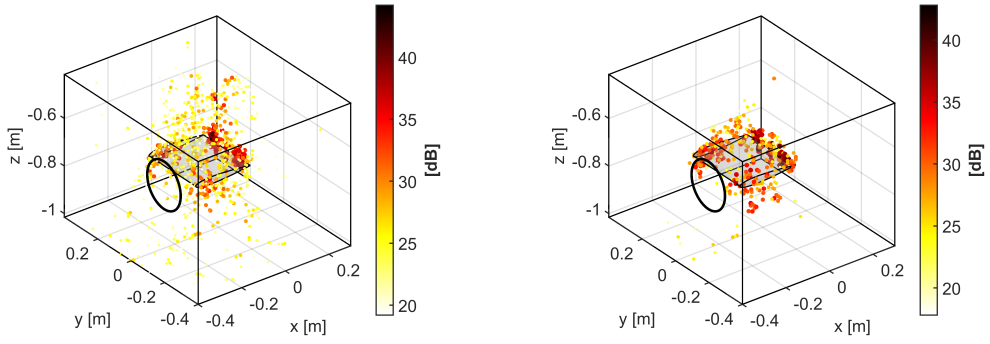

(a) ED (b) CSCD

Figure 5.8: 4000 Hz one-third octave band - 3D mapping on regular grid with 1 cm step - ESM-IRLS with $p = 0$.

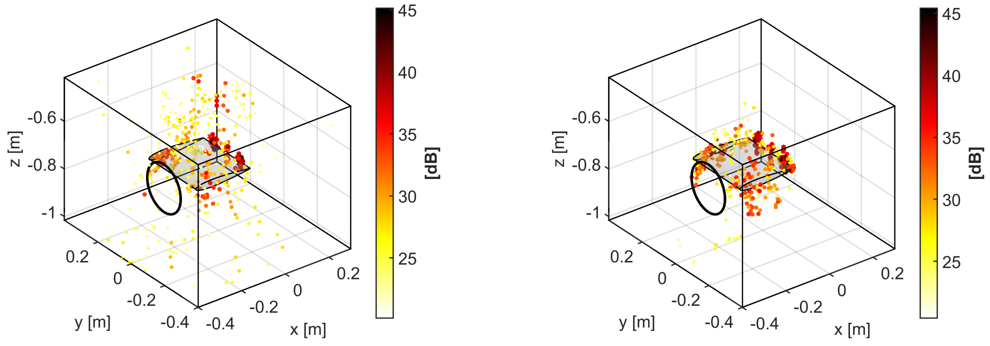

(a) ED (b) CSCD

Figure 5.9: 4000 Hz one-third octave band - 3D mapping on regular grid with 1 cm step - CMF-IRLS with $p = 0$.

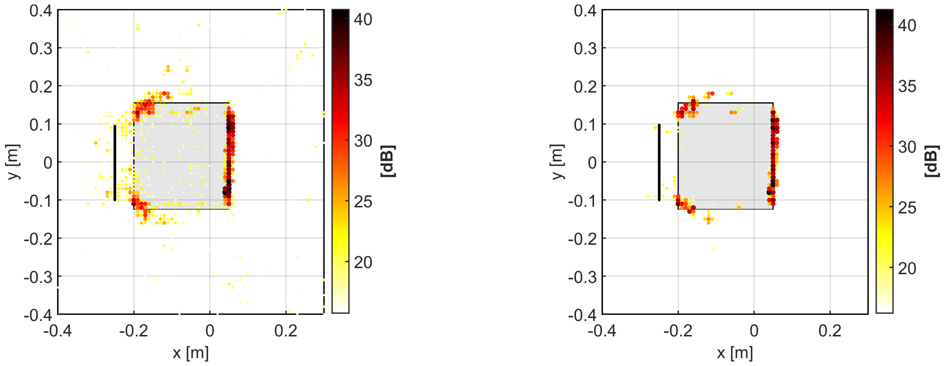

(a) ED (b) CSCD

Figure 5.10: 8000 Hz one-third octave band - 2D mapping on regular grid with 1 cm step - ESM-IRLS with $p = 0$.

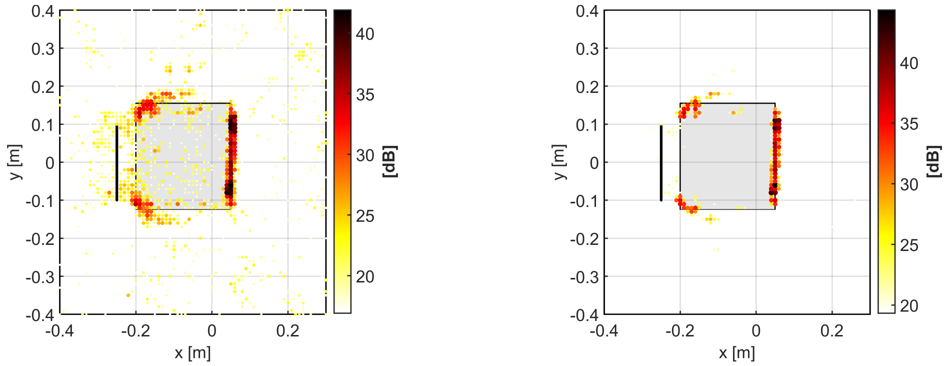

(a) ED (b) CSCD

Figure 5.11: 8000 Hz one-third octave band - 2D mapping on regular grid with 1 cm step - CMF-IRLS with $p = 0$.

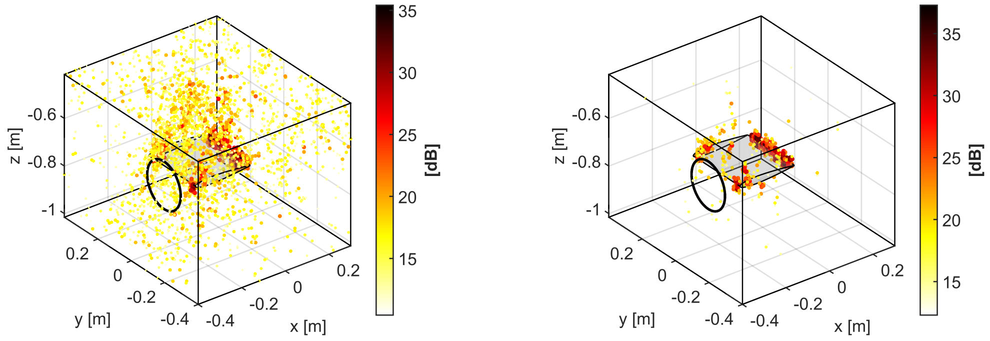

(a) ED (b) CSCD

Figure 5.12: 8000 Hz one-third octave band - 3D mapping on regular grid with 1 cm step - ESM-IRLS with $p = 0$.

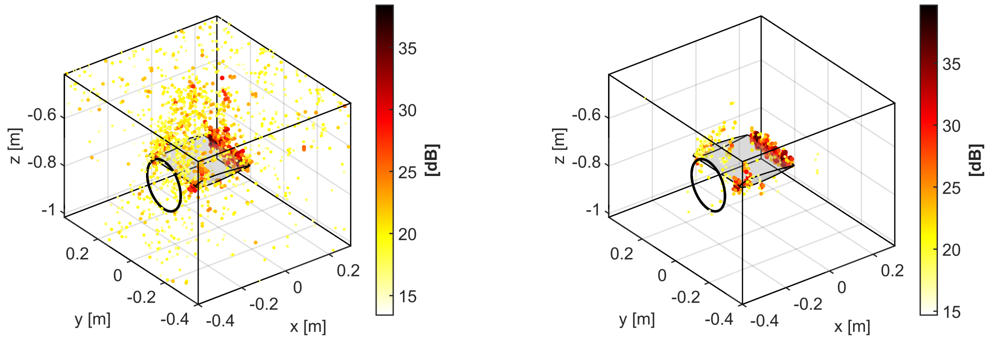

(a) ED (b) CSCD

Figure 5.13: 8000 Hz one-third octave band - 3D mapping on regular grid with 1 cm step - CMF-IRLS with $p = 0$.

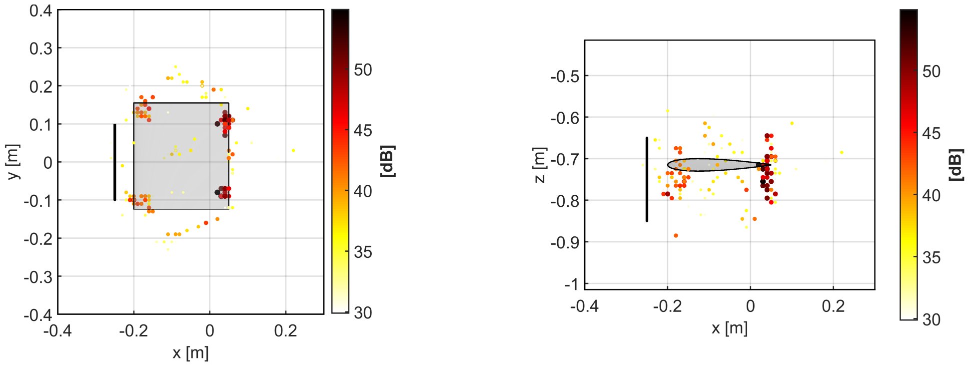

(a) Top view (b) Side view

Figure 5.14: 2000 Hz one-third octave band - Different views of 3D mapping on regular grid with 1 cm step - CMF-IRLS with $p = 0$ and CSCD.

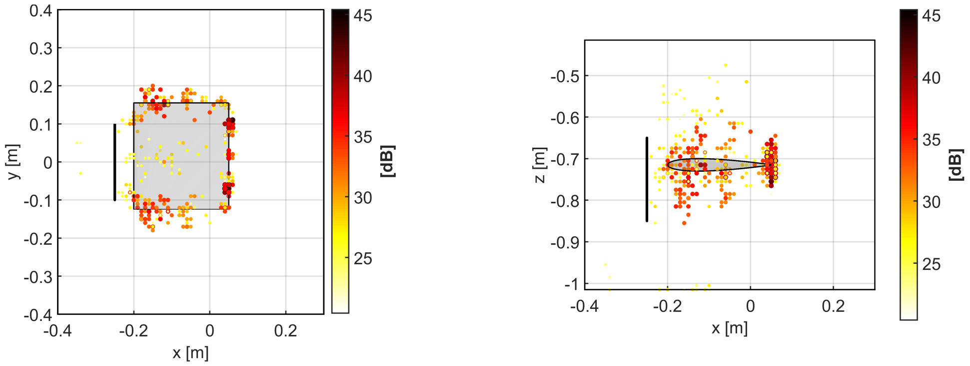

(a) Top view (b) Side view

Figure 5.15: 4000 Hz one-third octave band - Different views of 3D mapping on regular grid with 1 cm step - CMF-IRLS with $p = 0$ and CSCD.

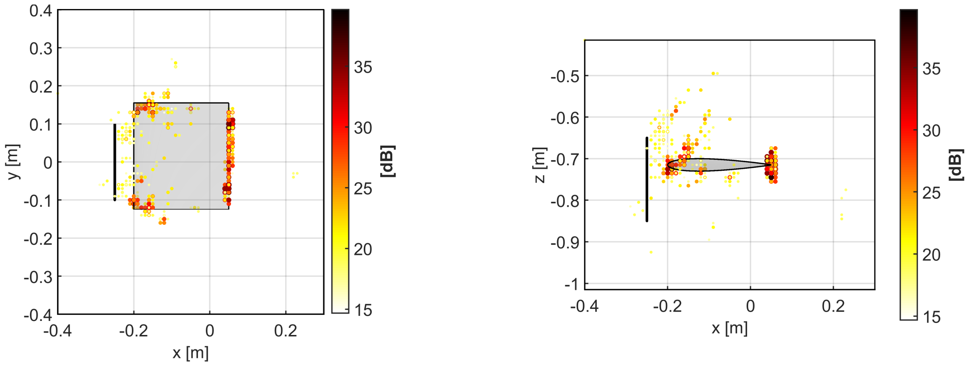

(a) Top view (b) Side view

Figure 5.16: 8000 Hz one-third octave band - Different views of 3D mapping on regular grid with 1 cm step - CMF-IRLS with $p = 0$ and CSCD.

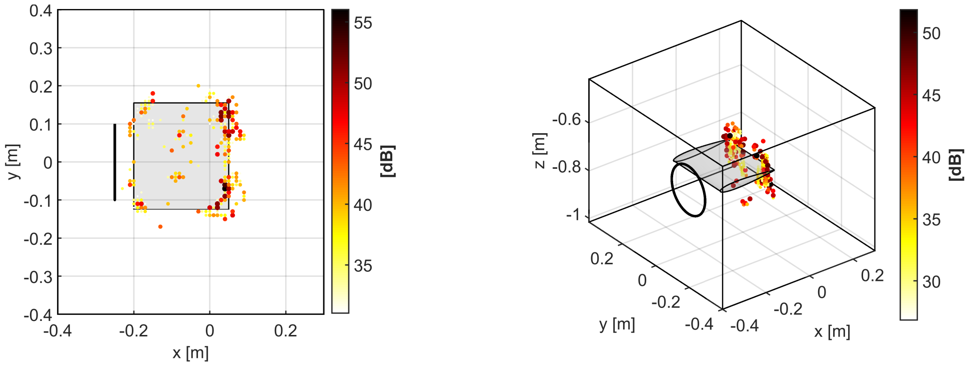

(a) 2D (b) 3D

Figure 5.17: 2000 Hz one-third octave band - mapping on regular grid with 1 cm step - CMF-IRLS on whole CSM with $p = 1$.

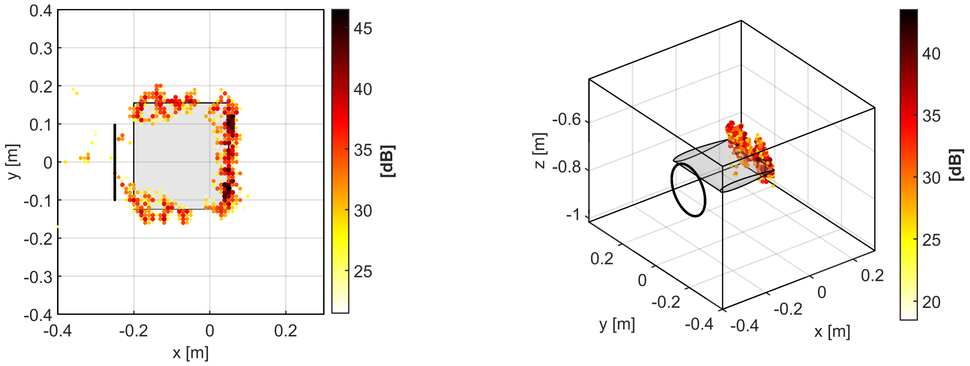

(a) 2D (b) 3D

Figure 5.18: 4000 Hz one-third octave band - mapping on regular grid with 1 cm step - CMF-IRLS on whole CSM with $p = 1$.

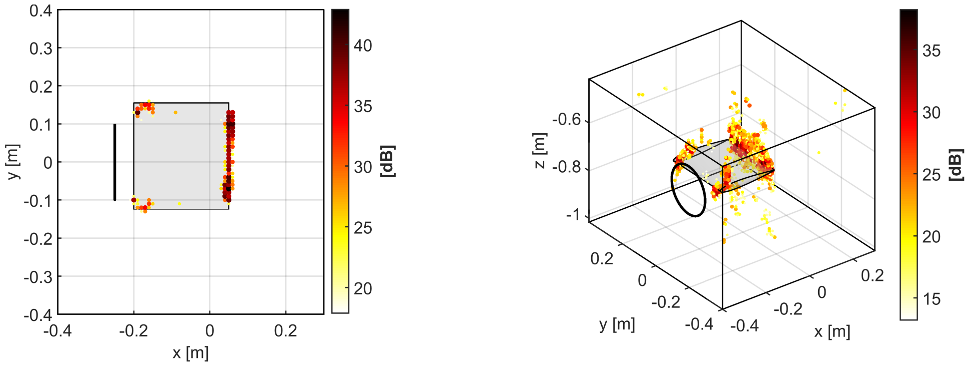

(a) 2D (b) 3D

Figure 5.19: 8000 Hz one-third octave band - mapping on regular grid with 1 cm step - CMF-IRLS on whole CSM with $p = 1$.

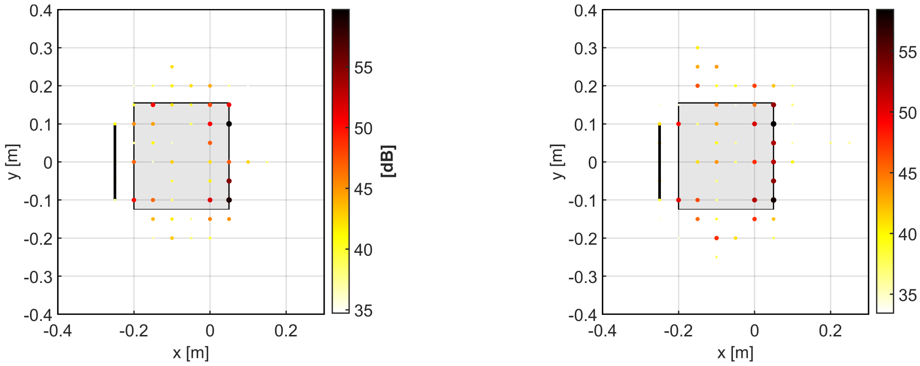

(a) ED (b) CSCD

Figure 5.20: 2000 Hz one-third octave band - 2D mapping on regular grid with 5 cm step - ESM-IRLS with $p = 0$.

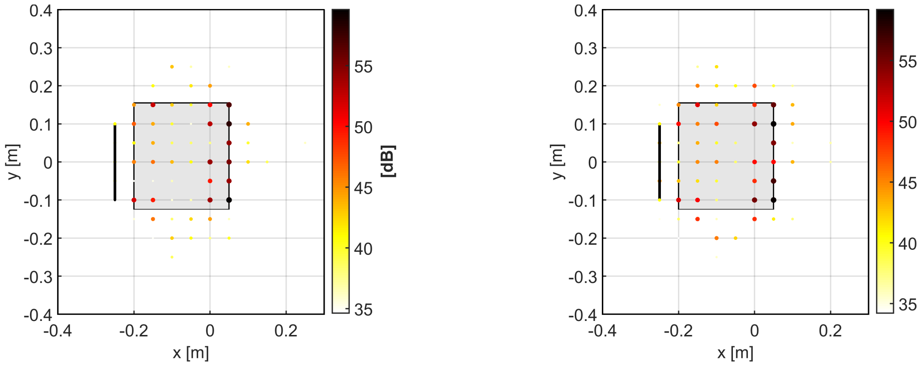

(a) ED (b) CSCD

Figure 5.21: 2000 Hz one-third octave band - 2D mapping on regular grid with 5 cm step - CMF-IRLS with $p = 0$.

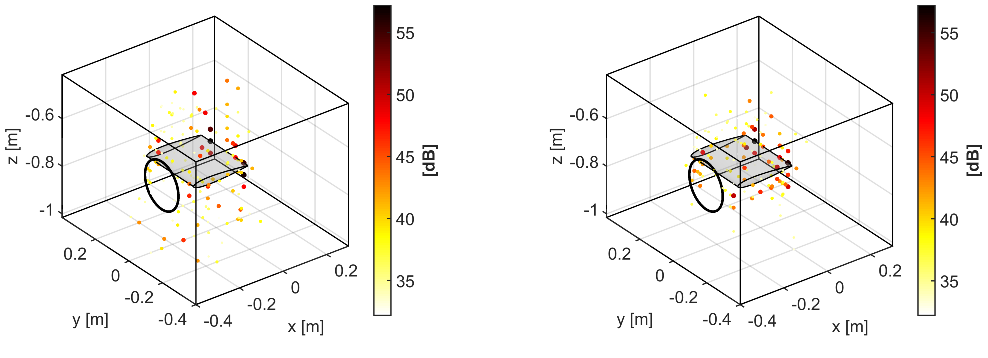

(a) ED (b) CSCD

Figure 5.22: 2000 Hz one-third octave band - 3D mapping on regular grid with 5 cm step - ESM-IRLS with $p = 0$.

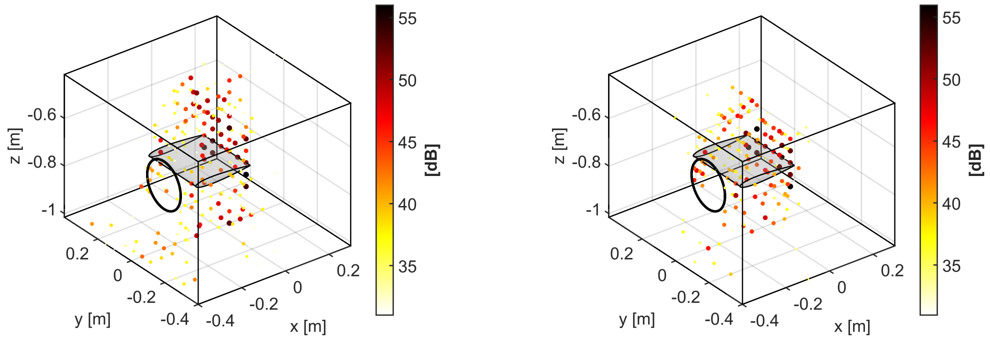

(a) ED (b) CSCD

Figure 5.23: 2000 Hz one-third octave band - 3D mapping on regular grid with 5 cm step - CMF-IRLS with $p = 0$.

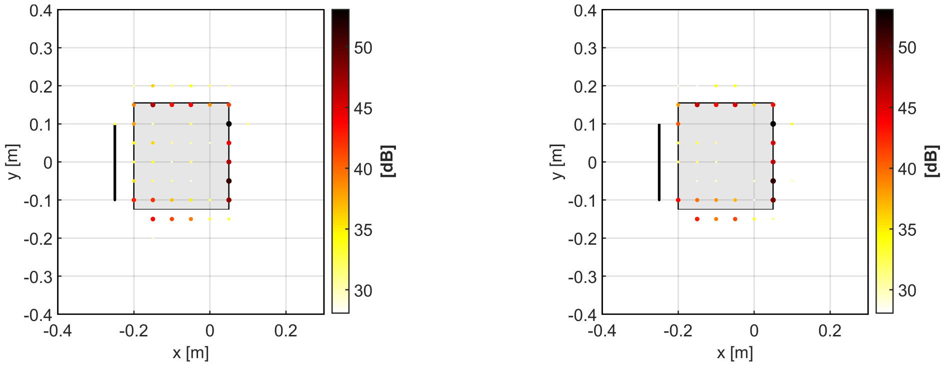

(a) ED (b) CSCD

Figure 5.24: 4000 Hz one-third octave band - 2D mapping on regular grid with 5 cm step - ESM-IRLS with $p = 0$.

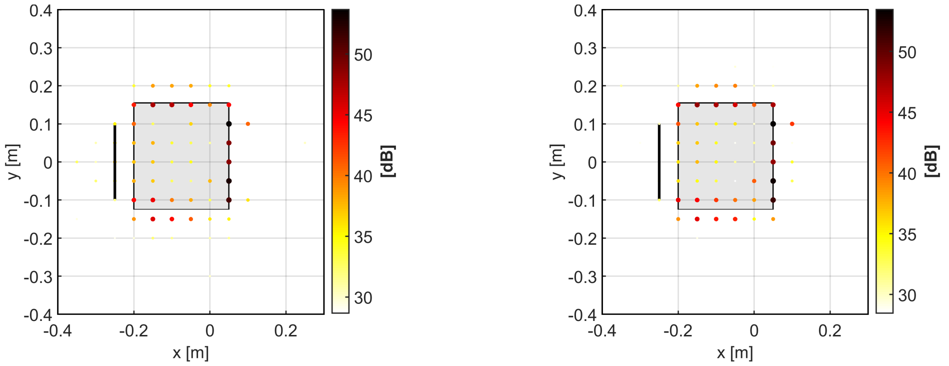

(a) ED (b) CSCD

Figure 5.25: 4000 Hz one-third octave band - 2D mapping on regular grid with 5 cm step - CMF-IRLS with $p = 0$.

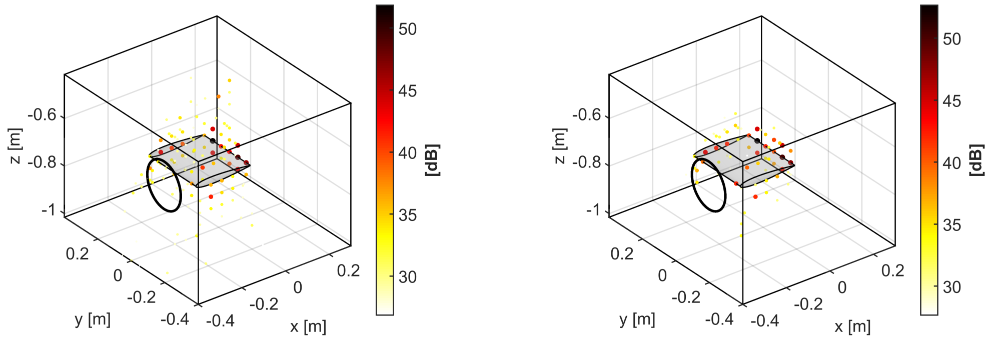

(a) ED (b) CSCD

Figure 5.26: 4000 Hz one-third octave band - 3D mapping on regular grid with 5 cm step - ESM-IRLS with $p = 0$.

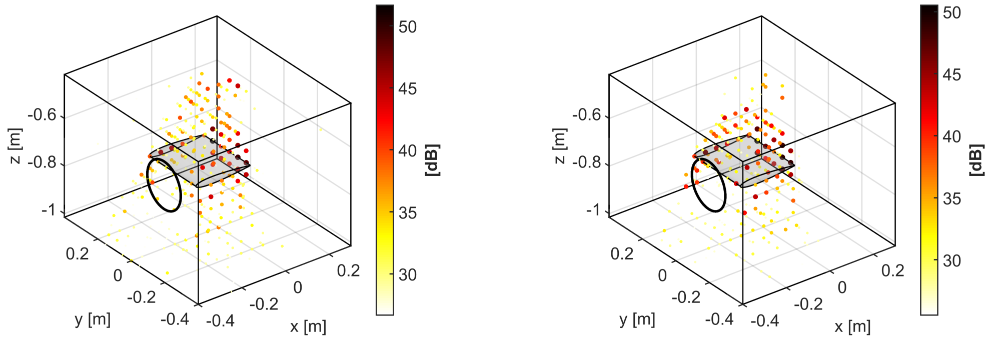

(a) ED (b) CSCD

Figure 5.27: 4000 Hz one-third octave band - 3D mapping on regular grid with 5 cm step - CMF-IRLS with $p = 0$.

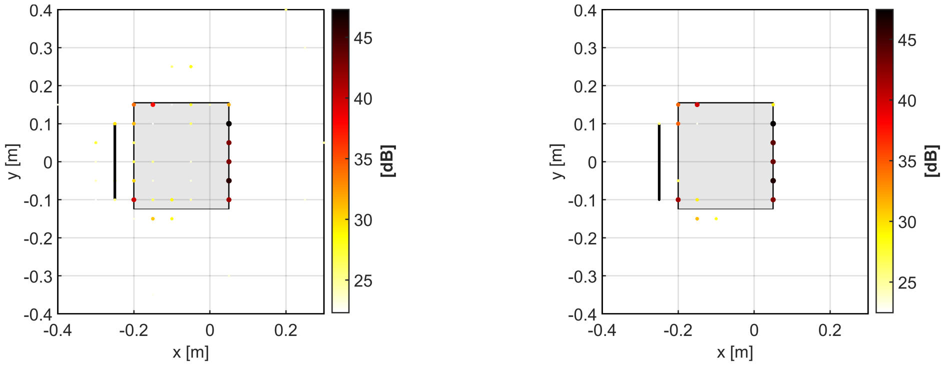

(a) ED (b) CSCD

Figure 5.28: 8000 Hz one-third octave band - 2D mapping on regular grid with 5 cm step - ESM-IRLS with $p = 0$.

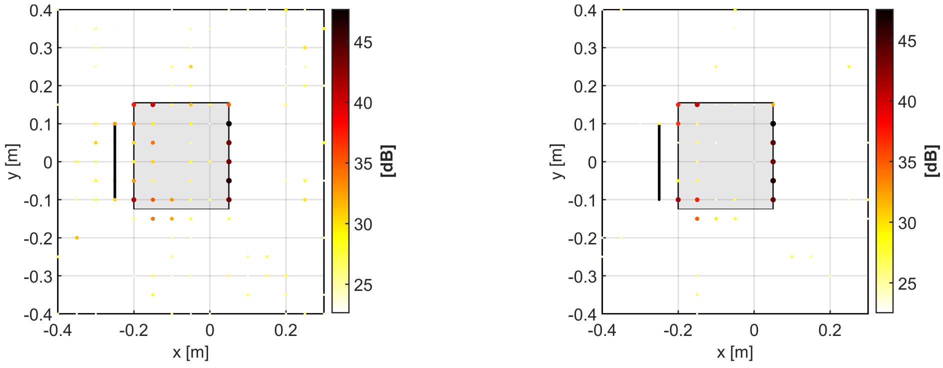

(a) ED (b) CSCD

Figure 5.29: 8000 Hz one-third octave band - 2D mapping on regular grid with 5 cm step - CMF-IRLS with $p = 0$.

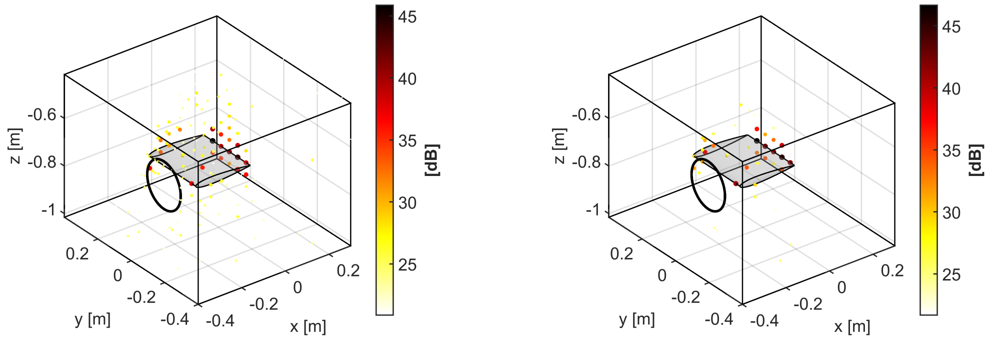

(a) ED (b) CSCD

Figure 5.30: 8000 Hz one-third octave band - 3D mapping on regular grid with 5 cm step - ESM-IRLS with $p = 0$.

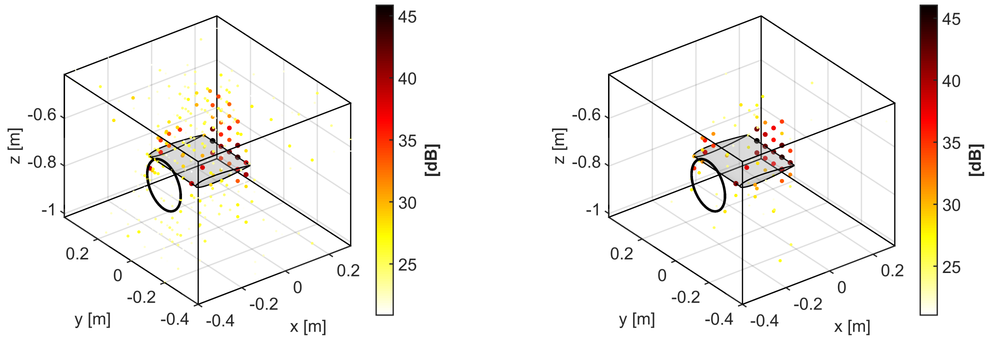

(a) ED (b) CSCD

Figure 5.31: 8000 Hz one-third octave band - 3D mapping on regular grid with 5 cm step - CMF-IRLS with $p = 0$.

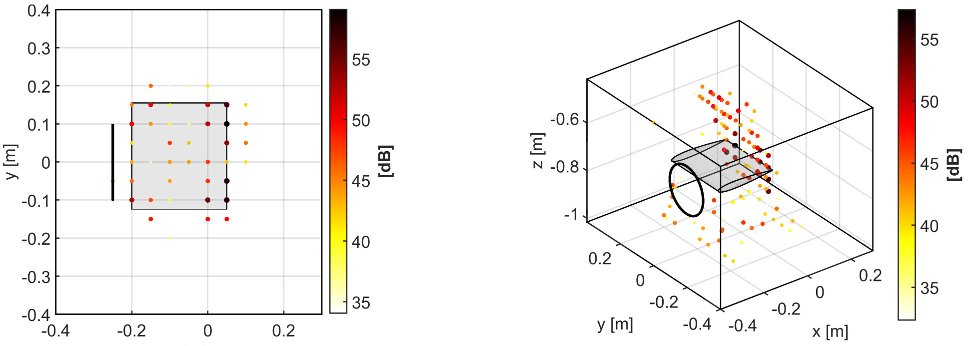

(a) 2D mapping on regular grid with 5 cm step

(b) 3D mapping on regular grid with 5 cm step

Figure 5.32: 2000 Hz one-third octave band - CMF-IRLS on whole CSM with $p = 1$.

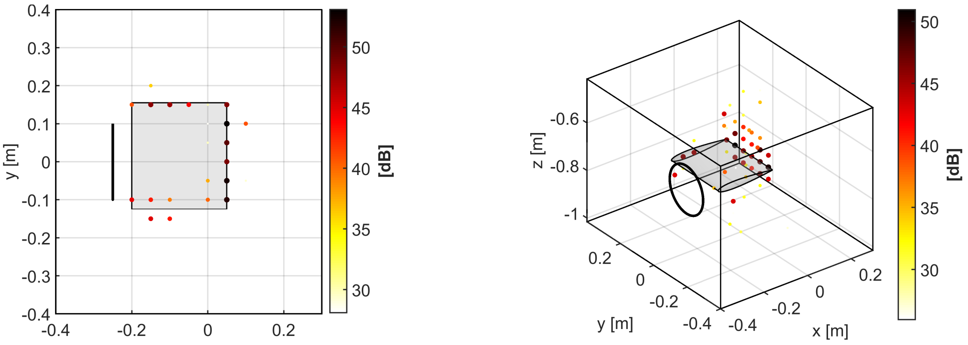

(a) 2D mapping on regular grid with 5 cm step

(b) 3D mapping on regular grid with 5 cm step

Figure 5.33: 4000 Hz one-third octave band - CMF-IRLS on whole CSM with $p = 1$.

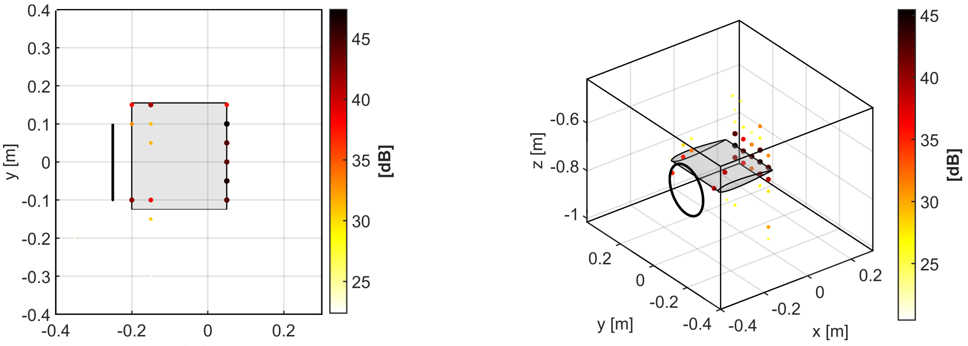

(a) 2D mapping on regular grid with 5 cm step

(b) 3D mapping on regular grid with 5 cm step

Figure 5.34: 8000 Hz one-third octave band - CMF-IRLS on whole CSM with $p = 1$.

5.1.2 Maps on non-uniform mesh

In order to reduce degrees of freedom of source space, a non uniform mesh of ROI can be used. The idea is to have dense distribution of equivalent sources where it is necessary and sparse elsewhere. For this application, the mesh utilized is made by two regular grids with different steps, but any kind of mesh can be used (e.g. tetrahedral mesh). Figure 5.35 depicts two zones that enclose the airfoil, while Table 5.3 reports the boundaries and the steps used to obtain grids with different resolutions for outer and inner regions. It is worth noticing the dramatic reduction of number of points with respect grids (2D and 3D) used in the previous section, when 1 cm step has been used for regular grid. Figure 5.36 depicts the discretization of planar ROI made with a grid having two different steps for inner and outer regions. This section aims at showing how this simple strategy allows to achieve results similar to those obtained with fine regular grid, but with smaller problem size and all benefits that comes from it. Since potential sources are not uniformly distributed over space, it happens that a sound source in a zone dense of equivalent sources is mapped into several of them, on the contrary in sparse zone, it would be mapped in few of them. This cause the energy of a sound source to be split into few or several equivalent sources depending on the zone. However, this does not need any change in the algorithm, but it can be an issue for localization purposes. To overcome this issue, maps can be visualized in terms of strength per volume, in this way density of equivalent sources is compensated. Normalization of solution by volumes/areas related to each potential sources is done using volumes/areas of Voronoi cells [2] of non-uniform mesh. Maps depicted in Figs. from 5.37 to 5.51 show each result as is, while maps in Figs. from 5.52 to 5.66 show the effect of compensation of non-uniform mesh. The latter are also normalized by its maximum, since are intended for localization purpose only.

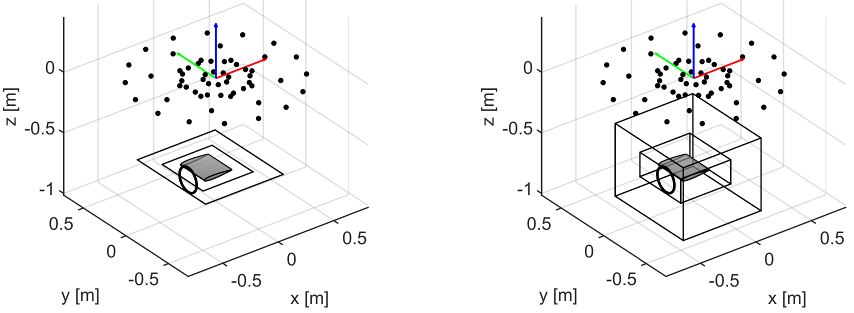

(a) 2D - Planar problem (b) 3D - Volumetric problem

Figure 5.35: Boundaries of different regions for non uniform meshing.

	x (m)	y (m)	z (m)	step (m)	N
Plane	$[-0.400, 0.300]$	$[-0.400, 0.400]$	-0.715	0.05	2149
	$[-0.300, 0.150]$	$[-0.240, 0.240]$		0.01	
Volume	$[-0.400, 0.300]$	$[-0.400, 0.400]$	$[-1.015, -0.415]$	0.05	50199
	$[-0.300, 0.150]$	$[-0.240, 0.240]$	$[-0.815, -0.615]$	0.01	

Table 5.3: Regions of interest and their discretization for non uniform meshing used for airfoil noise mapping. Both for plane and volume, first row is the outer region and second row is the inner region. The total number of points is N.

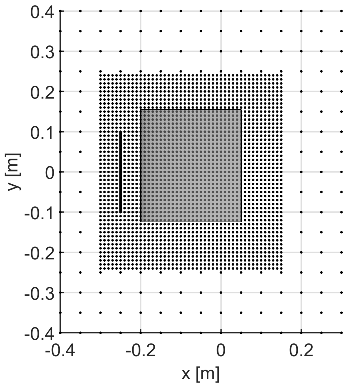

(a)

Figure 5.36: Double step grid in case of 2D ROI meshing.

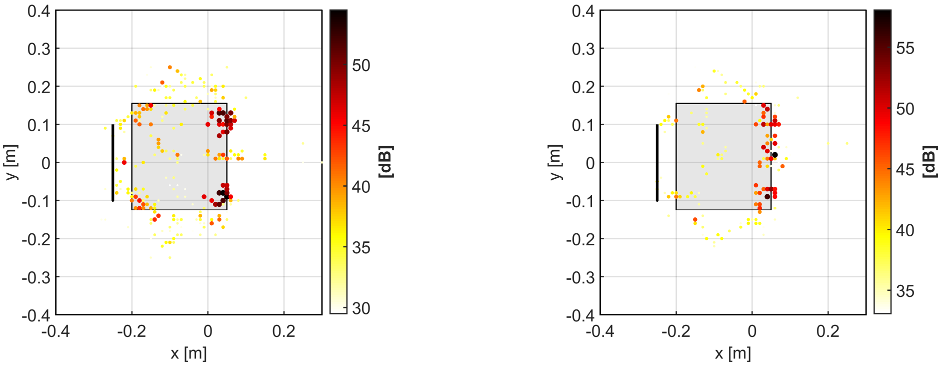

(a) ED

(b) CSCD

Figure 5.37: 2000 Hz one-third octave band - 2D mapping on double step grid - ESM-IRLS with $p = 0$.

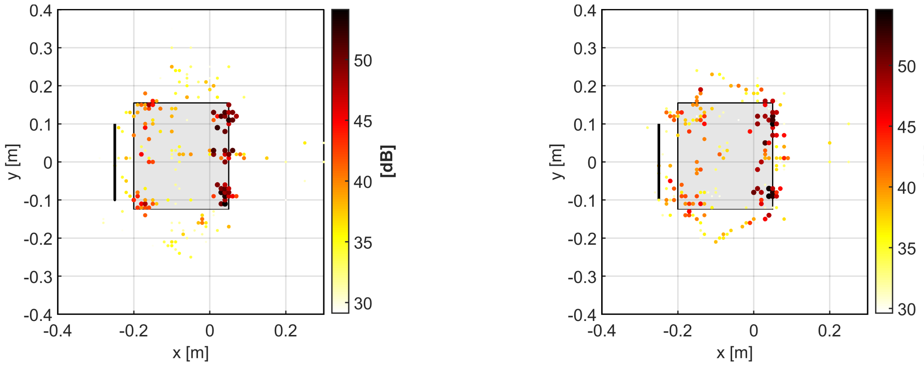

(a) ED (b) CSCD

Figure 5.38: 2000 Hz one-third octave band - 2D mapping on double step grid - CMF-IRLS with $p = 0$.

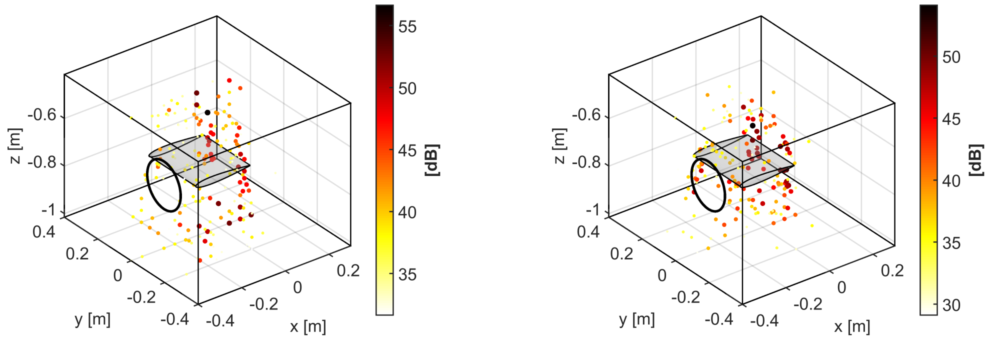

(a) ED (b) CSCD

Figure 5.39: 2000 Hz one-third octave band - 3D mapping on double step grid - ESM-IRLS with $p = 0$.

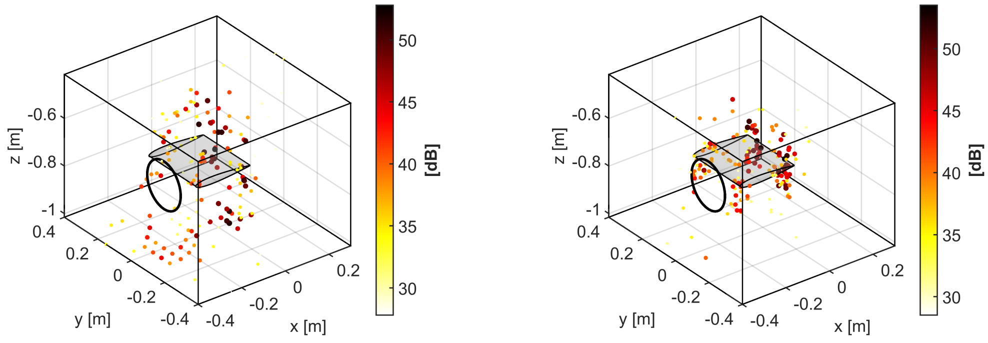

(a) ED (b) CSCD

Figure 5.40: 2000 Hz one-third octave band - 3D mapping on double step grid - CMF-IRLS with $p = 0$.

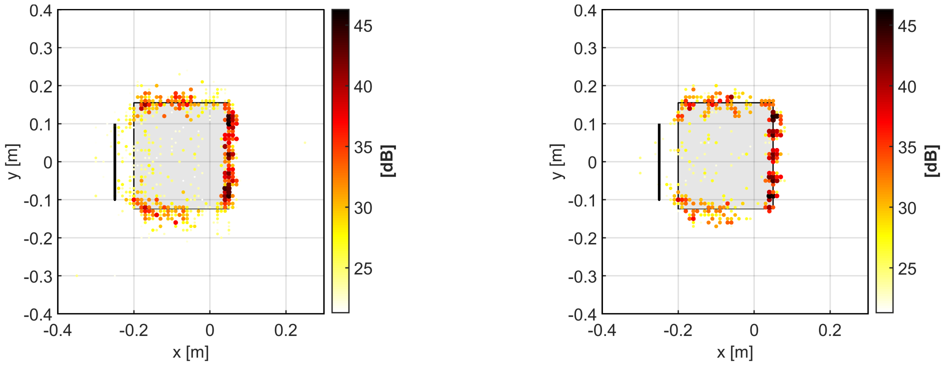

(a) ED

(b) CSCD

Figure 5.41: 4000 Hz one-third octave band - 2D mapping on double step grid - ESM-IRLS with $p = 0$.

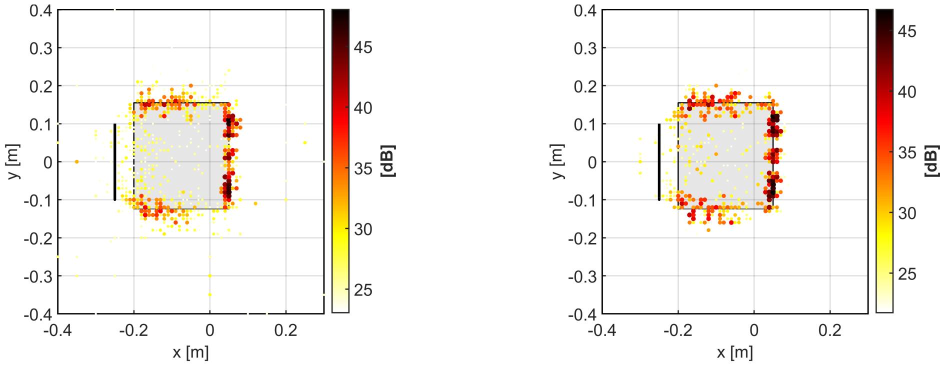

(a) ED

(b) CSCD

Figure 5.42: 4000 Hz one-third octave band - 2D mapping on double step grid - CMF-IRLS with $p = 0$.

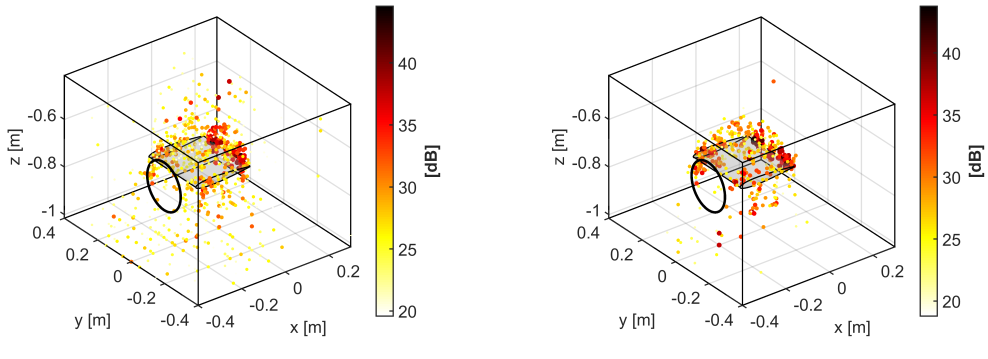

(a) ED

(b) CSCD

Figure 5.43: 4000 Hz one-third octave band - 3D mapping on double step grid - ESM-IRLS with $p = 0$.

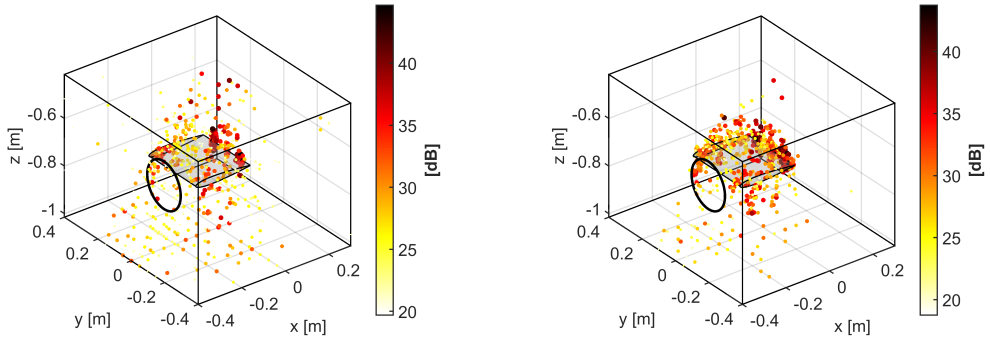

(a) ED (b) CSCD

Figure 5.44: 4000 Hz one-third octave band - 3D mapping on double step grid - CMF-IRLS with $p = 0$.

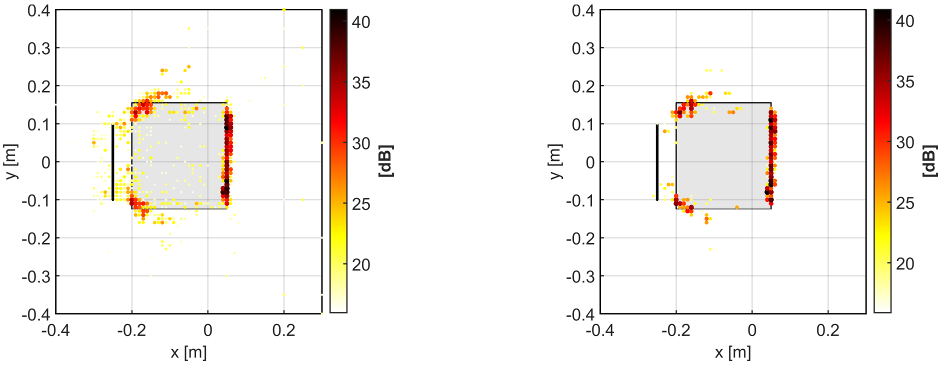

(a) ED (b) CSCD

Figure 5.45: 8000 Hz one-third octave band - 2D mapping on double step grid - ESM-IRLS with $p = 0$.

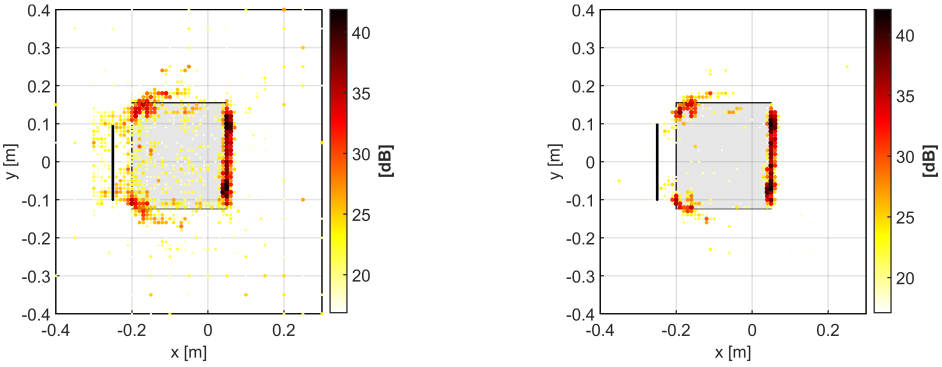

(a) ED (b) CSCD

Figure 5.46: 8000 Hz one-third octave band - 2D mapping on double step grid - CMF-IRLS with $p = 0$.

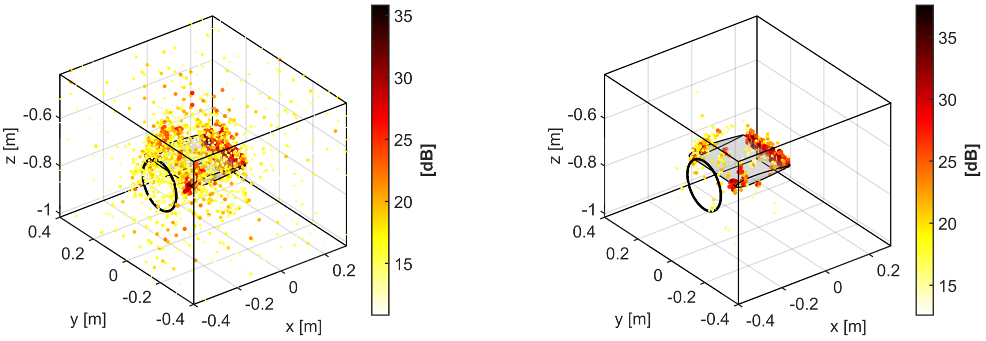

(a) ED (b) CSCD

Figure 5.47: 8000 Hz one-third octave band - 3D mapping on double step grid - ESM-IRLS with $p = 0$.

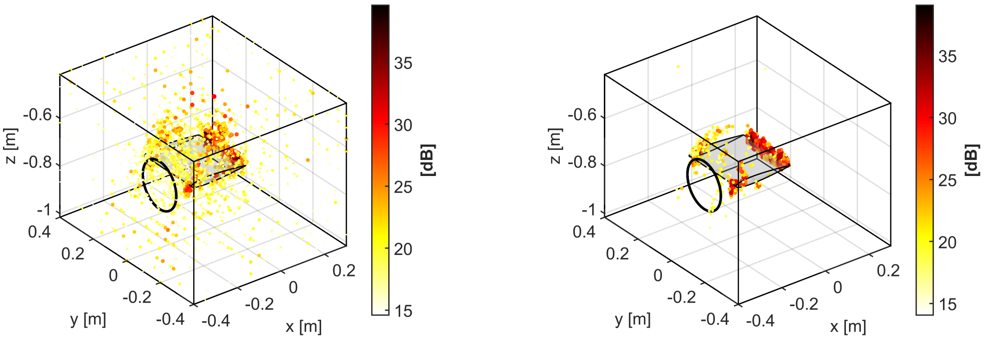

(a) ED (b) CSCD

Figure 5.48: 8000 Hz one-third octave band - 3D mapping on double step grid - CMF-IRLS with $p = 0$.

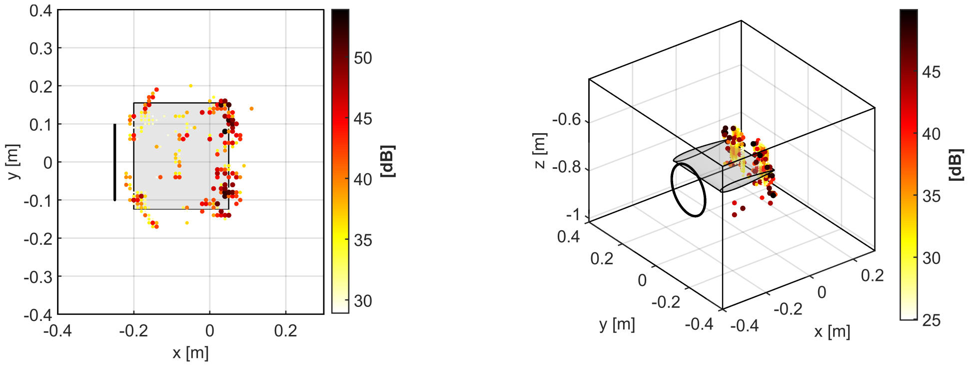

(a) 2D (b) 3D

Figure 5.49: 2000 Hz one-third octave band - mapping on double step grid - CMF-IRLS on whole CSM with $p = 1$.

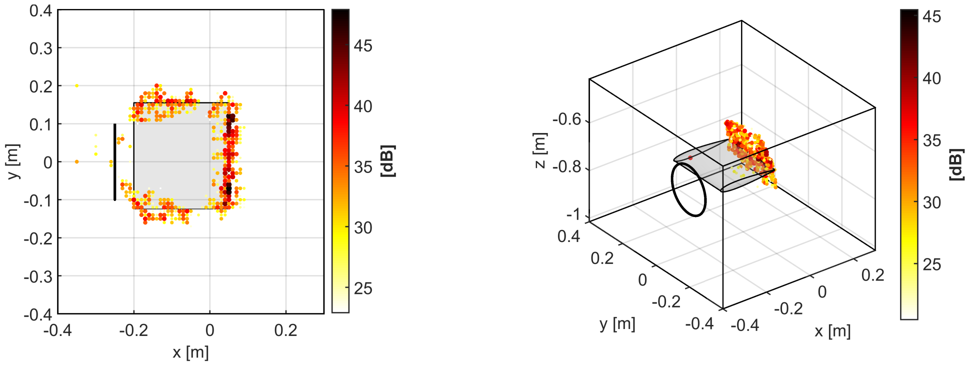

(a) 2D (b) 3D

Figure 5.50: 4000 Hz one-third octave band - mapping on double step grid - CMF-IRLS on whole CSM with $p = 1$.

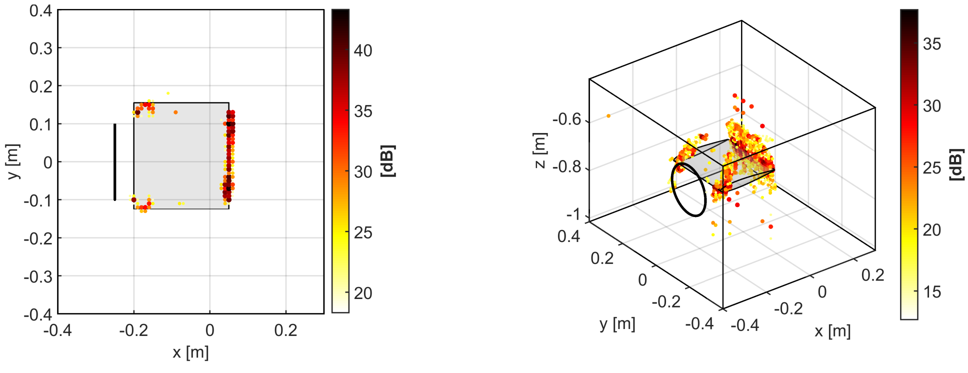

(a) 2D (b) 3D

Figure 5.51: 8000 Hz one-third octave band - mapping on double step grid - CMF-IRLS on whole CSM with $p = 1$.

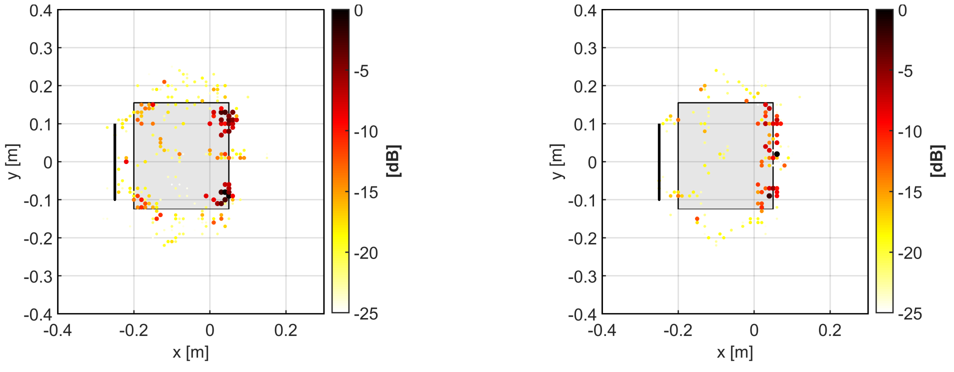

(a) ED (b) CSCD

Figure 5.52: 2000 Hz one-third octave band - 2D mapping on double step grid - ESM-IRLS with $p = 0$ - Compensation of non-uniform mesh.

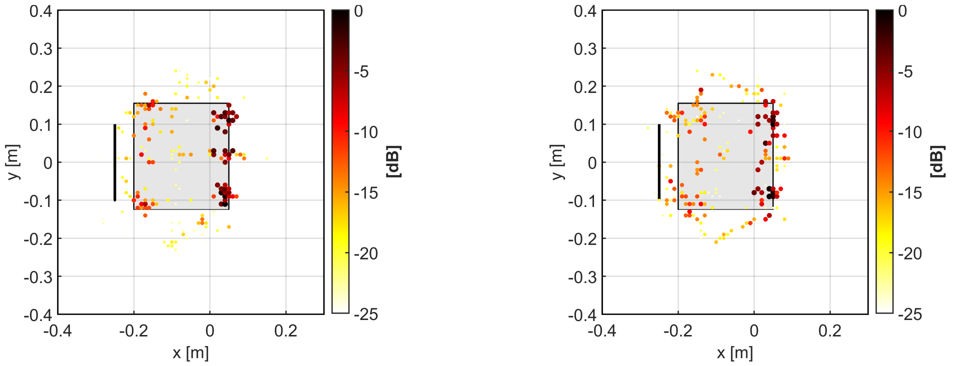

(a) ED (b) CSCD

Figure 5.53: 2000 Hz one-third octave band - 2D mapping on double step grid - CMF-IRLS with $p = 0$ - Compensation of non-uniform mesh.

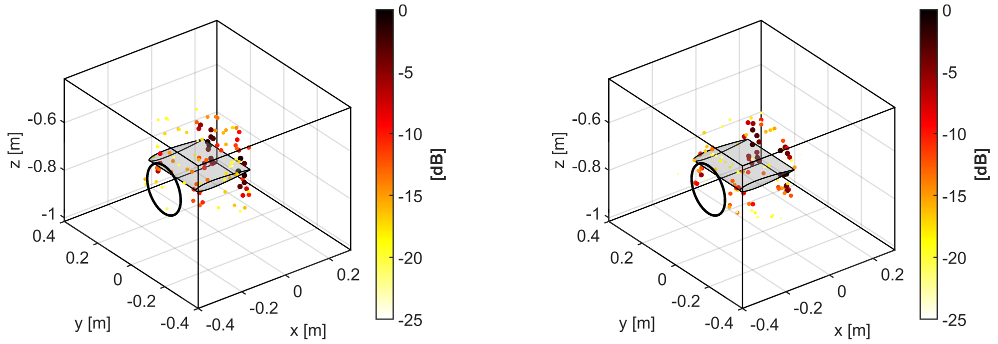

(a) ED (b) CSCD

Figure 5.54: 2000 Hz one-third octave band - 3D mapping on double step grid - ESM-IRLS with $p = 0$ - Compensation of non-uniform mesh.

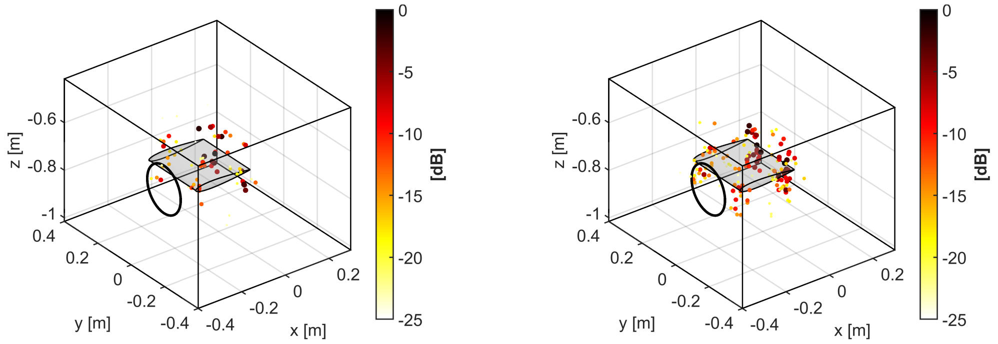

(a) ED (b) CSCD

Figure 5.55: 2000 Hz one-third octave band - 3D mapping on double step grid - CMF-IRLS with $p = 0$ - Compensation of non-uniform mesh.

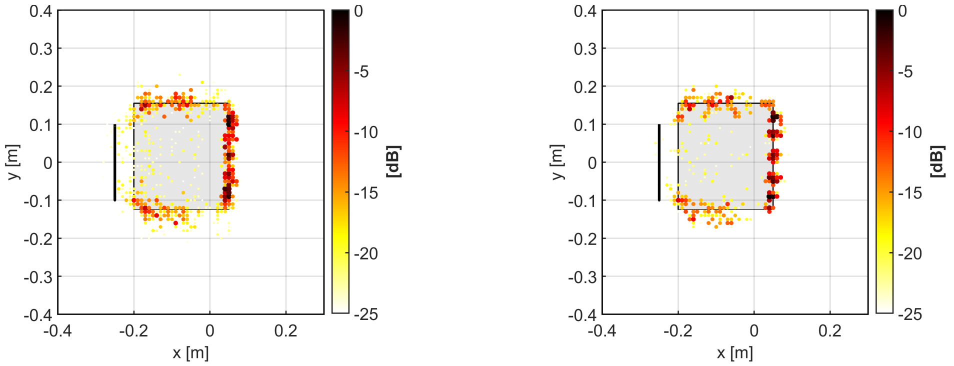

(a) ED (b) CSCD

Figure 5.56: 4000 Hz one-third octave band - 2D mapping on double step grid - ESM-IRLS with $p = 0$ - Compensation of non-uniform mesh.

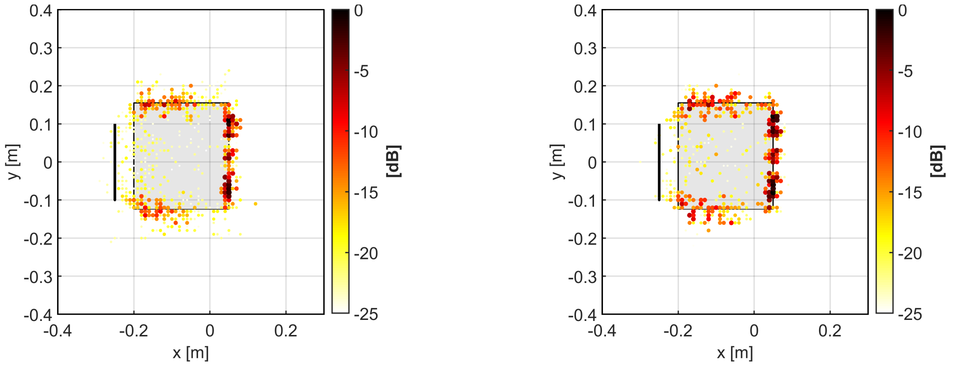

(a) ED (b) CSCD

Figure 5.57: 4000 Hz one-third octave band - 2D mapping on double step grid - CMF-IRLS with $p = 0$ - Compensation of non-uniform mesh.

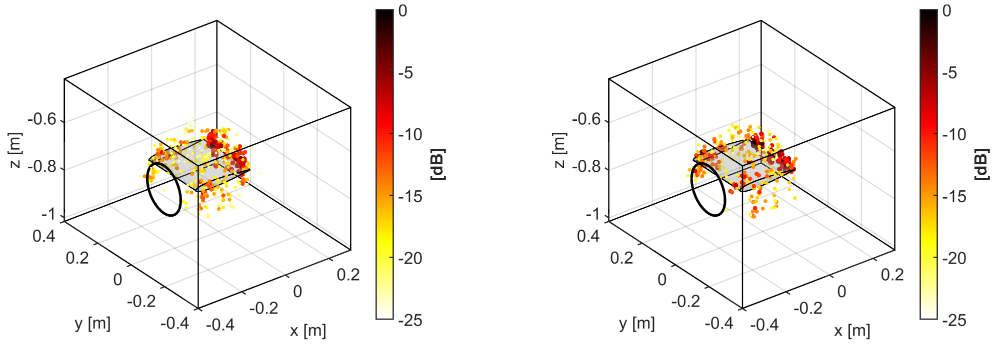

(a) ED (b) CSCD

Figure 5.58: 4000 Hz one-third octave band - 3D mapping on double step grid - ESM-IRLS with $p = 0$ - Compensation of non-uniform mesh.

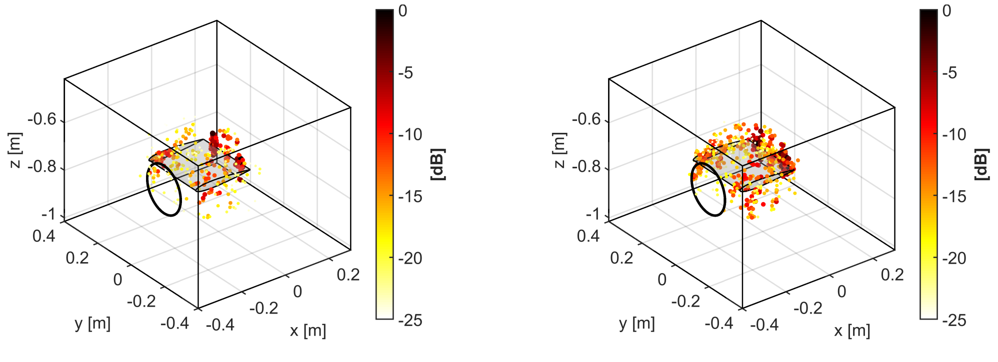

(a) ED (b) CSCD

Figure 5.59: 4000 Hz one-third octave band - 3D mapping on double step grid - CMF-IRLS with $p = 0$ - Compensation of non-uniform mesh.

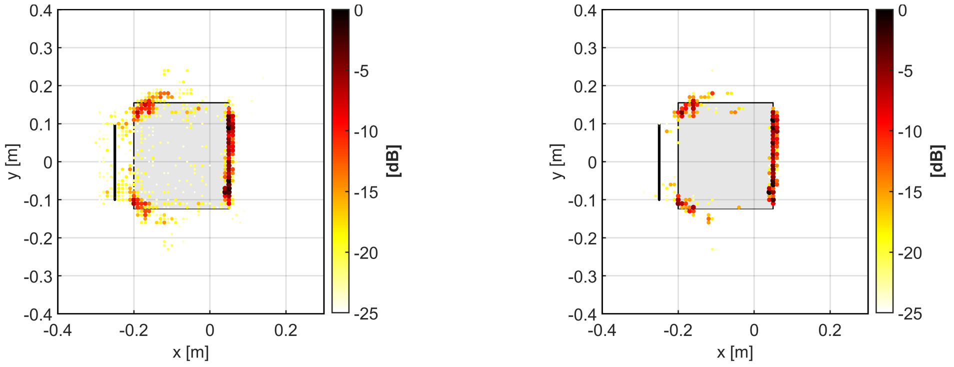

(a) ED (b) CSCD

Figure 5.60: 8000 Hz one-third octave band - 2D mapping on double step grid - ESM-IRLS with $p = 0$ - Compensation of non-uniform mesh.

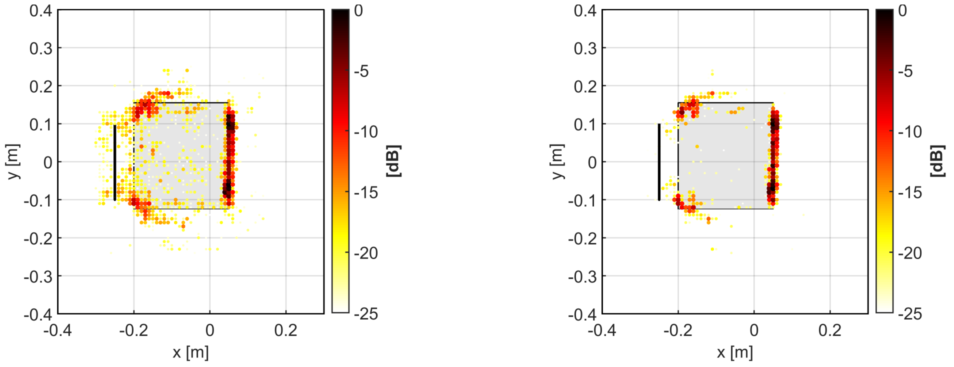

(a) ED (b) CSCD

Figure 5.61: 8000 Hz one-third octave band - 2D mapping on double step grid - CMF-IRLS with $p = 0$ - Compensation of non-uniform mesh.

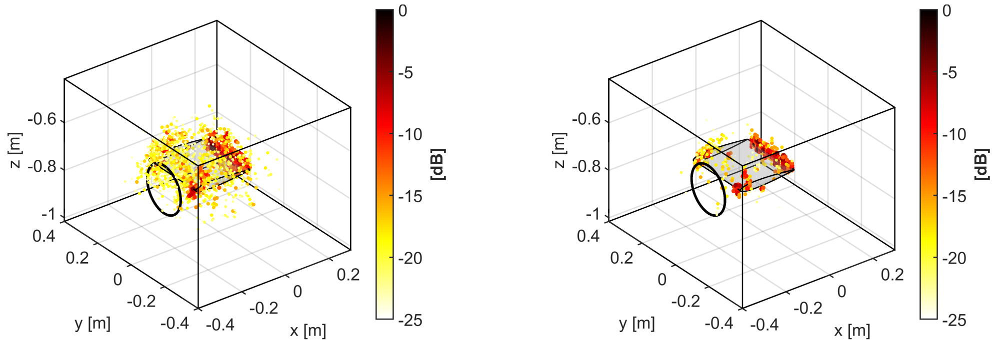

(a) ED

(b) CSCD

Figure 5.62: 8000 Hz one-third octave band - 3D mapping on double step grid - ESM-IRLS with $p = 0$ - Compensation of non-uniform mesh.

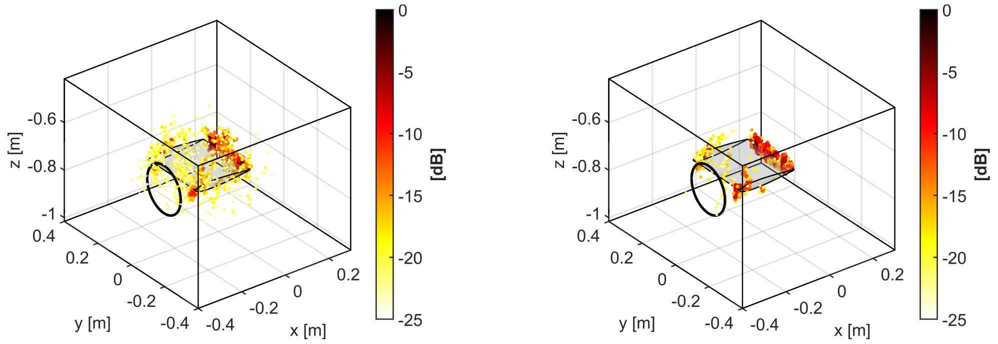

(a) ED

(b) CSCD

Figure 5.63: 8000 Hz one-third octave band - 3D mapping on double step grid - CMF-IRLS with $p = 0$ - Compensation of non-uniform mesh.

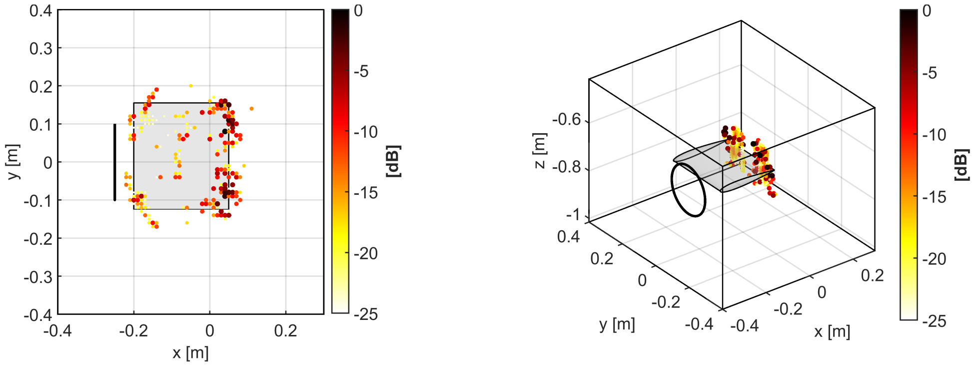

(a) 2D

(b) 3D

Figure 5.64: 2000 Hz one-third octave band - mapping on double step grid - CMF-IRLS on whole CSM with $p = 1$ - Compensation of non-uniform mesh.

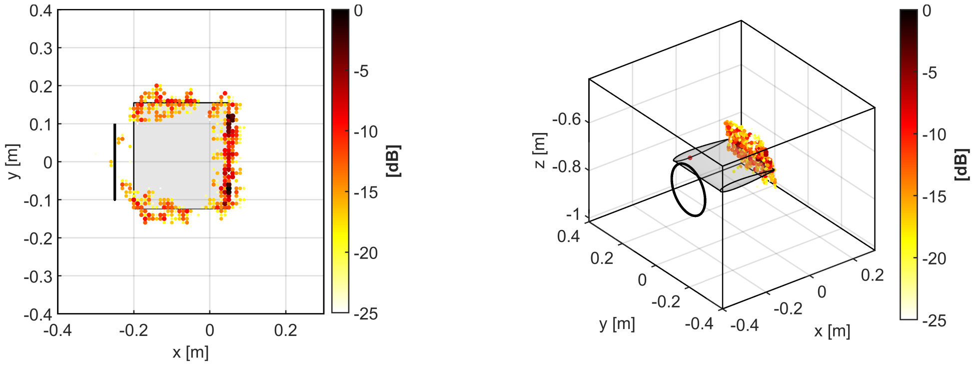

(a) 2D

(b) 3D

Figure 5.65: 4000 Hz one-third octave band - mapping on double step grid - CMF-IRLS on whole CSM with $p = 1$ - Compensation of non-uniform mesh.

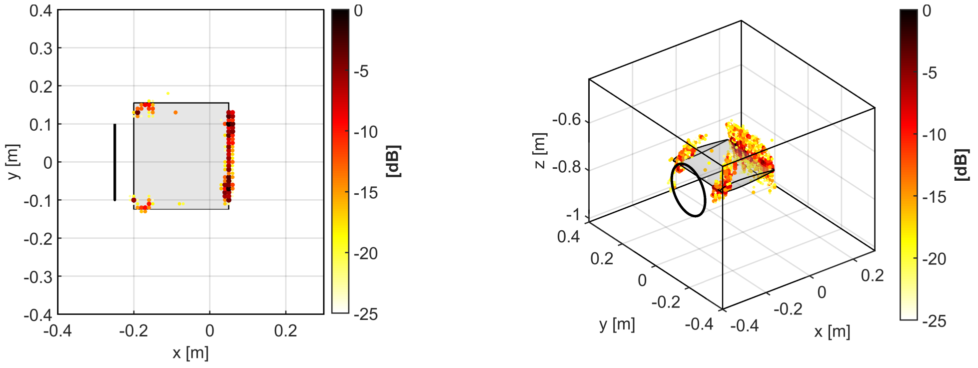

(a) 2D

(b) 3D

Figure 5.66: 8000 Hz one-third octave band - mapping on double step grid - CMF-IRLS on whole CSM with $p = 1$ - Compensation of non-uniform mesh.

These maps show clearly that non-uniform mesh allows to achieve results equivalent to those obtained with full fine regular grid, but with less computational demand. Only in few cases (mostly 3D), there is a relevant quantity of energy outside the inner box. This means, on one hand, that the main source of noise is the airfoil and, on the other hand, that the algorithms manage to suppress background noise. Even in this case, it is particularly evident the difference between ED and CSCD.

5.1.3 Computation time

It is useful to analyse here the time needed for computation of maps in all cases just shown. Since the same computer were used to calculate the solutions of inverse problems, differences in computation time depend only on the algorithm, its settings and size of the problem. Following tables reports computation time for planar and volumetric mapping. These values consider only net computation time attributed to the algorithm and not to other operations (e.g. loading data, CSM computation or saving data). In both cases, maps on regular grid with 1 cm step are considered as reference cases (Tables 5.4 for 2D and 5.7 for 3D) and expressed in seconds. For the other discretizations of ROI, it is reported the ratio with the value of analogous reference case. The number of spectral lines is different for each one-third octave band: 2000 Hz band contains 9 spectral lines, 4000 Hz band contains 18 spectral lines and 8000 Hz band contains 37 spectra lines.

Algorithm	Settings		2000 Hz	4000 Hz	8000 Hz
ESM-IRLS	$p = 0$	ED	73	153	351
		CSCD	41	89	185
CMF-IRLS	$p = 0$	ED	3649	7506	15932
		CSCD	2545	5592	11378
	$p = 1$	none	480	1069	1264

Table 5.4: Calculation time for planar maps on regular grid with 1 cm step (values in seconds used as reference for 2D).

Algorithm	Settings		2000 Hz	4000 Hz	8000 Hz
ESM-IRLS	$p = 0$	ED	0.494	0.500	0.411
		CSCD	0.565	0.524	0.296
CMF-IRLS	$p = 0$	ED	0.014	0.017	0.016
		CSCD	0.015	0.015	0.009
	$p = 1$	none	0.018	0.028	0.027

Table 5.5: Calculation time for planar maps on regular grid with 5 cm step (ratios with analogous values in Table 5.4).

Algorithm	Settings		2000 Hz	4000 Hz	8000 Hz
ESM-IRLS	$p = 0$	ED	0.777	0.794	0.746
		CSCD	0.838	0.788	0.698
CMF-IRLS	$p = 0$	ED	0.440	0.520	0.469
		CSCD	0.448	0.551	0.406
	$p = 1$	none	0.853	0.940	0.757

Table 5.6: Calculation time for planar maps on double step grid (ratios with analogous values in Table 5.4).

Algorithm	Settings		2000 Hz	4000 Hz	8000 Hz
ESM-IRLS	$p = 0$	ED	2774	5689	10306
		CSCD	1626	3604	6966
CMF-IRLS	$p = 0$	ED	51745	101991	234417
		CSCD	31220	69742	153186
	$p = 1$	none	6549	8360	16480

Table 5.7: Calculation time for volumetric maps on regular grid with 1 cm step (values in seconds used as reference for 3D).

Algorithm	Settings		2000 Hz	4000 Hz	8000 Hz
ESM-IRLS	$p = 0$	ED	0.027	0.034	0.027
		CSCD	0.032	0.036	0.017
CMF-IRLS	$p = 0$	ED	0.022	0.025	0.047
		CSCD	0.028	0.030	0.040
	$p = 1$	none	0.019	0.033	0.058

Table 5.8: Calculation time for volumetric maps on regular grid with 5 cm step (ratios with analogous values in Table 5.7).

Algorithm	Settings		2000 Hz	4000 Hz	8000 Hz
ESM-IRLS	$p = 0$	ED	0.134	0.131	0.156
		CSCD	0.126	0.152	0.154
CMF-IRLS	$p = 0$	ED	0.169	0.158	0.145
		CSCD	0.162	0.182	0.157
	$p = 1$	none	0.316	0.290	0.228

Table 5.9: Calculation time for volumetric maps on double step grid (ratios with analogous values in Table 5.7).

The analysis of these data shows the huge reduction of calculation time obtained when a non-uniform mesh is used with respect to a fine regular grid for the entire volume. Reduction of computation time is more than 80% for both ESM-IRLS and CMF-IRLS when CSM decomposition is performed, while is about 70 % when CMF is applied to whole CSM. It is worth noticing that, in the latter case, only one inverse problem is solved for each spectral, but L_1 norm minimization has the slowest convergence. The strategy of non-uniform mesh, with dense distribution only where needed, compensates the increase of spectral lines of bands at high frequency, thus keeping computation time at reasonable level.

5.2 Volumetric acoustic mapping with multiple arrays

In this section it will be shown the advantage of combining data of multiple planar arrays, in the context of volumetric acoustic mapping. This kind of setup is quite common in wind tunnel testing, i.e. planar arrays lying on orthogonal planes and looking the same object from different points of view. The test program was conducted at the Pininfarina Aerodynamic and Aeroacoustic Research Center in Turin, Italy within the EU WENEMOR project. Pininfarina's facility contains a test section of 8 m × 9.6 m × 4.2 m (see Figure 5.67(a)). The Pininfarina Wind Tunnel (WT) was specifically acoustically treated in order to reduce reverberation and background noise.

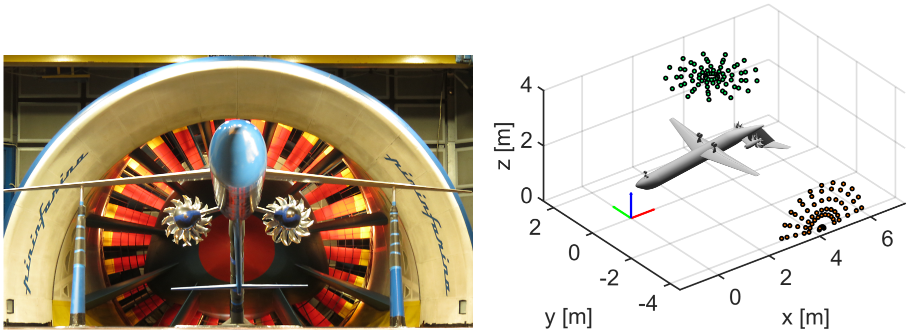

(a) Front view of the aircraft model

(b) Microphone array layout

Figure 5.67: Test set-up in Pininfarina Wind Tunnel.

The aircraft model tested featured two counter rotating open rotors (CRORs) of 12 blades each. Both left and right engines of the aircraft model were driven from a single power supply and controlled by dedicated control systems (one per motor). Strouhal number scaling was performed to represent flight conditions of the full scale aircraft. Different design configurations of the model were tested during the whole test campaign (different tails, CROR in pusher and tractor configuration, different distances of CRORs with respect to the model fuselage, etc.) at different flow speeds and angles of attack. Angle of attacks (AoA) differed also with respect to the take-off or approach model configuration. However, all the results discussed here refer to the T-tailed model, in approach condition with CRORs in pusher configuration for $AoA =$ 8 deg and flow speed of 28 m/s. The flow direction is considered to be the X positive axis of the coordinate system represented in Figure 5.67(b). In this application, the assumption of propagation in an uniform flow is made. This leads to the following expression for distances r_{mn} corresponding to the actual propagation path [26]:

$$\begin{aligned} r_{mn} &= \frac{\|\mathbf{r}_n - \mathbf{r}_m\|_2}{-C_{mn} + \sqrt{C_{mn}^2 - M_a^2 + 1}} \\ C_{mn} &= (\mathbf{r}_n - \mathbf{r}_m) \cdot \hat{\mathbf{f}}\, M_a \end{aligned} \tag{5.1}$$

where $\hat{\mathbf{f}}$ is a unitary vector representing the flow direction and M_a is the Mach number.

	x (m)	y (m)	z (m)	step (m)	N
Model	$[0.10, 6.00]$	$[-2.50, 3.00]$	$[0.00, 3.00]$	0.06	464508
Background noise				0.20	13440

Table 5.10: Region of interest and its discretization with regular grid used for aircraft noise and background noise mapping

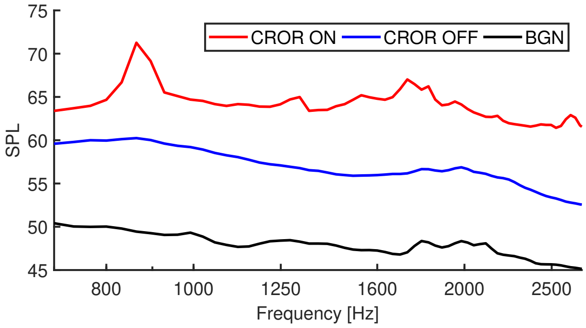

Figure 5.68: Average microphone auto-power spectra with side and top arrays. Red line: test with model CRORs switched on. Blue line: test with model CRORs switched off. Black line: test without model.

Two planar microphone arrays were installed at Pininfarina Wind Tunnel, as depicted in Figure 5.67(b): a 78 microphone wheel array (3 m diameter) placed at the ceiling of the WT at a distance of 2.5 m from the model axis and a 66 microphone half-wheel array (3 m diameter) located broadside, parallel to the axis of the open rotor and 4.2 m far from the longitudinal axis of the model. Acquisitions were performed in three different conditions: model with CRORs switched on, model with CRORs switched off and WT background noise without model in the test section. Signals were synchronously sampled at a sample rate of 32768 Hz for a total observation length of 10 s. Time data has been processed to estimate the CSM using Welch's method (block size: 1024 samples, overlap: 50%, window: Hanning).

Region of interest and its discretization with a regular grid of monopoles is defined in Table 5.10. Two different discretization are used: fine grid resolution to map the noise produced by the model and a coarse grid for background WT noise mapping. In this application, only regular grids are used. The number of relevant eigenmodes is empirically set to $C = 30$. Instead, all CSCD components extracted are processed resulting to be $C < 30$ for each frequency within the bands analysed. Only ESM-IRLS is applied, since the analysis here is focused on differences that results from the use of multiple arrays with respect to a single one. Problem size of CMF-IRLS is proportional to the square of the number of microphone, thus having a quite large matrix to be decomposed with SVD, that is computationally demanding especially at first iterations. Maximum sparsity constraint is applied in this case ($p = 0$). Reference point for acoustic propagator is the coordinate system origin $\mathbf{r}_0 = \mathbf{0}$.

Maps are calculated for one-third octave bands from 800 to 2500 Hz and are depicted using a dynamic range of 30 dB. Figure 5.68 shows the average microphone auto-power spectra measured with side and top arrays in each condition tested. When the rotors are switched on, the difference with the background noise is about 15 dB on the average, while, when only aerodynamic noise is present, the difference is only about 8 dB. The first analysis presented aims at showing the crucial effect of introduction of a priori information with CB map in such noisy conditions. For this purpose, maps at 2500 Hz are shown in Figs. from 5.69 to 5.72. It is possible to see that in some cases, in particular those with single array, great part of equivalent sources are concentrated near the microphone array. This means that source reconstruction process failed for some components due to the excessive level of noise and ill-conditioning. Contrarily, when CB map is introduced as a priori information, maps do not show these artefacts. Therefore, in severe SNR conditions or particularly ill-conditioned problems, the introduction of a priori information is mandatory to obtain meaningful results and not only a strategy to improve them. For this reason, maps of other bands are produced only with CB map as a priori (Figs. from 5.73 to 5.82). As frequency increases, source localization is more and more compact and accurate, since the problem tends to be less ill-conditioned and the spatial information introduced by CB become more refined. In addition, as already stated in this thesis, volumetric maps with single array has a practical low limit in frequency range that is influenced by source-array distance, noise level and other factors. In this application, maps with top array start to be meaningful from 1000 Hz, which corresponds approximately to $He \approx 8.7$, while maps with side and top arrays are meaningful even at 800 Hz. In any case, the accuracy and the compactness of source localization is improved by the use of the side array. Also the pressure decomposition method heavily influences the quality of results. Basically, almost in every case presented in this section CSCD outperforms ED. In fact, the former return maps with less artefacts, thus giving more accurate and intelligible map. Only in the lowest bands mapped with the top array, ED returns better maps. This is probably due to the bad accuracy of CB at lower frequencies (in all spatial directions) that does not allow a good component extraction by means of spatial coherence. Figures from 5.83 to 5.88 show maps, on coarse grid, of WT background noise only, obtained leaving empty the test section. This is useful to know the spatial distribution on maps of noise source not related to the model. Background noise is mainly located near the boundary of ROI and its spatial distribution changes for each band. It is likely that is generated outside the ROI.

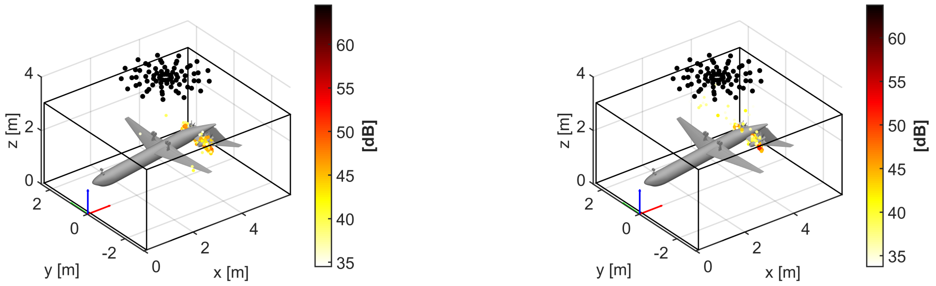

(a) CSCD - no a priori weighting

(b) ED - no a priori weighting

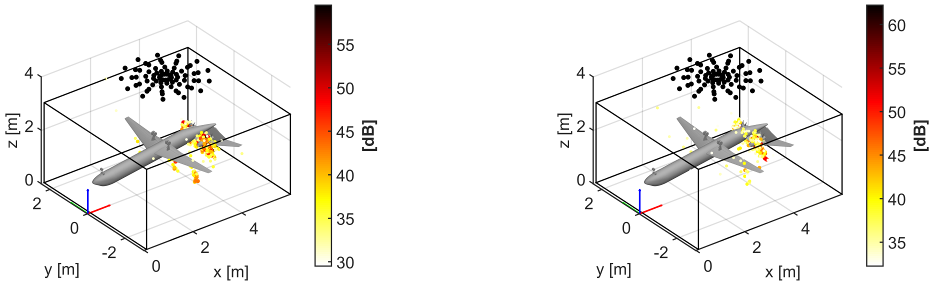

(c) CSCD - $\mathbf{W}_0$ = CB map

(d) ED - $\mathbf{W}_0$ = CB map

Figure 5.69: CRORs switched on - 2500 Hz one-third octave band - Top array

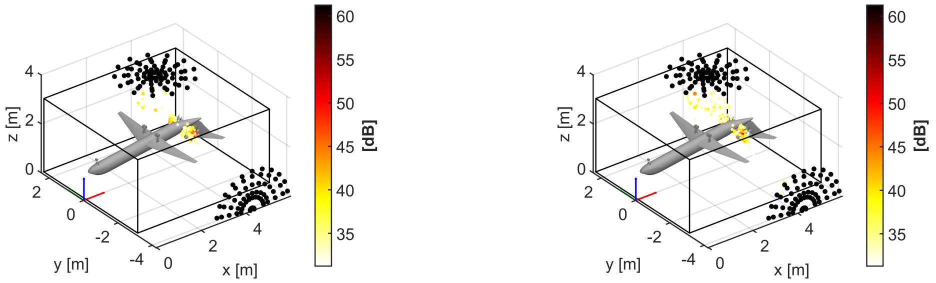

(a) CSCD - no a priori weighting

(b) ED - no a priori weighting

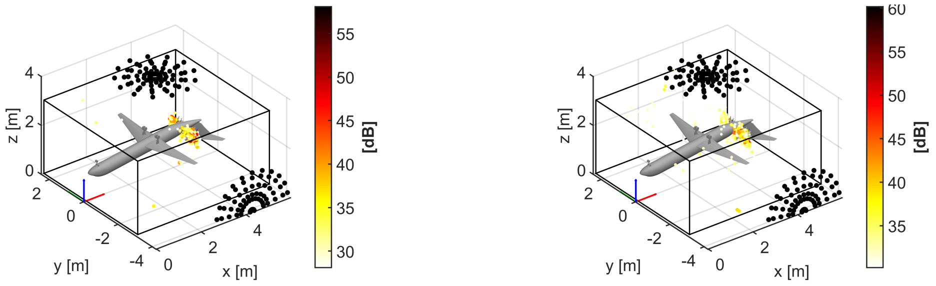

(c) CSCD - $\mathbf{W}_0$ = CB map

(d) ED - $\mathbf{W}_0$ = CB map

Figure 5.70: CRORs switched on - 2500 Hz one-third octave band - Side and top arrays

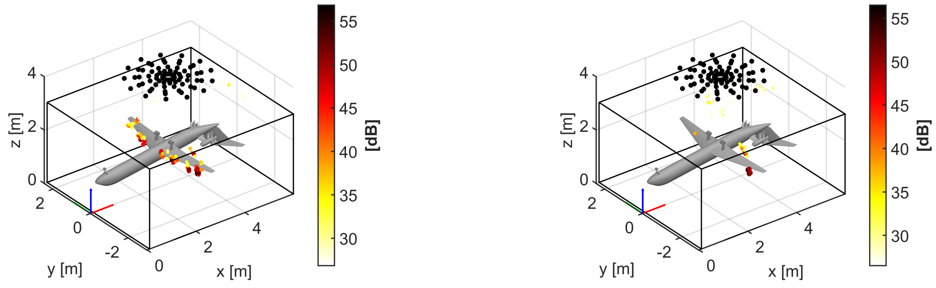

(a) CSCD - no a priori weighting

(b) ED - no a priori weighting

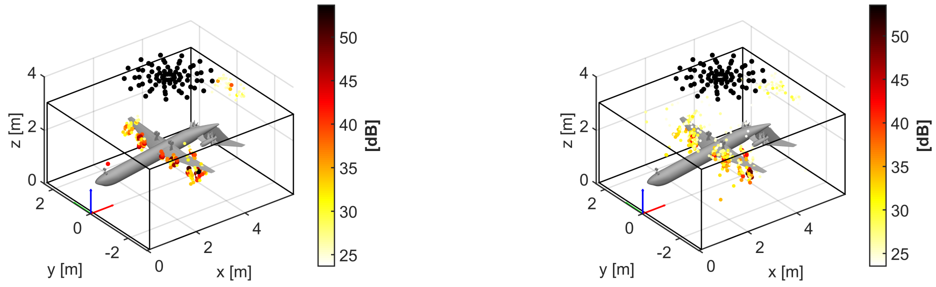

(c) CSCD - $\mathbf{W}_0$ = CB map

(d) ED - $\mathbf{W}_0$ = CB map

Figure 5.71: CRORs switched off - 2500 Hz one-third octave band - Top array

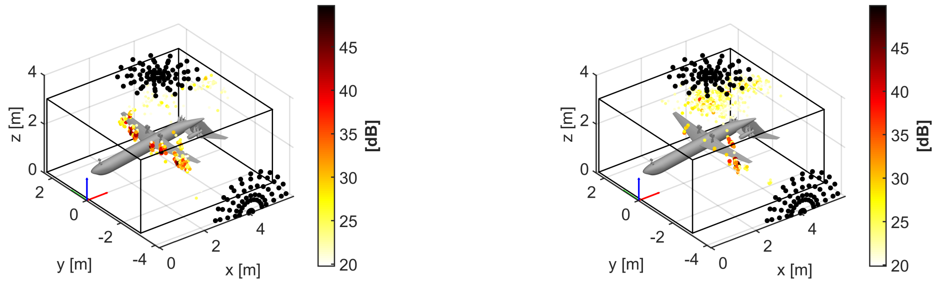

(a) CSCD - no a priori weighting

(b) ED - no a priori weighting

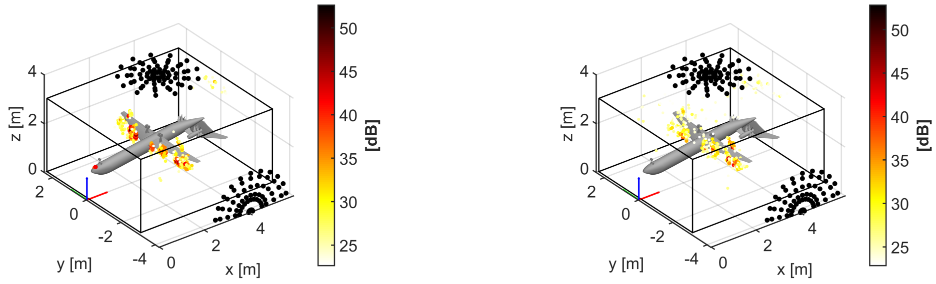

(c) CSCD - $\mathbf{W}_0$ = CB map

(d) ED - $\mathbf{W}_0$ = CB map

Figure 5.72: CRORs switched off - 2500 Hz one-third octave band - Side and top arrays

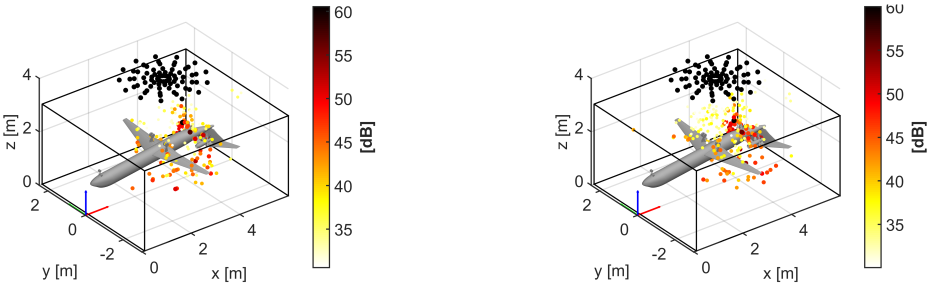

(a) CSCD - Top array (b) ED - Top array

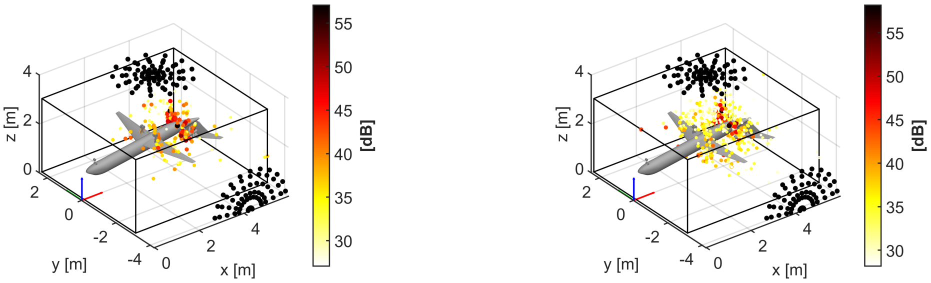

(c) CSCD - Side and top array (d) ED - Side and top array

Figure 5.73: CRORs switched on - 800 Hz one-third octave band - $\mathbf{W}_0$ = CB map

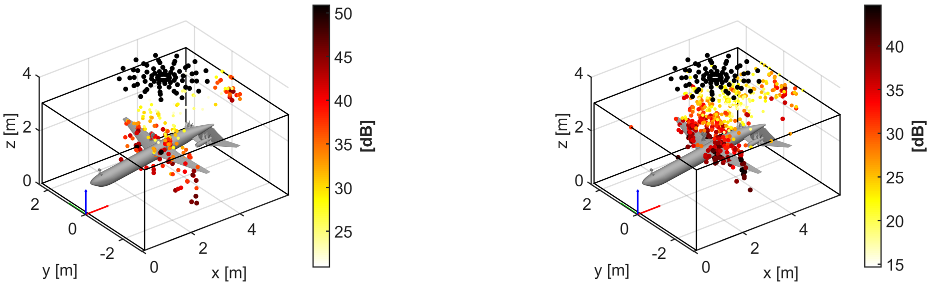

(a) CSCD - Top array (b) ED - Top array

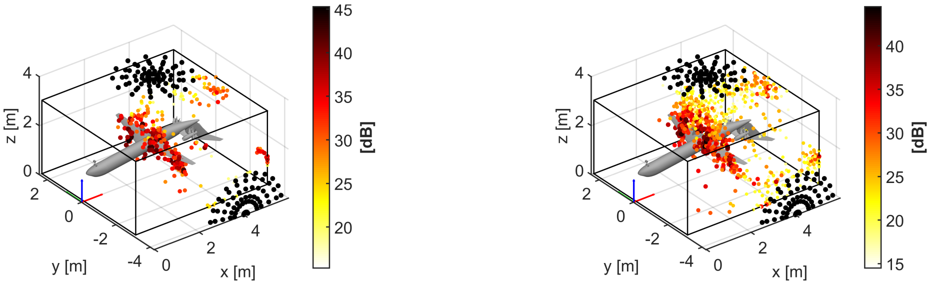

(c) CSCD - Side and top array (d) ED - Side and top array

Figure 5.74: CRORs switched off - 800 Hz one-third octave band - $\mathbf{W}_0$ = CB map

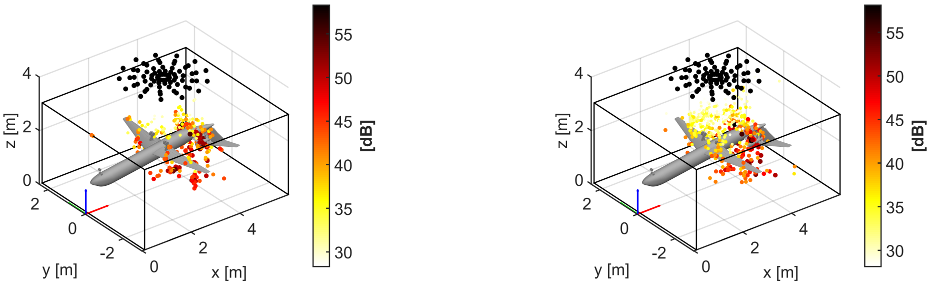

(a) CSCD - Top array

(b) ED - Top array

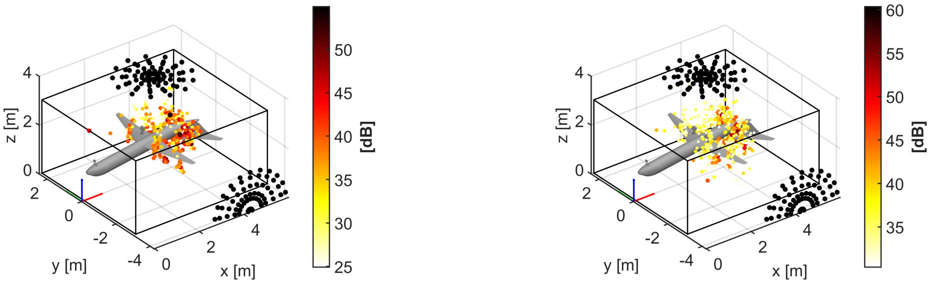

(c) CSCD - Side and top array

(d) ED - Side and top array

Figure 5.75: CRORs switched on - 1000 Hz one-third octave band - $\mathbf{W}_0$ = CB map

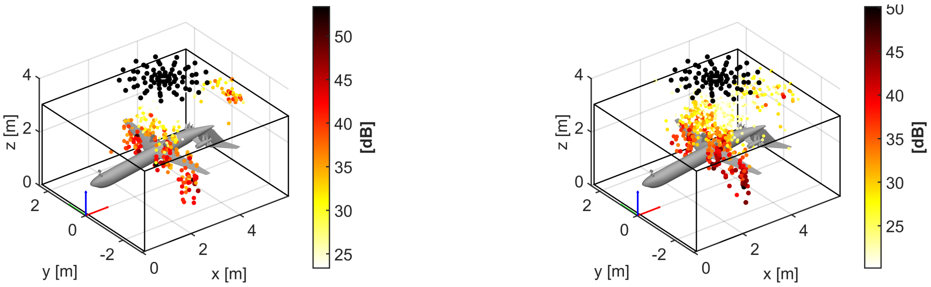

(a) CSCD - Top array

(b) ED - Top array

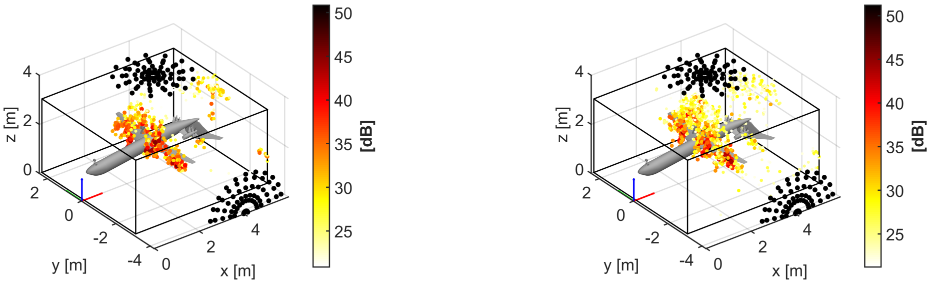

(c) CSCD - Side and top array

(d) ED - Side and top array

Figure 5.76: CRORs switched off - 1000 Hz one-third octave band - $\mathbf{W}_0$ = CB map

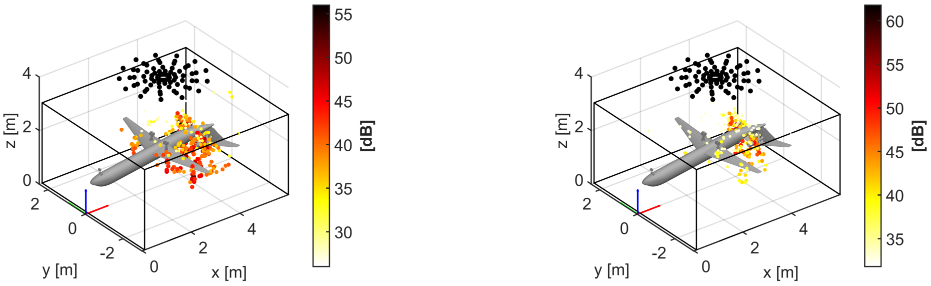

(a) CSCD - Top array

(b) ED - Top array

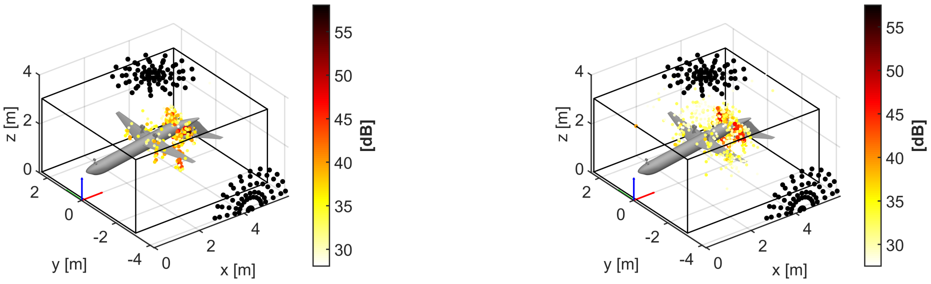

(c) CSCD - Side and top array

(d) ED - Side and top array

Figure 5.77: CRORs switched on - 1250 Hz one-third octave band - $\mathbf{W}_0$ = CB map

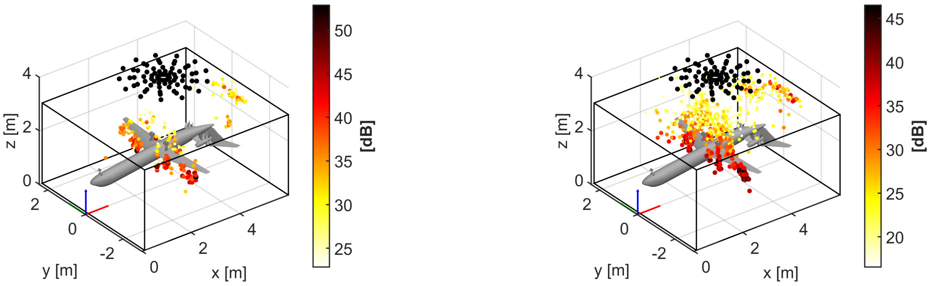

(a) CSCD - Top array

(b) ED - Top array

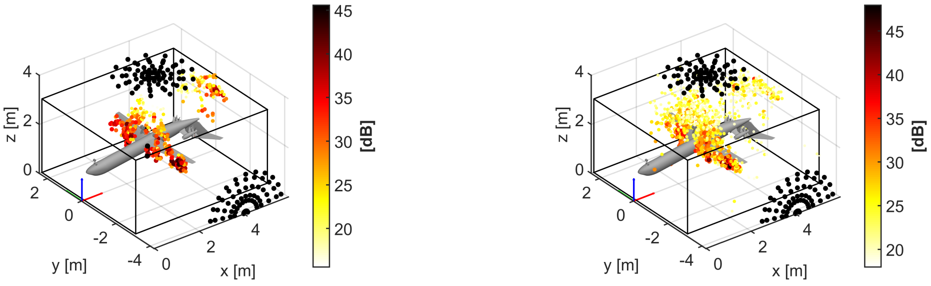

(c) CSCD - Side and top array

(d) ED - Side and top array

Figure 5.78: CRORs switched off - 1250 Hz one-third octave band - $\mathbf{W}_0$ = CB map

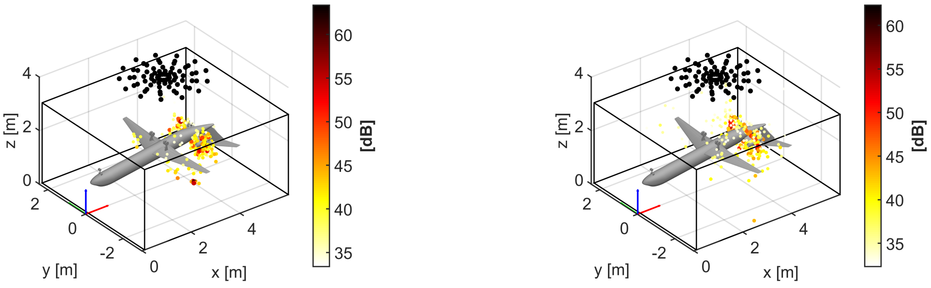

(a) CSCD - Top array (b) ED - Top array

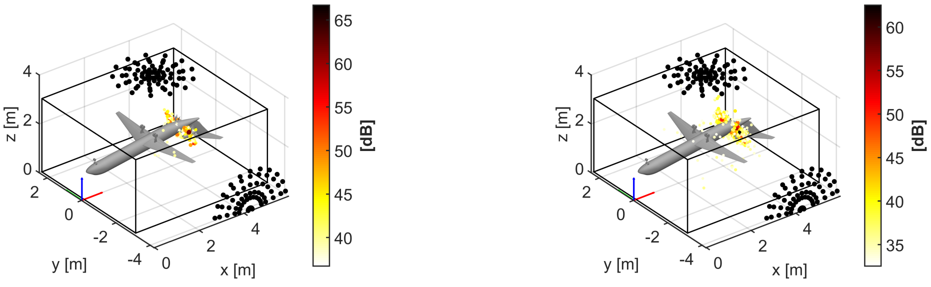

(c) CSCD - Side and top array (d) ED - Side and top array

Figure 5.79: CRORs switched on - 1600 Hz one-third octave band - $\mathbf{W}_0$ = CB map

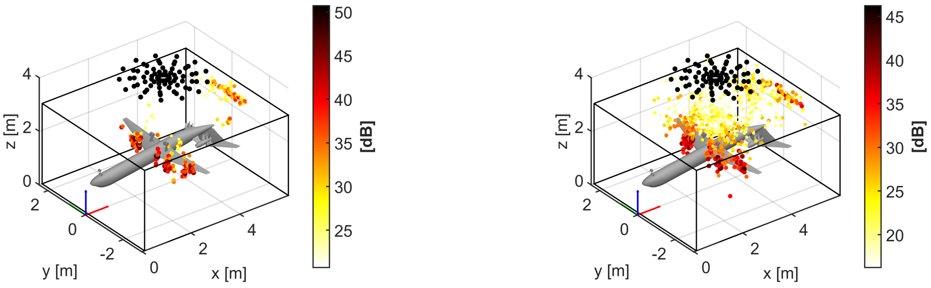

(a) CSCD - Top array (b) ED - Top array

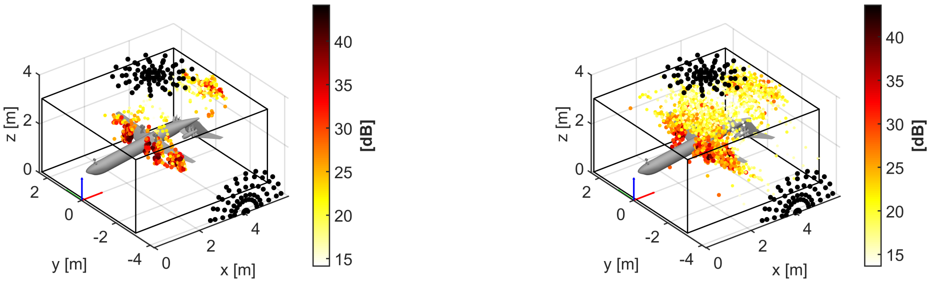

(c) CSCD - Side and top array (d) ED - Side and top array

Figure 5.80: CRORs switched off - 1600 Hz one-third octave band - $\mathbf{W}_0$ = CB map

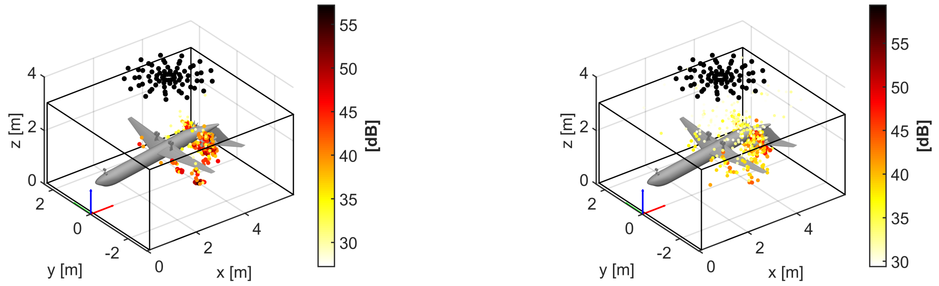

(a) CSCD - Top array (b) ED - Top array

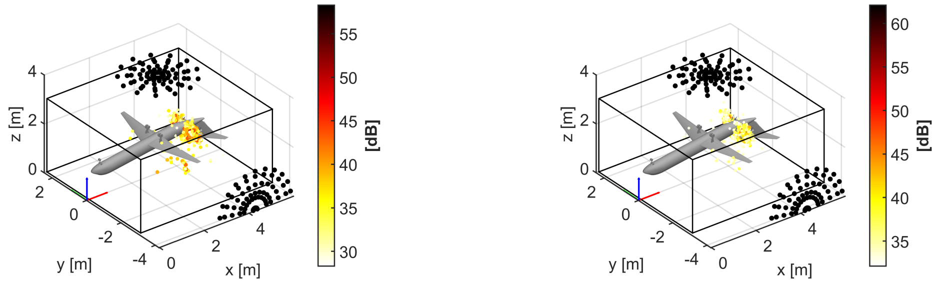

(c) CSCD - Side and top array (d) ED - Side and top array

Figure 5.81: CRORs switched on - 2000 Hz one-third octave band - $\mathbf{W}_0$ = CB map

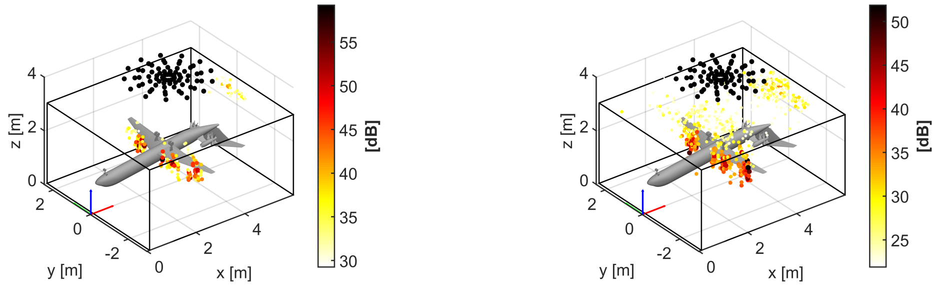

(a) CSCD - Top array (b) ED - Top array

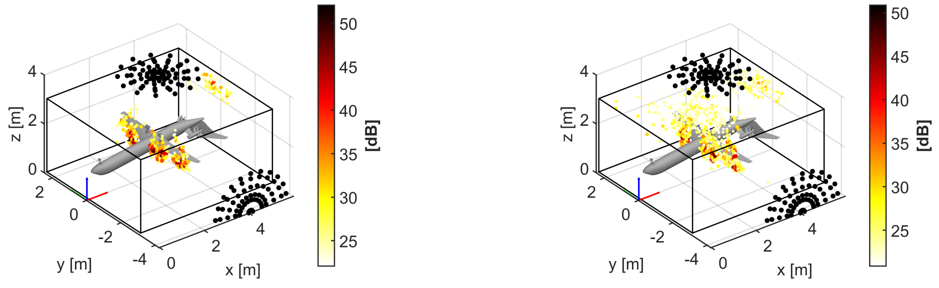

(c) CSCD - Side and top array (d) ED - Side and top array

Figure 5.82: CRORs switched off - 2000 Hz one-third octave band - $\mathbf{W}_0$ = CB map

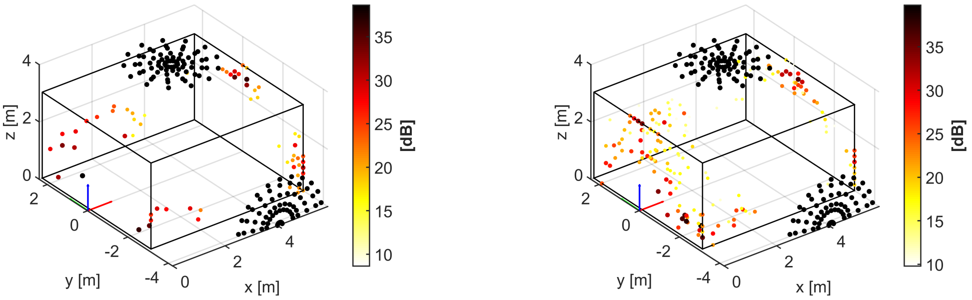

(a) CSCD (b) ED

Figure 5.83: Background noise - 800 Hz one-third octave band - $\mathbf{W}_0$ = CB map

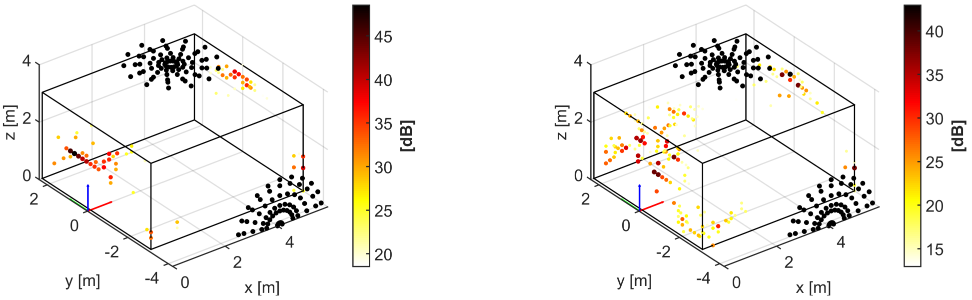

(a) CSCD (b) ED

Figure 5.84: Background noise - 1000 Hz one-third octave band - $\mathbf{W}_0$ = CB map

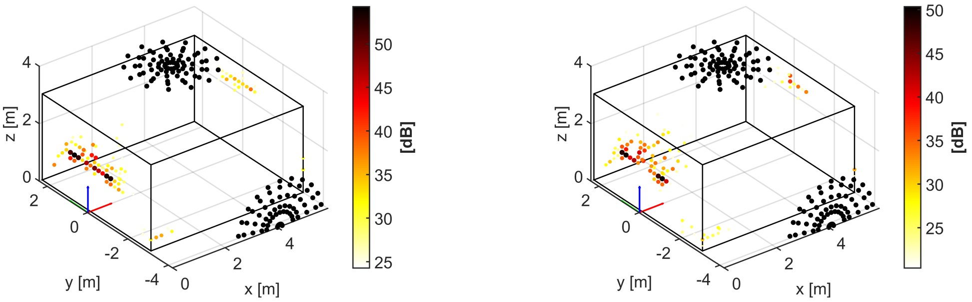

(a) CSCD (b) ED

Figure 5.85: Background noise - 1250 Hz one-third octave band - $\mathbf{W}_0$ = CB map

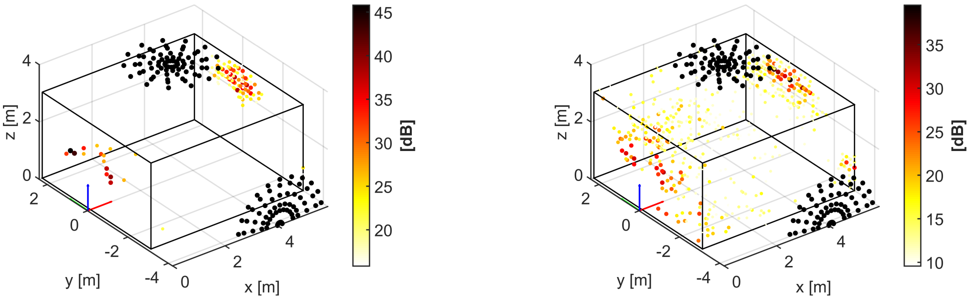

(a) CSCD (b) ED

Figure 5.86: Background noise - 1600 Hz one-third octave band - $\mathbf{W}_0$ = CB map

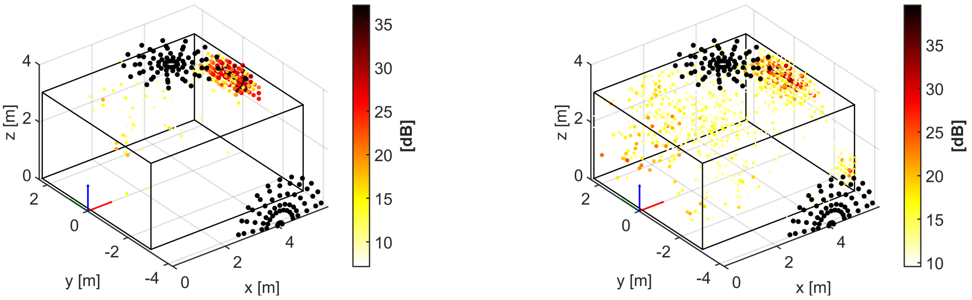

(a) CSCD (b) ED

Figure 5.87: Background noise - 2000 Hz one-third octave band - $\mathbf{W}_0$ = CB map

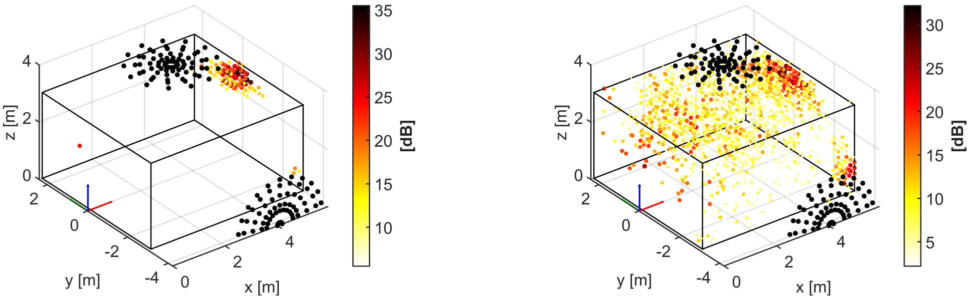

(a) CSCD (b) ED

Figure 5.88: Background noise - 2500 Hz one-third octave band - $\mathbf{W}_0$ = CB map

Chapter 6

Conclusions and future works

6.1 Theoretical and user-oriented conclusions

This work has been conducted in order to investigate the field of volumetric acoustic mapping. The extension of acoustic source mapping from a surface to a volume was not fully treated in literature. In fact, most part of previous attempts were simply applications of existing techniques to an extended spatial domain. Among different approaches, inverse methods have been chosen to deal with the problem of volumetric acoustic mapping. The drawback is that inverse problems in this application have typical characteristics of ill-posed problems. Nevertheless, this thesis demonstrated that inverse methods can successfully cope also the additional issues that volumetric mapping entails with respect to standard surface mapping. Three additional issues have been identified when dealing with volumetric imaging:

- potential sources located at very different distances from the array centre;
- poor spatial resolution of arrays in radial direction from the array centre;
- high number of potential sources with no contribution to the acoustic field.

The first issue of the list requests the balance of energy needed by each potential source to cause a certain pressure at microphone locations, in fact, potential sources near the array may be advantaged in the inversion process. This issue can be settled using the acoustic propagator in pressure-to-pressure formulation. In this way, there are no sources ”preferred” when a solution is sought. Spatial resolution of arrays is good in lateral direction and much worse in radial direction from the array centre, due to the way the acoustic field is sampled. In conventional surface imaging, only lateral spatial resolution is usually considered since the distance between the array and the surface to map is fixed. However, when dealing with volumetric mapping, also the radial spatial resolution becomes important, because source position must be retrieved in the three-dimensional space and not on a surface. The radial direction is the most critical and the resolution worsens as the source-array distance increases. The third item of the list means that only ”few” potential sources are actually sufficient, amongst all present in the region of interest, to approximate the real ones. This suggests to introduce the assumption of sparse source field when a solution to the inverse problem is sought. The sparsity constraint on solution fits well also with the issue of spatial resolution of array in radial direction.

Several approaches to obtain sparse solutions to inverse problems are available in literature. The method of Iteratively Re-weighted Least Squares has been chosen because it enables to adjust the amount of sparsity desired. This method yield a sparse solution using the result of current iteration to obtain a more refined result in the next iteration, therefore, the sparsity is progressively achieved. The algorithm developed is endowed with a strategy to discard potential sources that do not contribute significantly to the acoustic field. Moreover, a robust convergence criterion is proposed. The inverse method proposed has a strong connection with the Bayesian approach to inverse acoustic problems. Indeed, each iteration of IRLS can be seen from Bayesian perspective: the estimate of source field produced in the previous iteration is injected as a priori information in the current one. In addition to this, any other a priori knowledge on the source field can be introduced to improve the source reconstruction. This mechanism is also known as Bayesian focusing. This procedure can be used to calculate a solution to inverse problems in linear formulation, so to have the Equivalent Source Method based on IRLS (ESM-IRLS). While, under the assumption of uncorrelated sources, the same procedure can be also used to solve inverse problems in quadratic formulation. The latter leads to the Covariance Matrix Fitting approach based on IRLS (CMF-IRLS).

A critical aspect of inverse methods is the estimation of the proper amount of regularization, that is problem and data dependant. Each IRLS iteration requires the estimate of a regularization parameter and the final result is heavily affected by the particular regularization mechanism adopted. Bayesian regularization has been chosen to accomplish this task since it is the best performer among all regularization criteria available in literature, to the best of author's knowledge. Bayesian Regularization boils down to search for the minimum of a cost function to have an estimate of the regularization parameter. Different cost functions are available in Bayesian framework, but all of them share the property of having a unique global minimum, under some conditions. This is a rather unique property among regularization criteria. However, some issues are experienced when Bayesian Regularization is combined with IRLS. When the number of potential sources left in the problem approaches to one, Bayesian Regularization gives unstable estimate of regularization parameter. To overcome this problem, the artifice of dummy columns has been implemented to keep a well defined minimum of cost functions. Despite Bayesian Regularization has been stabilized, the final result of IRLS may not be satisfying, especially in terms of source quantification, because of an high risk of under/over-regularized solutions that produces unwanted fluctuations of reconstructed source spectra. In order to obtain an accurate final result, IRLS needs to produce reliable, rather than optimal, solution at each iteration, since only the "shape" of solution is injected in the next IRLS iteration. This can be translated into the principle that over-regularization is preferred to under-regularization, at least when the solution is not yet addressed, i.e. in the early IRLS iterations. The strategy of Bayesian Iterative Regularization has been proposed in this work to fulfil the needs of IRLS. In fact, it always increases the estimate of regularization parameter, with respect to simple Bayesian Regularization. The increment obtained is more evident in the early iteration of IRLS. Once the estimate of source field has been addressed, the amount of regularization needed decreases. This effect makes it possible to obtain more accurate and reliable results with IRLS.

Another aspect has been considered in this thesis: pre-processing of pressure data. Commonly, microphone pressure data is provided to acoustic imaging methods as

Cross-Spectral Matrix. When multiple sources having different levels are present in a scenario, it is useful to separate source components and set an inverse problem for each of them. Two different methods of Cross-Spectral Matrix decomposition have been used in combination with inverse methods: the standard Eigenmode Decomposition and a novel use of CLEAN-SC to extract spatially coherent source components. Eigenmode Decomposition produced poor results in aeroacoustic applications. Components extracted by this approach are very often a mixture of several contributions. The effect of this is twofold: a source component may be highly contaminated by noise and the hypothesis of sparsity may be contradicted when the inverse problem is solved. Another issue is the automatic selection of relevant source components. Conversely, CLEAN-SC decomposition produced high quality results in aeroacoustic applications, when combined with inverse methods described in this thesis. The CLEAN-SC procedure was originally developed as deconvolution algorithm of Conventional Beamforming maps, but in this thesis its use as CSM decomposition is proposed for the first time, to the best of author's knowledge. This method exploits the concept of spatial source coherence to get single coherent source components. As consequence of this, the assumption of sparsity is more likely fulfilled and major robustness to noise is achieved with respect to Eigenmode decomposition. The other meaningful advantage is that CLEAN-SC decomposition provides an automatic estimation of the number of relevant source component.

All theoretical aspects of volumetric source mapping discussed in this thesis have been validated on simulation of simplified test cases. These tests represent the different conditions of 2D versus 3D mapping with a planar array. The aim was to show the increase of difficulty in retrieving correct source location and strength when also the source-array distance is unknown. From the analysis of results, the necessity of imposing a sparsity constraint and introducing a priori information on source field arises to obtain very accurate results. The benefit is evident both in localization and quantification of sound sources. Both methods suffer the issues of CSM decompositions in component separation at low frequency, thus leading, in some cases, to wrong source localization. Generally, CMF outperformed ESM resulting much more reliable in two aspects: source localization at low frequency and reconstruction of correct source strength. It was experienced that CMF applied to the whole CSM is still able to recover exact source position and level in the full frequency range tested. On the other hand, ESM can better deal with correlated sources. In fact, the presence of correlated sources is in contrast with the hypothesis of IRLS-CMF. The main difference between ESM-IRLS and CMF-IRLS is that the former returns amplitude and phase information, making it possible to propagate the equivalent sources, while the latter produces only information about amplitude. This is likely the reason of better accuracy of CMF in source level estimation. From these results emerges a rule of thumb: ESM-IRLS and CMF-IRLS are able to produce accurate results in volumetric mapping for Helmholtz numbers greater than 8, when single planar array is used.

The first experimental test case was an airfoil placed in an open jet. This experiment demonstrated the feasibility of volumetric acoustic mapping with inverse methods using a single planar array in real configurations. Since planar arrays are the most used for acoustic imaging, the techniques proposed in this thesis may have great impact because they do not require any change in experimental setup. In fact, they make it possible to obtain much more spatial information, with respect to the standard planar mapping, only with computation requirements. In this context, CMF-IRLS often outperforms ESM-IRLS, especially at low frequency, but it is much more computationally expensive. When CMF-IRLS is applied to whole CSM, only the strongest sources sensed by the array are recovered in the map. This is the reason why it is preferred to apply CMF to single source components, despite the computational demand. It is convenient to apply CMF to whole CSM only when source decomposition is not effective. A practical aspect has been considered too: the increase of problem size and computational cost with any method utilised when dealing with volumetric problems. If ESM-IRLS produces good results in reasonable time even with problems having hundred thousands of unknowns, CMF-IRLS takes much more time to produce a result for the same problem. The effect of non-uniform mesh within the calculation volume has been tested. The idea is to use different densities of equivalent sources to have fine resolution only where needed. The aim is to have a drastic reduction of the number of potential sources. Results with non-uniform mesh are comparable to those obtained with fine regular grid, but drastic reduction of computation time is experienced. Indeed, reduction of about 80% of computation time is experienced for CMF-IRLS and ESM-IRLS with the implementation of this simple strategy.

The second experimental application aimed at showing the advantage of combining data of multiple planar arrays, in the context of volumetric mapping. An aircraft model was tested in Pininfarina Wind Tunnel using one array on top and one broadside. As expected, the combined use of two arrays increases the compactness and accuracy of localization. Moreover, it moves to a lower frequency the limit experienced with a single array. In such challenging and noisy environment, the introduction of a priori information does not only increase accuracy, but it turns out to be necessary to obtain meaningful maps, especially with a single array.

Both experimental applications have highlighted the great difference between two decompositions, at least for aeroacoustic applications. Maps obtained with Eigenmode Decomposition of CSM are usually spoiled by several artefacts that can not be attributed to mapped sources. Contrarily, CSM decomposition based on CLEAN-SC returns maps without those artefacts, thus resulting in wider dynamic range and more intelligibility of maps.

The feasibility of volumetric acoustic source mapping with inverse methods has been clearly demonstrated. Aeroacoustic source mapping is the application that surely will gain more benefit from these techniques. An important feature of methods proposed is the applicability to any kind of array layout. Indeed, multiple planar arrays produce high quality results in a large frequency range. However, it has been shown that even a single planar microphone array returns satisfying results with some limitations at lower frequencies. This aspect turns out useful because it enables to obtain more information from data already acquired with the commonest measurement setup at cost of simply re-processing data.

6.2 Future works

Some general guidelines on how to set-up an inverse problem are provided in this thesis. However, it is still a matter of experience and trial-and-error procedure. Thus, it is important for industrial applications to provide well-defined rules for defining the region of interest, its discretization and other aspects that influence the final result. For example, it could be useful a rule which provides a suggestion on how dense the mesh should be to have the best results for a certain frequency. In other words, a relationship between the wavelength (or Helmholtz number) and grid resolution (or mesh density). Such information would help to avoid excessive degrees of freedom in the inverse problem, thus reducing the ill-conditioning. A deeper study on the use of non-uniform meshes of region of interest can improve the effectiveness of inverse methods proposed and, as already shown, the computation demand. In addition to the definition of the inverse problem, a systematic characterisation of different strength of sparsity constraint could help the user to impose the optimal sparsity for a particular problem.

Further research could be focused also on the extension of the frequency range of applicability, especially towards low frequencies when a single array is utilized. This aspect can be faced from different directions. One is the introduction of fine a priori information that can be retrieved in different ways. Instead, a better source component separation of CSM could make the hypothesis of sparse source field well respected, thus leading to better results with IRLS. In addition, it could enable an accurate source localization with other simple acoustic imaging methods and again it could help to define very focused a priori information. Another aspect that can be improved is the quantification of source strength with ESM-IRLS, that demonstrated to be more problem dependant with respect to CMF-IRLS. A possible solution could be to somehow correct outcomes of IRLS in function of the regularization parameter to obtain more accurate source quantification. Finally, an optimal array design for volumetric acoustic mapping can be studied, instead of combining multiple planar arrays.

Appendix A

Results of simulated experiments

This appendix shows the complete set of results obtained with inverse methods developed in this thesis and applied to three simulated experiments described in Section 4.1. All maps show the output of these methods obtained with the acoustic transfer function of Eq. 3.2, i.e. pressure induced at the reference point by a monopole in a generic point of the region of interest. In this case, the reference point is the array centre, that is the origin of coordinate system $\mathbf{r}_0 = \mathbf{0}$. Dynamics of maps shown here is fixed at 30 dB. Maps of 1D ROI show the results for all spectral lines in the range $He = [2, 16]$. While for 2D ROI, only maps of 4 spectral lines are shown, i.e. $He = 2, 4, 8, 16$. Exact source position is depicted on maps by means of green vertical dotted lines for 1D maps and blue diamonds for 2D maps. Source quantification is also evaluated. Reconstructed source spectra are obtained from integration of maps over a circle of 0.1 m radius around the exact source position. The error between real and reconstructed spectra is reported in terms of difference in dB.

A.1 Test Case 1 (TC1) - Figures

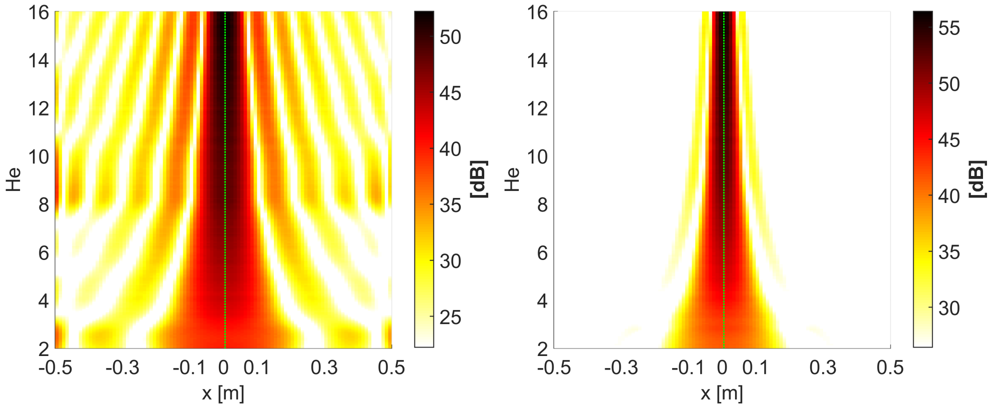

(a) $p = 2$ (b) $p = 2$ - $\mathbf{W}_0 = \text{CB}$

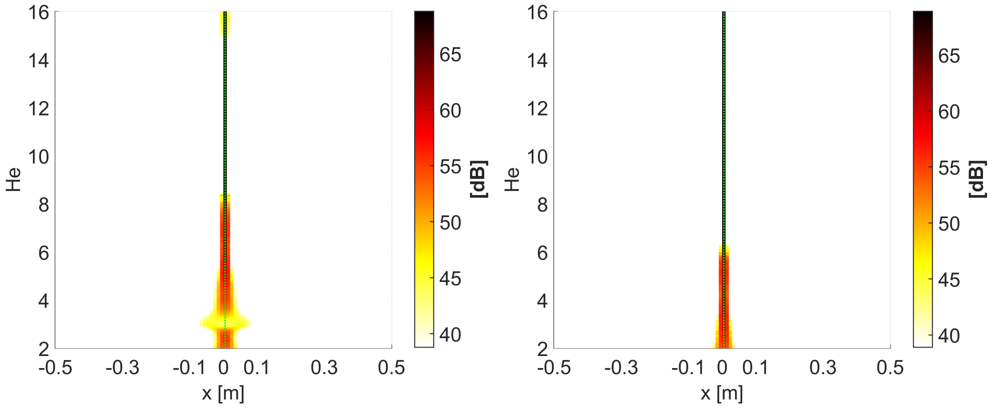

(c) $p = 1$ (d) $p = 1$ - $\mathbf{W}_0 = \text{CB}$

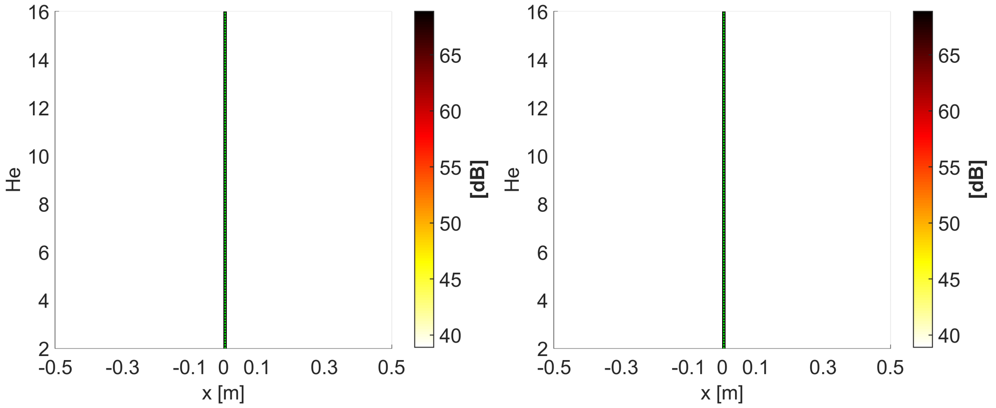

(e) $p = 0$ (f) $p = 0$ - $\mathbf{W}_0 = \text{CB}$

Figure A.1: Test Case 1 (1D) - ESM-IRLS

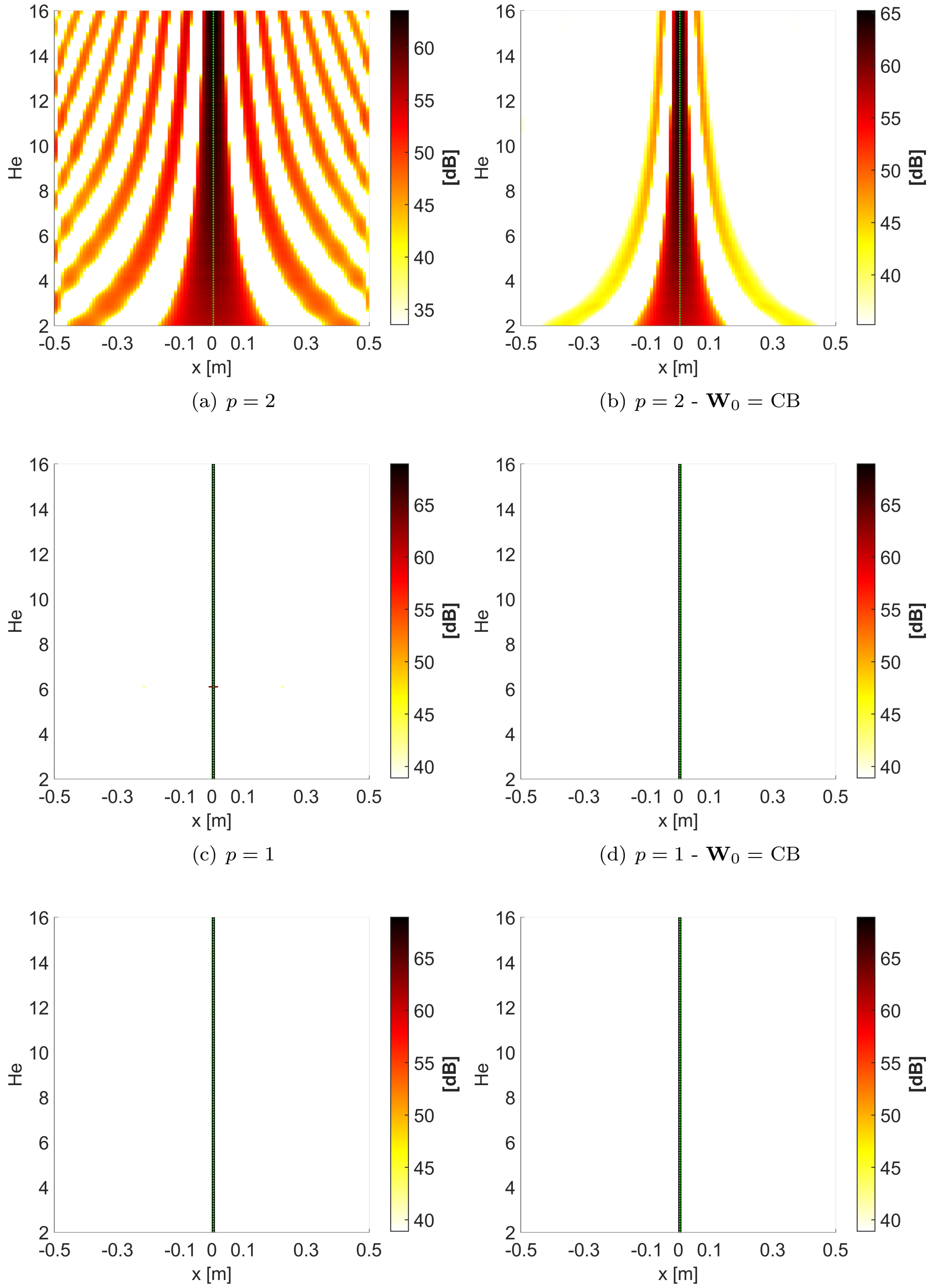

(a) $p = 2$

(b) $p = 2$ - $\mathbf{W}_0 = \text{CB}$

(c) $p = 1$

(d) $p = 1$ - $\mathbf{W}_0 = \text{CB}$

(e) $p = 0$

(f) $p = 0$ - $\mathbf{W}_0 = \text{CB}$

Figure A.2: Test Case 1 (1D) - CMF-IRLS on whole CSM

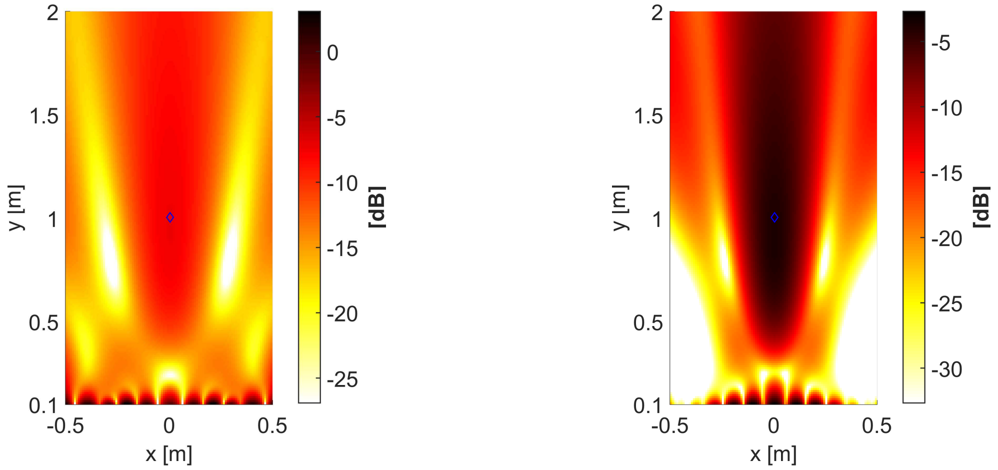

(a) $p = 2$

(b) $p = 2$ - $\mathbf{W}_0 = \mathrm{CB}$

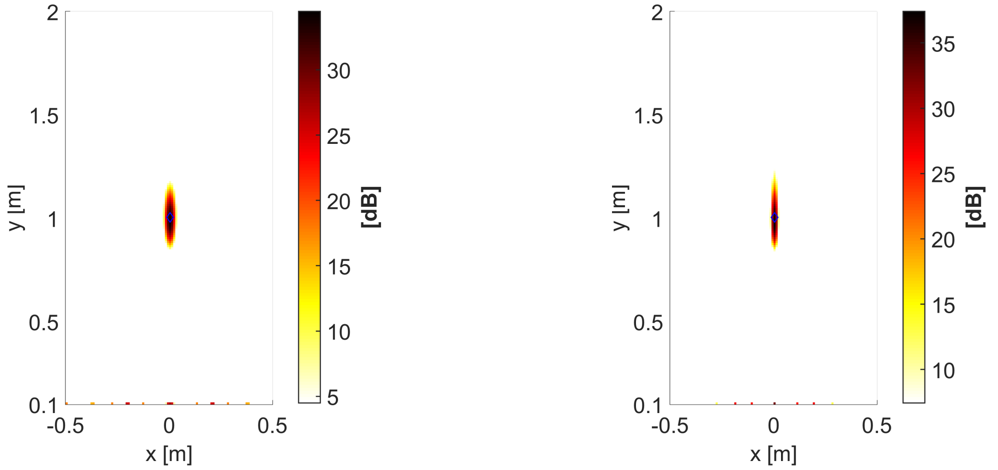

(c) $p = 1$

(d) $p = 1$ - $\mathbf{W}_0 = \mathrm{CB}$

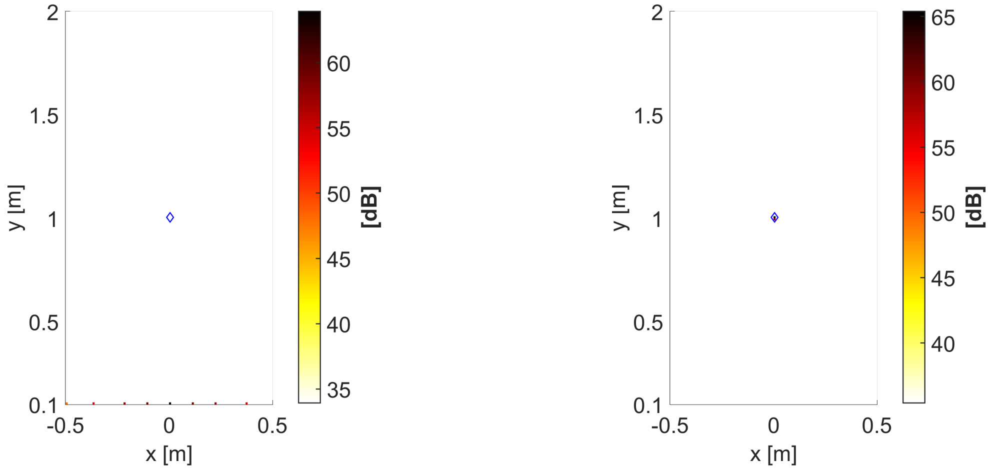

(e) $p = 0$

(f) $p = 0$ - $\mathbf{W}_0 = \mathrm{CB}$

Figure A.3: Test Case 1 (2D) at $He = 2$ - ESM-IRLS

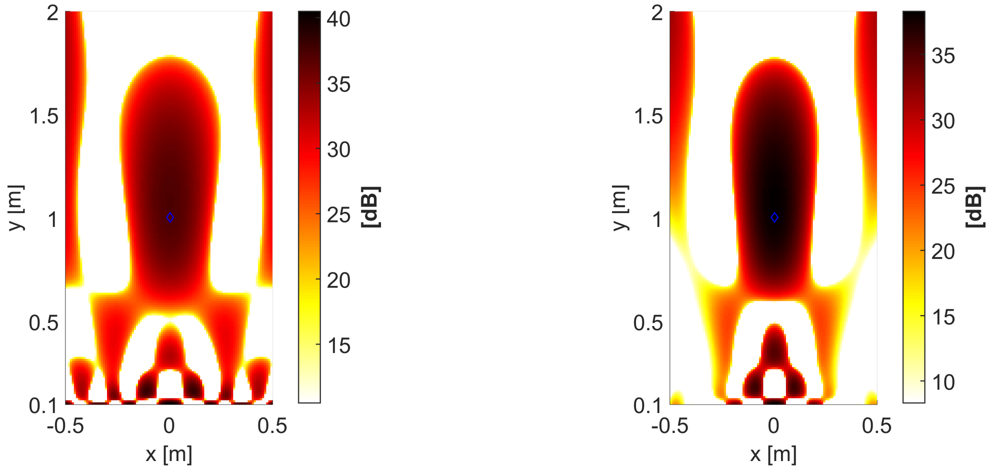

(a) $p = 2$ (b) $p = 2$ - $\mathbf{W}_0 = \text{CB}$

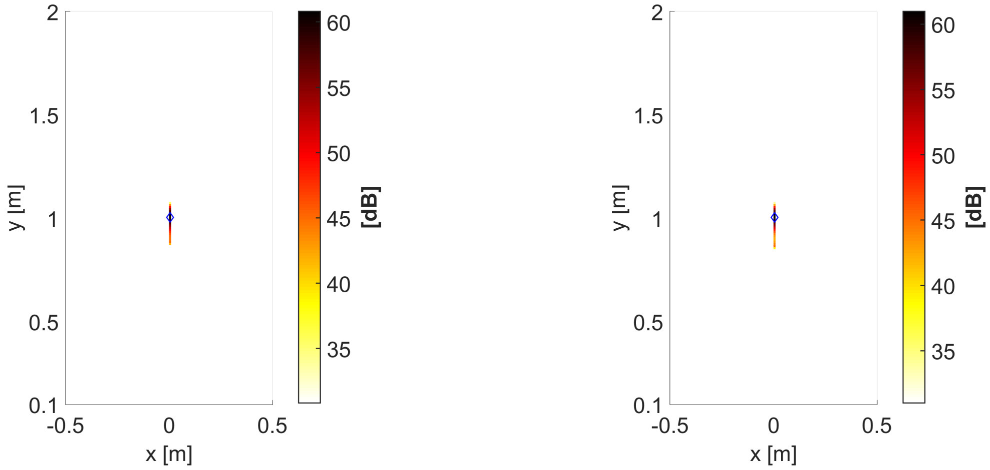

(c) $p = 1$ (d) $p = 1$ - $\mathbf{W}_0 = \text{CB}$

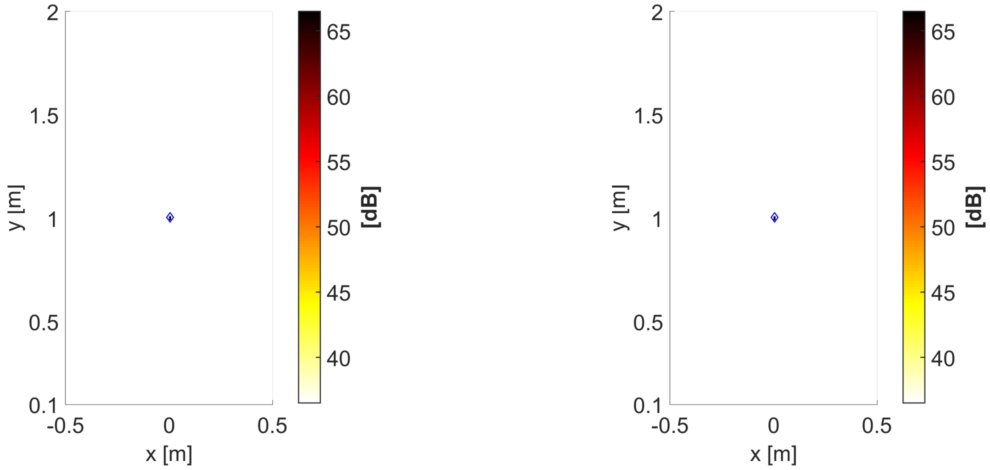

(e) $p = 0$ (f) $p = 0$ - $\mathbf{W}_0 = \text{CB}$

Figure A.4: Test Case 1 (2D) at $He = 2$ - CMF-IRLS on whole CSM

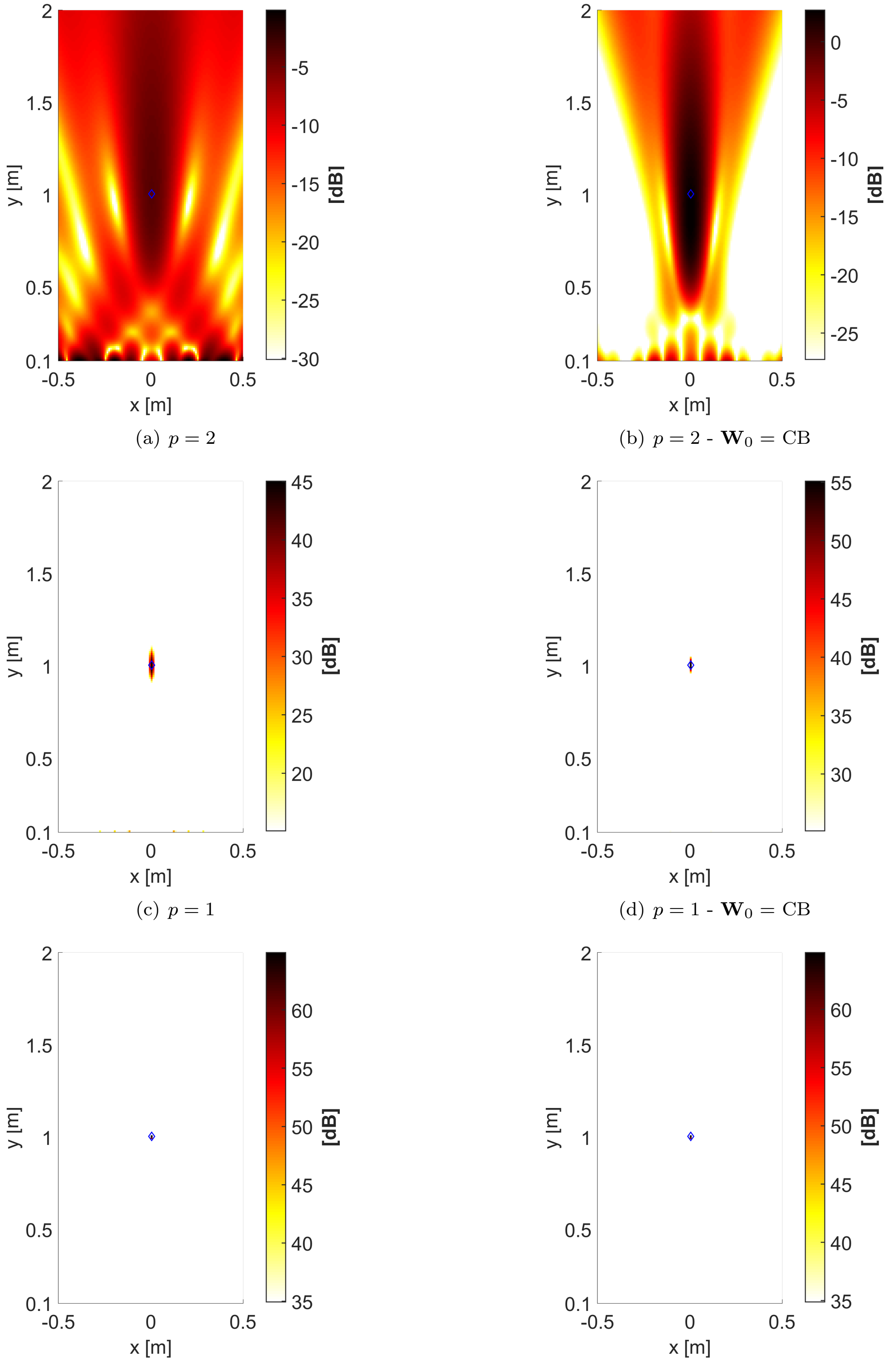

(a) $p = 2$

(b) $p = 2$ - $\mathbf{W}_0 = \mathrm{CB}$

(c) $p = 1$

(d) $p = 1$ - $\mathbf{W}_0 = \mathrm{CB}$

(e) $p = 0$

(f) $p = 0$ - $\mathbf{W}_0 = \mathrm{CB}$

Figure A.5: Test Case 1 (2D) at $He = 4$ - ESM-IRLS

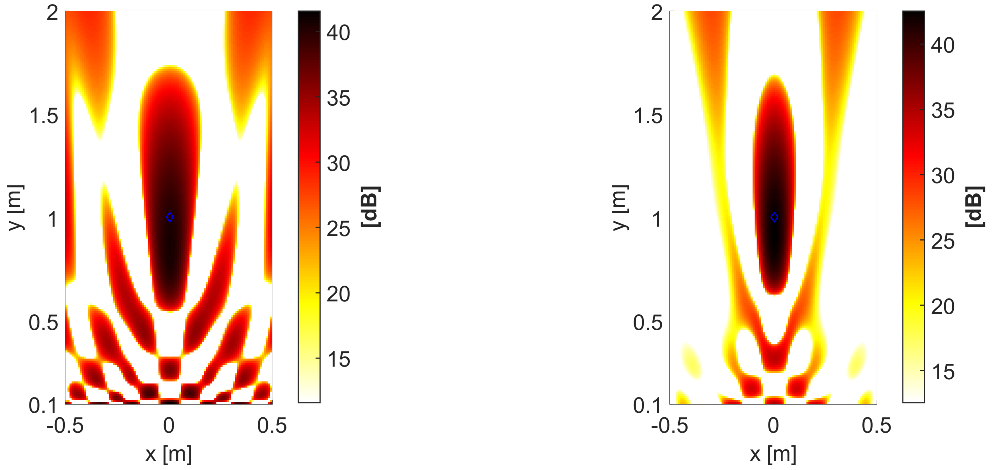

(a) $p = 2$ (b) $p = 2$ - $\mathbf{W}_0 = \text{CB}$

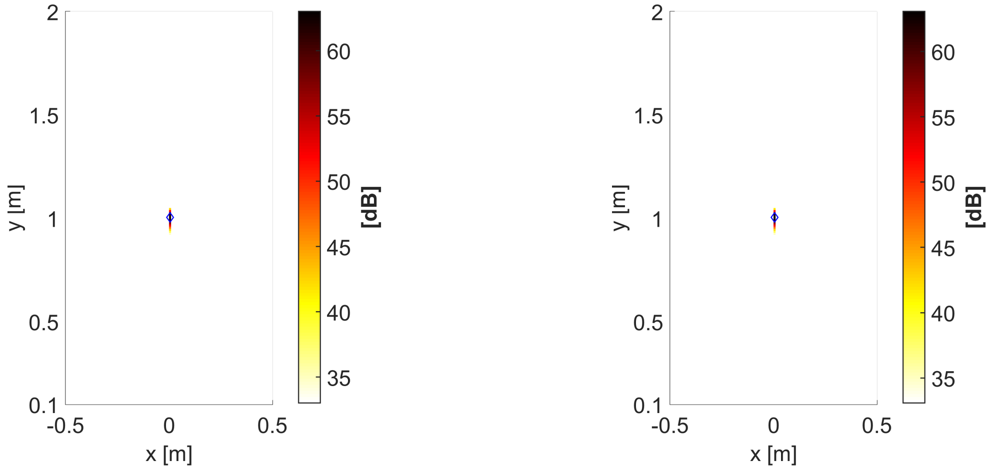

(c) $p = 1$ (d) $p = 1$ - $\mathbf{W}_0 = \text{CB}$

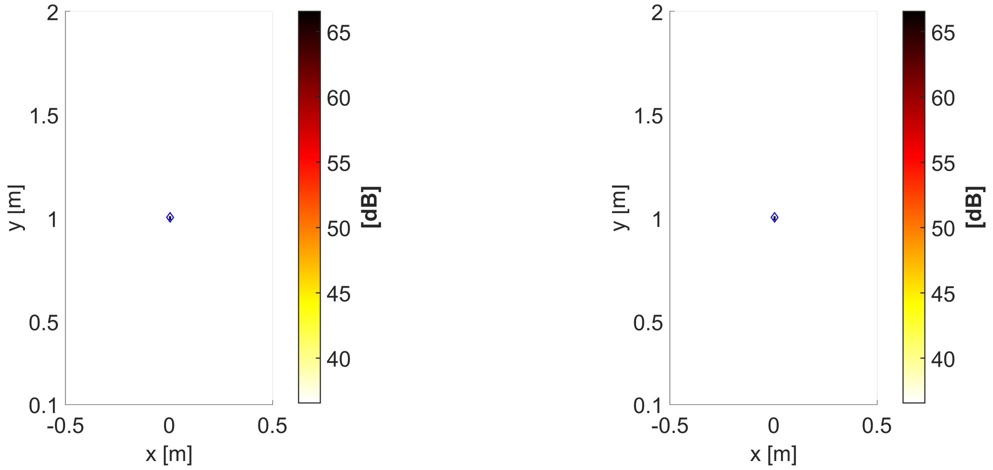

(e) $p = 0$ (f) $p = 0$ - $\mathbf{W}_0 = \text{CB}$

Figure A.6: Test Case 1 (2D) at $He = 4$ - CMF-IRLS on whole CSM

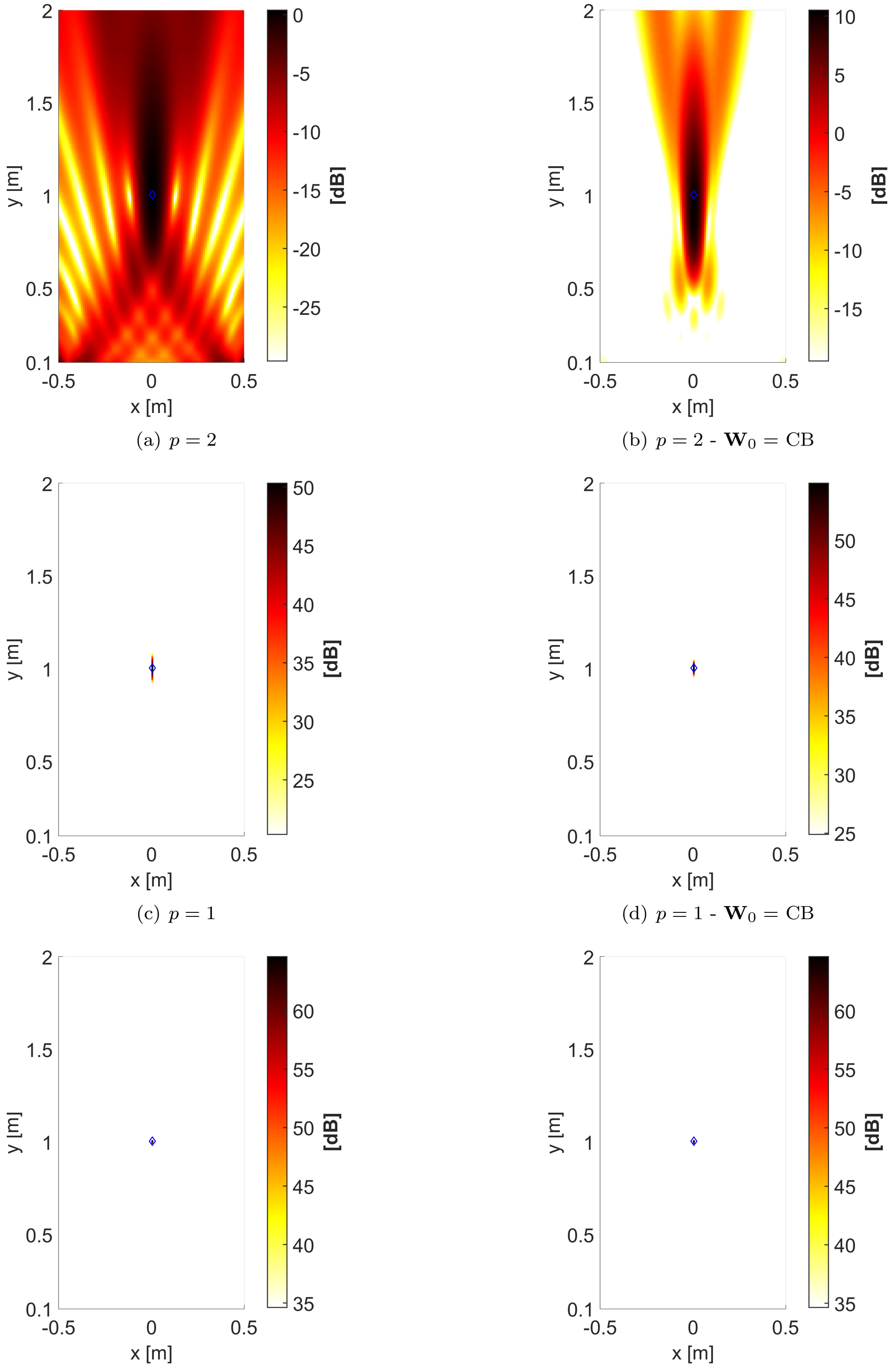

(a) $p = 2$

(b) $p = 2$ - $\mathbf{W}_0 =$ CB

(c) $p = 1$

(d) $p = 1$ - $\mathbf{W}_0 =$ CB

(e) $p = 0$

(f) $p = 0$ - $\mathbf{W}_0 =$ CB

Figure A.7: Test Case 1 (2D) at $He = 8$ - ESM-IRLS

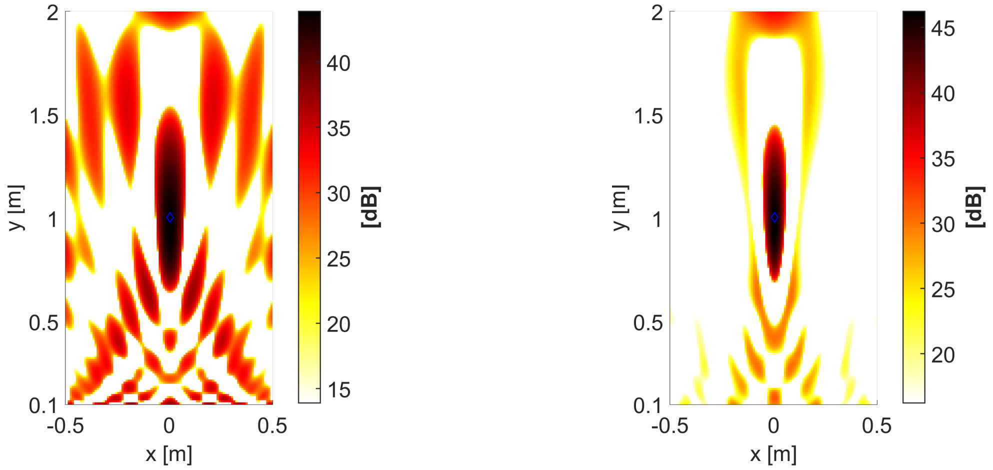

(a) $p = 2$ (b) $p = 2$ - $\mathbf{W}_0 = \text{CB}$

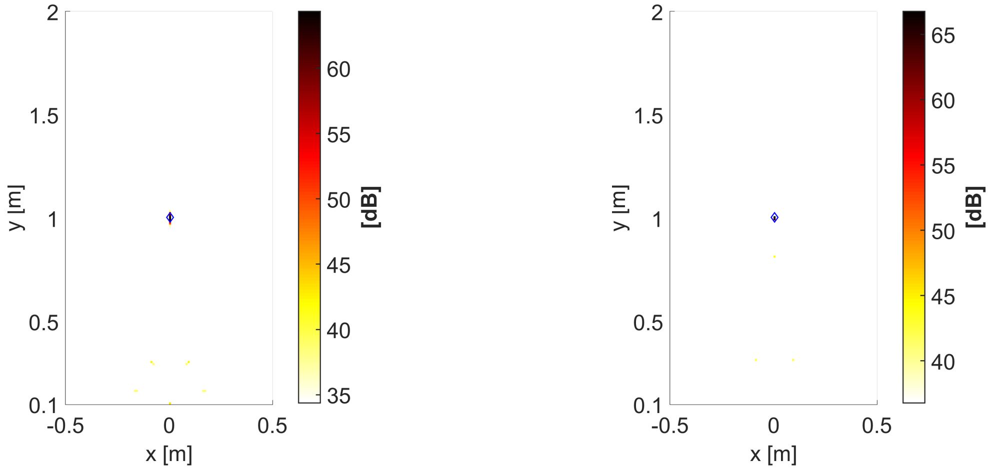

(c) $p = 1$ (d) $p = 1$ - $\mathbf{W}_0 = \text{CB}$

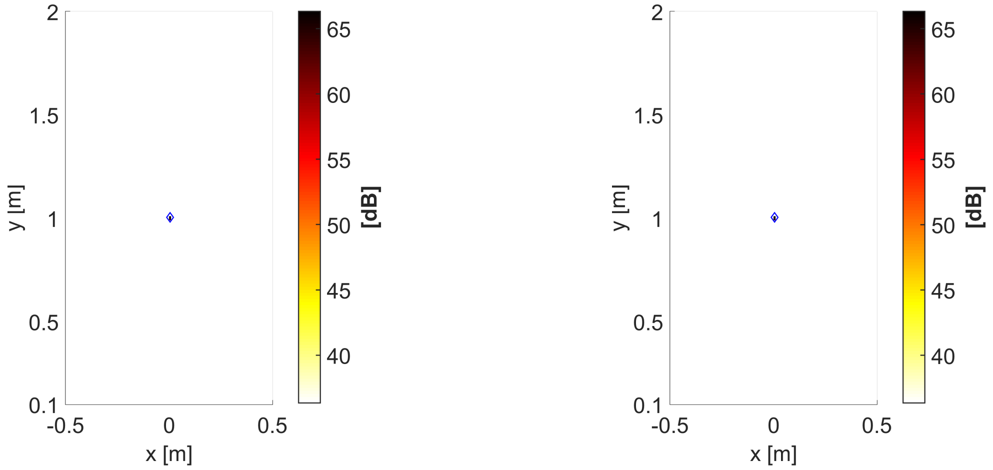

(e) $p = 0$ (f) $p = 0$ - $\mathbf{W}_0 = \text{CB}$

Figure A.8: Test Case 1 (2D) at $He = 8$ - CMF-IRLS on whole CSM

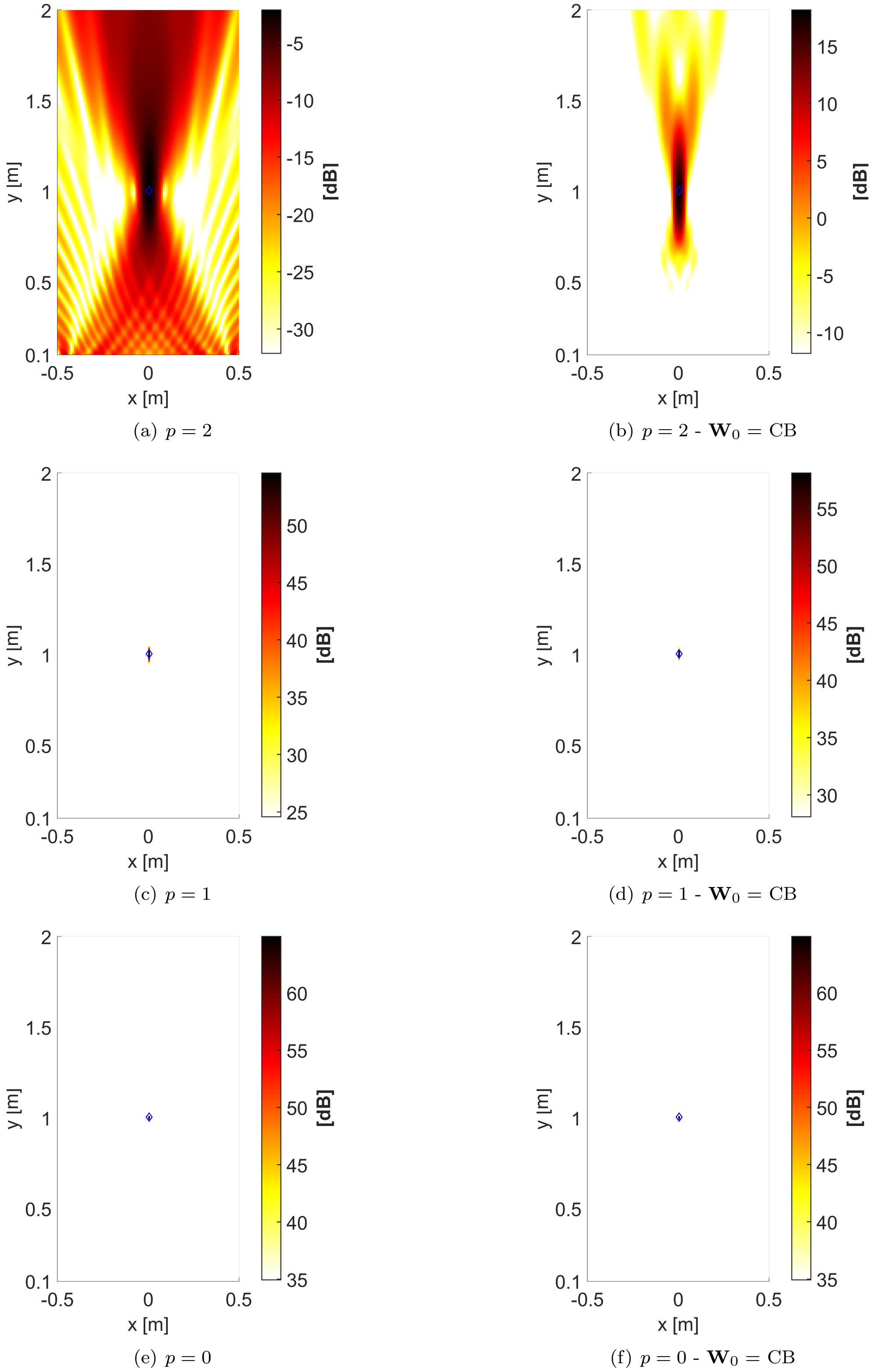

(a) $p = 2$

(b) $p = 2$ - $\mathbf{W}_0 = \mathrm{CB}$

(c) $p = 1$

(d) $p = 1$ - $\mathbf{W}_0 = \mathrm{CB}$

(e) $p = 0$

(f) $p = 0$ - $\mathbf{W}_0 = \mathrm{CB}$

Figure A.9: Test Case 1 (2D) at $He = 16$ - ESM-IRLS

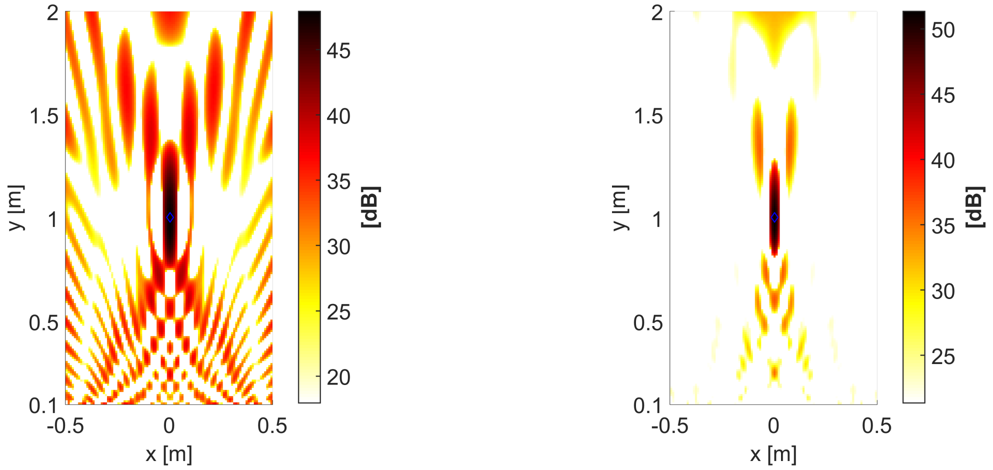

(a) $p = 2$

(b) $p = 2$ - $\mathbf{W}_0$ = CB

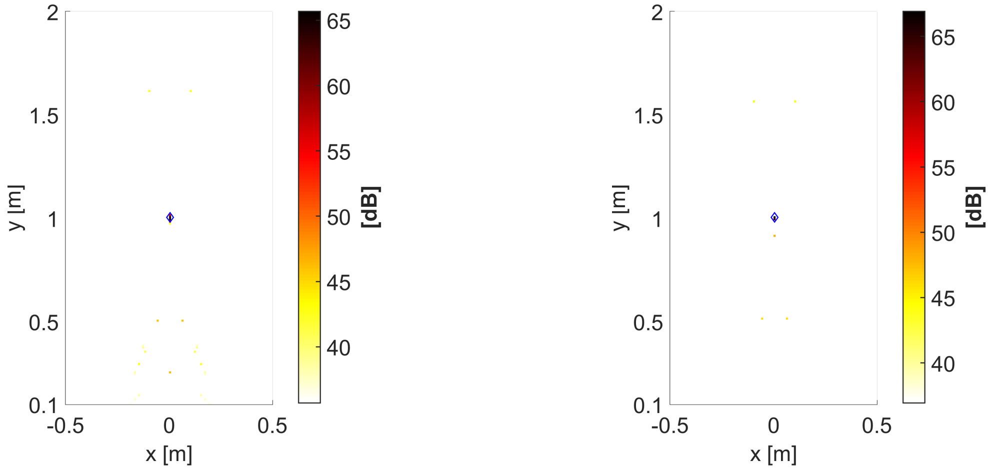

(c) $p = 1$

(d) $p = 1$ - $\mathbf{W}_0$ = CB

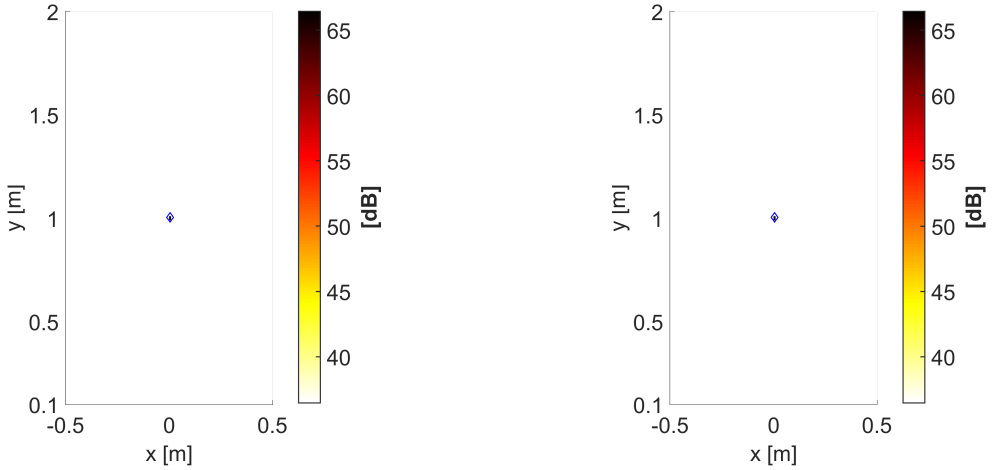

(e) $p = 0$

(f) $p = 0$ - $\mathbf{W}_0$ = CB

Figure A.10: Test Case 1 (2D) at $He = 16$ - CMF-IRLS on whole CSM

A.1.1 Reconstructed source spectra of Test Case 1

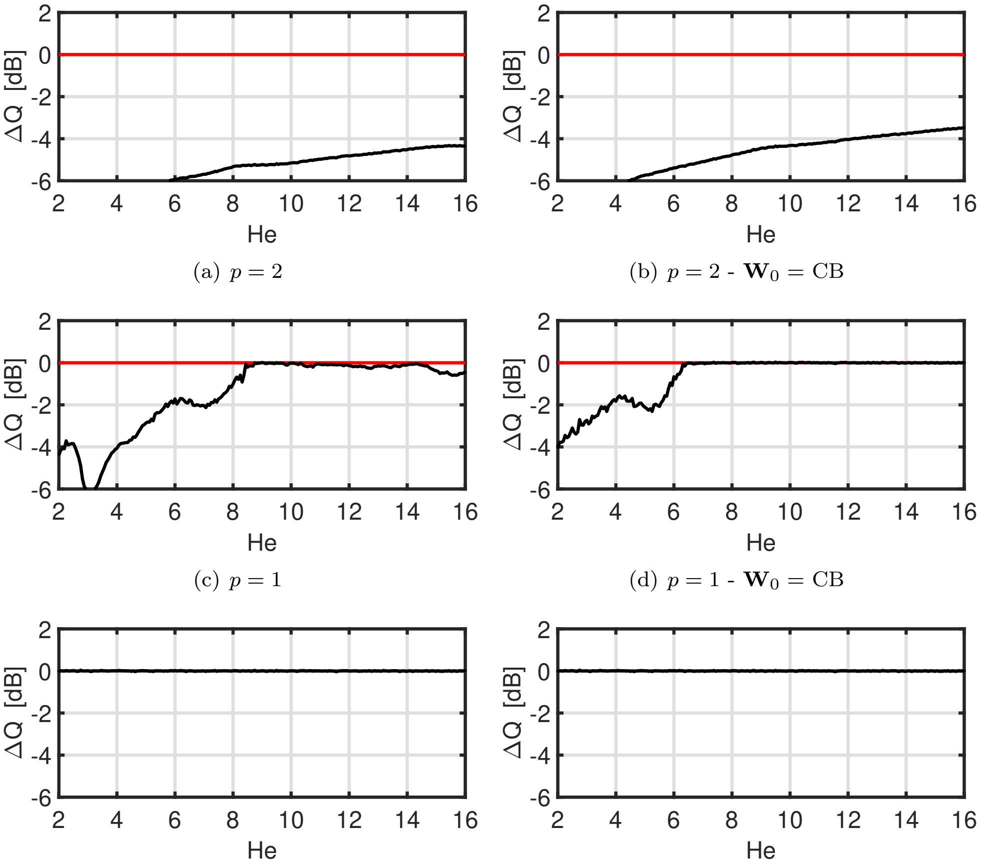

(a) $p = 2$

(b) $p = 2$ - $\mathbf{W}_0$ = CB

(c) $p = 1$

(d) $p = 1$ - $\mathbf{W}_0$ = CB

(e) $p = 0$

(f) $p = 0$ - $\mathbf{W}_0$ = CB

Figure A.11: Test Case 1 (1D) - Errors in source spectrum reconstruction with ESM-IRLS. Red line: target error. Black line: error of reconstructed spectrum.

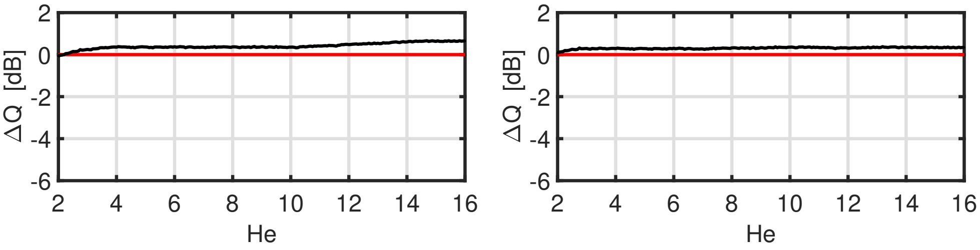

(a) $p = 2$ (b) $p = 2$ - $\mathbf{W}_0 = \mathrm{CB}$

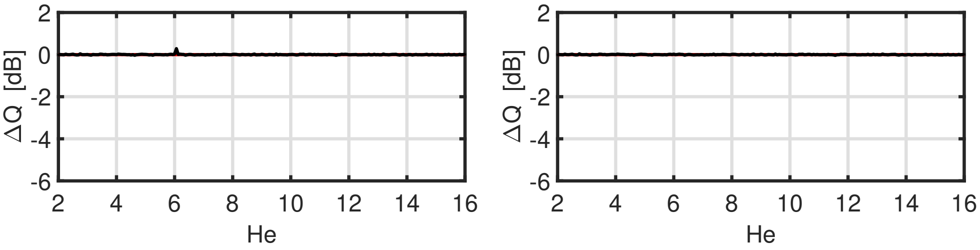

(c) $p = 1$ (d) $p = 1$ - $\mathbf{W}_0 = \mathrm{CB}$

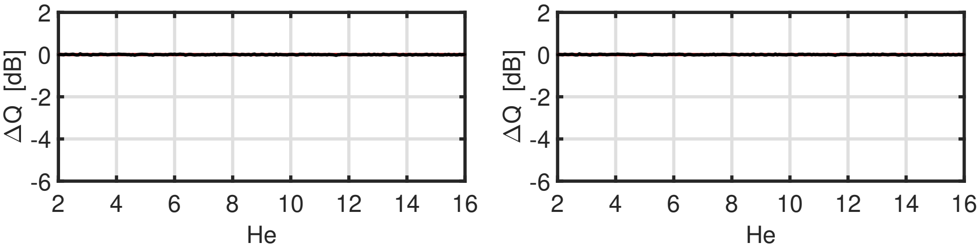

(e) $p = 0$ (f) $p = 0$ - $\mathbf{W}_0 = \mathrm{CB}$

Figure A.12: Test Case 1 (1D) - Errors in source spectrum reconstruction with CMF-IRLS. Red line: target error. Black line: error of reconstructed spectrum.

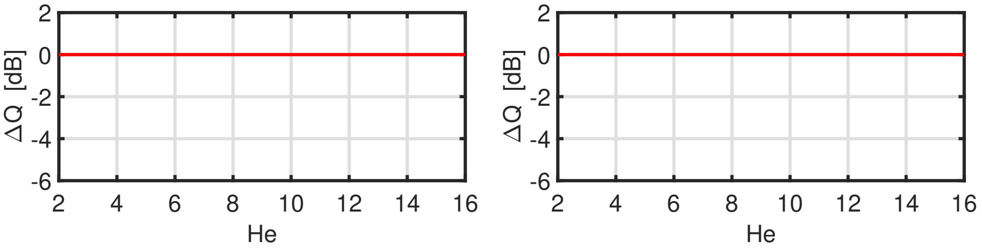

(a) $p = 2$ (b) $p = 2$ - $\mathbf{W}_0 = \mathrm{CB}$

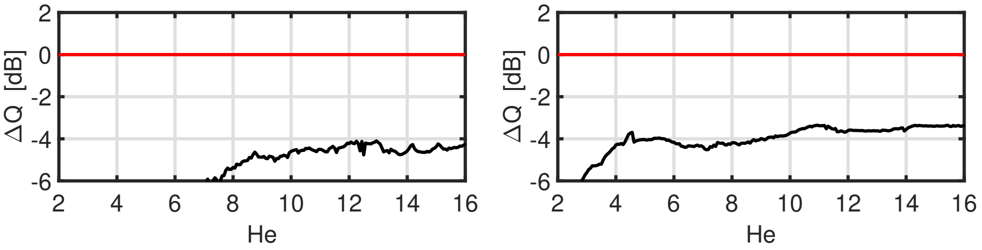

(c) $p = 1$ (d) $p = 1$ - $\mathbf{W}_0 = \mathrm{CB}$

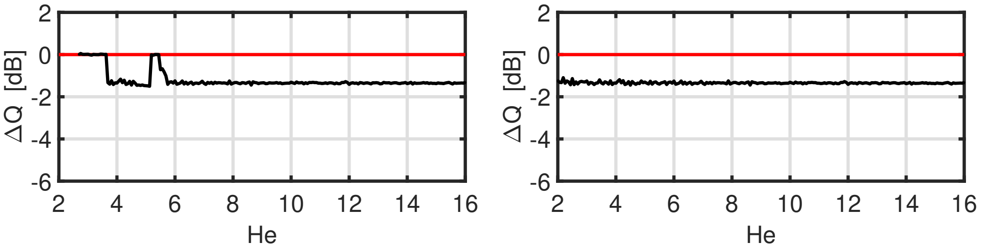

(e) $p = 0$ (f) $p = 0$ - $\mathbf{W}_0 = \mathrm{CB}$

Figure A.13: Test Case 1 (2D) - Errors in source spectrum reconstruction with ESM-IRLS. Red line: target error. Black line: error of reconstructed spectrum.

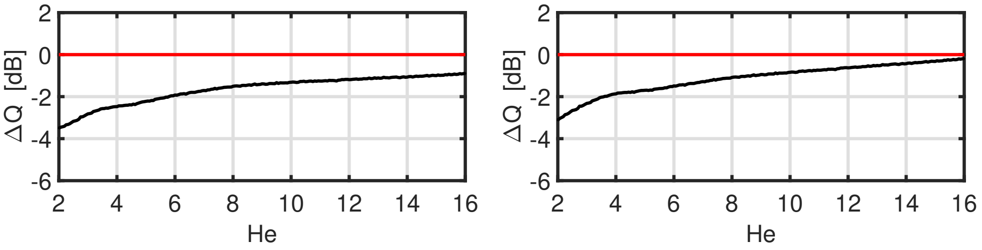

(a) $p = 2$ (b) $p = 2$ - $\mathbf{W}_0$ = CB

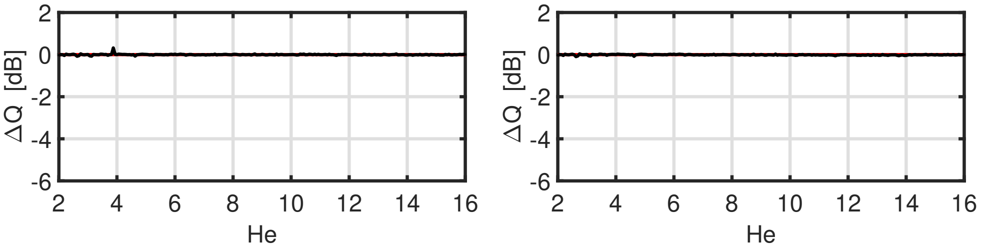

(c) $p = 1$ (d) $p = 1$ - $\mathbf{W}_0$ = CB

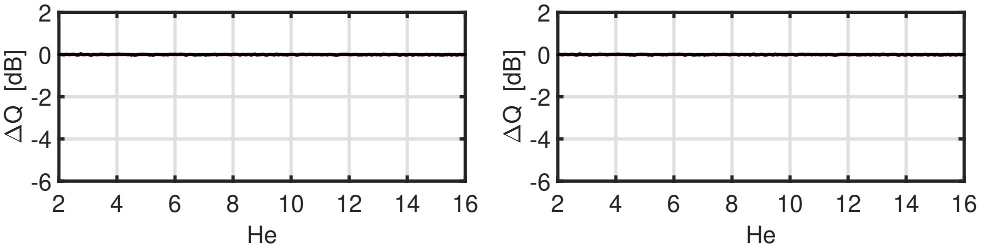

(e) $p = 0$ (f) $p = 0$ - $\mathbf{W}_0$ = CB

Figure A.14: Test Case 1 (2D) - Errors in source spectrum reconstruction with CMF-IRLS. Red line: target error. Black line: error of reconstructed spectrum.

A.2 Test Case 2 (TC2) - Figures

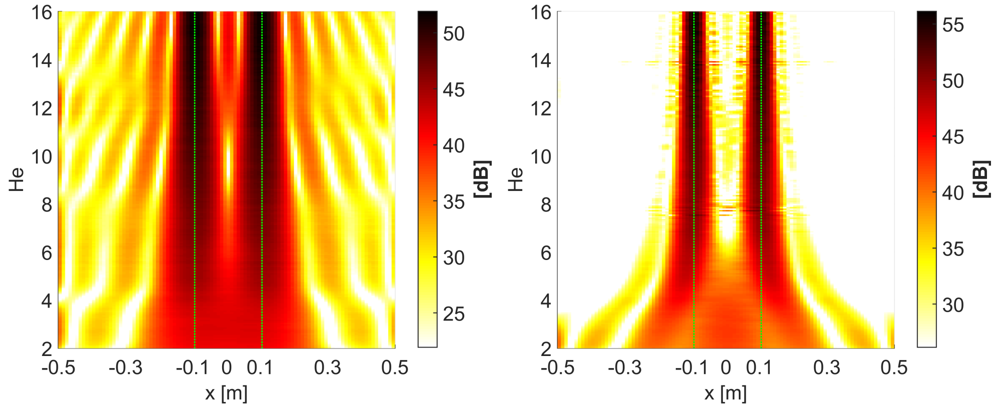

(a) $p = 2$ (b) $p = 2$ - $\mathbf{W}_0 = \mathrm{CB}$

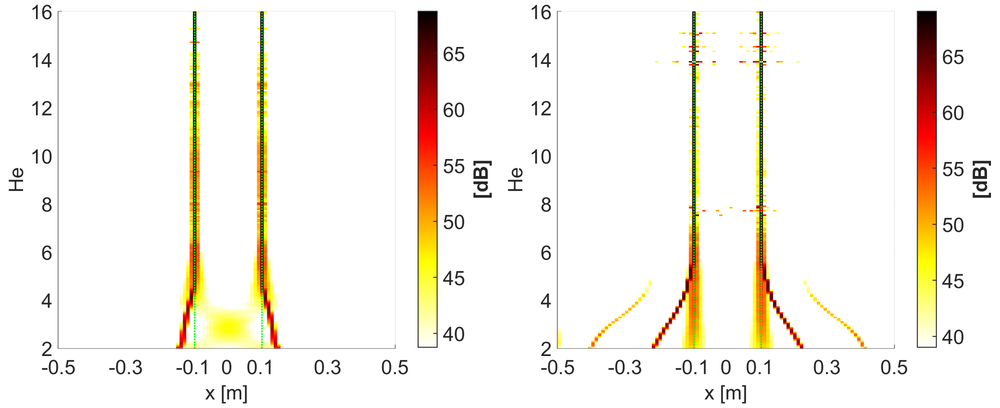

(c) $p = 1$ (d) $p = 1$ - $\mathbf{W}_0 = \mathrm{CB}$

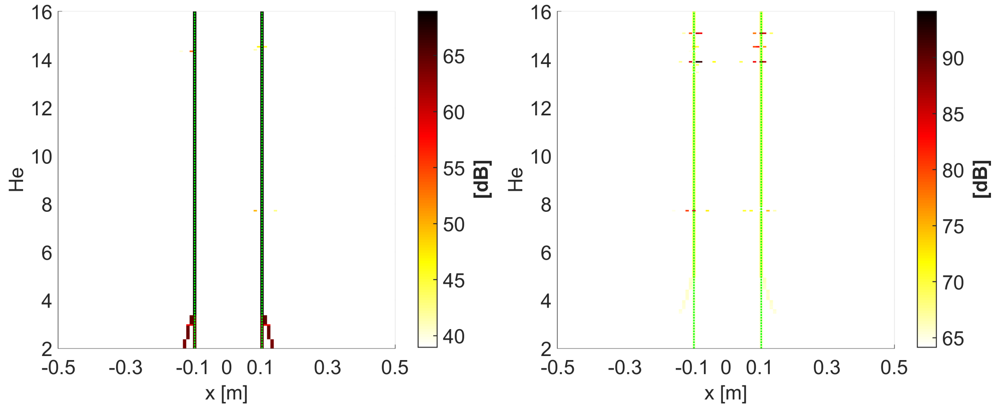

(e) $p = 0$ (f) $p = 0$ - $\mathbf{W}_0 = \mathrm{CB}$

Figure A.15: Test Case 2 (1D) - ESM-IRLS - ED

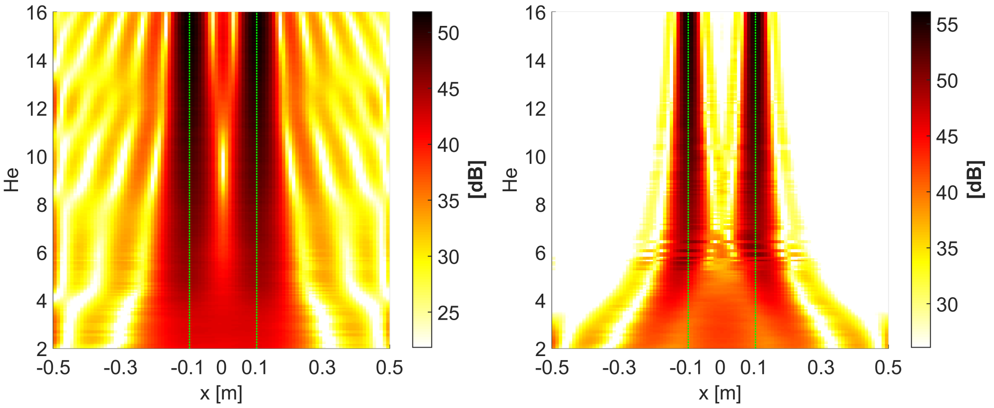

(a) $p = 2$ (b) $p = 2$ - $\mathbf{W}_0 = \mathrm{CB}$

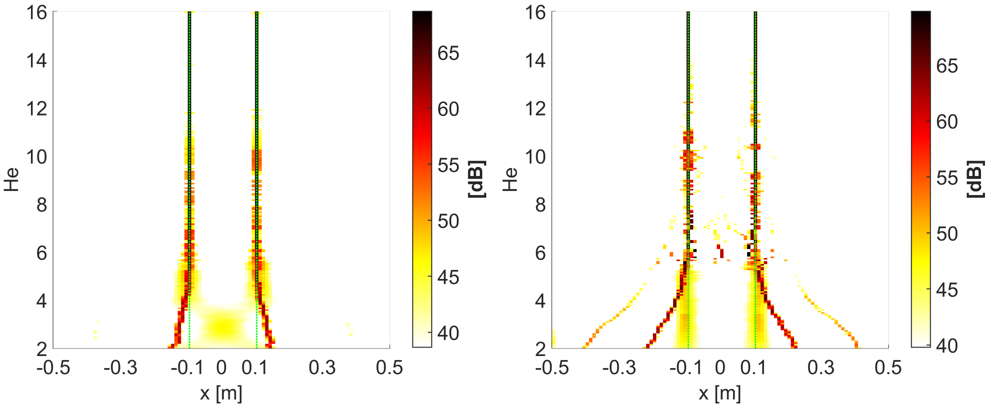

(c) $p = 1$ (d) $p = 1$ - $\mathbf{W}_0 = \mathrm{CB}$

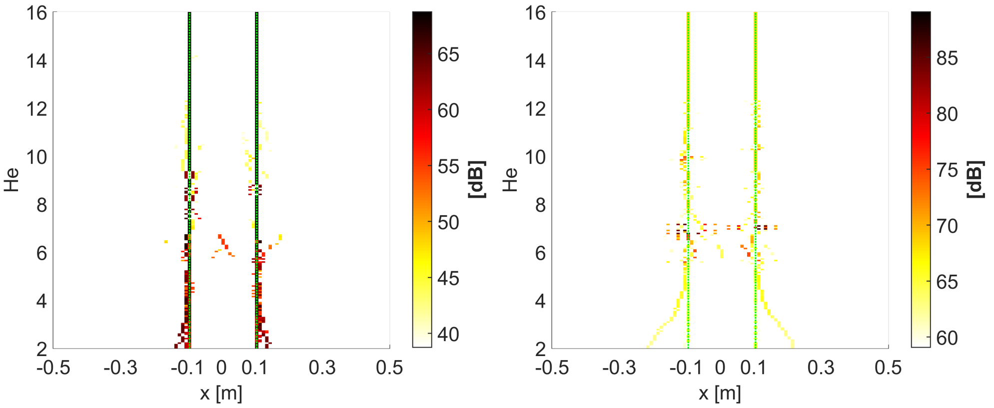

(e) $p = 0$ (f) $p = 0$ - $\mathbf{W}_0 = \mathrm{CB}$

Figure A.16: Test Case 2 (1D) - ESM-IRLS - CSCD

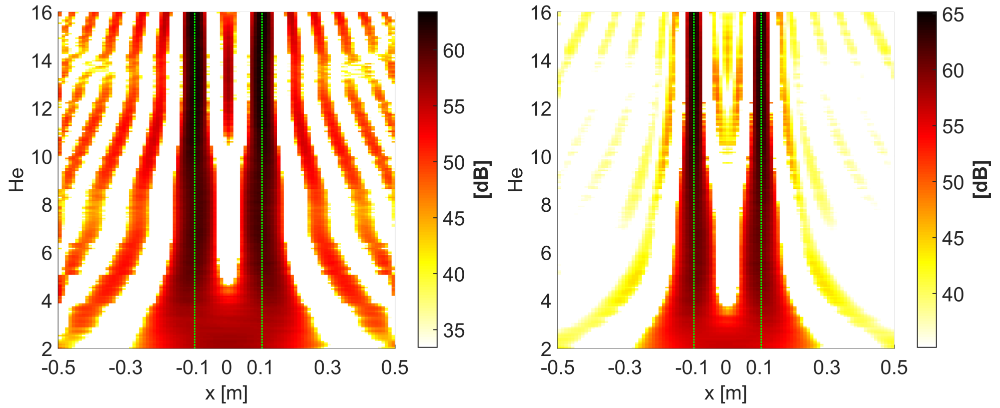

(a) $p = 2$ (b) $p = 2$ - $\mathbf{W}_0 = \mathrm{CB}$

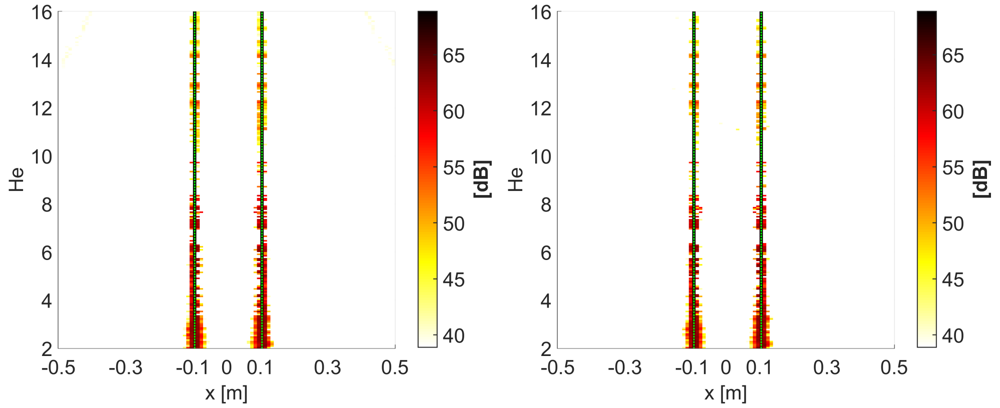

(c) $p = 1$ (d) $p = 1$ - $\mathbf{W}_0 = \mathrm{CB}$

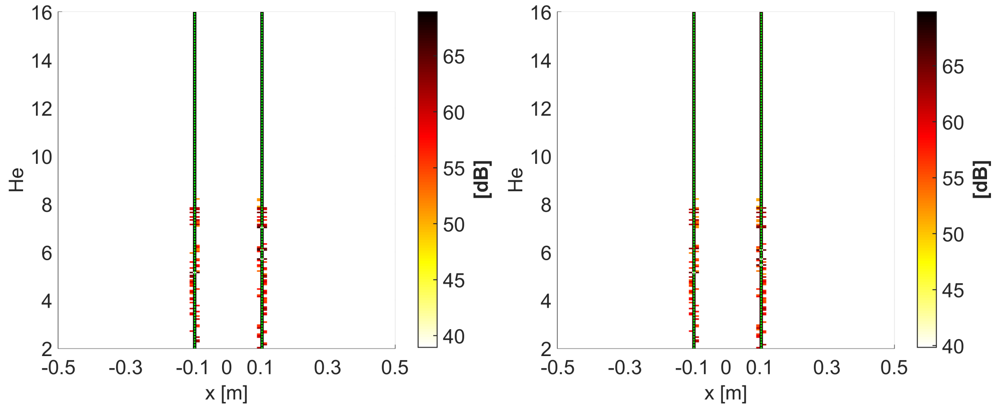

(e) $p = 0$ (f) $p = 0$ - $\mathbf{W}_0 = \mathrm{CB}$

Figure A.17: Test Case 2 (1D) - CMF-IRLS on whole CSM

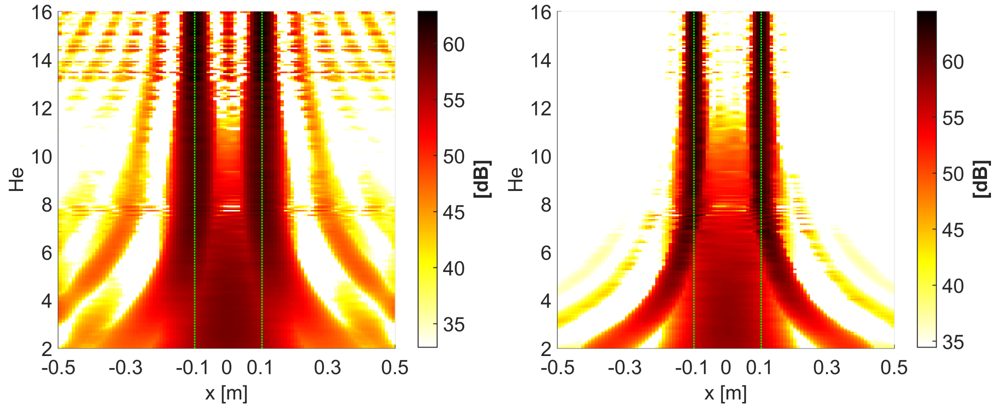

(a) $p = 2$ (b) $p = 2$ - $\mathbf{W}_0 = \text{CB}$

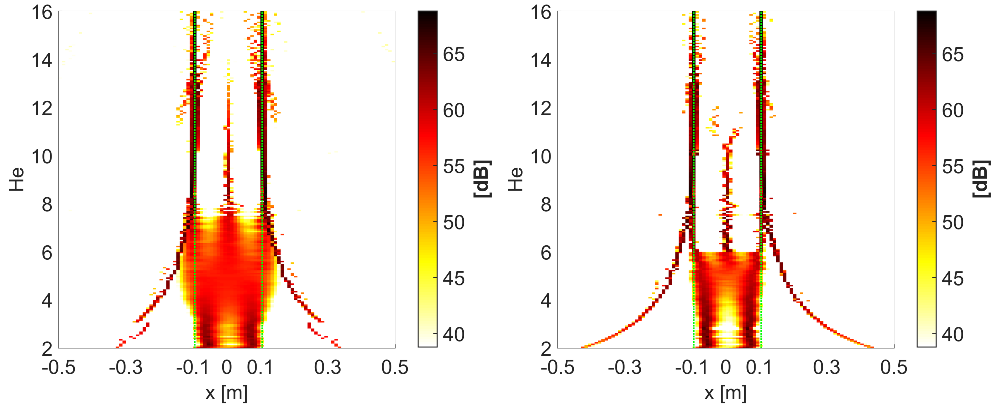

(c) $p = 1$ (d) $p = 1$ - $\mathbf{W}_0 = \text{CB}$

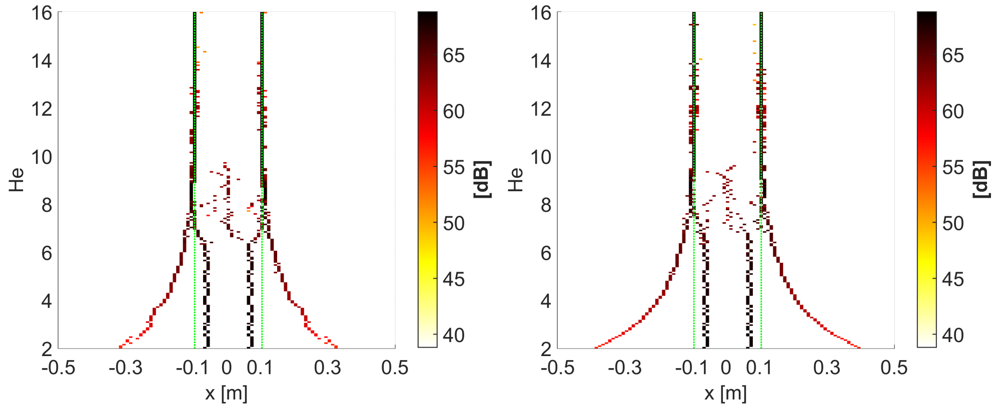

(e) $p = 0$ (f) $p = 0$ - $\mathbf{W}_0 = \text{CB}$

Figure A.18: Test Case 2 (1D) - CMF-IRLS - ED

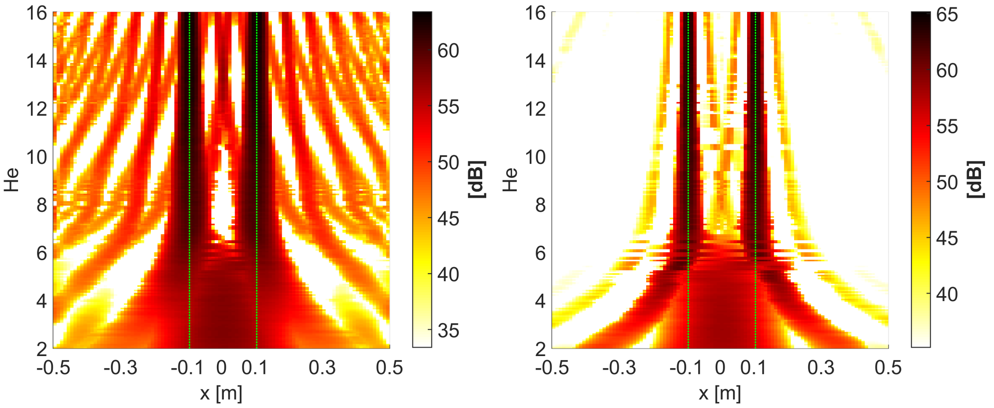

(a) $p = 2$ (b) $p = 2$ - $\mathbf{W}_0 = \mathrm{CB}$

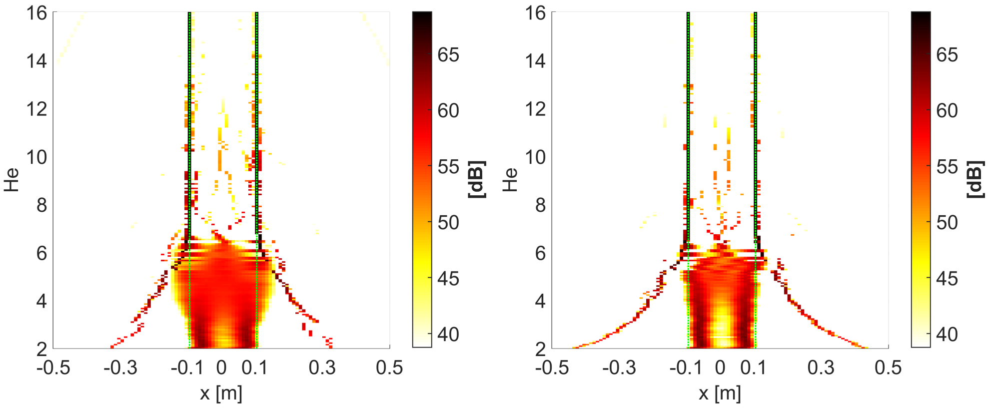

(c) $p = 1$ (d) $p = 1$ - $\mathbf{W}_0 = \mathrm{CB}$

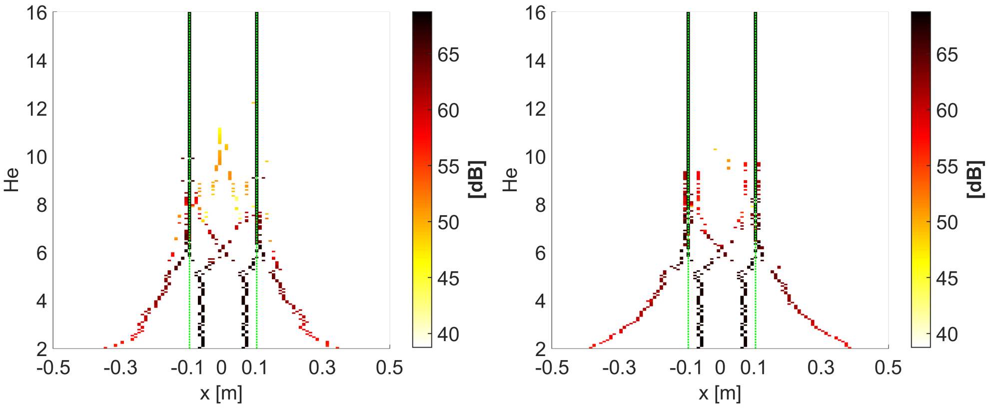

(e) $p = 0$ (f) $p = 0$ - $\mathbf{W}_0 = \mathrm{CB}$

Figure A.19: Test Case 2 (1D) - CMF-IRLS - CSCD

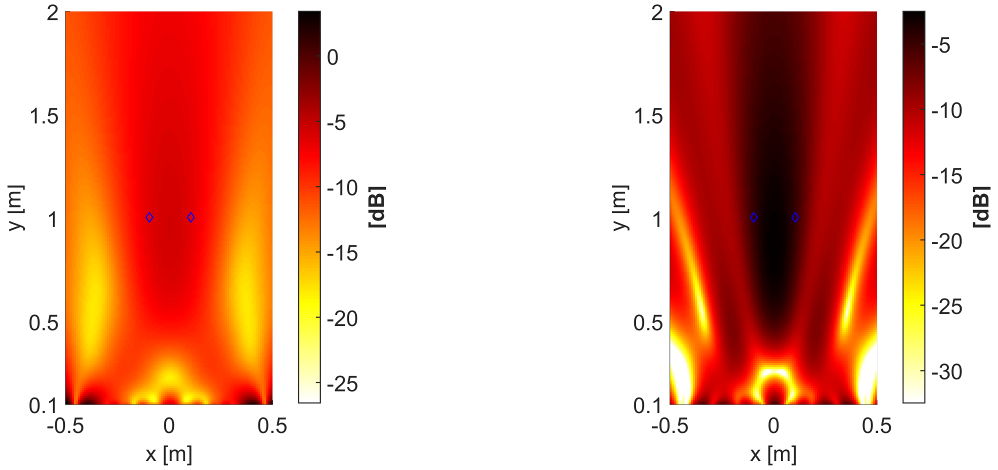

(a) $p = 2$ (b) $p = 2$ - $\mathbf{W}_0 = \text{CB}$

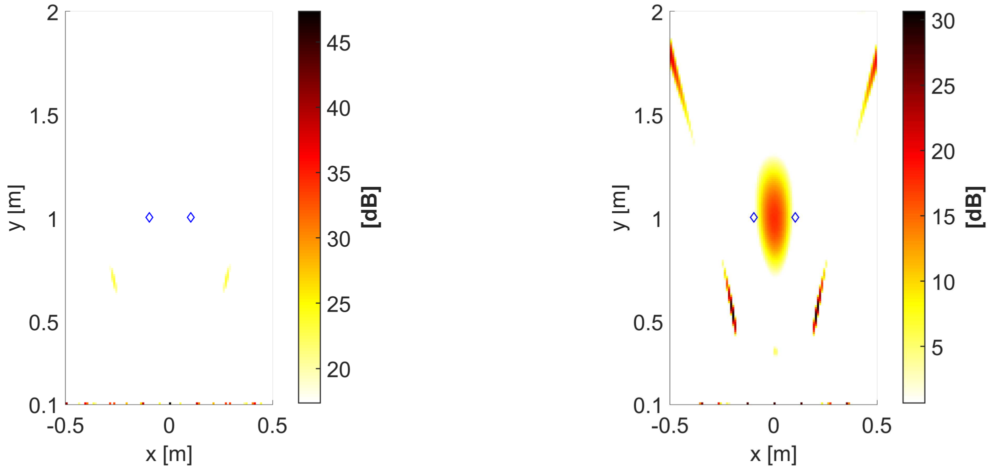

(c) $p = 1$ (d) $p = 1$ - $\mathbf{W}_0 = \text{CB}$

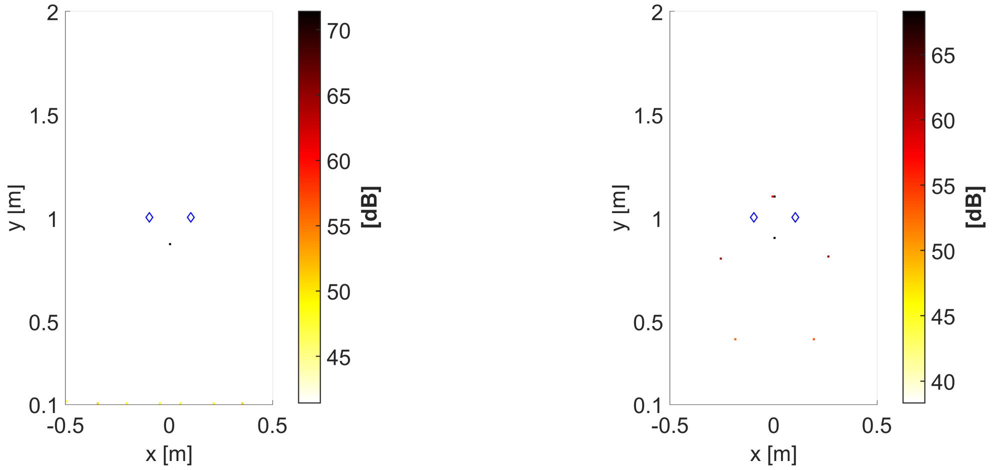

(e) $p = 0$ (f) $p = 0$ - $\mathbf{W}_0 = \text{CB}$

Figure A.20: Test Case 2 (2D) at $He = 2$ - ESM-IRLS - ED

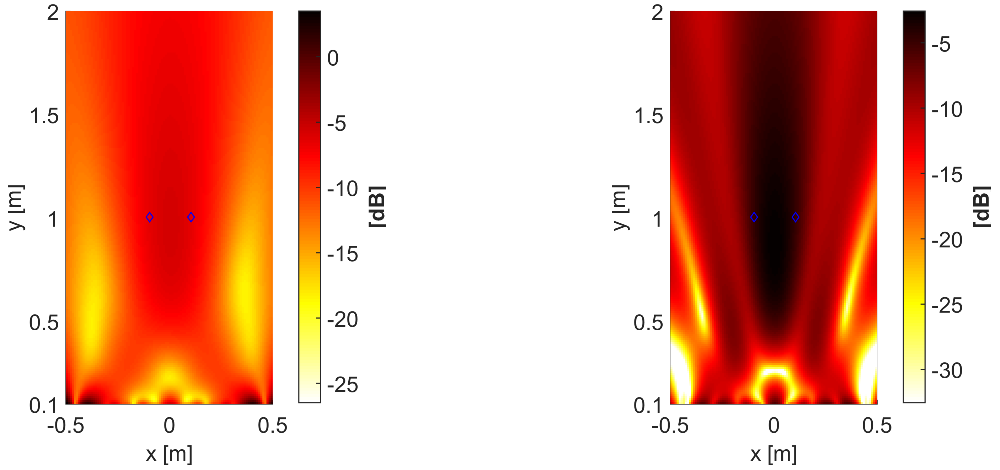

(a) $p = 2$ (b) $p = 2$ - $\mathbf{W}_0 = \mathrm{CB}$

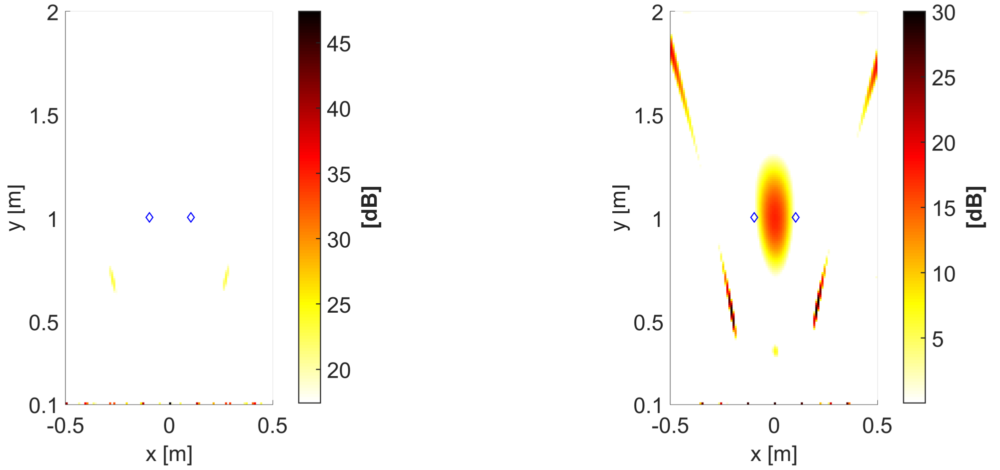

(c) $p = 1$ (d) $p = 1$ - $\mathbf{W}_0 = \mathrm{CB}$

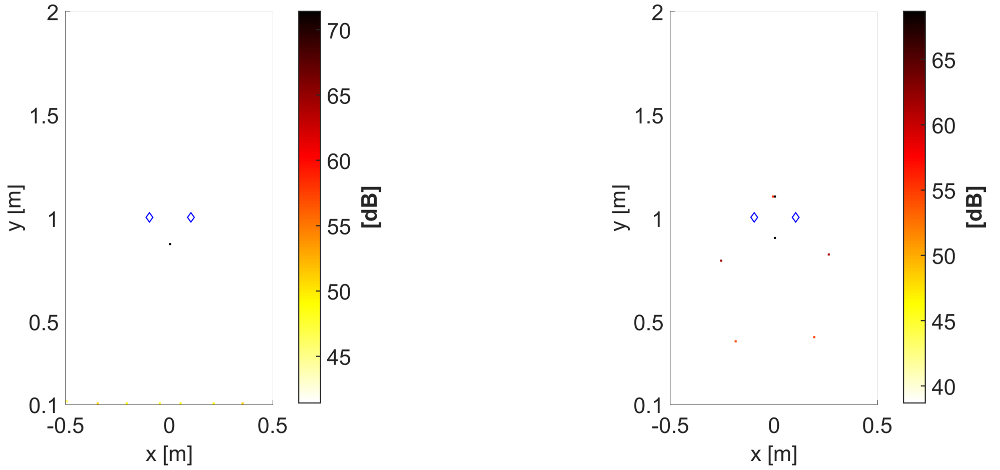

(e) $p = 0$ (f) $p = 0$ - $\mathbf{W}_0 = \mathrm{CB}$

Figure A.21: Test Case 2 (2D) at $He = 2$ - ESM-IRLS - CSCD

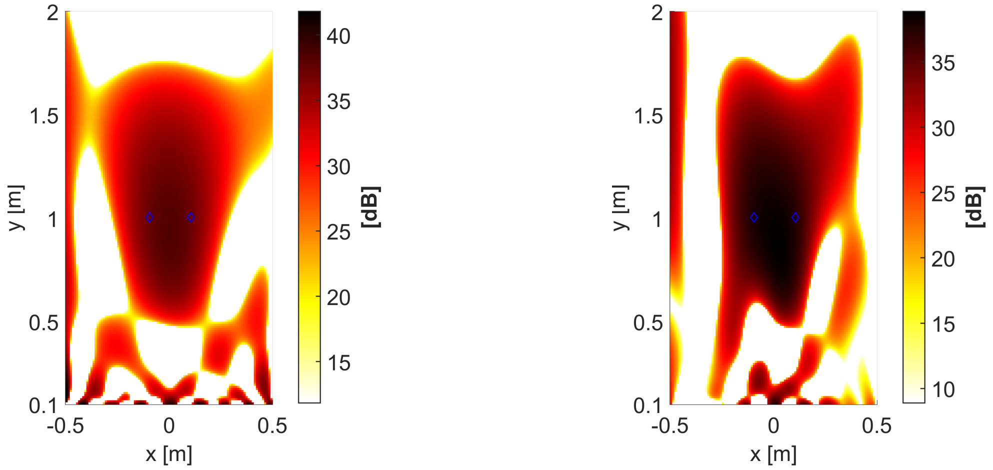

(a) $p = 2$

(b) $p = 2$ - $\mathbf{W}_0 = \text{CB}$

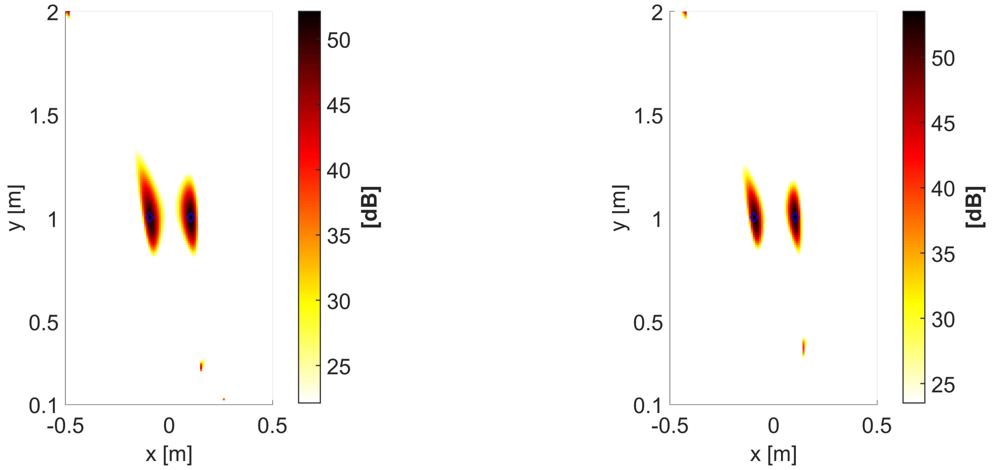

(c) $p = 1$

(d) $p = 1$ - $\mathbf{W}_0 = \text{CB}$

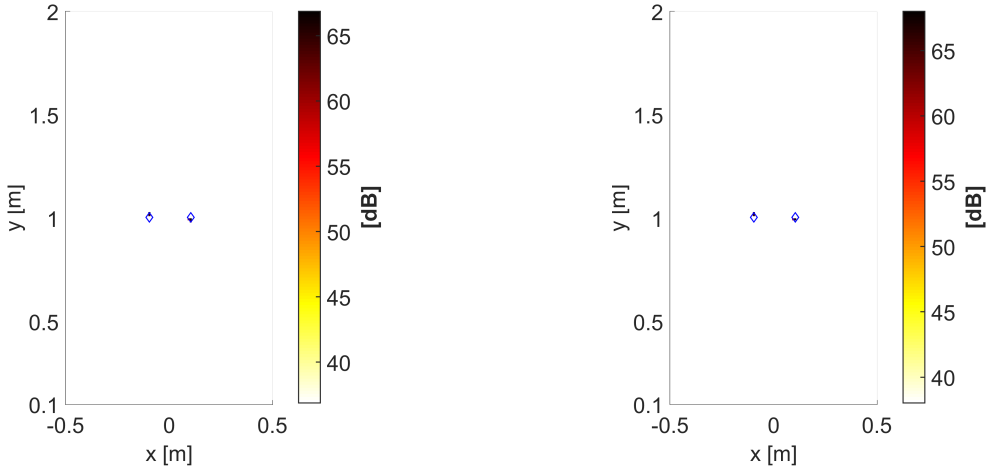

(e) $p = 0$

(f) $p = 0$ - $\mathbf{W}_0 = \text{CB}$

Figure A.22: Test Case 2 (2D) at $He = 2$ - CMF-IRLS on whole CSM

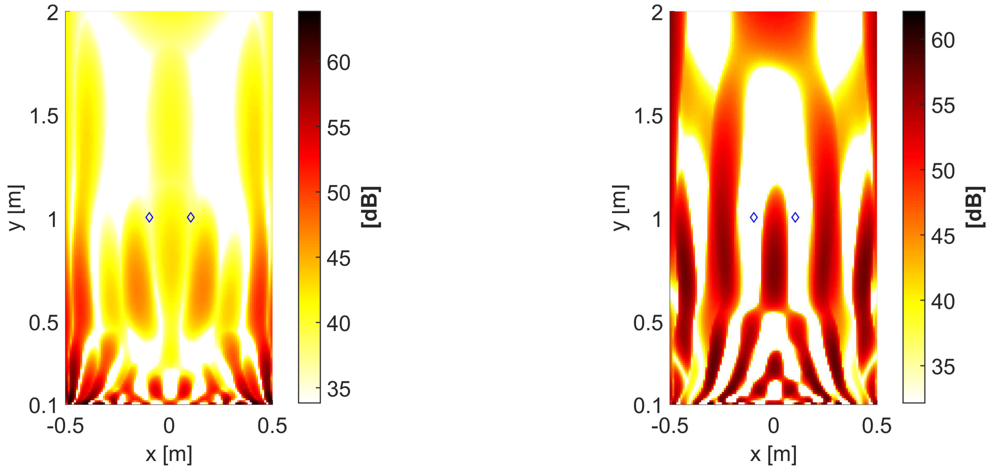

(a) $p = 2$

(b) $p = 2$ - $\mathbf{W}_0 = \text{CB}$

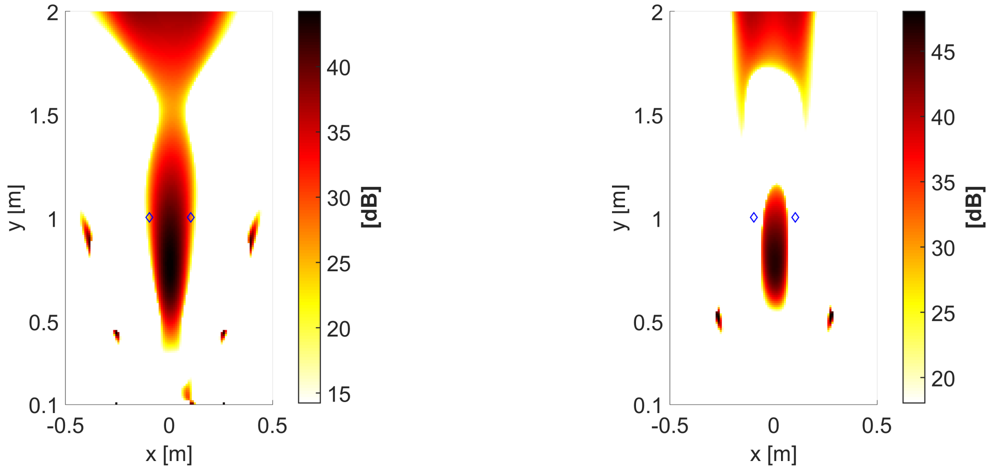

(c) $p = 1$

(d) $p = 1$ - $\mathbf{W}_0 = \text{CB}$

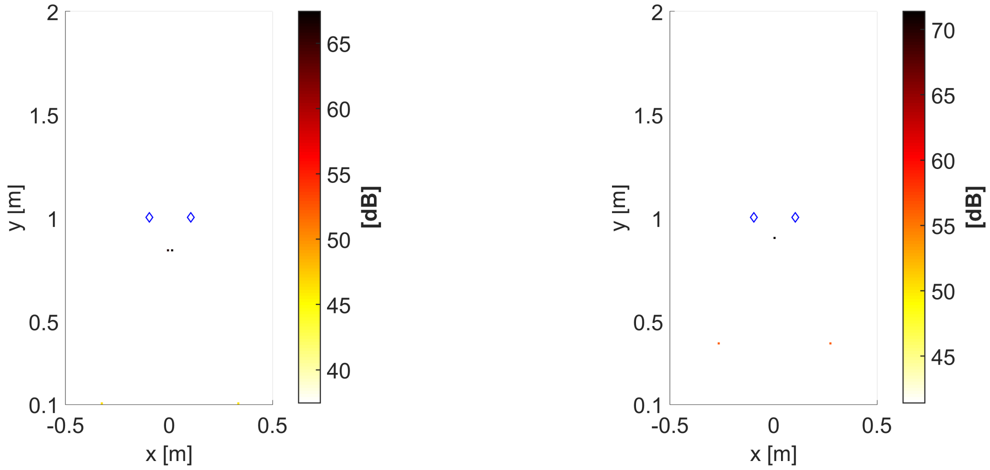

(e) $p = 0$

(f) $p = 0$ - $\mathbf{W}_0 = \text{CB}$

Figure A.23: Test Case 2 (2D) at $He = 2$ - CMF-IRLS - ED

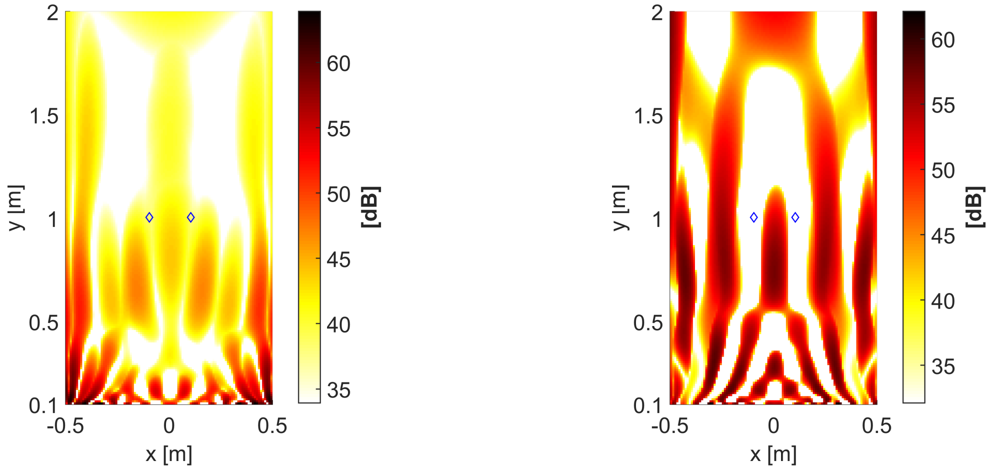

(a) $p = 2$ (b) $p = 2$ - $\mathbf{W}_0$ = CB

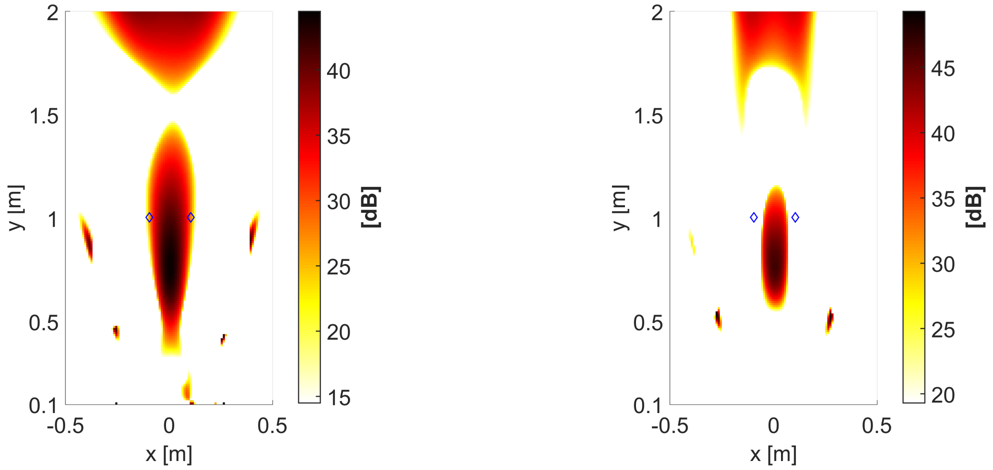

(c) $p = 1$ (d) $p = 1$ - $\mathbf{W}_0$ = CB

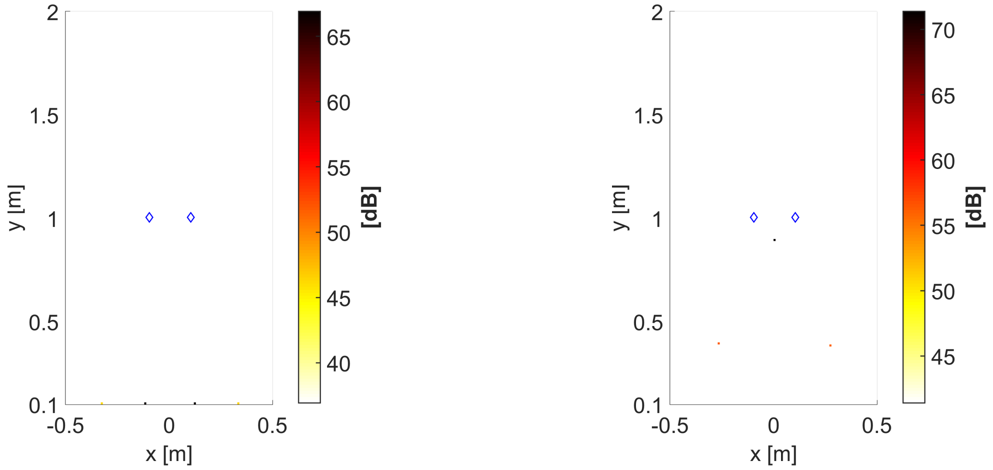

(e) $p = 0$ (f) $p = 0$ - $\mathbf{W}_0$ = CB

Figure A.24: Test Case 2 (2D) at $He = 2$ - CMF-IRLS - CSCD

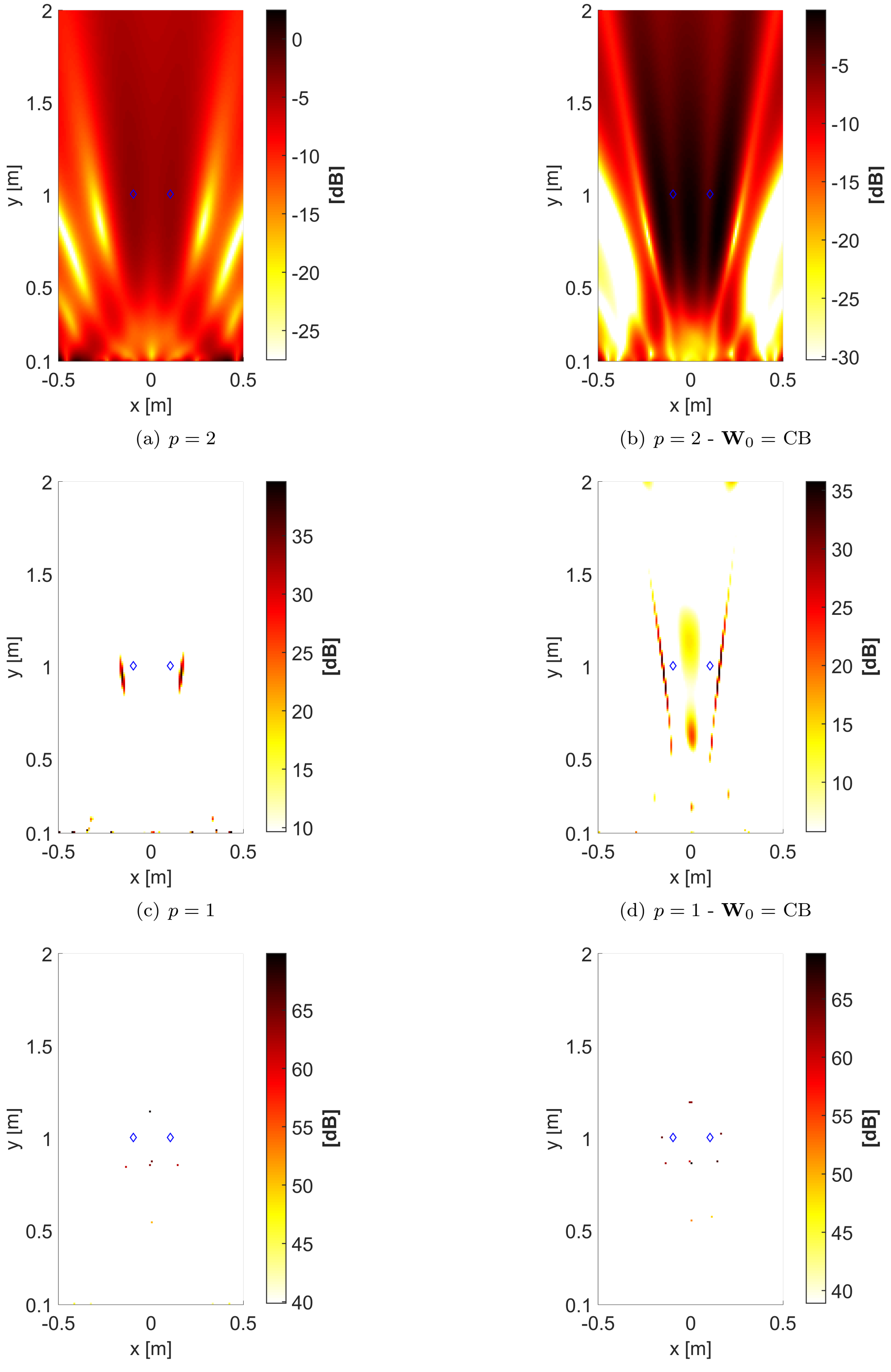

(a) $p = 2$

(b) $p = 2$ - $\mathbf{W}_0 = \mathrm{CB}$

(c) $p = 1$

(d) $p = 1$ - $\mathbf{W}_0 = \mathrm{CB}$

(e) $p = 0$

(f) $p = 0$ - $\mathbf{W}_0 = \mathrm{CB}$

Figure A.25: Test Case 2 (2D) at $He = 4$ - ESM-IRLS - ED

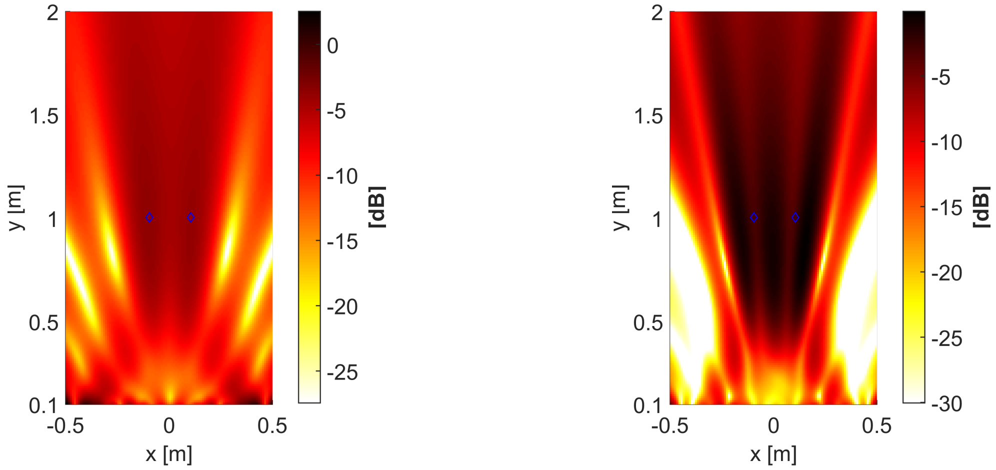

(a) $p = 2$

(b) $p = 2$ - $\mathbf{W}_0$ = CB

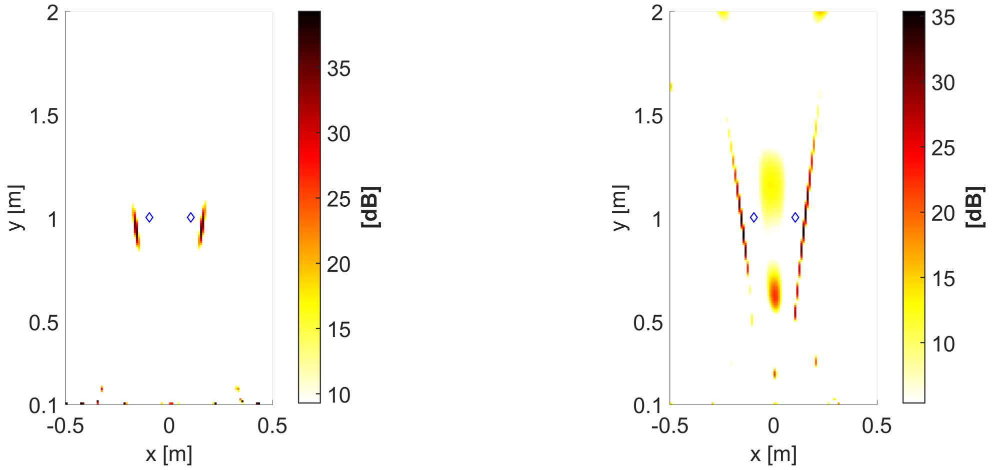

(c) $p = 1$

(d) $p = 1$ - $\mathbf{W}_0$ = CB

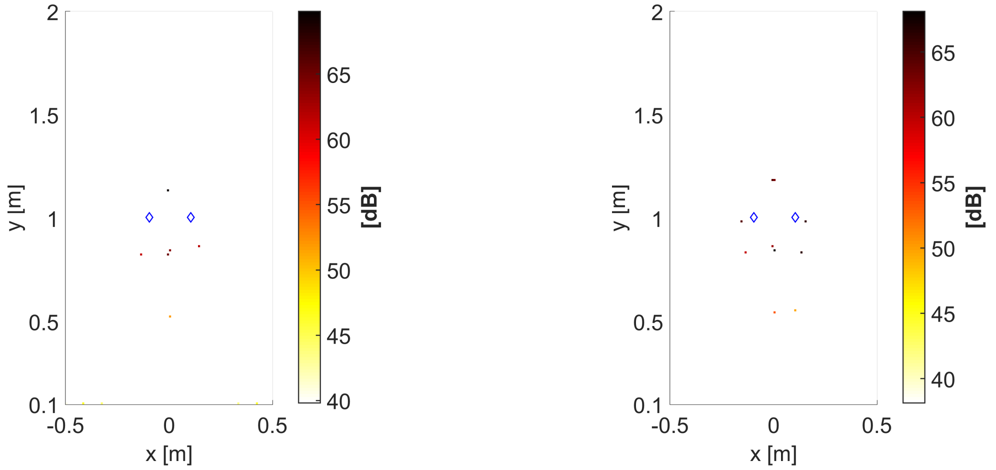

(e) $p = 0$

(f) $p = 0$ - $\mathbf{W}_0$ = CB

Figure A.26: Test Case 2 (2D) at $He = 4$ - ESM-IRLS - CSCD

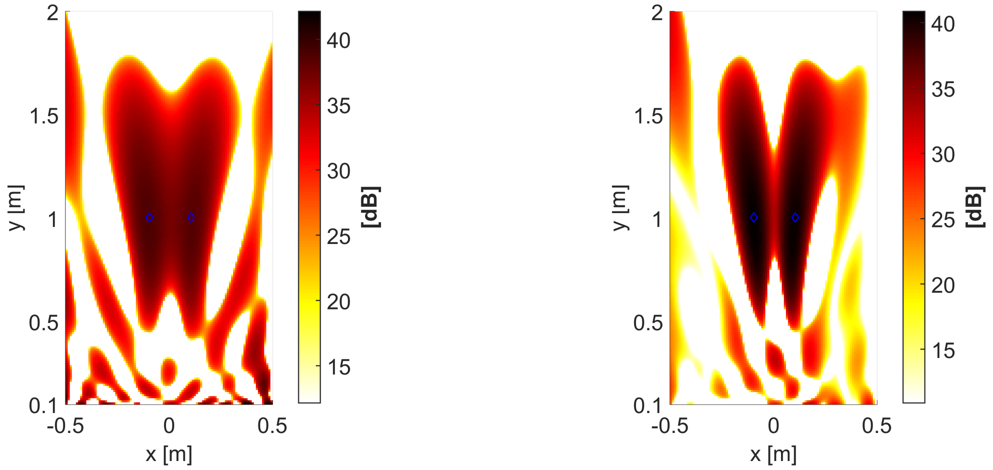

(a) $p = 2$ (b) $p = 2$ - $\mathbf{W}_0 = \mathrm{CB}$

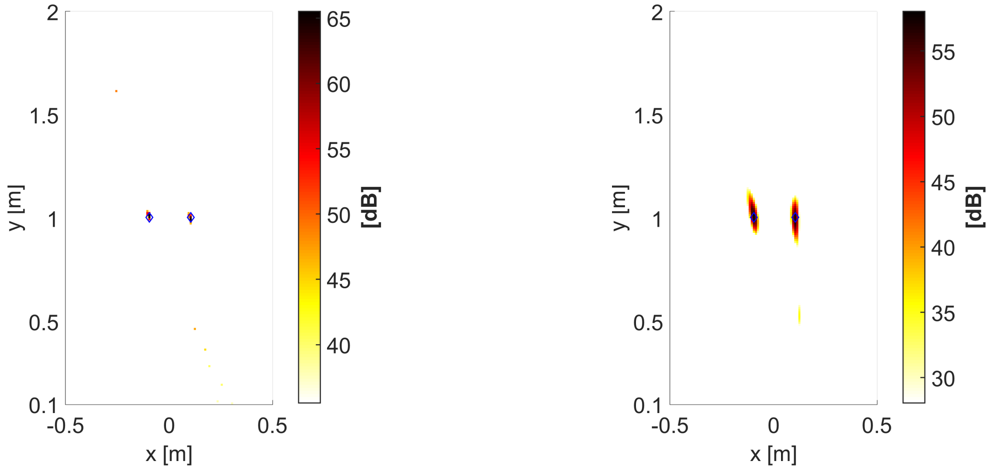

(c) $p = 1$ (d) $p = 1$ - $\mathbf{W}_0 = \mathrm{CB}$

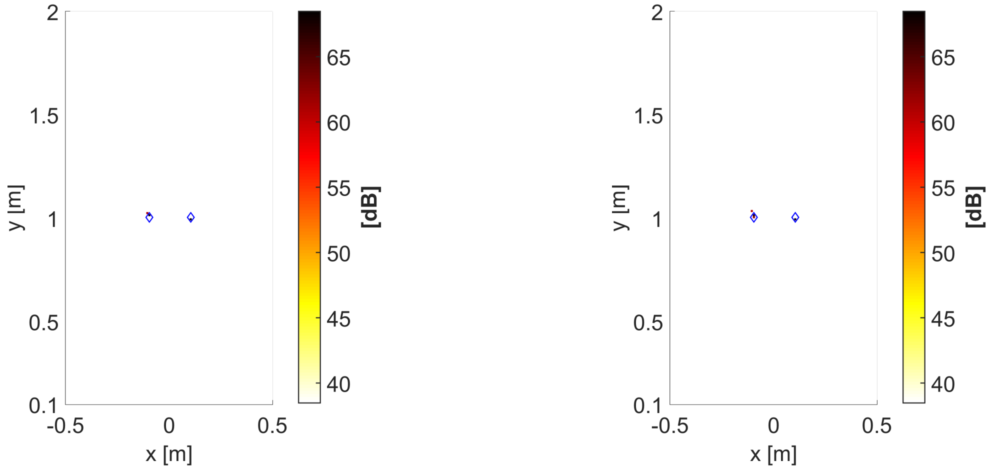

(e) $p = 0$ (f) $p = 0$ - $\mathbf{W}_0 = \mathrm{CB}$

Figure A.27: Test Case 2 (2D) at $He = 4$ - CMF-IRLS on whole CSM

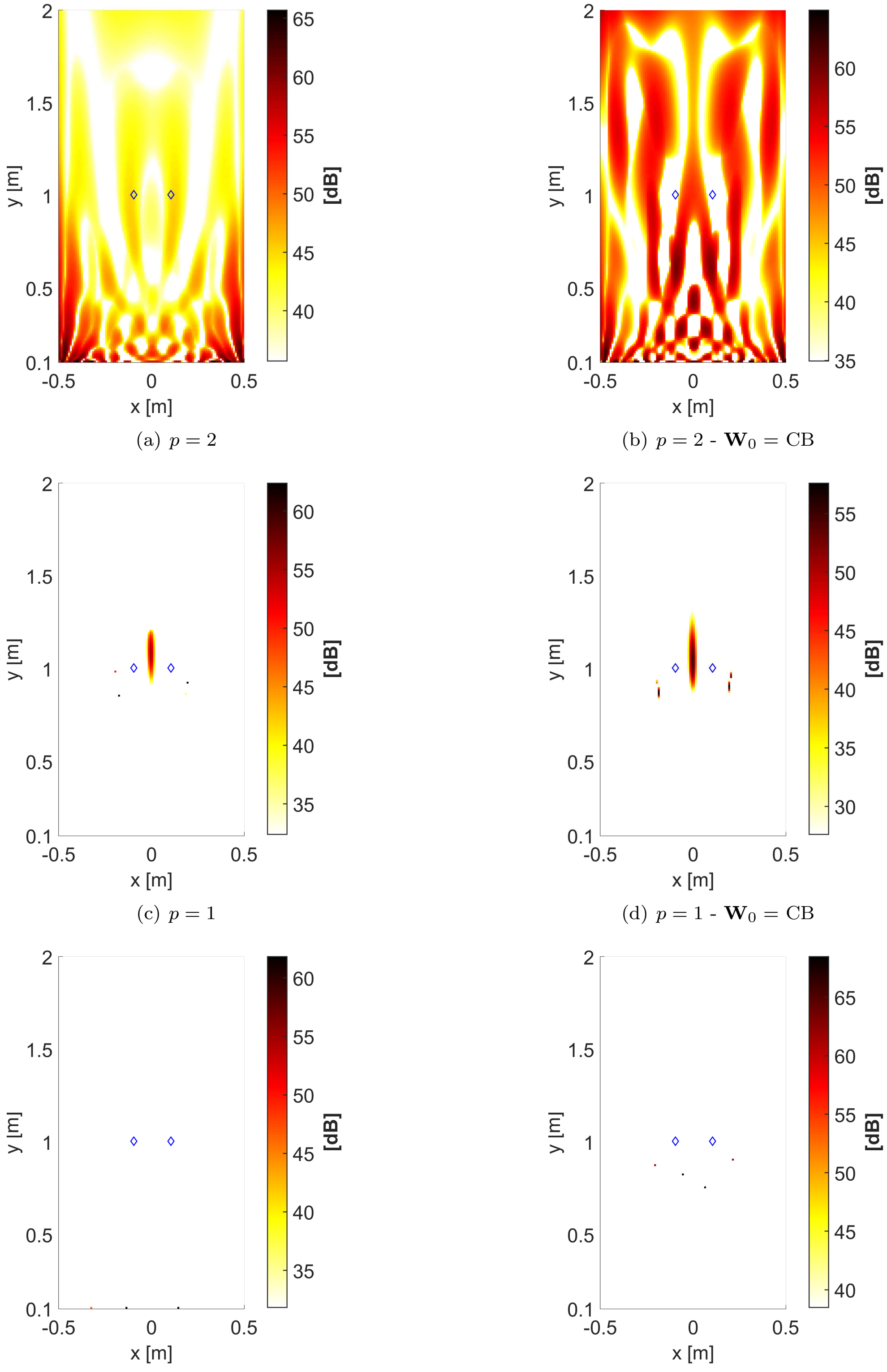

(a) $p = 2$

(b) $p = 2$ - $\mathbf{W}_0 = \mathrm{CB}$

(c) $p = 1$

(d) $p = 1$ - $\mathbf{W}_0 = \mathrm{CB}$

(e) $p = 0$

(f) $p = 0$ - $\mathbf{W}_0 = \mathrm{CB}$

Figure A.28: Test Case 2 (2D) at $He = 4$ - CMF-IRLS - ED

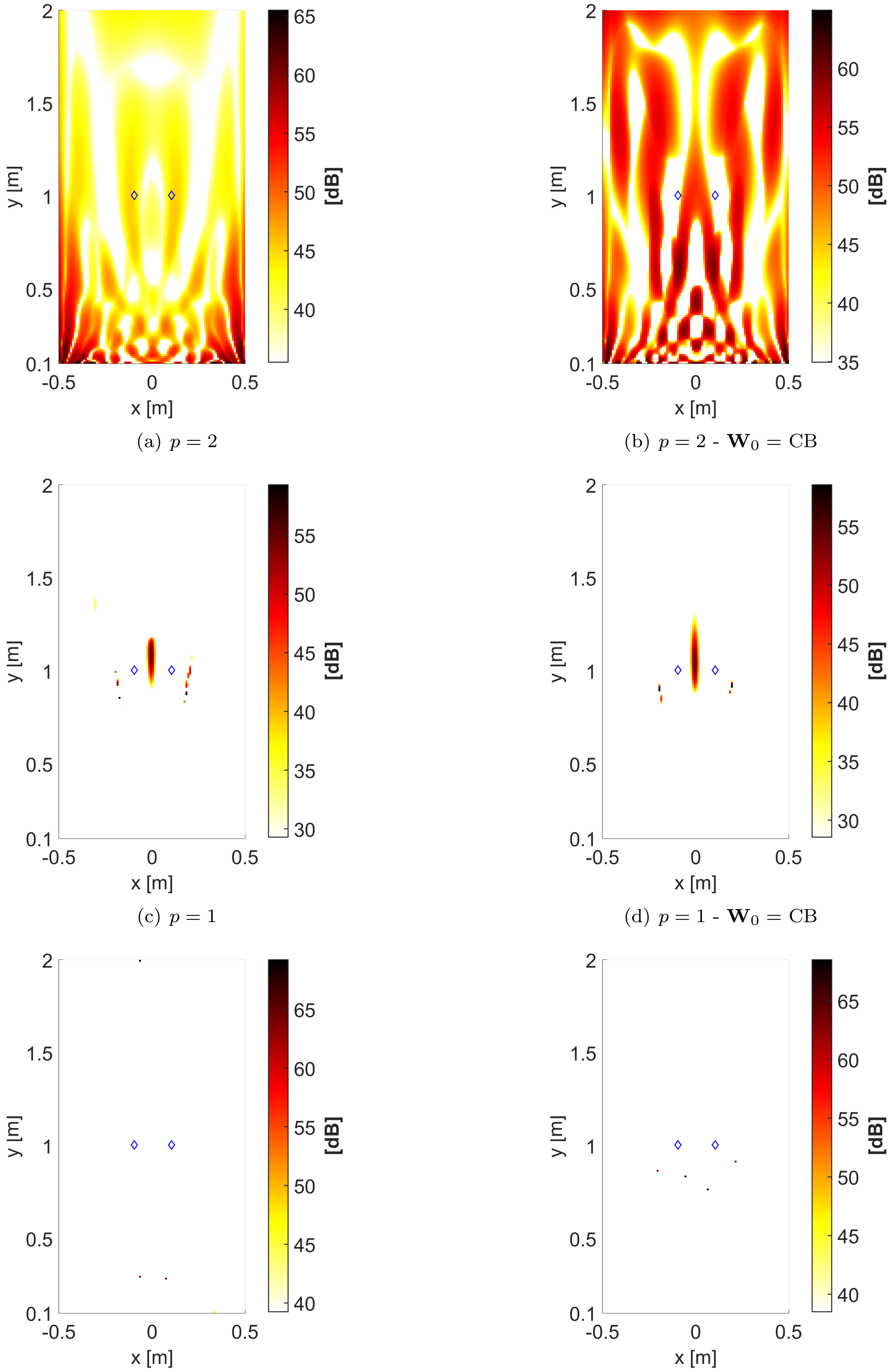

(a) $p = 2$

(b) $p = 2$ - $\mathbf{W}_0 = \mathrm{CB}$

(c) $p = 1$

(d) $p = 1$ - $\mathbf{W}_0 = \mathrm{CB}$

(e) $p = 0$

(f) $p = 0$ - $\mathbf{W}_0 = \mathrm{CB}$

Figure A.29: Test Case 2 (2D) at $He = 4$ - CMF-IRLS - CSCD

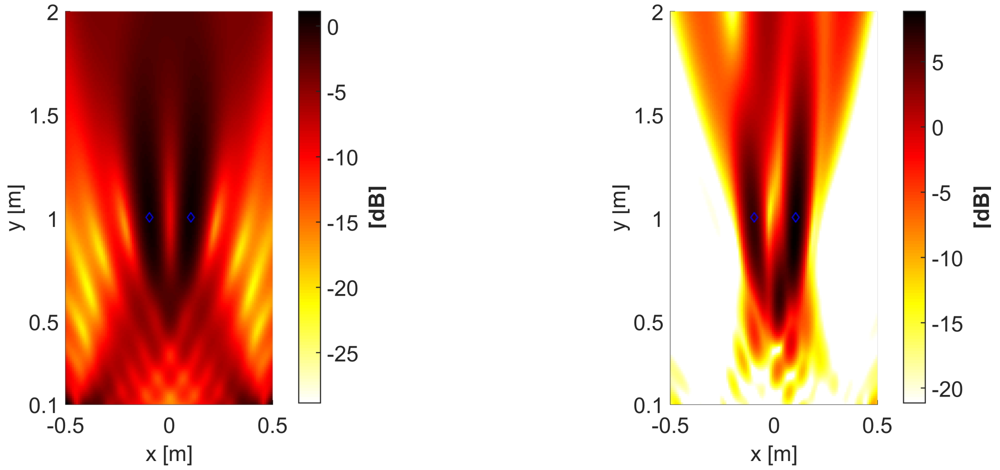

(a) $p = 2$ (b) $p = 2$ - $\mathbf{W}_0 = \text{CB}$

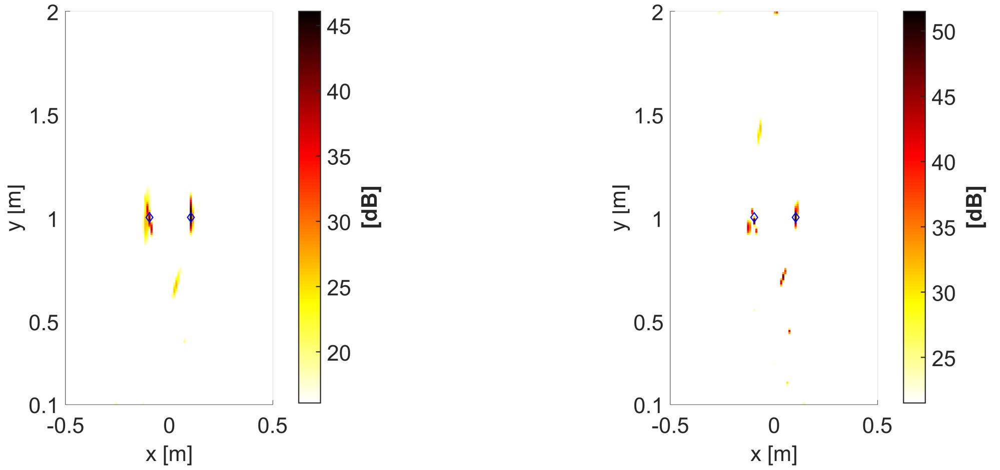

(c) $p = 1$ (d) $p = 1$ - $\mathbf{W}_0 = \text{CB}$

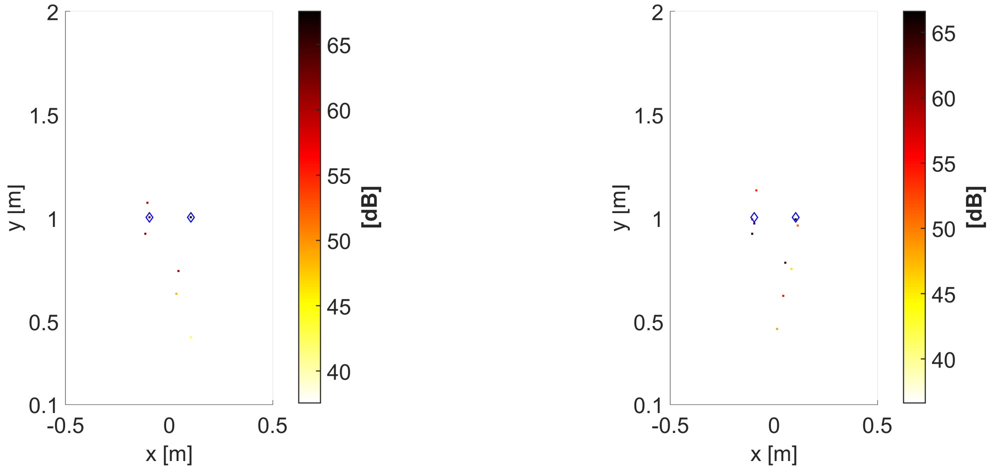

(e) $p = 0$ (f) $p = 0$ - $\mathbf{W}_0 = \text{CB}$

Figure A.30: Test Case 2 (2D) at $He = 8$ - ESM-IRLS - ED

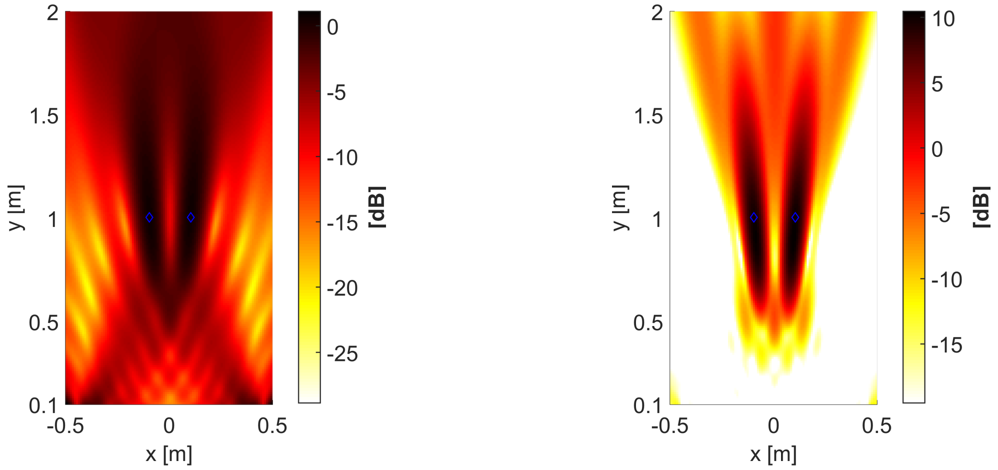

(a) $p = 2$ (b) $p = 2$ - $\mathbf{W}_0 = \mathrm{CB}$

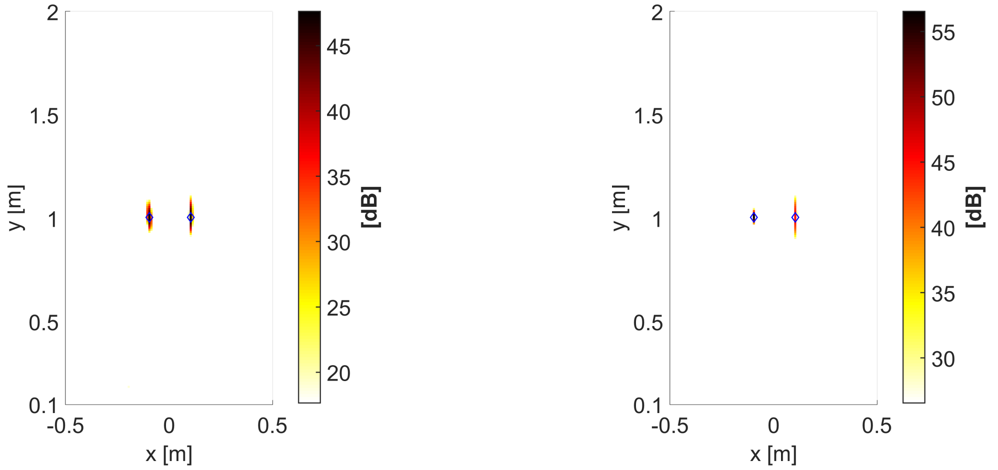

(c) $p = 1$ (d) $p = 1$ - $\mathbf{W}_0 = \mathrm{CB}$

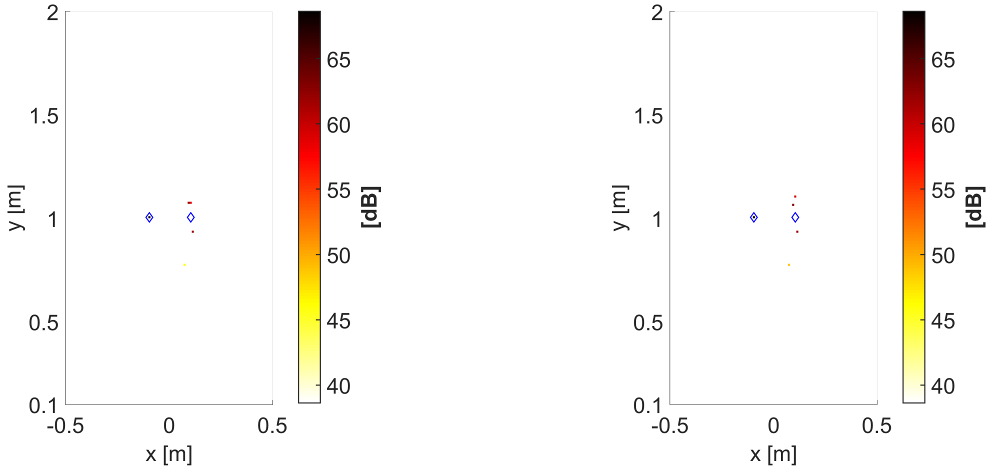

(e) $p = 0$ (f) $p = 0$ - $\mathbf{W}_0 = \mathrm{CB}$

Figure A.31: Test Case 2 (2D) at $He = 8$ - ESM-IRLS - CSCD

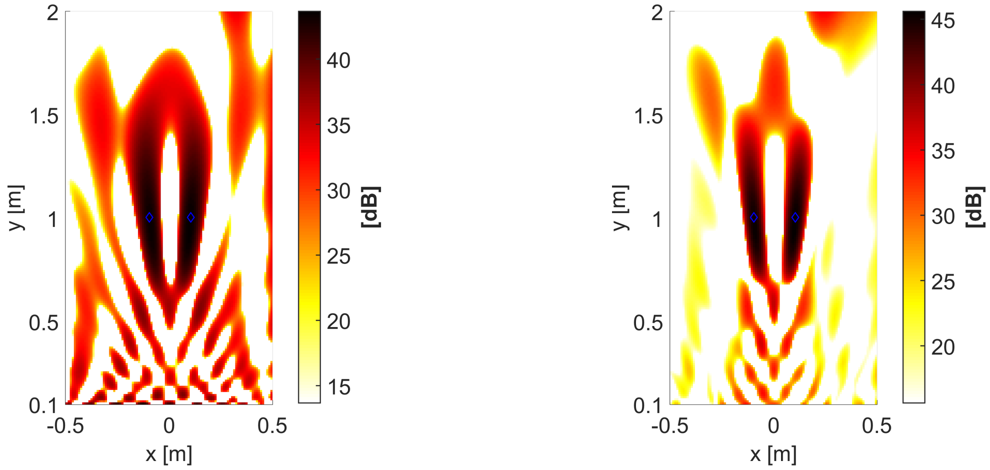

(a) $p = 2$ (b) $p = 2$ - $\mathbf{W}_0 = \mathrm{CB}$

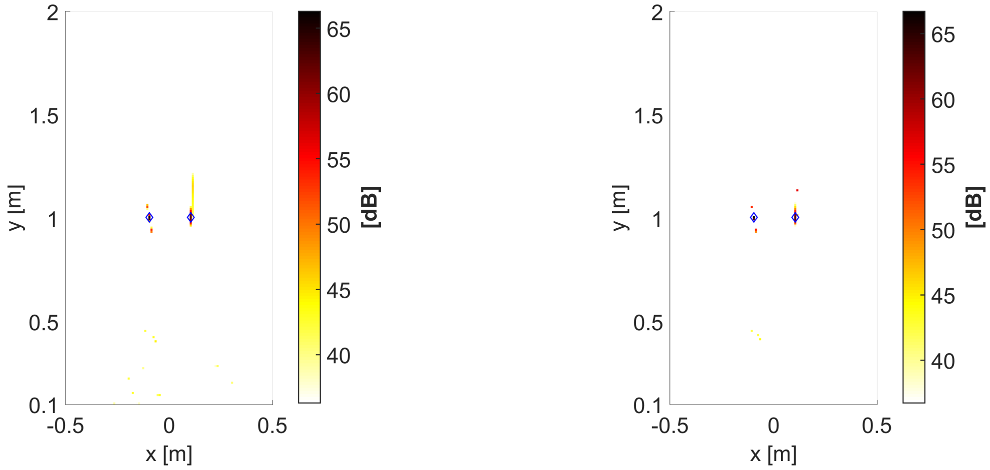

(c) $p = 1$ (d) $p = 1$ - $\mathbf{W}_0 = \mathrm{CB}$

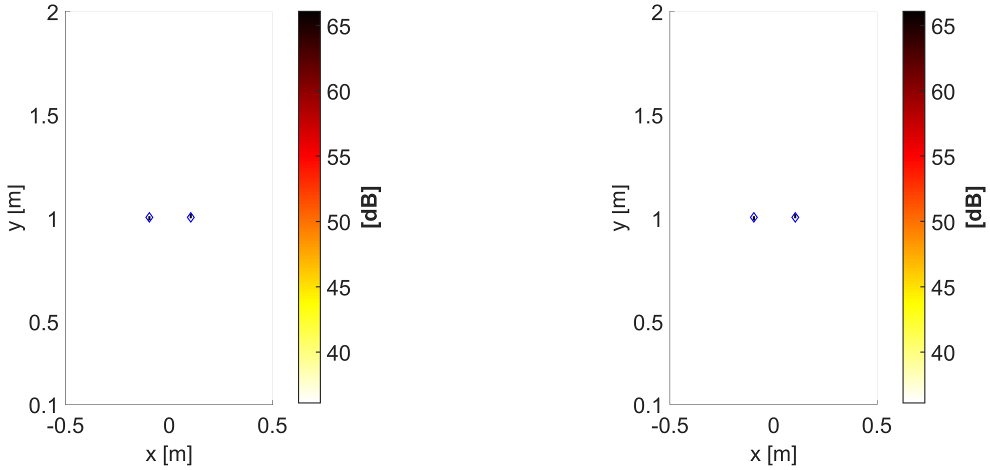

(e) $p = 0$ (f) $p = 0$ - $\mathbf{W}_0 = \mathrm{CB}$

Figure A.32: Test Case 2 (2D) at $He = 8$ - CMF-IRLS on whole CSM

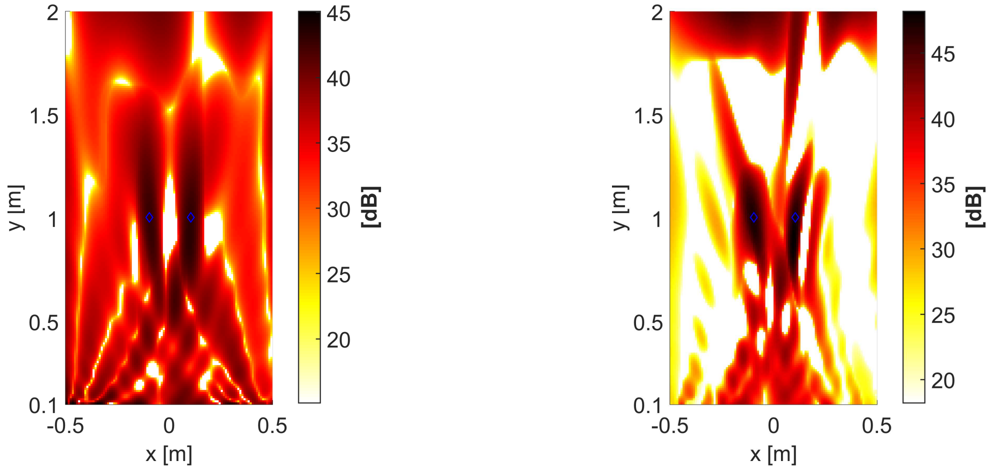

(a) $p = 2$ (b) $p = 2$ - $\mathbf{W}_0 = \mathrm{CB}$

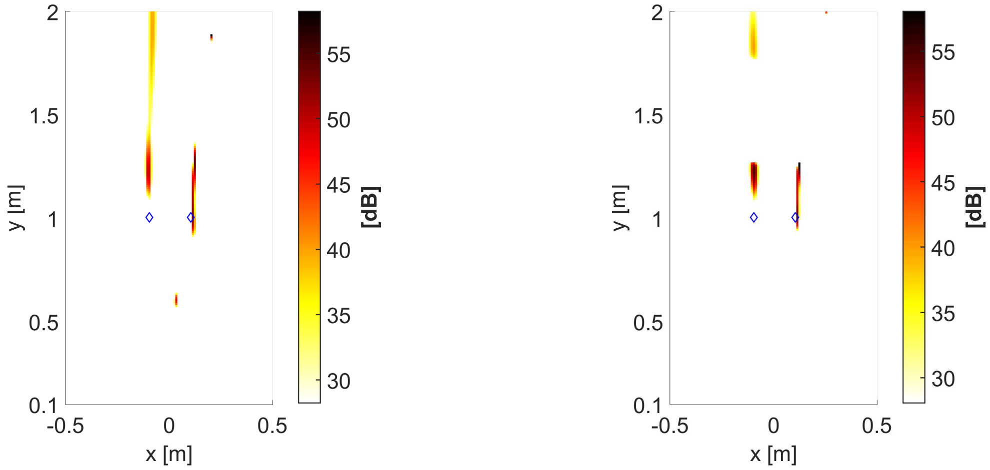

(c) $p = 1$ (d) $p = 1$ - $\mathbf{W}_0 = \mathrm{CB}$

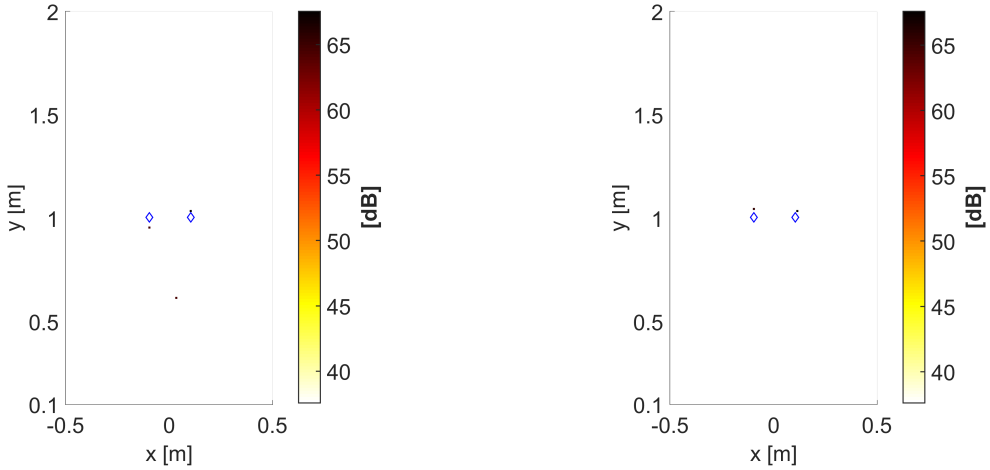

(e) $p = 0$ (f) $p = 0$ - $\mathbf{W}_0 = \mathrm{CB}$

Figure A.33: Test Case 2 (2D) at $He = 8$ - CMF-IRLS - ED

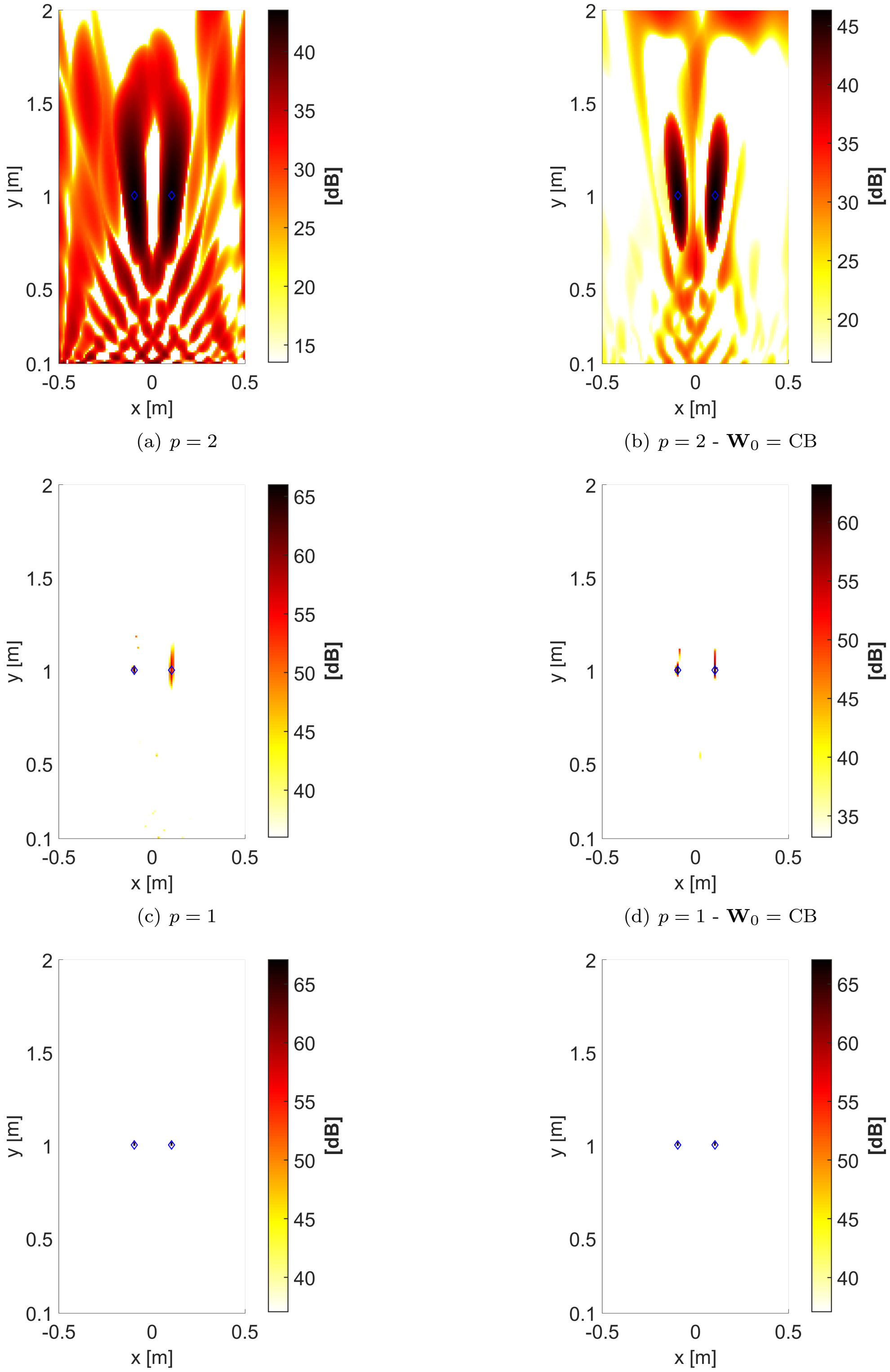

(a) $p = 2$

(b) $p = 2$ - $\mathbf{W}_0 = \mathrm{CB}$

(c) $p = 1$

(d) $p = 1$ - $\mathbf{W}_0 = \mathrm{CB}$

(e) $p = 0$

(f) $p = 0$ - $\mathbf{W}_0 = \mathrm{CB}$

Figure A.34: Test Case 2 (2D) at $He = 8$ - CMF-IRLS - CSCD

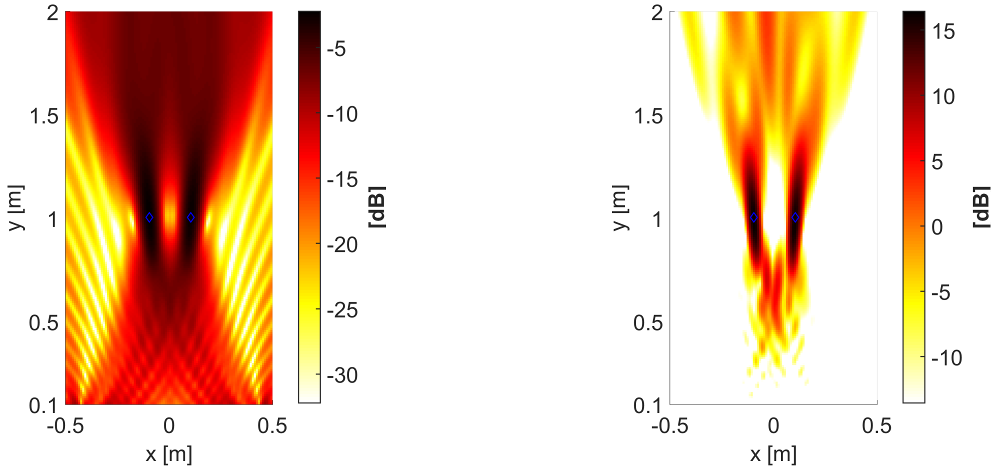

(a) $p = 2$ (b) $p = 2$ - $\mathbf{W}_0 = \text{CB}$

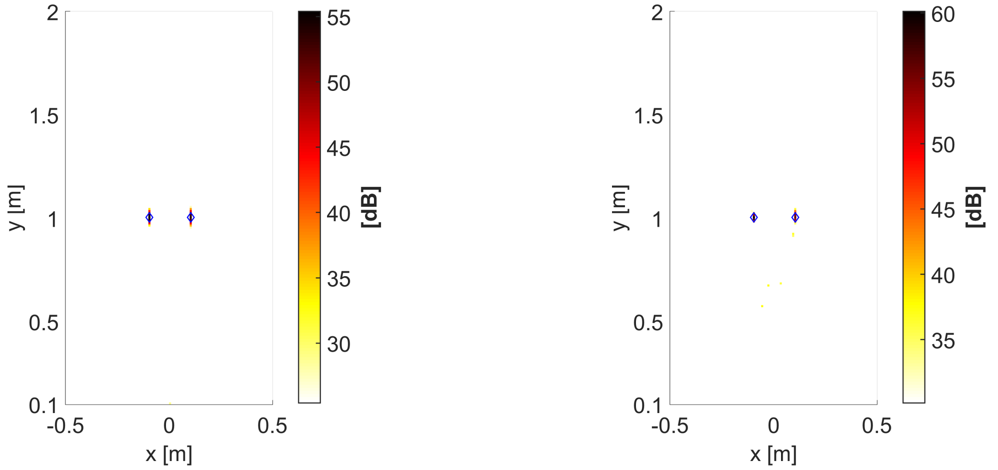

(c) $p = 1$ (d) $p = 1$ - $\mathbf{W}_0 = \text{CB}$

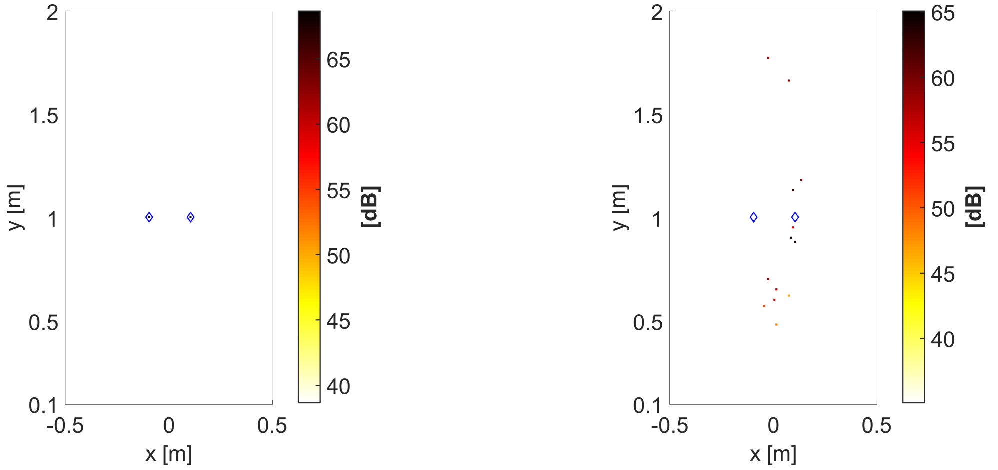

(e) $p = 0$ (f) $p = 0$ - $\mathbf{W}_0 = \text{CB}$

Figure A.35: Test Case 2 (2D) at $He = 16$ - ESM-IRLS - ED

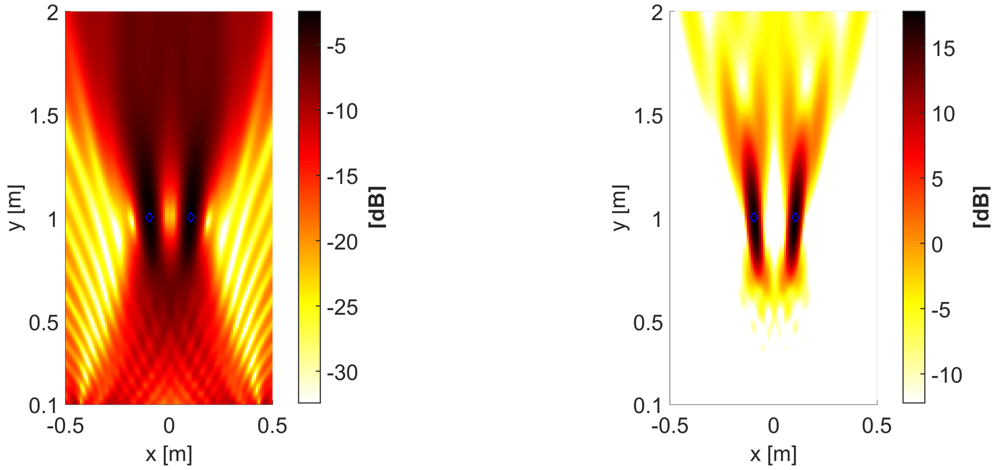

(a) $p = 2$ (b) $p = 2$ - $\mathbf{W}_0 = \text{CB}$

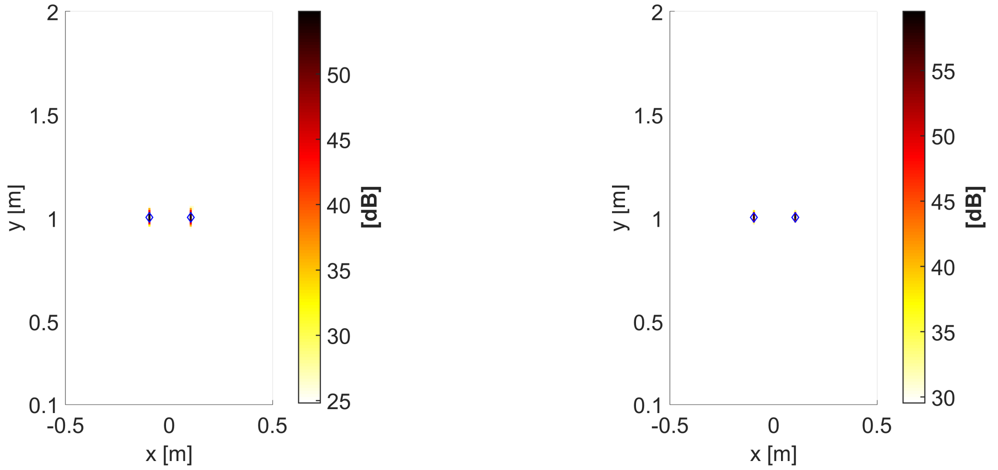

(c) $p = 1$ (d) $p = 1$ - $\mathbf{W}_0 = \text{CB}$

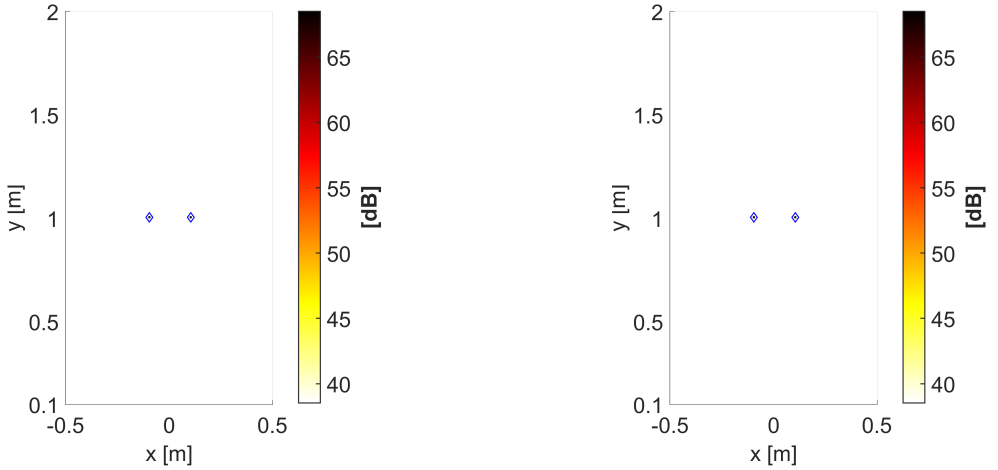

(e) $p = 0$ (f) $p = 0$ - $\mathbf{W}_0 = \text{CB}$

Figure A.36: Test Case 2 (2D) at $He = 16$ - ESM-IRLS - CSCD

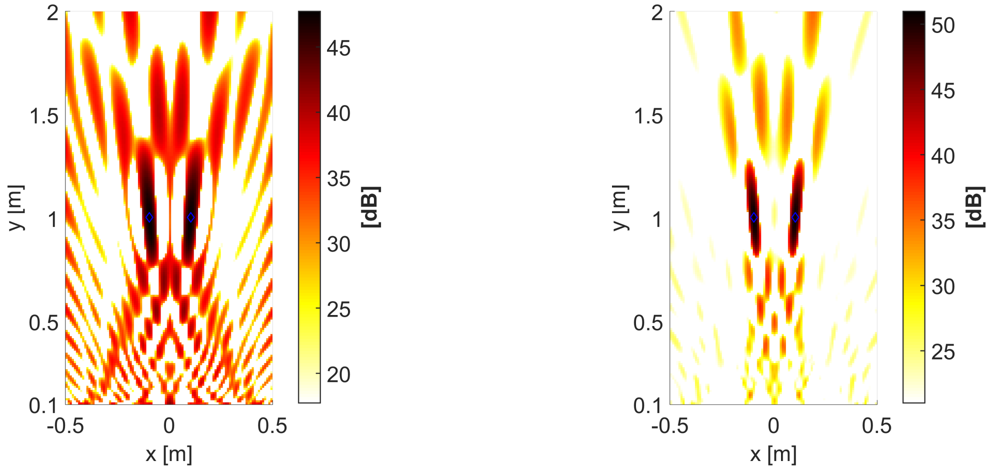

(a) $p = 2$ (b) $p = 2$ - $\mathbf{W}_0$ = CB

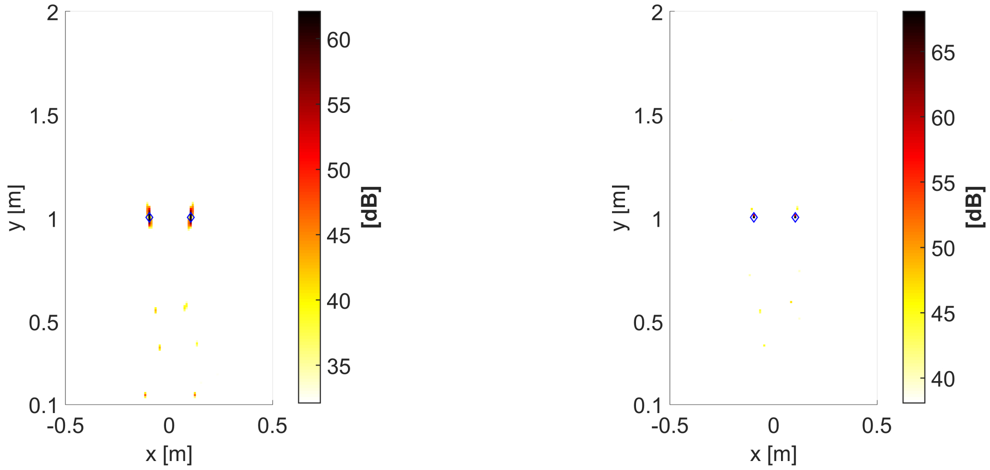

(c) $p = 1$ (d) $p = 1$ - $\mathbf{W}_0$ = CB

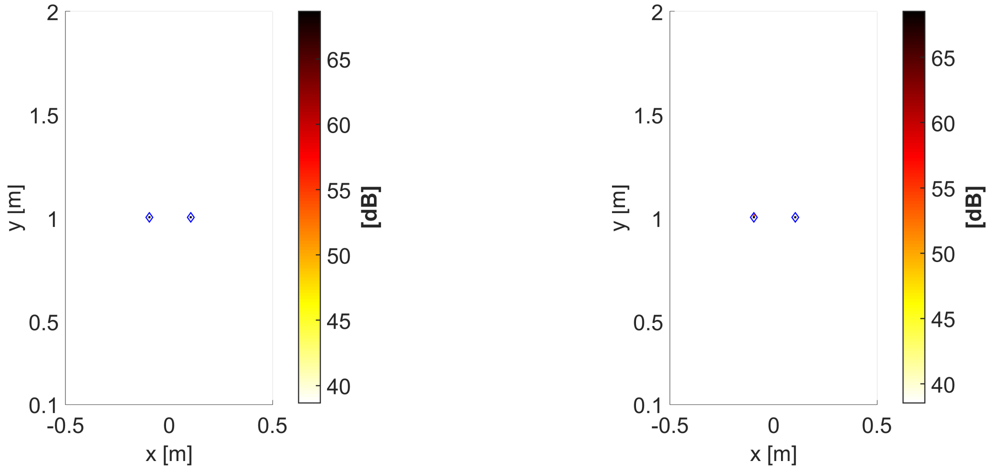

(e) $p = 0$ (f) $p = 0$ - $\mathbf{W}_0$ = CB

Figure A.37: Test Case 2 (2D) at $He = 16$ - CMF-IRLS on whole CSM

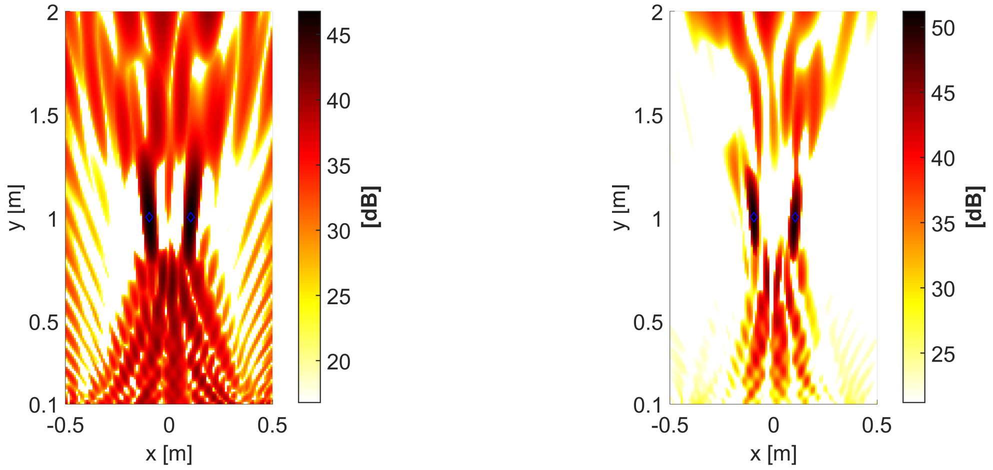

(a) $p = 2$ (b) $p = 2$ - $\mathbf{W}_0 = \mathrm{CB}$

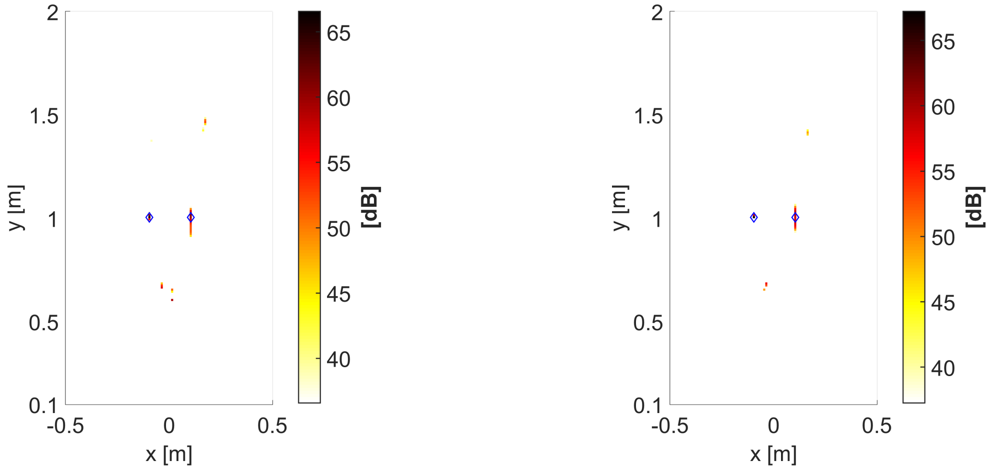

(c) $p = 1$ (d) $p = 1$ - $\mathbf{W}_0 = \mathrm{CB}$

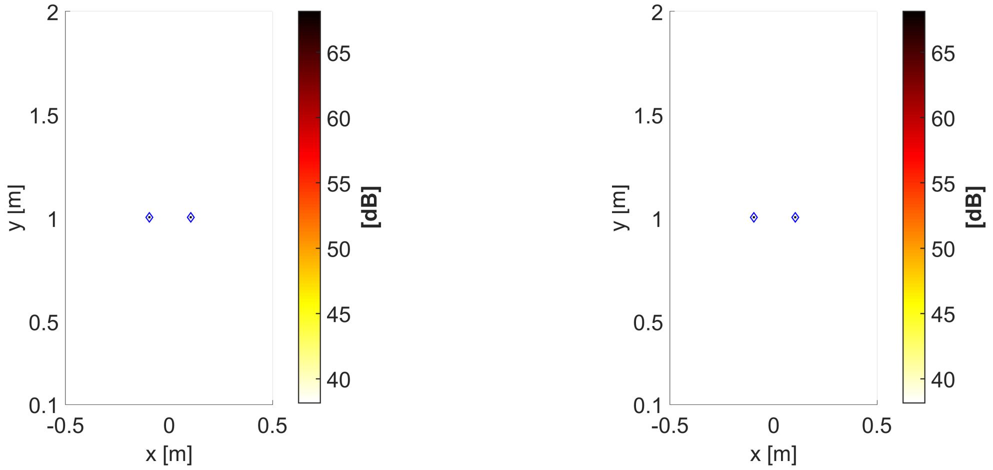

(e) $p = 0$ (f) $p = 0$ - $\mathbf{W}_0 = \mathrm{CB}$

Figure A.38: Test Case 2 (2D) at $He = 16$ - CMF-IRLS - ED

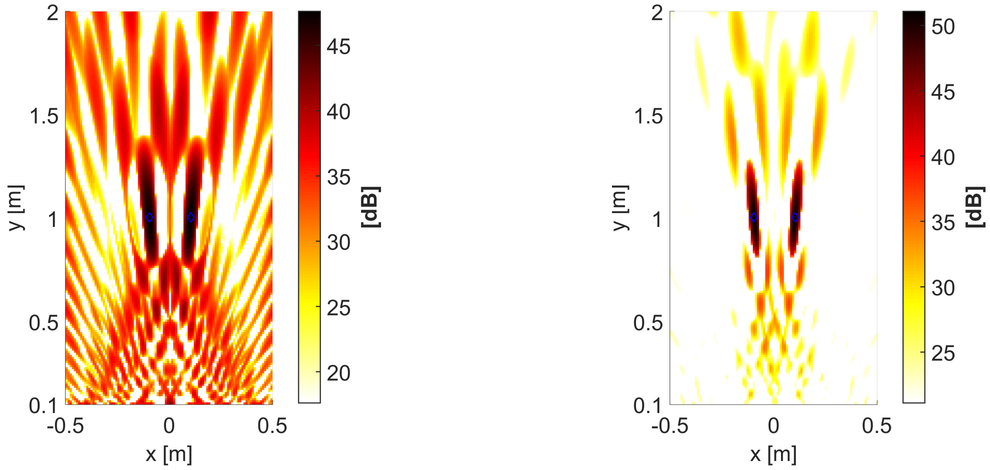

(a) $p = 2$ (b) $p = 2$ - $\mathbf{W}_0 = \text{CB}$

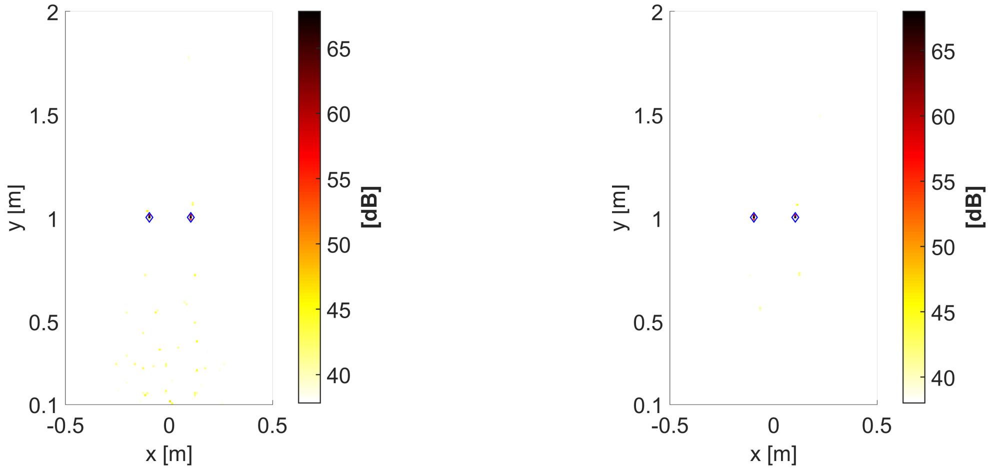

(c) $p = 1$ (d) $p = 1$ - $\mathbf{W}_0 = \text{CB}$

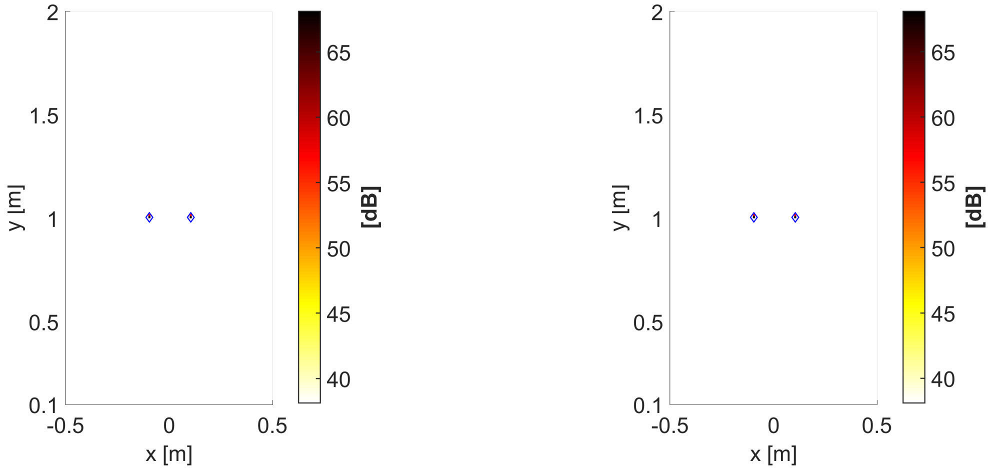

(e) $p = 0$ (f) $p = 0$ - $\mathbf{W}_0 = \text{CB}$

Figure A.39: Test Case 2 (2D) at $He = 16$ - CMF-IRLS - CSCD

A.2.1 Reconstructed source spectra of Test Case 2

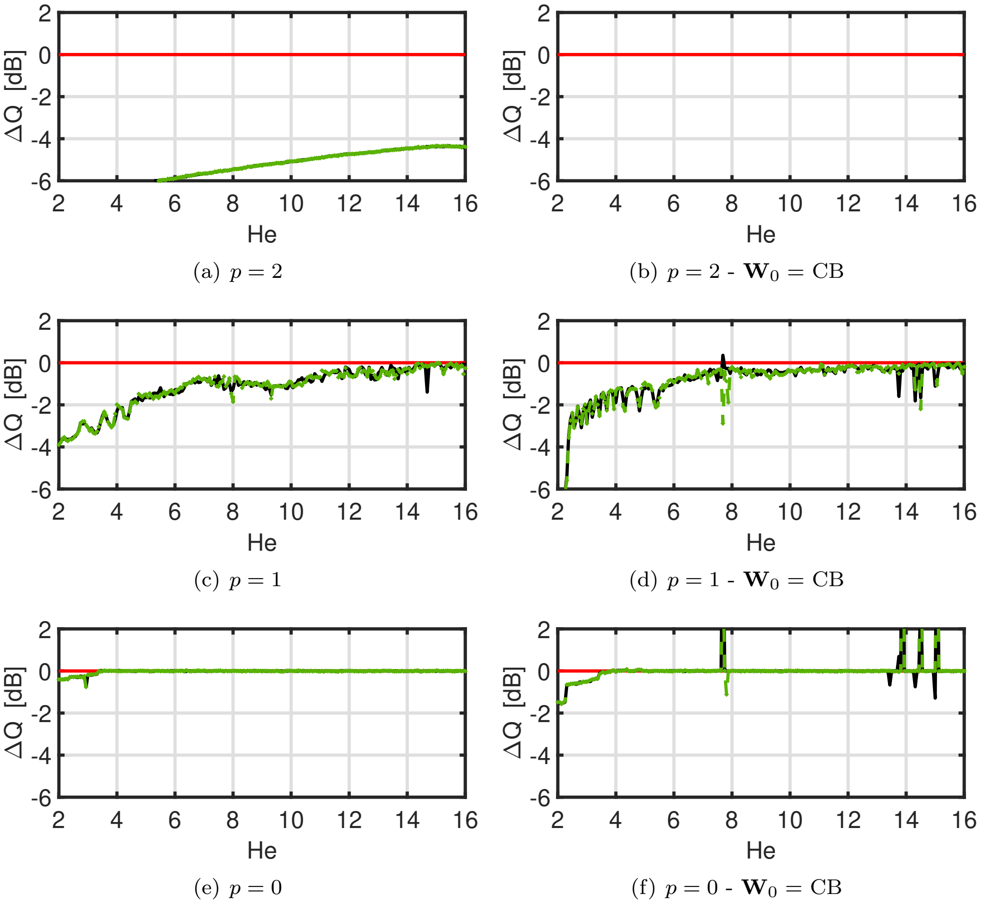

(a) $p = 2$

(b) $p = 2$ - $\mathbf{W}_0$ = CB

(c) $p = 1$

(d) $p = 1$ - $\mathbf{W}_0$ = CB

(e) $p = 0$

(f) $p = 0$ - $\mathbf{W}_0$ = CB

Figure A.40: Test Case 2 (1D) - Errors in source spectrum reconstruction with ESM-IRLS with ED. Red line: target error. Black line: error of reconstructed spectrum (left source). Green line: error of reconstructed spectrum (right source).

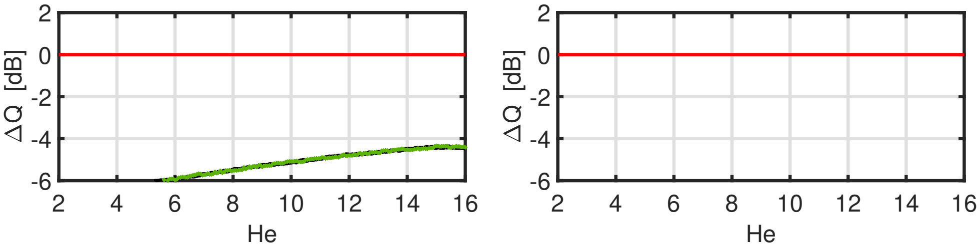

(a) $p = 2$ (b) $p = 2$ - $\mathbf{W}_0 = \mathrm{CB}$

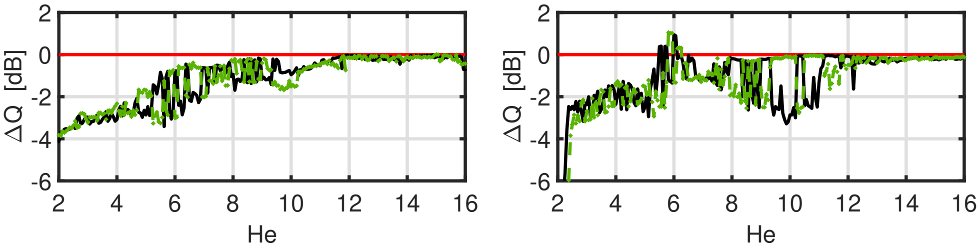

(c) $p = 1$ (d) $p = 1$ - $\mathbf{W}_0 = \mathrm{CB}$

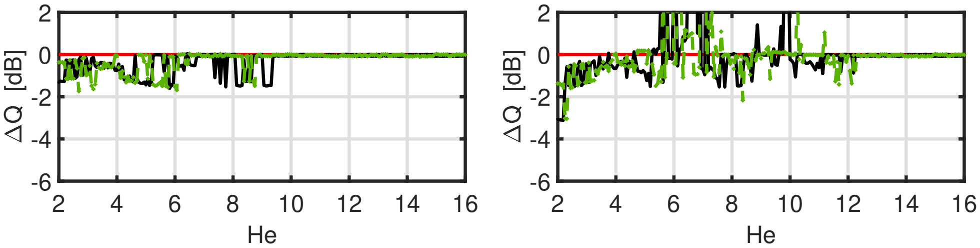

(e) $p = 0$ (f) $p = 0$ - $\mathbf{W}_0 = \mathrm{CB}$

Figure A.41: Test Case 2 (1D) - Errors in source spectrum reconstruction with ESM-IRLS with CSCD. Red line: target error. Black line: error of reconstructed spectrum (left source). Green line: error of reconstructed spectrum (right source).

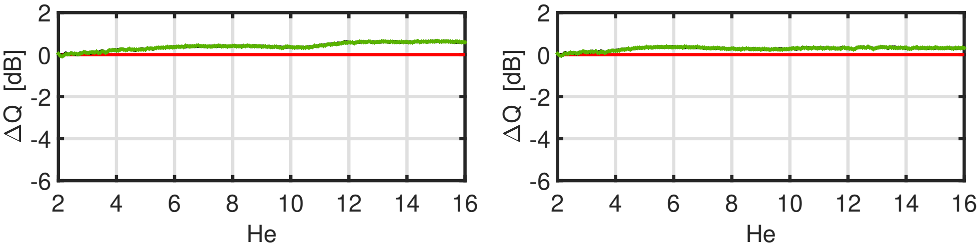

(a) $p = 2$ (b) $p = 2$ - $\mathbf{W}_0 = \mathrm{CB}$

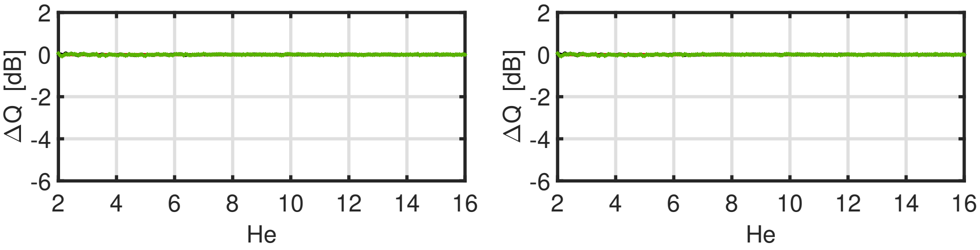

(c) $p = 1$ (d) $p = 1$ - $\mathbf{W}_0 = \mathrm{CB}$

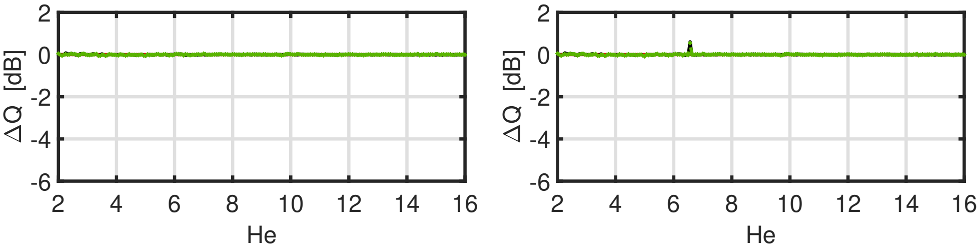

(e) $p = 0$ (f) $p = 0$ - $\mathbf{W}_0 = \mathrm{CB}$

Figure A.42: Test Case 2 (1D) - Errors in source spectrum reconstruction with CMF-IRLS on whole CSM. Red line: target error. Black line: error of reconstructed spectrum (left source). Green line: error of reconstructed spectrum (right source).

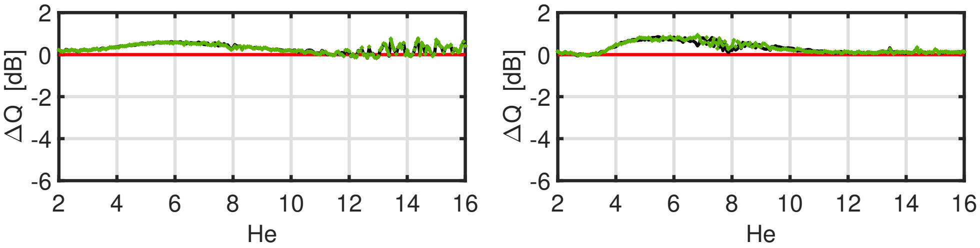

(a) $p = 2$ (b) $p = 2$ - $\mathbf{W}_0 = \mathrm{CB}$

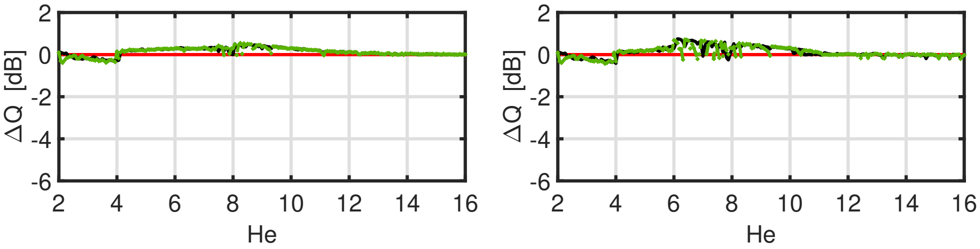

(c) $p = 1$ (d) $p = 1$ - $\mathbf{W}_0 = \mathrm{CB}$

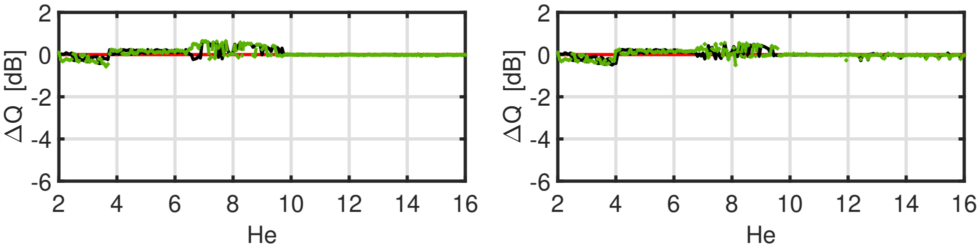

(e) $p = 0$ (f) $p = 0$ - $\mathbf{W}_0 = \mathrm{CB}$

Figure A.43: Test Case 2 (1D) - Errors in source spectrum reconstruction with CMF-IRLS with ED. Red line: target error. Black line: error of reconstructed spectrum (left source). Green line: error of reconstructed spectrum (right source).

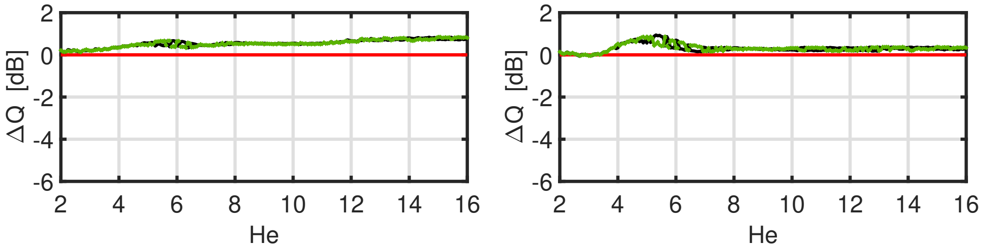

(a) $p = 2$ (b) $p = 2$ - $\mathbf{W}_0 = \mathrm{CB}$

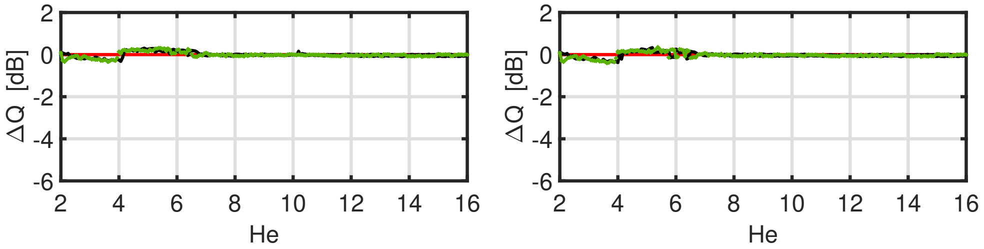

(c) $p = 1$ (d) $p = 1$ - $\mathbf{W}_0 = \mathrm{CB}$

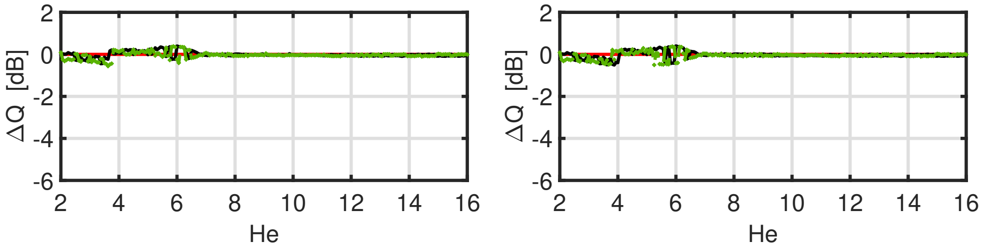

(e) $p = 0$ (f) $p = 0$ - $\mathbf{W}_0 = \mathrm{CB}$

Figure A.44: Test Case 2 (1D) - Errors in source spectrum reconstruction with CMF-IRLS with CSCD. Red line: target error. Black line: error of reconstructed spectrum (left source). Green line: error of reconstructed spectrum (right source).

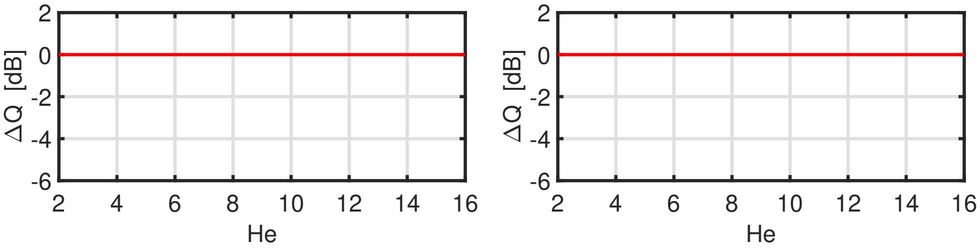

(a) $p = 2$ (b) $p = 2$ - $\mathbf{W}_0 = \mathrm{CB}$

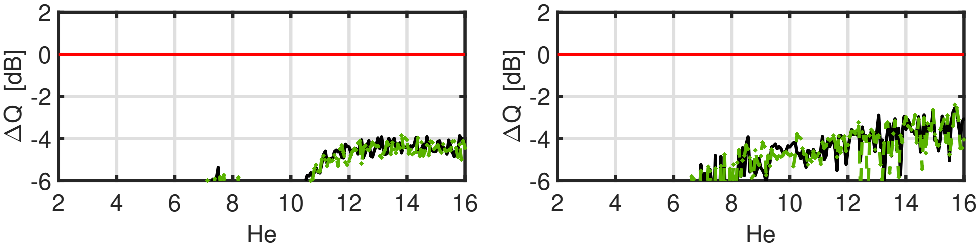

(c) $p = 1$ (d) $p = 1$ - $\mathbf{W}_0 = \mathrm{CB}$

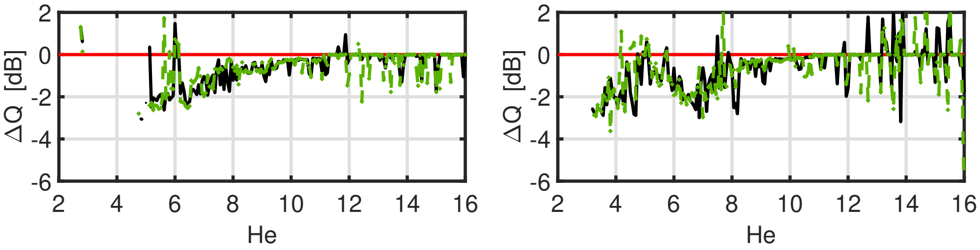

(e) $p = 0$ (f) $p = 0$ - $\mathbf{W}_0 = \mathrm{CB}$

Figure A.45: Test Case 2 (2D) - Errors in source spectrum reconstruction with ESM-IRLS with ED. Red line: target error. Black line: error of reconstructed spectrum (left source). Green line: error of reconstructed spectrum (right source).

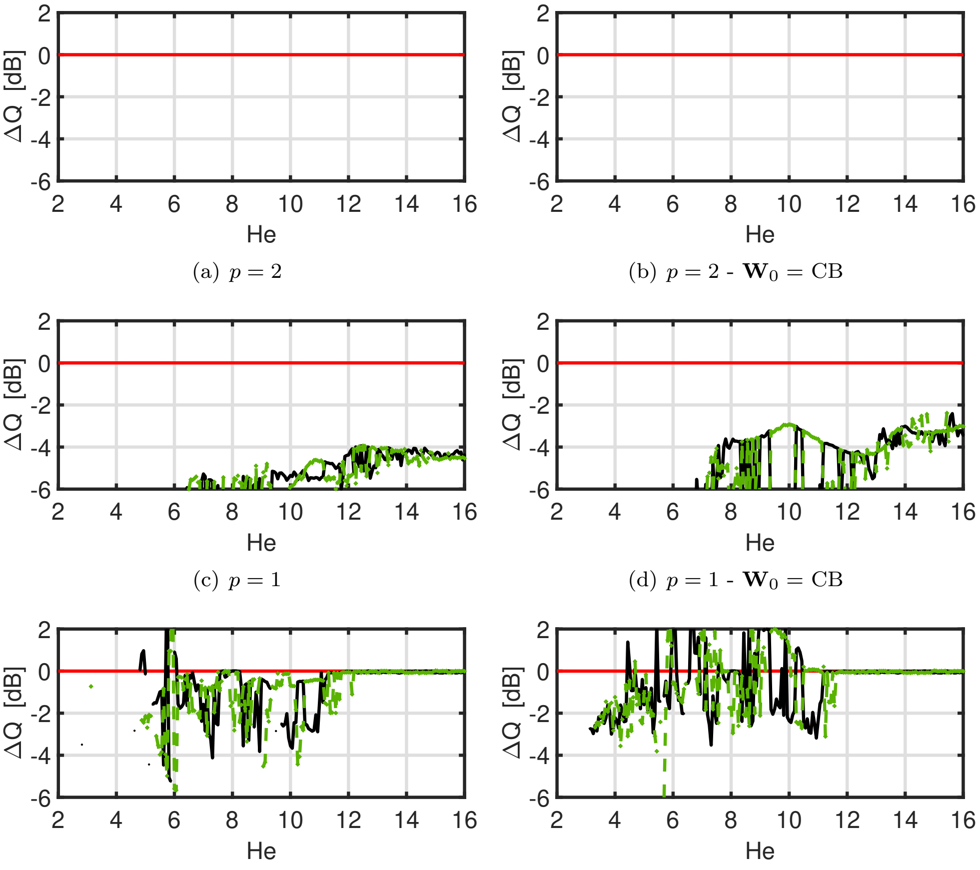

(a) $p = 2$

(b) $p = 2$ - $\mathbf{W}_0 = \mathrm{CB}$

(c) $p = 1$

(d) $p = 1$ - $\mathbf{W}_0 = \mathrm{CB}$

(e) $p = 0$

(f) $p = 0$ - $\mathbf{W}_0 = \mathrm{CB}$

Figure A.46: Test Case 2 (2D) - Errors in source spectrum reconstruction with ESM-IRLS with CSCD. Red line: target error. Black line: error of reconstructed spectrum (left source). Green line: error of reconstructed spectrum (right source).

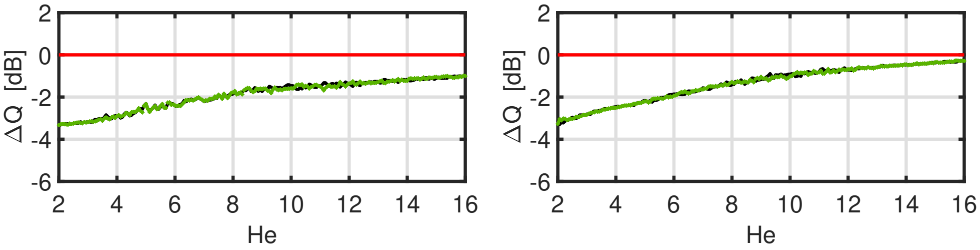

(a) $p = 2$

(b) $p = 2$ - $\mathbf{W}_0 = \mathrm{CB}$

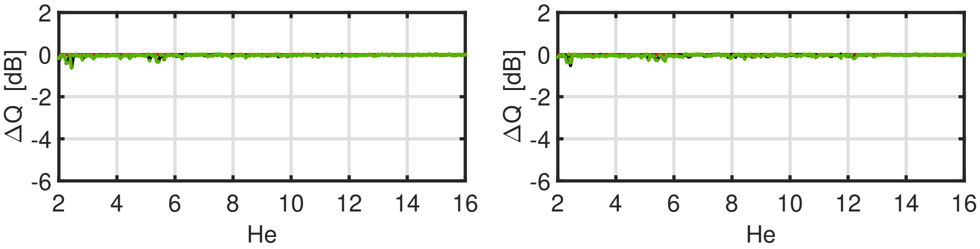

(c) $p = 1$

(d) $p = 1$ - $\mathbf{W}_0 = \mathrm{CB}$

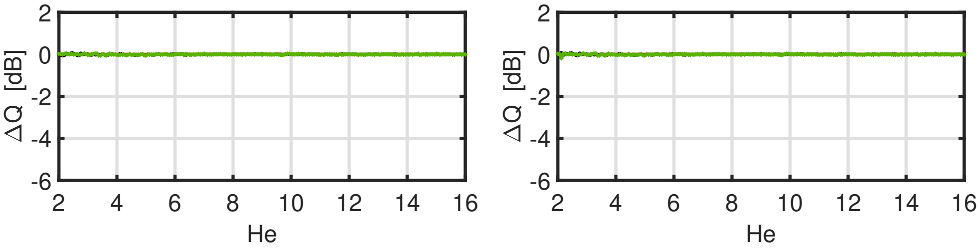

(e) $p = 0$

(f) $p = 0$ - $\mathbf{W}_0 = \mathrm{CB}$

Figure A.47: Test Case 2 (2D) - Errors in source spectrum reconstruction with CMF-IRLS on whole CSM. Red line: target error. Black line: error of reconstructed spectrum (left source). Green line: error of reconstructed spectrum (right source).

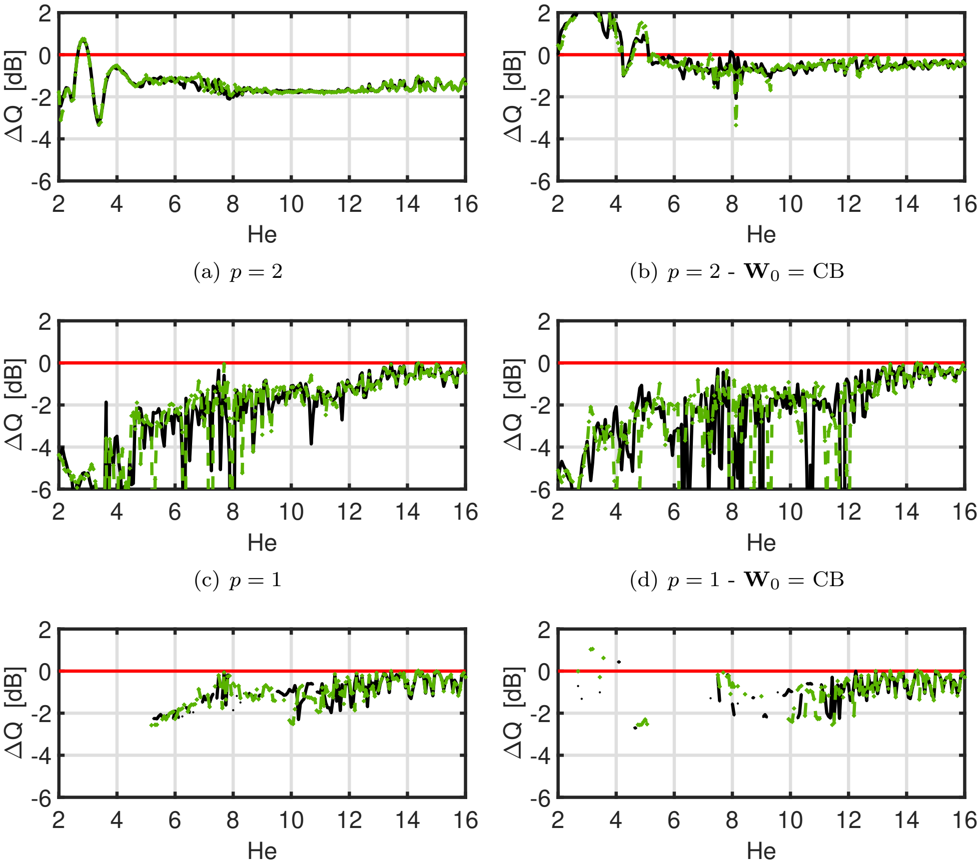

(a) $p = 2$

(b) $p = 2$ - $\mathbf{W}_0 = \mathrm{CB}$

(c) $p = 1$

(d) $p = 1$ - $\mathbf{W}_0 = \mathrm{CB}$

(e) $p = 0$

(f) $p = 0$ - $\mathbf{W}_0 = \mathrm{CB}$

Figure A.48: Test Case 2 (2D) - Errors in source spectrum reconstruction with CMF-IRLS with ED. Red line: target error. Black line: error of reconstructed spectrum (left source). Green line: error of reconstructed spectrum (right source).

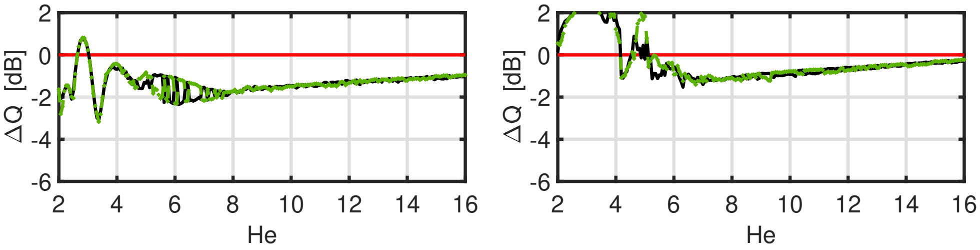

(a) $p = 2$ (b) $p = 2$ - $\mathbf{W}_0 = \mathrm{CB}$

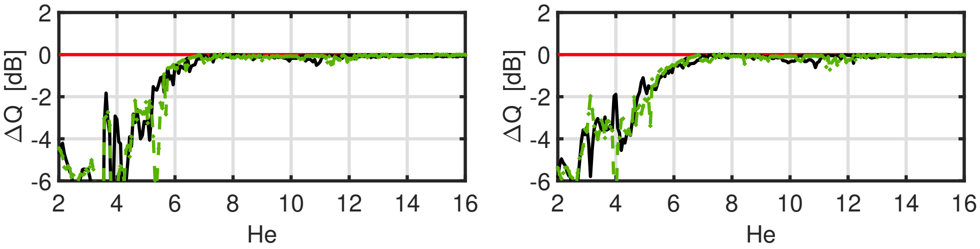

(c) $p = 1$ (d) $p = 1$ - $\mathbf{W}_0 = \mathrm{CB}$

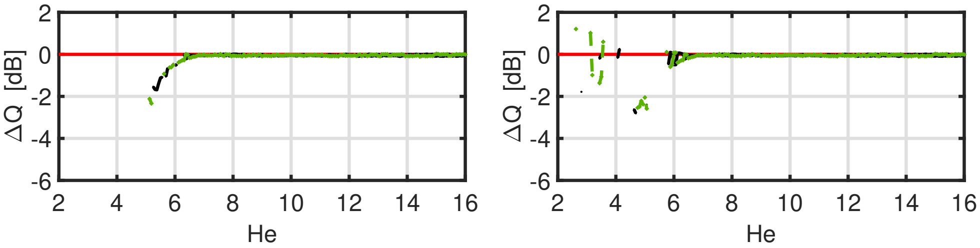

(e) $p = 0$ (f) $p = 0$ - $\mathbf{W}_0 = \mathrm{CB}$

Figure A.49: Test Case 2 (2D) - Errors in source spectrum reconstruction with CMF-IRLS with CSCD. Red line: target error. Black line: error of reconstructed spectrum (left source). Green line: error of reconstructed spectrum (right source).

A.3 Test Case 3 (TC3) - Figures

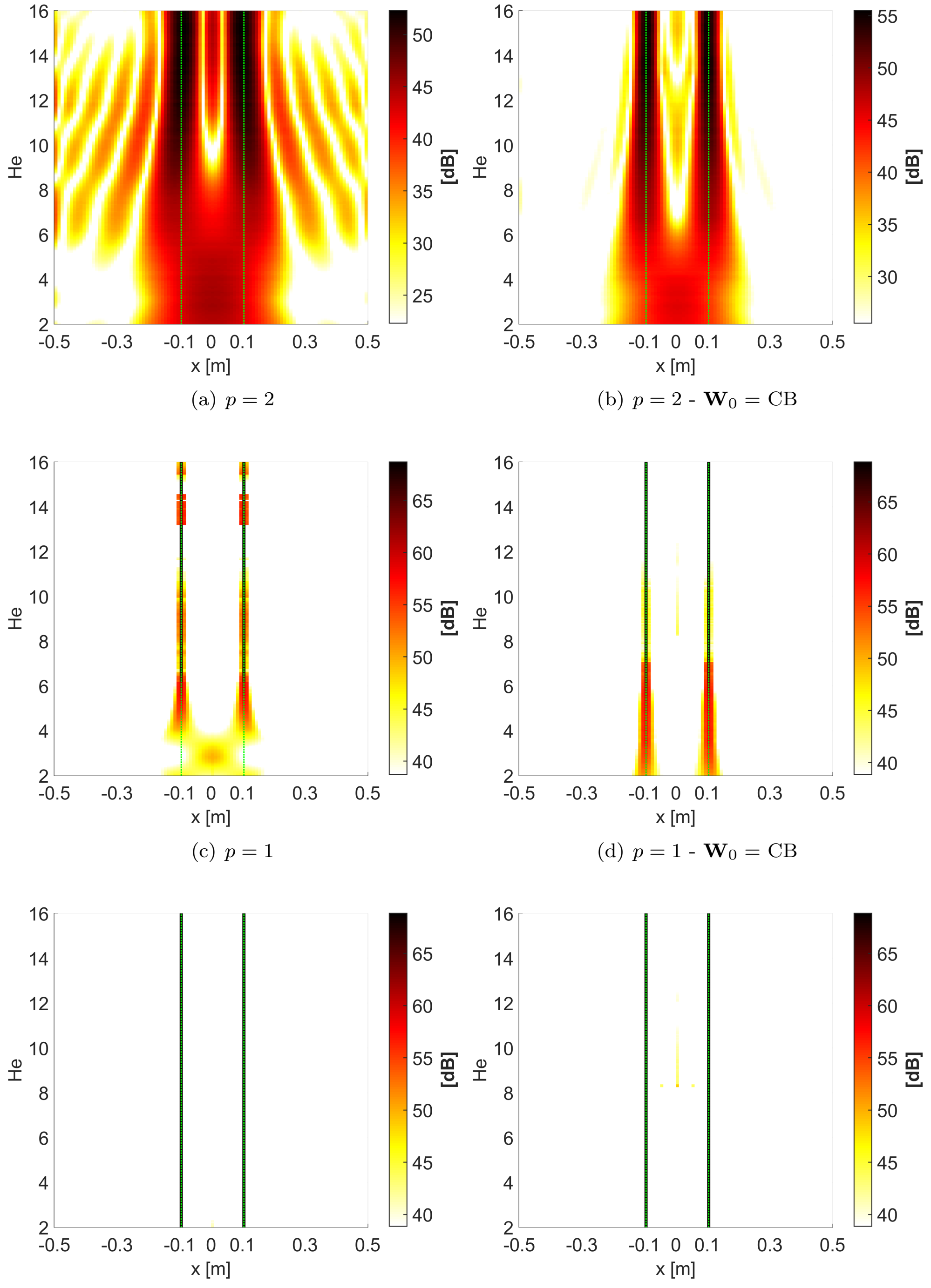

(a) $p = 2$ (b) $p = 2$ - $\mathbf{W}_0 = \mathrm{CB}$

(c) $p = 1$ (d) $p = 1$ - $\mathbf{W}_0 = \mathrm{CB}$

(e) $p = 0$ (f) $p = 0$ - $\mathbf{W}_0 = \mathrm{CB}$

Figure A.50: Test Case 3 (1D) - ESM-IRLS

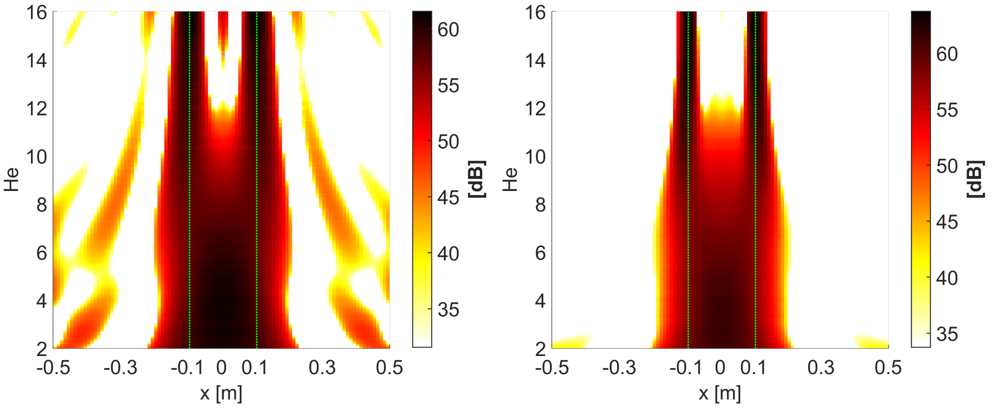

(a) $p = 2$ (b) $p = 2$ - $\mathbf{W}_0 = \text{CB}$

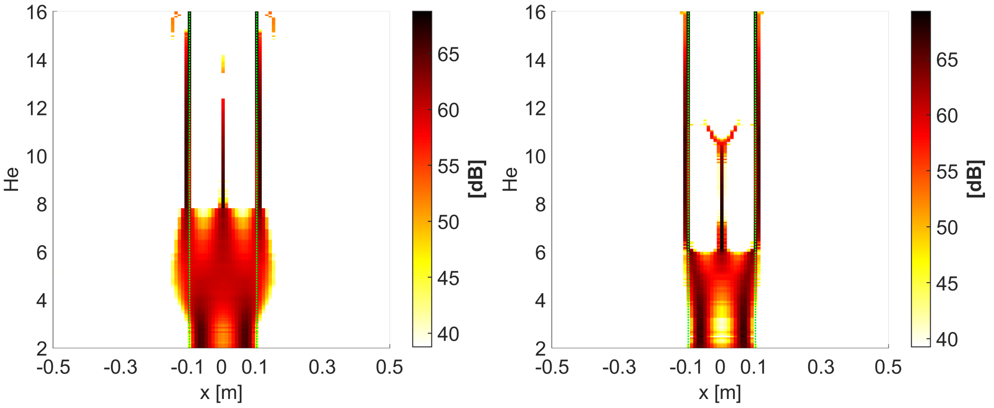

(c) $p = 1$ (d) $p = 1$ - $\mathbf{W}_0 = \text{CB}$

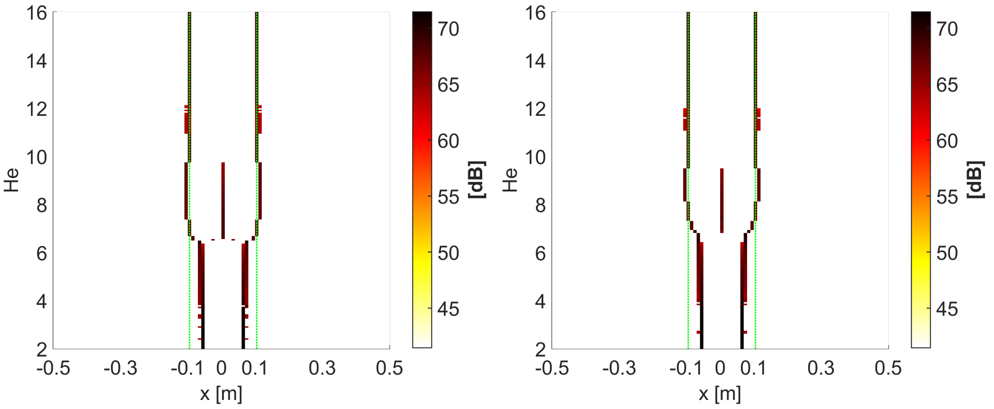

(e) $p = 0$ (f) $p = 0$ - $\mathbf{W}_0 = \text{CB}$

Figure A.51: Test Case 3 (1D) - CMF-IRLS on whole CSM

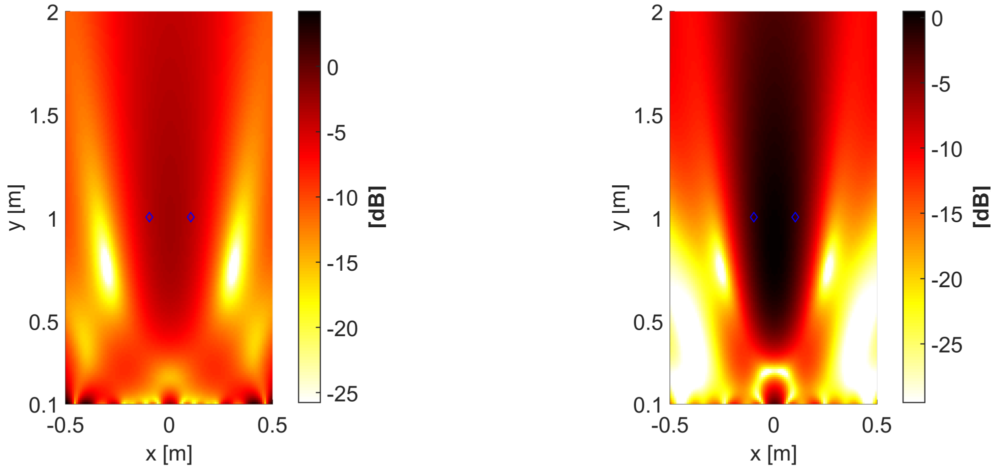

(a) $p = 2$ (b) $p = 2$ - $\mathbf{W}_0$ = CB

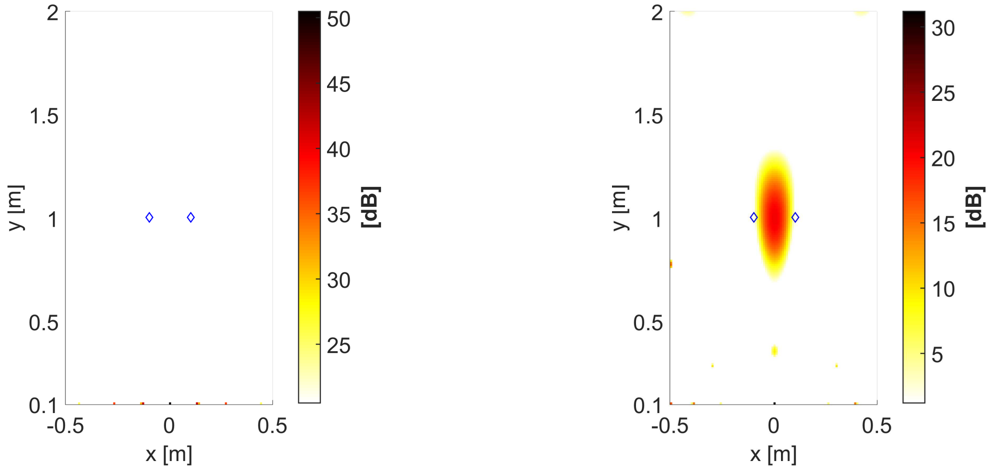

(c) $p = 1$ (d) $p = 1$ - $\mathbf{W}_0$ = CB

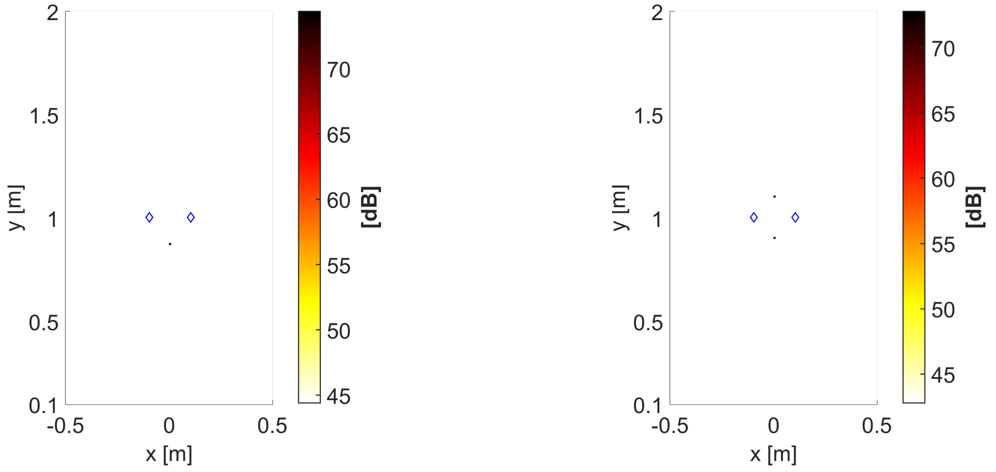

(e) $p = 0$ (f) $p = 0$ - $\mathbf{W}_0$ = CB

Figure A.52: Test Case 3 (2D) at $He = 2$ - ESM-IRLS

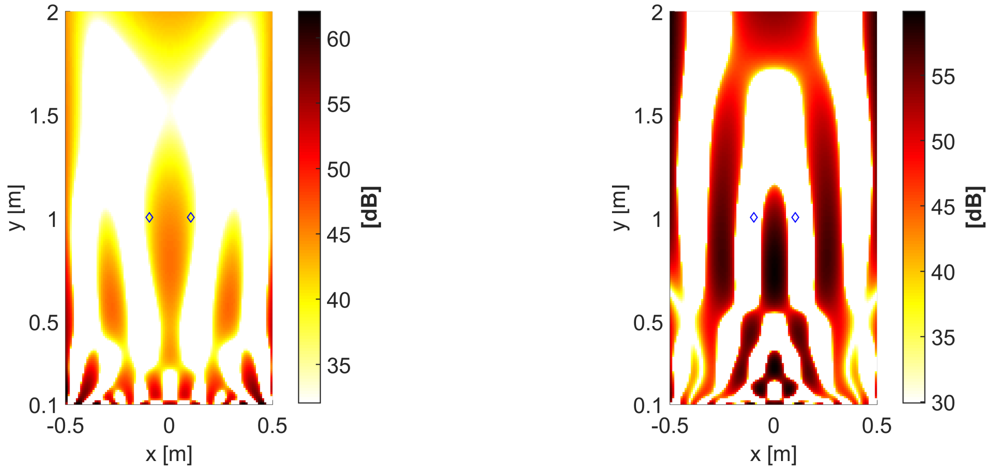

(a) $p = 2$ (b) $p = 2$ - $\mathbf{W}_0 = \mathrm{CB}$

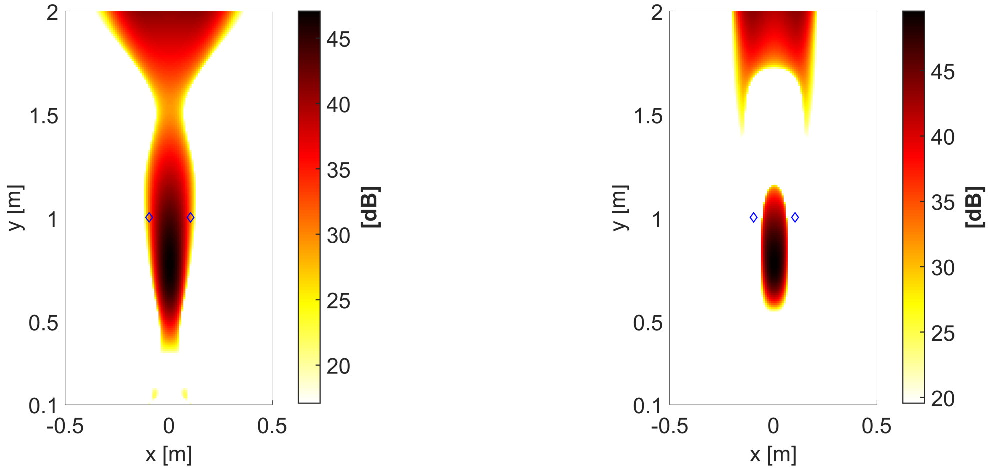

(c) $p = 1$ (d) $p = 1$ - $\mathbf{W}_0 = \mathrm{CB}$

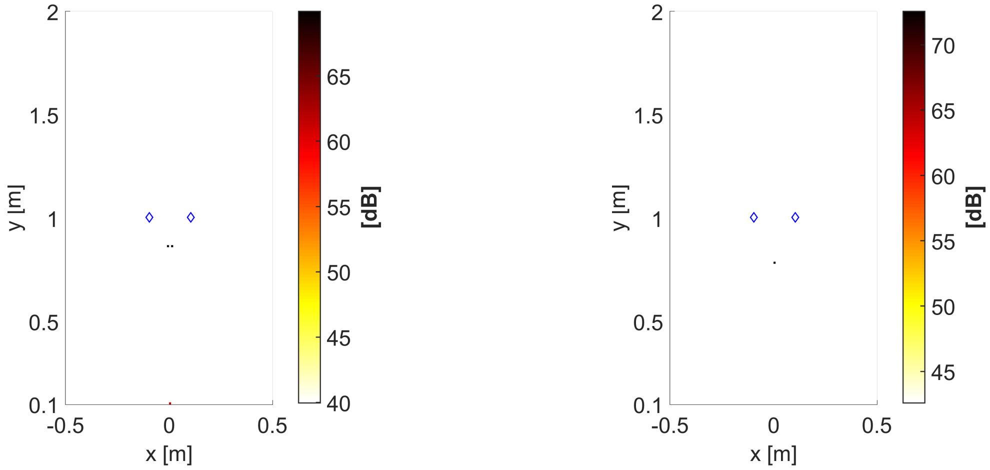

(e) $p = 0$ (f) $p = 0$ - $\mathbf{W}_0 = \mathrm{CB}$

Figure A.53: Test Case 3 (2D) at $He = 2$ - CMF-IRLS on whole CSM

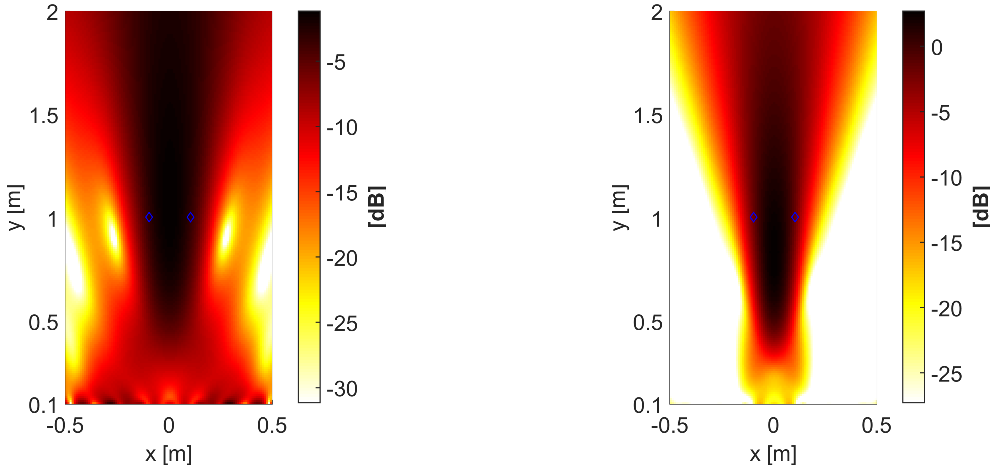

(a) $p = 2$ (b) $p = 2$ - $\mathbf{W}_0 = \mathrm{CB}$

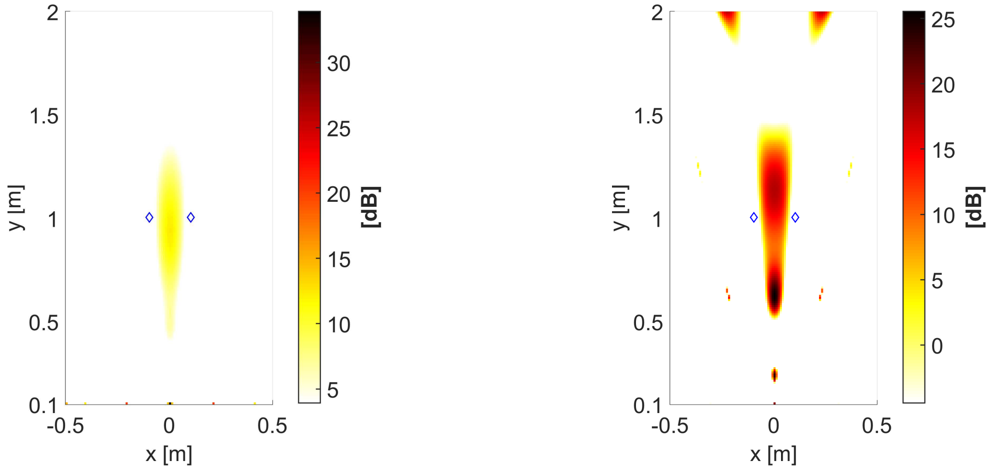

(c) $p = 1$ (d) $p = 1$ - $\mathbf{W}_0 = \mathrm{CB}$

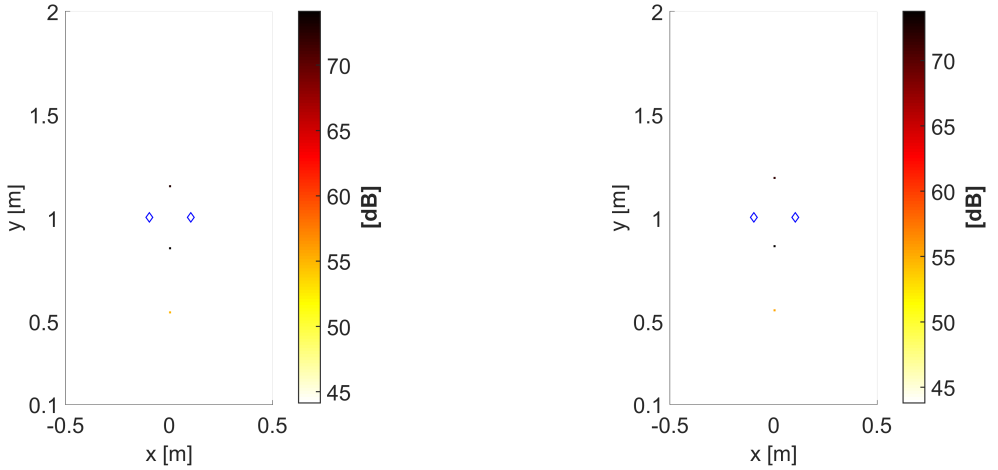

(e) $p = 0$ (f) $p = 0$ - $\mathbf{W}_0 = \mathrm{CB}$

Figure A.54: Test Case 3 (2D) at $He = 4$ - ESM-IRLS

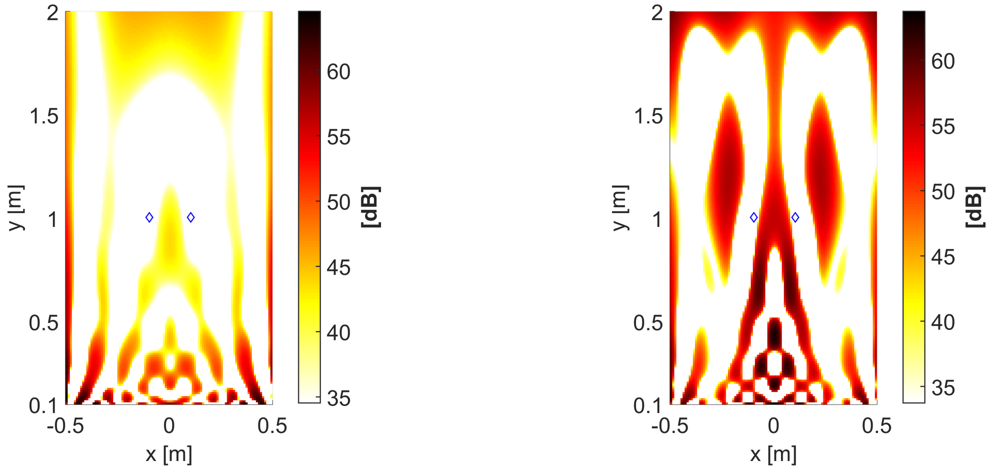

(a) $p = 2$ (b) $p = 2$ - $\mathbf{W}_0 = \text{CB}$

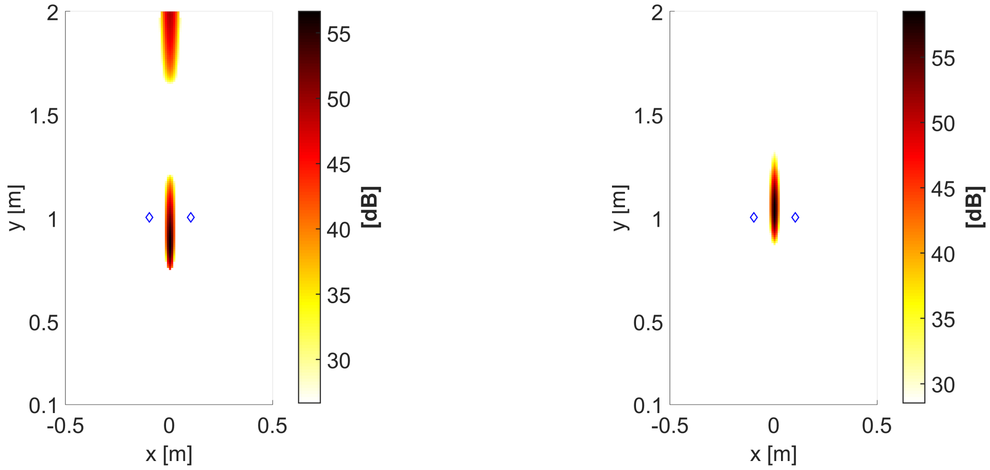

(c) $p = 1$ (d) $p = 1$ - $\mathbf{W}_0 = \text{CB}$

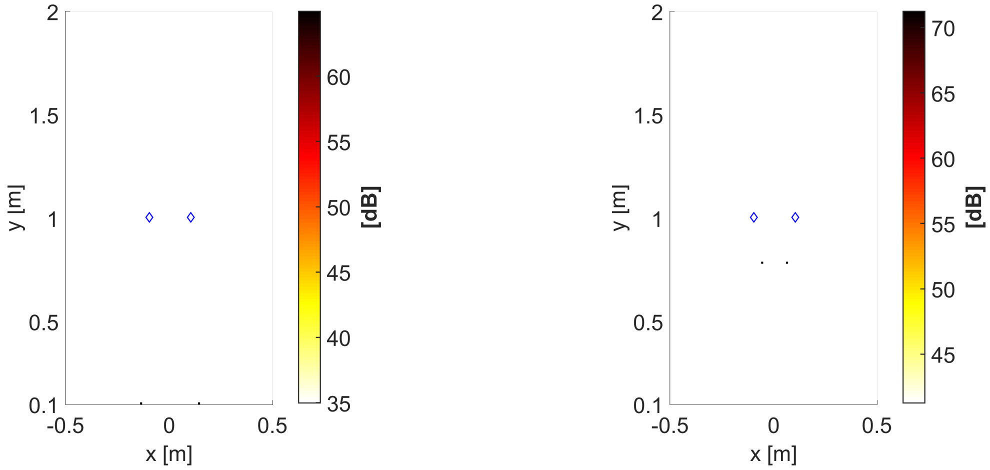

(e) $p = 0$ (f) $p = 0$ - $\mathbf{W}_0 = \text{CB}$

Figure A.55: Test Case 3 (2D) at $He = 4$ - CMF-IRLS on whole CSM

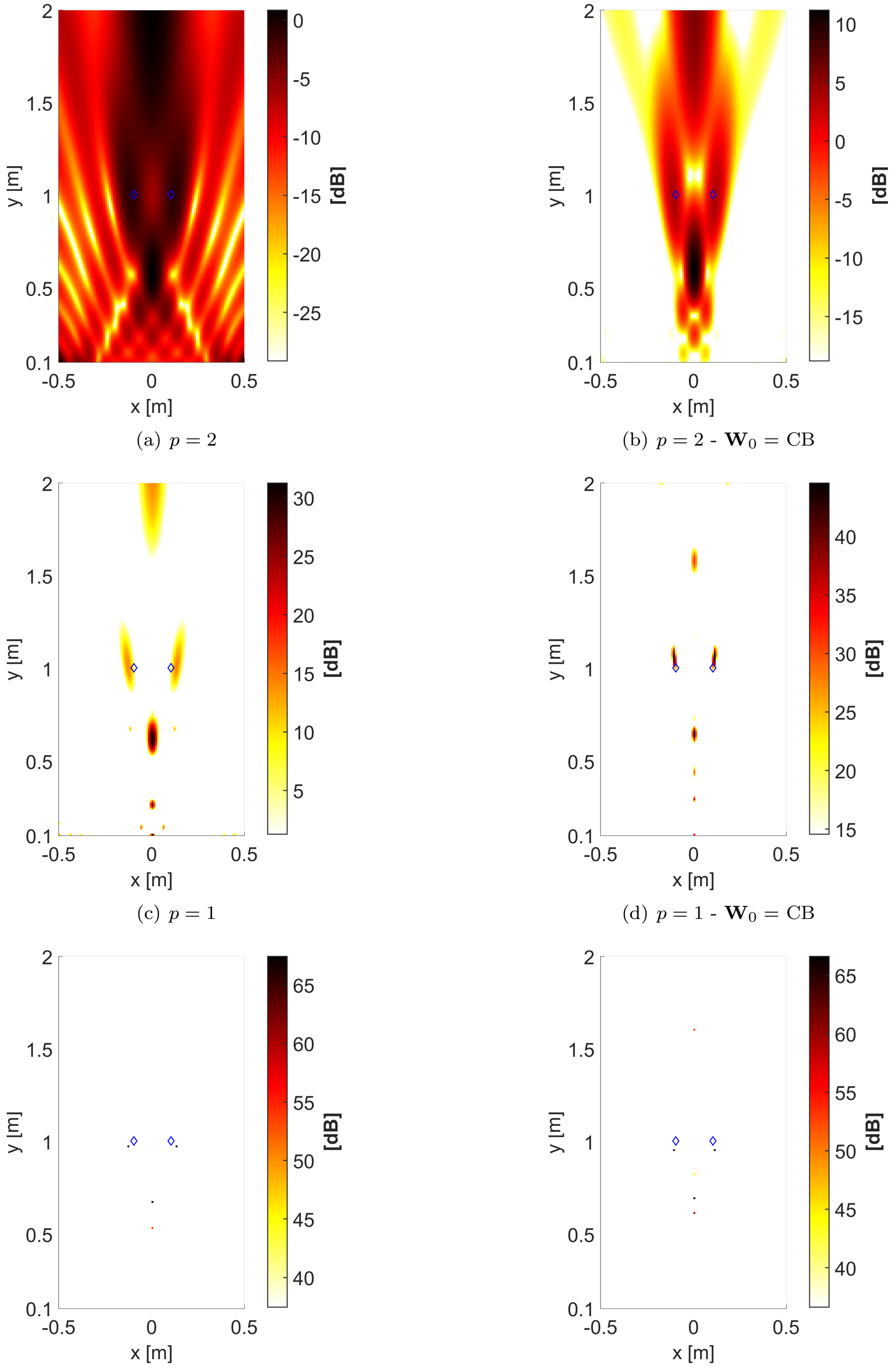

(a) $p = 2$

(b) $p = 2$ - $\mathbf{W}_0 = \text{CB}$

(c) $p = 1$

(d) $p = 1$ - $\mathbf{W}_0 = \text{CB}$

(e) $p = 0$

(f) $p = 0$ - $\mathbf{W}_0 = \text{CB}$

Figure A.56: Test Case 3 (2D) at $He = 8$ - ESM-IRLS

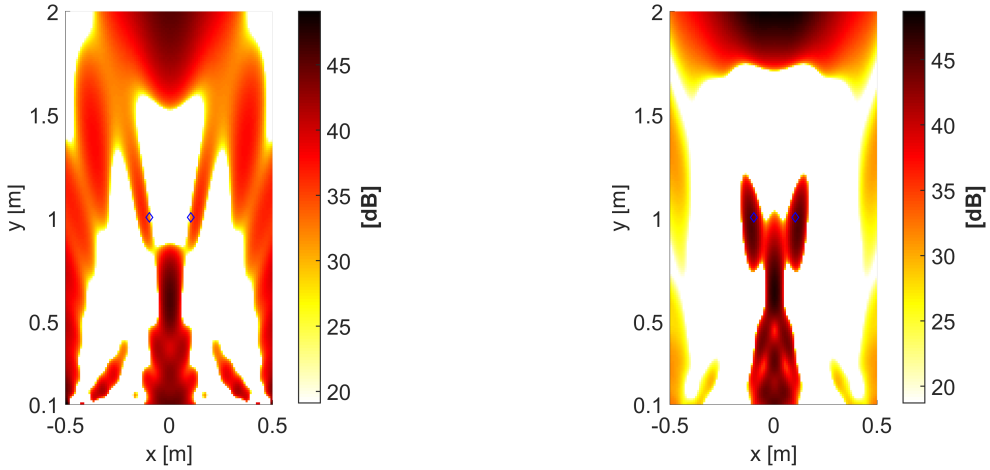

(a) $p = 2$ (b) $p = 2$ - $\mathbf{W}_0 = \mathrm{CB}$

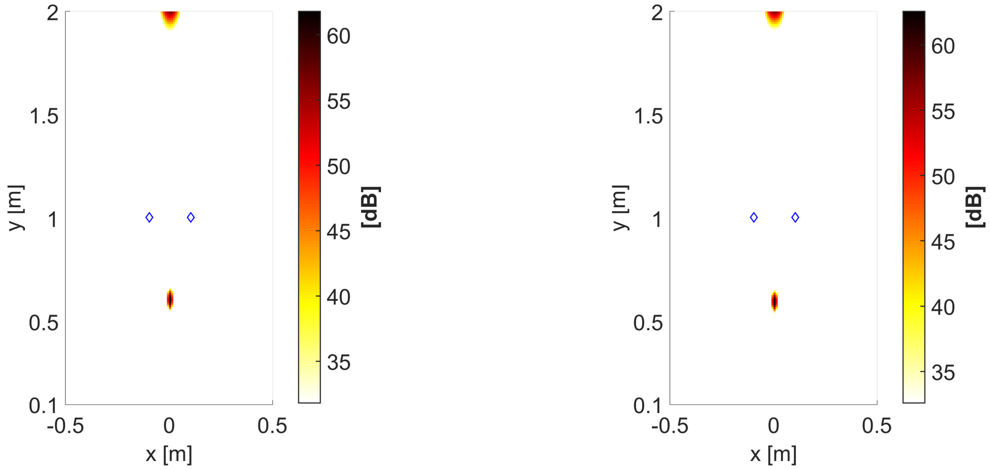

(c) $p = 1$ (d) $p = 1$ - $\mathbf{W}_0 = \mathrm{CB}$

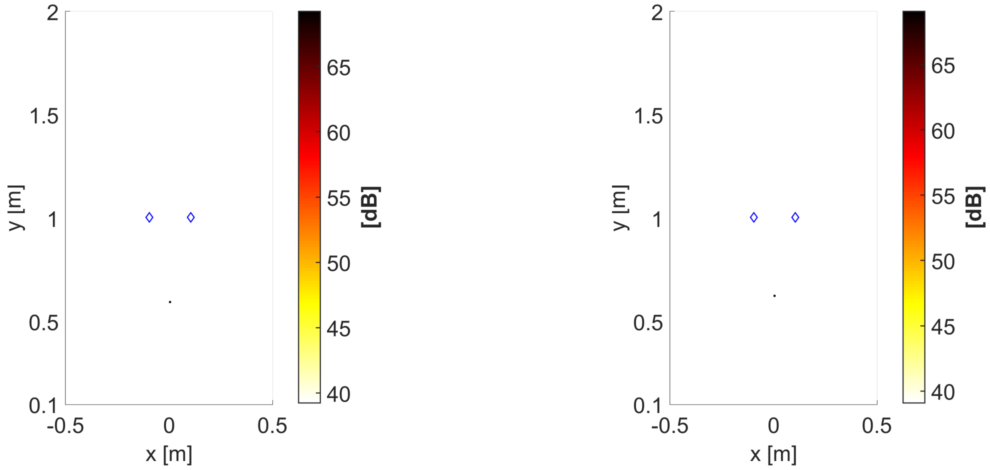

(e) $p = 0$ (f) $p = 0$ - $\mathbf{W}_0 = \mathrm{CB}$

Figure A.57: Test Case 3 (2D) at $He = 8$ - CMF-IRLS on whole CSM

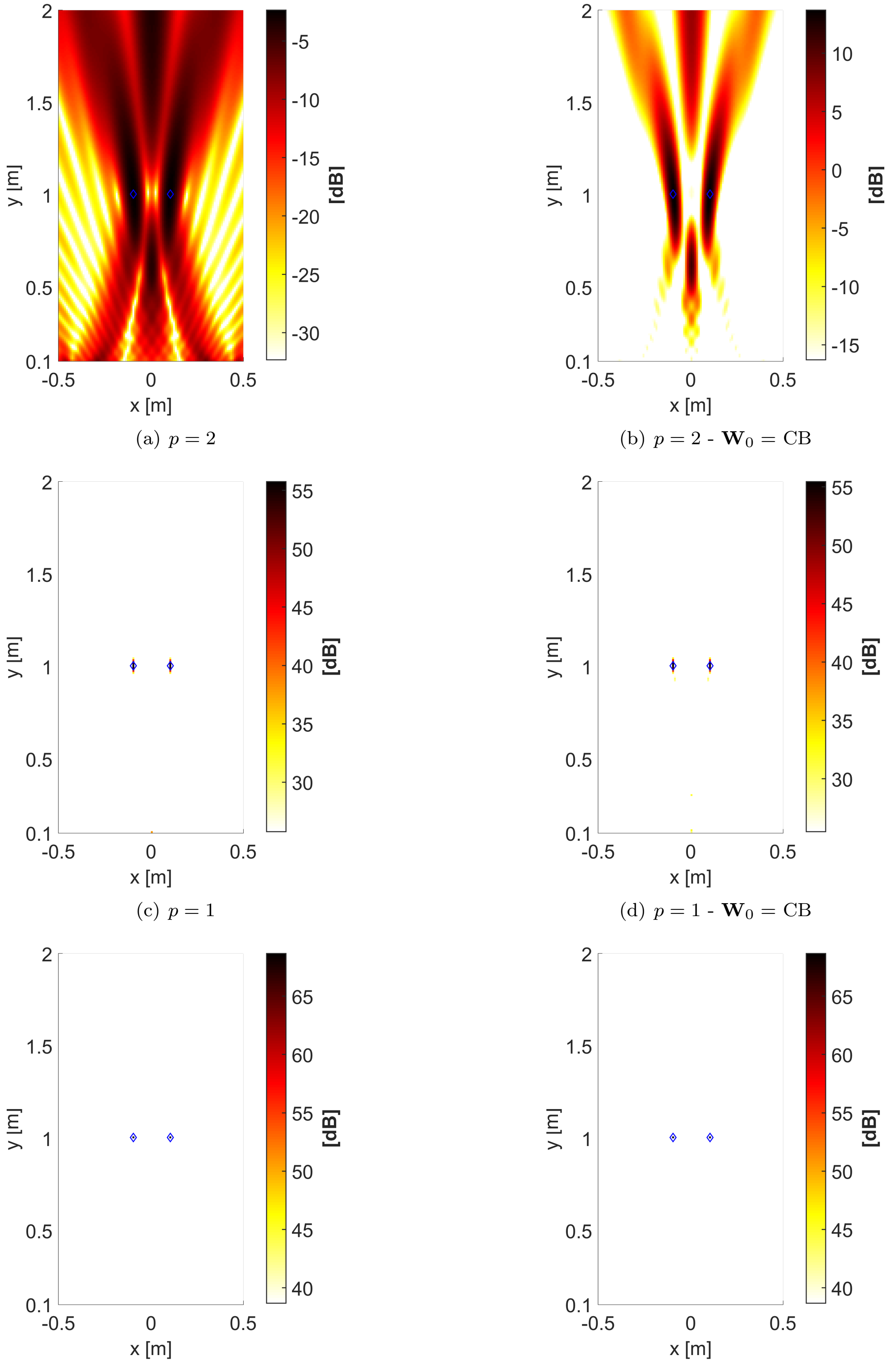

(a) $p = 2$

(b) $p = 2$ - $\mathbf{W}_0 = \mathrm{CB}$

(c) $p = 1$

(d) $p = 1$ - $\mathbf{W}_0 = \mathrm{CB}$

(e) $p = 0$

(f) $p = 0$ - $\mathbf{W}_0 = \mathrm{CB}$

Figure A.58: Test Case 3 (2D) at $He = 16$ - ESM-IRLS

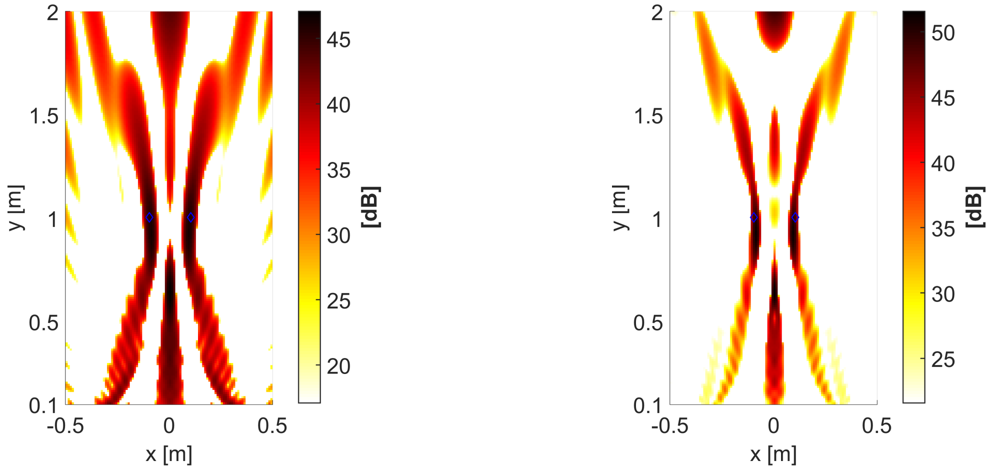

(a) $p = 2$ (b) $p = 2$ - $\mathbf{W}_0 = \text{CB}$

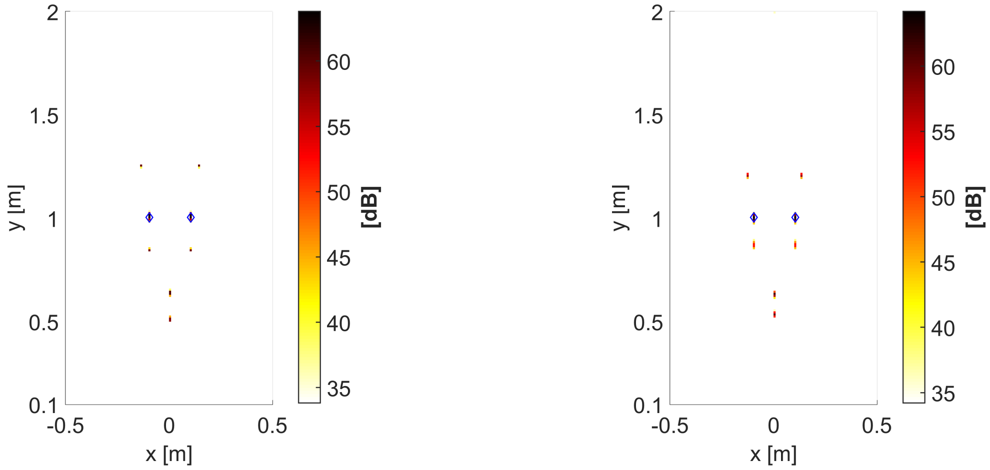

(c) $p = 1$ (d) $p = 1$ - $\mathbf{W}_0 = \text{CB}$

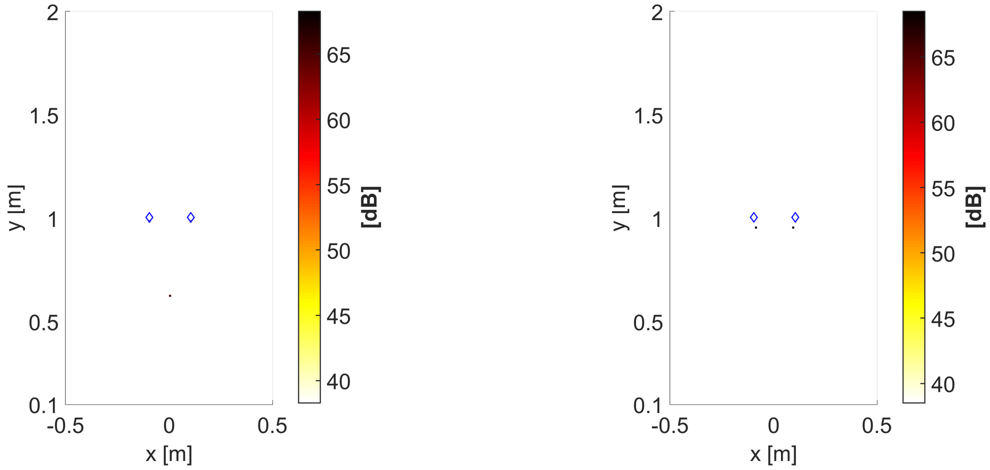

(e) $p = 0$ (f) $p = 0$ - $\mathbf{W}_0 = \text{CB}$

Figure A.59: Test Case 3 (2D) at $He = 16$ - CMF-IRLS on whole CSM

A.3.1 Reconstructed source spectra of Test Case 3

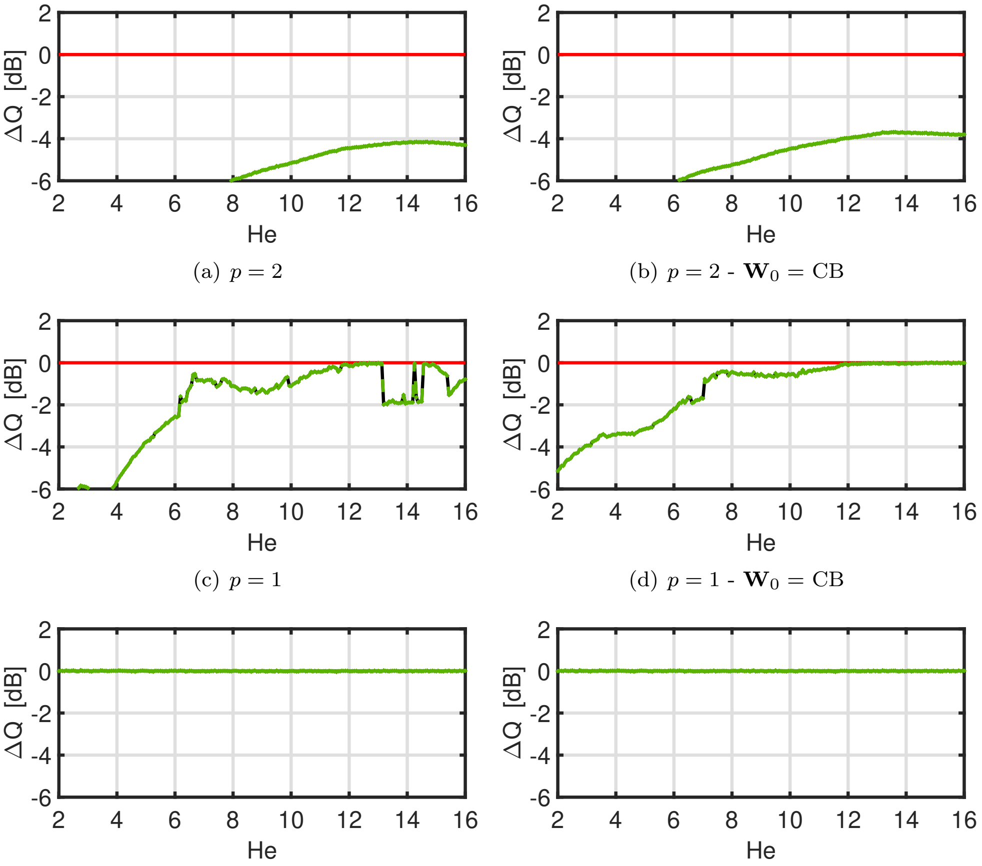

(a) $p = 2$

(b) $p = 2$ - $\mathbf{W}_0 = \mathrm{CB}$

(c) $p = 1$

(d) $p = 1$ - $\mathbf{W}_0 = \mathrm{CB}$

(e) $p = 0$

(f) $p = 0$ - $\mathbf{W}_0 = \mathrm{CB}$

Figure A.60: Test Case 3 (1D) - Errors in source spectrum reconstruction with ESM-IRLS. Red line: target error. Black line: error of reconstructed spectrum (left source). Green line: error of reconstructed spectrum (right source).

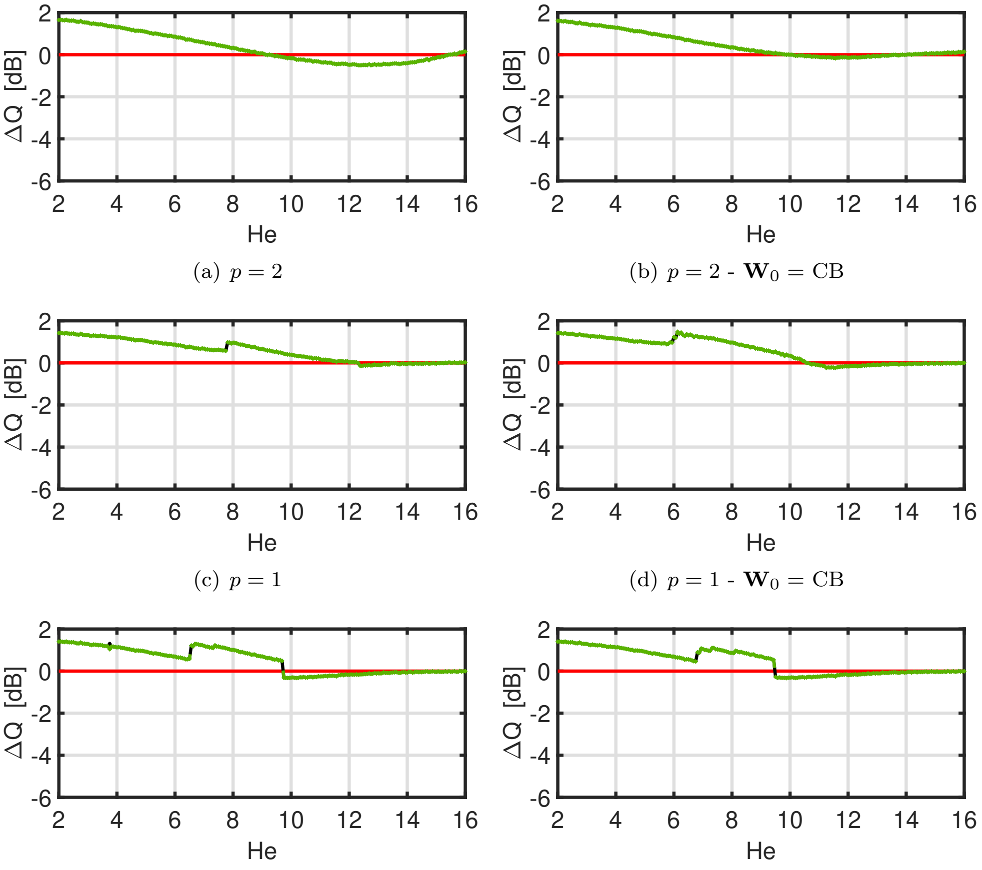

(a) $p = 2$

(b) $p = 2$ - $\mathbf{W}_0 = \mathrm{CB}$

(c) $p = 1$

(d) $p = 1$ - $\mathbf{W}_0 = \mathrm{CB}$

(e) $p = 0$

(f) $p = 0$ - $\mathbf{W}_0 = \mathrm{CB}$

Figure A.61: Test Case 3 (1D) - Errors in source spectrum reconstruction with CMF-IRLS. Red line: target error. Black line: error of reconstructed spectrum (left source). Green line: error of reconstructed spectrum (right source).

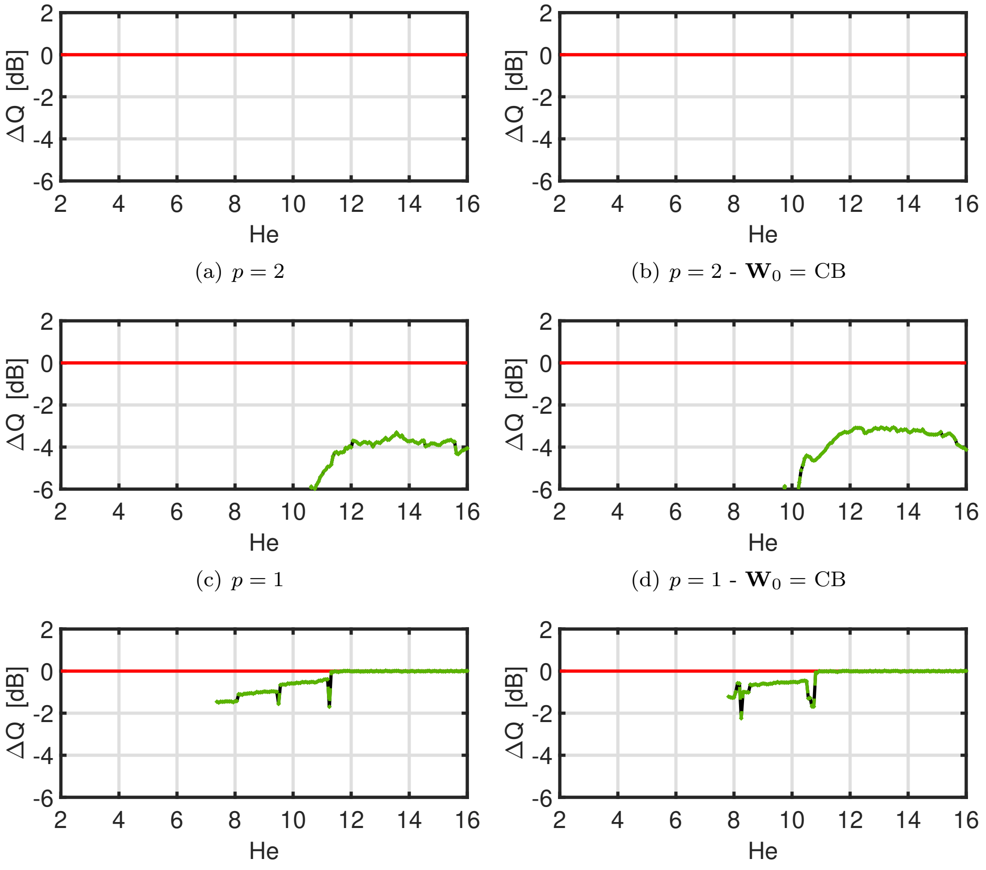

(a) $p = 2$

(b) $p = 2$ - $\mathbf{W}_0 = \mathrm{CB}$

(c) $p = 1$

(d) $p = 1$ - $\mathbf{W}_0 = \mathrm{CB}$

(e) $p = 0$

(f) $p = 0$ - $\mathbf{W}_0 = \mathrm{CB}$

Figure A.62: Test Case 3 (2D) - Errors in source spectrum reconstruction with ESM-IRLS. Red line: target error. Black line: error of reconstructed spectrum (left source). Green line: error of reconstructed spectrum (right source).

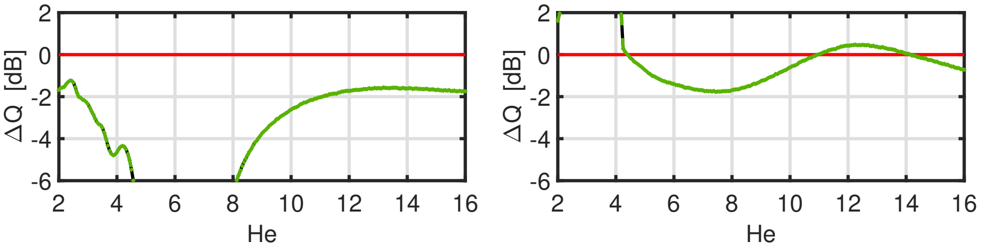

(a) $p = 2$

(b) $p = 2$ - $\mathbf{W}_0 = \mathrm{CB}$

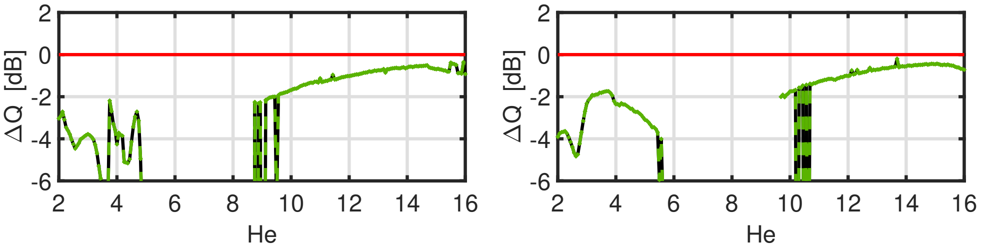

(c) $p = 1$

(d) $p = 1$ - $\mathbf{W}_0 = \mathrm{CB}$

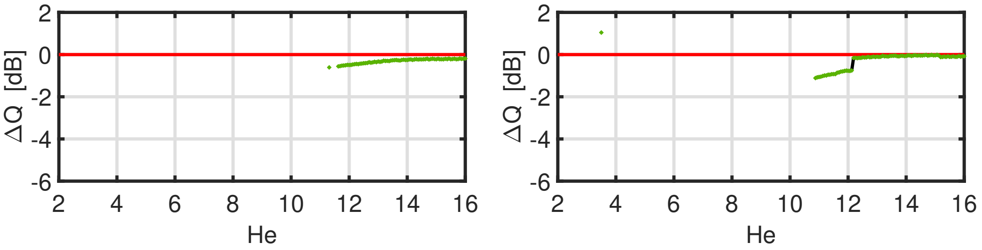

(e) $p = 0$

(f) $p = 0$ - $\mathbf{W}_0 = \mathrm{CB}$

Figure A.63: Test Case 3 (2D) - Errors in source spectrum reconstruction with CMF-IRLS. Red line: target error. Black line: error of reconstructed spectrum (left source). Green line: error of reconstructed spectrum (right source).

Bibliography

[1] Jérôme Antoni. A bayesian approach to sound source reconstruction: Optimal basis, regularization, and focusing. *The Journal of the Acoustical Society of America*, 131(4):2873–2890, apr 2012.

[2] Franz Aurenhammer. Voronoi diagrams—a survey of a fundamental geometric data structure. *ACM Computing Surveys*, 23(3):345–405, sep 1991.

[3] Gianmarco Battista, Paolo Chiariotti, Gert Herold, Ennes Sarradj, and Paolo Castellini. Inverse methods for three-dimensional acoustic mapping with a single planar array. In *Proceedings of the 7th Berlin Beamforming Conference*, 2018.

[4] J. Billingsley and R. Kinns. The Acoustic Telescope. *Journal of Sound and Vibration*, 48:485–510, 1976.

[5] T. F. Brooks and W. M. Humphreys, Jr. A Deconvolution Approach for the Mapping of Acoustic Sources (DAMAS) Determined from Phased Microphone Arrays. In *10th AIAA/CEAS Aeroacoustics Conference*, 2004.

[6] T. F. Brooks and W. M. Humphreys, Jr. A deconvolution approach for the mapping of acoustic sources (DAMAS) determined from phased microphone array. *Journal of Sound and Vibration*, 294(4-5):856–879, 2006.

[7] Humphreys W.M. Brooks T.F. A deconvolution approach for the mapping of acoustic sources (damas) determined from phased microphone arrays. *Journal of Sound and Vibration*, 294:856–879, 2006.

[8] Humphreys W.M. Brooks T.F. Extension of damas phased array processing for spatial coherence determination (damas-c). *12th AIAA/CEAS Aeroacoustics Conference*, May 2006.

[9] J. Capon. High-resolution frequency-wavenumber spectrum analysis. *IEEE*, 57(8):1408–1418, 1969.

[10] F. Champagnat and J. Idier. A connection between half-quadratic criteria and EM algorithms. *IEEE Signal Processing Letters*, 11(9):709–712, sep 2004.

[11] Rick Chartrand and Wotao Yin. Iteratively reweighted algorithms for compressive sensing. In *2008 IEEE International Conference on Acoustics, Speech and Signal Processing*. IEEE, mar 2008.

[12] Paolo Chiariotti, Milena Martarelli, and Paolo Castellini. Acoustic beamforming for noise source localization – reviews, methodology and applications. *Mechanical Systems and Signal Processing*, 120:422–448, apr 2019.

[13] Ingrid Daubechies, Ronald DeVore, Massimo Fornasier, and C. Sinan Güntürk. Iteratively reweighted least squares minimization for sparse recovery. *Communications on Pure and Applied Mathematics*, 63(1):1–38, jan 2010.

[14] Dirk Döbler, Jörg Ocker, and Christof Puhle. On 3D-beamforming in the wind tunnel. 2016.

[15] Bin Dong, Jérôme Antoni, and Erliang Zhang. Blind separation of sound sources from the principle of least spatial entropy. *Journal of Sound and Vibration*, 333(9):2643–2668, 2014.

[16] R. P. Dougherty. Extensions of DAMAS and Benefits and Limitations of Deconvolution in Beamforming. In *11th AIAA/CEAS Aeroacoustics Conference, Monterey, California, May 23-25, 2005*, 2005.

[17] R. P. Dougherty. What is Beamforming? In *2nd BeBec*, 2008.

[18] R. P. Dougherty. Functional beamforming. In *5th BeBec*, 2014.

[19] G. Elias. Source localization with a two-dimensional focused array: Optimal signal processing for a cross-shaped array. *Inter-Noise*, pages 1175–1178, 1995. cited By 21.

[20] Gianmarco Battista, Paolo Chiariotti, Milena Martarelli, and Paolo Castellini. Inverse methods in aeroacoustic three-dimensional volumetric noise source localization. In *Proceedings o ISMA-USD 2018*, 2018.

[21] Jacques Hadamard. Sur les problèmes aux dérivés partielles et leur signification physique. *Princeton University Bulletin*, 13:49–52, 1902.

[22] Per Christian Hansen. The discrete picard condition for discrete ill-posed problems. *BIT*, 30(4):658–672, dec 1990.

[23] Per Christian Hansen. Regularization tools: A matlab package for analysis and solution of discrete ill-posed problems. *Numerical algorithms*, 6(1):1–35, 1994.

[24] Per Christian Hansen. *Rank-deficient and discrete ill-posed problems.* SIAM Monographs on Mathematical Modeling and Computation. Society for Industrial and Applied Mathematics (SIAM), Philadelphia, PA, 1998. Numerical aspects of linear inversion.

[25] Gert Herold, Thomas F. Geyer, and Ennes Sarradj. Comparison of inverse deconvolution algorithms for high-resolution aeroacoustic source characterization. In *23rd AIAA/CEAS Aeroacoustics Conference*. American Institute of Aeronautics and Astronautics, jun 2017.

[26] Amiet R. K. Correction of open jet wind tunnel measurements for shear layer refraction. *AIAA Journal*, 1975.

[27] Y. Kim and P.A. Nelson. Optimal regularisation for acoustic source reconstruction by inverse methods. *Journal of Sound and Vibration*, 275(3-5):463–487, aug 2004.

[28] Gary H. Koopmann, Limin Song, and John B. Fahnline. A method for computing acoustic fields based on the principle of wave superposition. *The Journal of the Acoustical Society of America*, 86(6):2433–2438, dec 1989.

[29] Q. Leclère. Acoustic imaging using under-determined inverse approaches: Frequency limitations and optimal regularization. *Journal of Sound and Vibration*, 321(3-5):605–619, 2009.

[30] Q. Leclere, Antonio A. Pereira, and Jérôme Antoni. Une approche bayésienne de la parcimonie pour l'identification de sources acoustiques. In *Congrès Français d'Acoustique*, pages –, Poitiers, France, 2014.

[31] Quentin Leclère, Antonio Pereira, Christophe Bailly, Jerome Antoni, and Christophe Picard. A unified formalism for acoustic imaging techniques: illustrations in the frame of a didactic numerical benchmark. In *Proceedings on CD of the 6th Berlin Beamforming Conference, 29 February-1 March 2016*, February 2016.

[32] Anwar Malgoezar, Mirjam Snellen, Pieter Sijtsma, and Dick Simons. Improving beamforming by optimization of acoustic array microphones positions. In *6th Berlin Beamforming Conference*, 2016.

[33] S.G. Mallat and Zhifeng Zhang. Matching pursuits with time-frequency dictionaries. *IEEE Transactions on Signal Processing*, 41(12):3397–3415, 1993.

[34] U. Michel. History of acoustic beamforming. In *1st BeBec*, 2006.

[35] Fangli Ning, Jingang Wei, Lianfang Qiu, Hongbing Shi, and Xiaofan Li. Three-dimensional acoustic imaging with planar microphone arrays and compressive sensing. *Journal of Sound and Vibration*, 380:112–128, oct 2016.

[36] S. Oerlemans and P. Sijtsma. Determination of Absolute Levels from Phased Array Measurements Using Spatial Source Coherence. In *8th AIAA/CEAS Aeroacoustics Conference and Exhibit, Breckenridge, Colorado, June 17-19, 2002*, 2002.

[37] B. Oudompheng, A. Pereira, C. Picard, Q Leclère, and B. Nicolas. A theoretical and experimental comparison of the iterative equivalent source method and the generalized inverse beamforming. In *5th BeBec*, 2014.

[38] Sijtsma P. Clean based on spatial source coherence. *International Journal of Aeroacoustics*, 6(4):357–374, December 2007.

[39] Thomas Padois and Alain Berry. Two and three-dimensional sound source localization with beamforming and several deconvolution techniques. *Acta Acustica united with Acustica*, 103(3):392–400, may 2017.

[40] Y. C. Pati, R. Rezaiifar, and P. S. Krishnaprasad. Orthogonal matching pursuit: Recursive function approximation with applications to wavelet decomposition. In *in Conference Record of The Twenty-Seventh Asilomar Conference on Signals, Systems and Computers*, pages 1–3, 1993.

[41] A. Pereira, J. Antoni, and Q. Leclère. Empirical bayesian regularization of the inverse acoustic problem. *Applied Acoustics*, 97:11–29, oct 2015.

[42] A. Pereira and Q. Leclère. Improving the Equivalent Source Method for noise source identification in enclosed spaces. In *18th International Congress on Sound and Vibration (ICSV 18)*, page R31, Brazil, July 2011.

[43] Antonio Pereira. *Acoustic imaging in enclosed spaces.* PhD thesis, INSA de Lyon, 2014.

[44] Ric Porteous, Zebb Prime, Con.J. Doolan, Danielle.J. Moreau, and Vincent Valeau. Three-dimensional beamforming of dipolar aeroacoustic sources. *Journal of Sound and Vibration*, 355:117–134, oct 2015.

[45] E. Sarradj. Three-dimensional acoustic source mapping. In *4th Bebec*, 2012.

[46] E. Sarradj. Three-dimensional acoustic source mapping with different beamforming steering vector formulations. *Advances in Acoustics and Vibration*, 2012(292695):1–12, 2012.

[47] E. Sarradj, C. Schulze, and A. Zeibig. Identification of Noise Source Mechanisms using Orthogonal Beamforming. In *Noise and Vibration: Emerging Methods*, 2005.

[48] Ennes Sarradj. A generic approach to synthesize optimal array microphone arrangements. In *6th Berlin Beamforming Conference*, 2016.

[49] Ennes Sarradj and Gert Herold. A python framework for microphone array data processing. *Applied Acoustics*, 116:50–58, jan 2017.

[50] Takao Suzuki. L1 generalized inverse beam-forming algorithm resolving coherent/incoherent, distributed and multipole sources. *Journal of Sound and Vibration*, 330:5835–5851, 2011.

[51] Yardibi T, Liy J, Stoica P, and Cattafesta L N. Sparsity constrained deconvolution approaches for acoustic source mapping. *14th AIAA/CEAS Aeroacoustics Conference*, AIAA 2008-2956, 2008.

[52] A. N. Tikhonov. Solution of incorrectly formulated problems and the regularization method. *Soviet Math. Dokl.*, 4:1035–1038, 1963.

[53] E. van den Berg and M. P. Friedlander. SPGL1: A solver for large-scale sparse reconstruction, June 2007. http://www.cs.ubc.ca/labs/scl/spgl1.

[54] E. van den Berg and M. P. Friedlander. Probing the pareto frontier for basis pursuit solutions. *SIAM Journal on Scientific Computing*, 31(2):890–912, 2008.

[55] Jack R. Williams. Fast beam-forming algorithm. *The Journal of the Acoustical Society of America*, 44(5):1454–1455, nov 1968.

[56] Tarik Yardibi, Jian Li, Petre Stoica, and Louis N. Cattafesta. Sparsity constrained deconvolution approaches for acoustic source mapping. *The Journal of the Acoustical Society of America*, 123(5):2631–2642, 2008.

[57] Tarik Yardibi, Jian Li, Petre Stoica, Nikolas S. Zawodny, and Louis N. Cattafesta. A covariance fitting approach for correlated acoustic source mapping. *The Journal of the Acoustical Society of America*, 127(5):2920–2931, may 2010.